



LAWRENCE  
LIVERMORE  
NATIONAL  
LABORATORY

# Arc Initiation of High Explosives: Final Report

J. F. McCarrick, C. D. Grant, V. Tang, E. A.  
Glascoe, J. M. Zaug, H. Wang

March 22, 2012

## **Disclaimer**

---

This document was prepared as an account of work sponsored by an agency of the United States government. Neither the United States government nor Lawrence Livermore National Security, LLC, nor any of their employees makes any warranty, expressed or implied, or assumes any legal liability or responsibility for the accuracy, completeness, or usefulness of any information, apparatus, product, or process disclosed, or represents that its use would not infringe privately owned rights. Reference herein to any specific commercial product, process, or service by trade name, trademark, manufacturer, or otherwise does not necessarily constitute or imply its endorsement, recommendation, or favoring by the United States government or Lawrence Livermore National Security, LLC. The views and opinions of authors expressed herein do not necessarily state or reflect those of the United States government or Lawrence Livermore National Security, LLC, and shall not be used for advertising or product endorsement purposes.

This work performed under the auspices of the U.S. Department of Energy by Lawrence Livermore National Laboratory under Contract DE-AC52-07NA27344.

## **Arc Initiation of High Explosives: Final Report**

09-ERD-042  
November 28, 2011

Sponsoring Directorate: WCI

P.I.: James F. McCarrick

Team: Christian D. Grant, Vincent Tang, Elizabeth A. Glascoe, Joseph M. Zaug, Han Wang

This work performed under the auspices of the U. S. Department of Energy by Lawrence Livermore National Laboratory under Contract DE-AC52-07NA27344 and supported by the Laboratory Directed Research and Development Program (09-ERD-042) at LLNL.

# Table of Contents

<b>Project Summary</b>	4
Planned Scope	4
Executed Scope	4
Technical Accomplishments	4
Milestones and Publications	8
Project Exit	8
<b>1. Introduction</b>	9
1.1. Approach	10
1.2. Layout of this document	11
<b>2. Pulsar Design and Operation</b>	12
2.1. Pulsar Design	12
2.2. Coupon and Holder Design (For Plasma Characterization)	15
2.3. Pulsar Output Characterization	16
2.4. Revised Holder Designs (For TRIR)	18
<b>3. Discharge Characterization with Energetic and Inert Thin Films</b>	22
3.1. Summary of Diagnostics	22
3.2. Summary of Results	23
<b>4. Time-Resolved Infrared Spectroscopy of Thin Films</b>	27
4.1. Methodology	27
4.2. Results, First Campaign	28
4.3. Preliminary Results, Second Campaign: Noise Issues	31
4.4. Hardware Failure and Attempted Recovery	38
<b>5. Pumped Convective Burn</b>	40
5.1. Background	40
5.2. Physical Model	42
5.3. Mathematical Model	44
5.4. Various Empirical Choices	47
5.4.1. Heat Transfer and Viscous Shear	47
5.4.2. External Heating	48
5.4.3. Burn Model	49
5.4.3.1. Hard Threshold Limit	50
5.4.3.2. Single-step Arrhenius with Constant Heat Flux	51
5.4.3.3. Concluding Remarks on Burn Velocity	56
5.5. Some Cylindrical Time-Dependent Threshold Results	57
5.6. Burn Rate from Multi-Step Models	61
5.6.1. Eigenvalue Calculations with Existing Multi-Step Models	61
5.6.2. Comparison with DAC Data	64
5.7. Derivation of a Steady PCB Wave	66
5.7.1. Planar Time-Dependent Simulations	67

5.7.2. Details of the Derivation	72
5.7.1.1. The Heating Region	74
5.7.1.2. The Burning Region	76
5.7.1.3. The Self-Similar Region	77
5.7.3. Discussion of Results	80
5.8. Concluding Comments	81
5.9. Selected References	82
<b>6. Comparative Response of PETN and TATB: A Preliminary Study</b>	<b>84</b>
6.1. Description of the Configuration	84
6.2. Results	86
6.3. Recommendations for Future Capillary Testing	90
<b>Appendix A. Listing of PCB Modeling Tools</b>	<b>91</b>
<b>Appendix B. MATLAB Code for RLC Fits to Pulser Waveforms</b>	<b>99</b>
<b>Appendix C. MATLAB Code for Fitting Temperature and Density</b>	<b>102</b>
<b>Appendix D. Summer Student Report on Numerical Approach to Hydro Modeling.</b>	<b>109</b>
<b>Appendix E. MATLAB Code for Processing TRIR Data</b>	<b>133</b>
<b>Appendix F. Drawings of Clamp and Holder Hardware</b>	<b>138</b>

## **Project Summary**

Arc initiation of high explosives (HE) can occur when electrical breakdown takes place at an interface or through the bulk of the HE. It can occur in accidental scenarios involving electrostatic discharge (ESD), natural scenarios such as lightning, and engineered scenarios such as spark detonators. The unique combination of short time scale, extremely high temperature, and relatively low pressure results in an initiation regime for which there was no first-principles understanding. The continuing need to understand and improve the safety of HE initiation systems in industrial, conventional munitions, and nuclear explosives environments drives us to acquire such first-principles understanding.

### Planned Scope

This LDRD was funded for three years (FY09-11) at levels of \$340k, \$306k, and \$306k sequentially. At those levels, the planned scope included:

- Design and characterization of a high-power, low-energy “pulser” arc source;
- Thorough characterization of arc discharges across HE surfaces, using thin films for spectroscopic transmission;
- Time-resolved infrared spectroscopy (TRIR) of HE thin films, to study the kinetics at extremely high temperatures. Given the tight resources, only one HE type was planned for study; PETN was chosen because the films are relatively easy to make and it is a common detonator HE.
- Support for modeling was included on a best-effort basis.

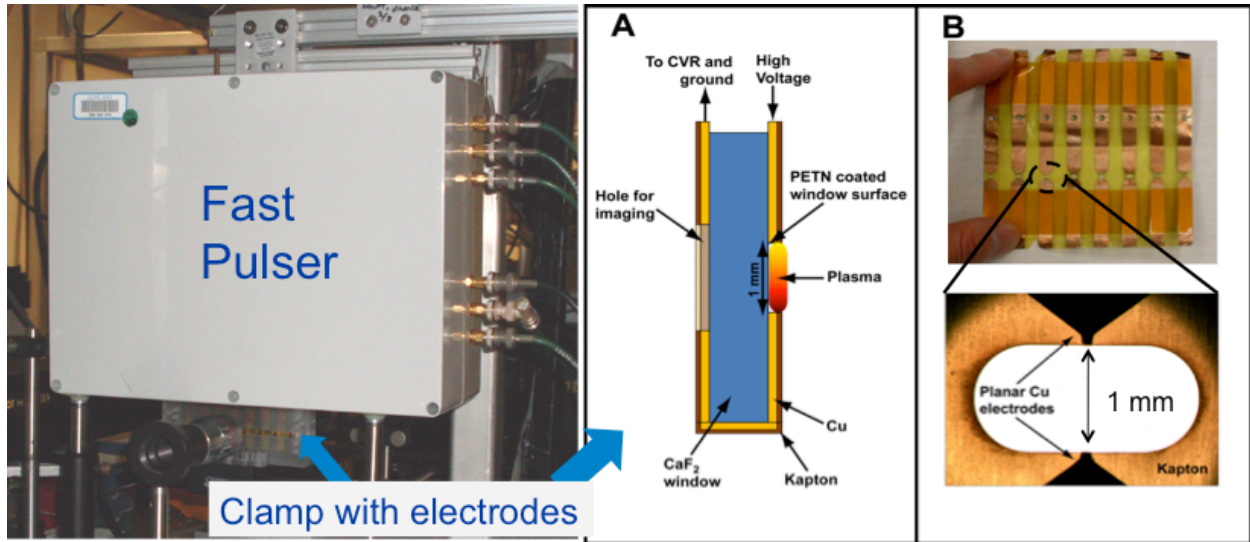
### Executed Scope

As ultimately executed, the scope included much less TRIR and more modeling, plus an extremely preliminary comparison of behavior between PETN and TATB. These changes evolved from a) the discovery that using a strong electrical source as the pump in the TRIR pump-probe configuration is extremely difficult to implement in a low-noise fashion, and b) from the unexpected failure of the TRIR femtosecond laser system at the beginning of the main experimental campaign. The repair and re-commissioning of the TRIR system could not be completed within the 36-month bounds of the LDRD and a request to delay the schedule was not granted.

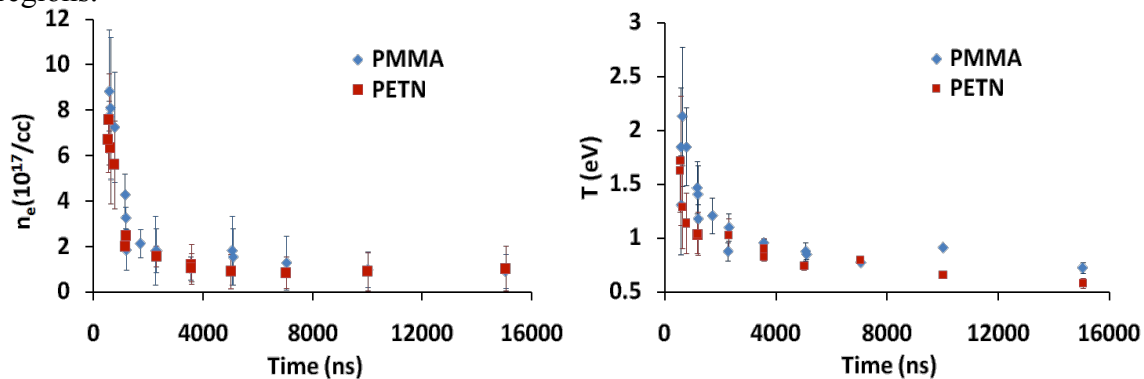
### Technical Accomplishments

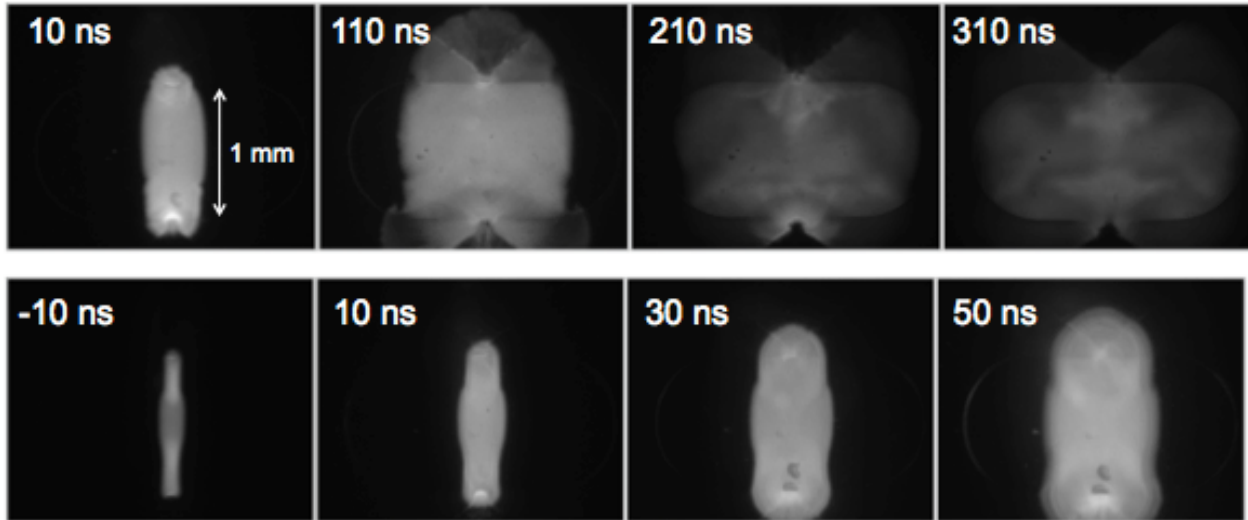
Aside from the disheartening failure of the TRIR system, the execution of the remainder of the scope included several substantial technical successes detailed in the remainder of this document (consult the relevant sections for more information on the figures copied below), including:

- Construction and successful operation of a 10 kV, 400 mJ, ~4 MW pulser capable of reliable and repeatable operation. The pulser also turned out to be a useful source for the Nuclear Forensics SI, 10-SI-016.



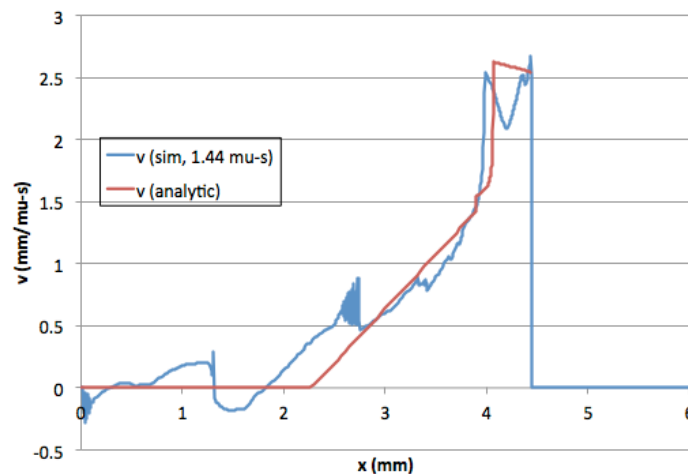
- Thorough spatial and temporal characterization of the temperature and density of typical surface discharges over inert (PMMA) and energetic (PETN) thin films. Temperatures of the discharge are quickly driven to a few eV during the input pulse, cooling to 1 eV in a few microseconds and persisting at a substantial fraction of an eV over ten microseconds. Peak electron densities are of order  $10^{18} \text{ cm}^{-3}$ . In the point-to-point geometry between the pulser electrodes, a discharge is created which undergoes rapid radial expansion at  $\sim 2 \text{ mm}/\mu\text{s}$ ; the properties behind the expansion front are spatially uniform. Even in a confined configuration, the discharge is created in the air above the HE, not through the solid HE itself; convective transport dominates as the top  $\sim 300 \text{ nm}$  ablates, and energetic reactions do not propagate to adjacent regions.





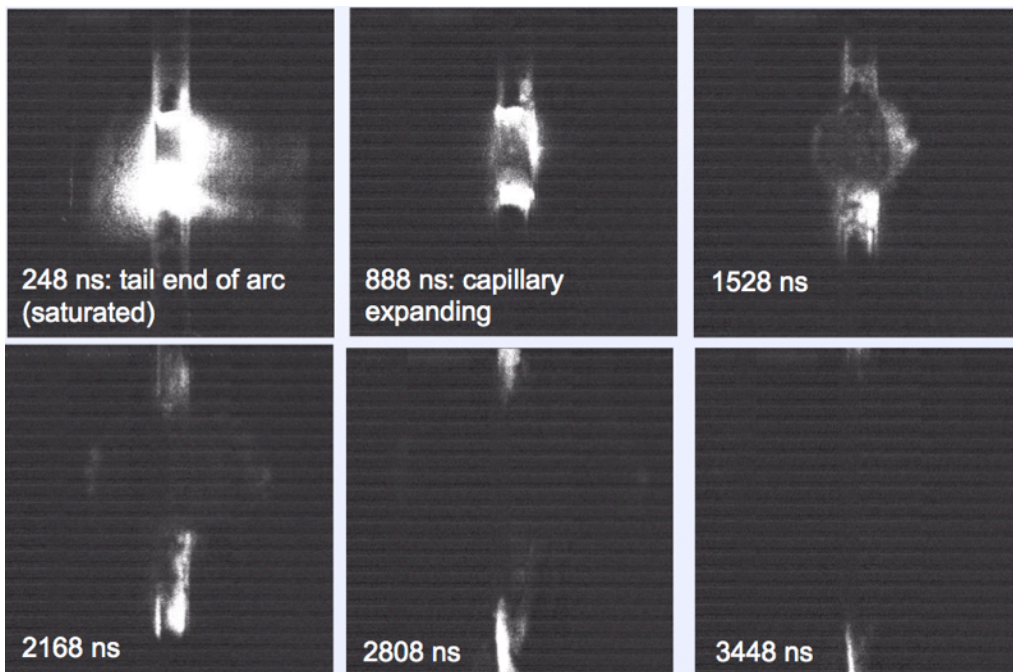
- Development of a model called “pumped convective burn” (PCB), which shows considerable promise at providing first-principles understanding of the arc initiation mechanism in low-density HEs. The modeling work includes analytic derivation (using an ideal EOS) of the existence of a quasi-steady PCB wave that can release energy on a fast time scale and short length scale without requiring either shock compression of the solid-phase HE (as in a detonation), or compaction of low-density material (as required in a traditional deflagration-to-detonation transition, or DDT). We believe this is the first time such a wave has been identified.

$$\frac{v_{PCB}}{c_o} \approx \sqrt{\frac{2(\gamma + 1)T_{react}}{\gamma T_o}}$$

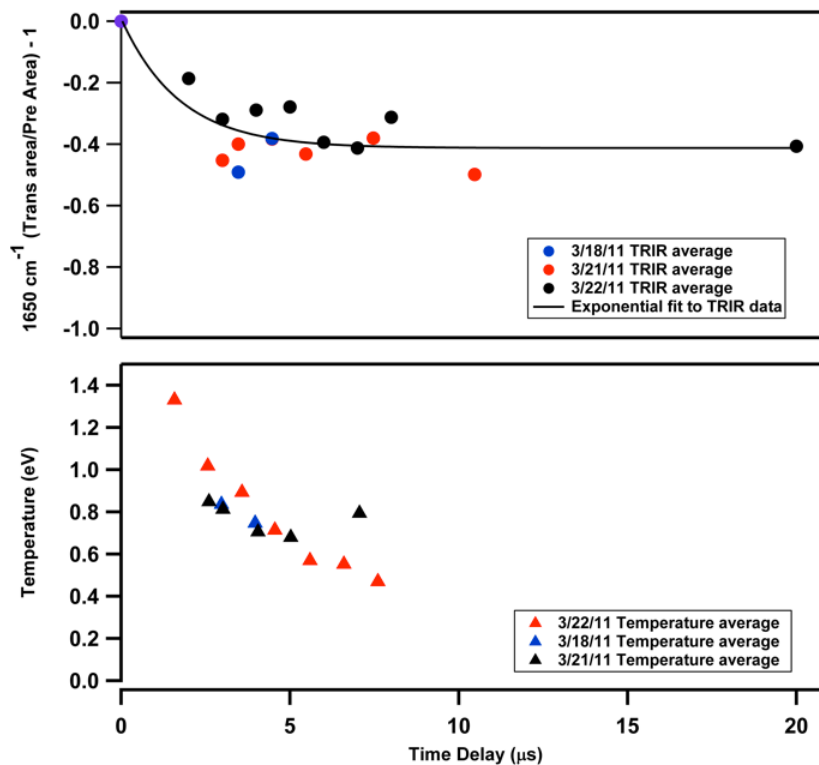


- A first baby-steps study of PCB in a 0-d capillary geometry, which shows that arc-driven PETN can drive expansion of a thin-walled capillary tube at  $\sim 1.7 \text{ mm}/\mu\text{s}$  in a geometry that precludes any type of run-up to a propagating wave. In the same geometry given the same input arc stimulus, TATB behavior is indistinguishable from that of an inert powder.





Finally, the preliminary TRIR results that were obtained before the system failure show that an arc-driven pump-probe experiment can be performed, although considerable effort must be made to overcome electrical noise. Simultaneous temperature measurements were also obtained. Some suggestions for how the experiment could be executed successfully in the future are provided in this document.



## Milestones and Publications

At the beginning of the second year of this LDRD, Chris Grant was successfully converted from post-doctoral appointment to full staff. U.C. Berkeley summer student Han Wang created a modeling tool well above the expectations for a sophomore undergraduate; his work won Best Poster for that year. Mr. Wang returned subsequent years to help with other projects and has applied for a one-year Post College Appointment at LLNL prior to beginning his graduate studies.

The paper “Towards the Understanding of PETN Initiation by a Fast, High-Power Arc Source,” by Chris Grant, Vincent Tang, Elizabeth Glascoe, and James McCarrick was published in the peer-reviewed venue of the 14<sup>th</sup> International Symposium on Detonation, April 2010, pp. 543-551. This is also available through IMS as LLNL-CONF-425208.

The paper “Spatiotemporal Temperature and Density Characterization of High Power Atmospheric Flashover Discharges Over Inert PMMA and Energetic PETN Dielectric Surfaces,” by Vincent Tang, Chris Grant, James McCarrick, Elizabeth Glascoe, and Han Wang has been published by the Journal of Applied Physics (J. Appl. Phys. 111, 053303 2012). It is also available through IMS as LLNL-JRNL-505792.

Additional papers on the pulser hardware and on the pumped convective burn model are forthcoming; in the meantime, the details are preserved in this report.

## Project Exit

The original exit plan included transfer of the model and techniques developed by this LDRD to both the Nuclear Safety R&D (NSR&D) portfolio in WCI/NWE, and the Joint Munitions Program (JMP) TCG-X activities. When the study of TATB was dropped from the original scope, much of the appeal to JMP was lost. However, we have successfully transferred to programmatic NSR&D funding in FY12, where the follow-on step is generalization from ESD-scale arcs to the more general and timely topic of prompt thermal initiation.

## 1. Introduction

Initiation of high explosives (HE) is the process of transitioning a macroscopic sample of HE from a completely quiescent state to one containing a self-sustained, propagating release of chemical energy. Arc initiation is driven by an electrical discharge across the surface or through the volume of the HE. It can occur in accident scenarios involving electrostatic discharge (ESD) or lightning, and also has had engineered applications such as spark detonators.

Experiments have found that at least one conventional high explosive (pure, low-density pentaerythritol tetranitrate, or PETN) can be arc-initiated with fairly low input energies, as low as a fraction of a mJ per mil of arc length in a point-to-point discharge geometry. PETN is a common detonator HE and thus its susceptibility to arc initiation is of interest to the safety of operations in a number of settings, including industry, conventional munitions with the DoD, and plant operations within the NNSA complex.

No predictive capability for arc initiation of HE existed prior to this work. The underlying physics was not known and existing simulation tools could not reproduce the observed behavior. Our ability to understand the thresholds is crucial to the analysis of the safety of existing weapon systems and handling operations. Our ability to predict or engineer them is critical to our capability to design inherently safer initiation systems.

There is presently a significant gap between our understanding of HE initiation at the microscopic level, and the macroscopic level required for real-world applications (note that understanding *detonation* and understanding *initiation* are not the same thing!). Predicting the thermal explosion of HE that is heated *gradually* (“cookoff”) is an area that has had success, but the underlying models are often highly empirical with many knobs. By far the largest body of data that exists is for *shock* initiation, caused by mechanical impacts from supersonic (relative to the HE sound speed) projectiles. The empirical descriptions of shocked HE reaction rates and equations of state are described almost exclusively in terms of pressure; explicit temperature dependence, if present at all, is ad-hoc and calibrated to narrow ranges of data.

In an arc, however, the pressure is too low to drive a significant shock, but the temperature is quite high, corresponding to thermal energies of the same order as the chemical bond strengths ( $\sim$  eV). Relative to such levels, existing thermal models such as multi-step Arrhenius kinetics models are calibrated at fairly low temperatures and it is not obvious how well they scale to the arc regime. Also, unlike in a cookoff experiment that can take place over a period of many hours, the arc electrical pulse length is tens of nanoseconds. Thus, in contrast to other modes, arc initiation must rely on fast thermal effects followed by a separate process that leads to propagation in the absence of an initial shock wave.

Thus, the goals of this LDRD are to develop basic understanding of:

- the energy transport mechanism from the arc plasma into the HE;
- the local chemical kinetics driven by very high temperatures; and
- the process by which a locally coupled volume of HE that is driven at a high reaction rate evolves into a propagating reaction with a lower rate.

## 1.1. Approach

The project plan for this LDRD evolved from the proposal stages according to actual allocated funding and, of course, lessons learned as the work proceeded. Once the actual funding levels were established (\$340k in year 1; \$306k in subsequent years), the following tasks were planned:

- Design, fabrication, and characterization of a low-energy, high-power pulser to serve as a repeatable arc source for the experiments.
- Thorough spatial and temporal characterization of the temperature, density, and dynamics of discharges over an HE surface, using emission spectroscopy and gated imaging.
- Time-resolved infrared spectroscopy, to infer high-temperature kinetics of arc-driven HE by observing the characteristic decay times of vibrational signatures of unreacted material, and the growth times of the signatures of products. Given PETN as a relevant HE from a historical perspective and TATB (triamino trinitrobenzene) from a contemporary one, resource and schedule constraints forced us to choose just one; we chose PETN because it is far easier to manufacture into the thin films necessary for IR transmission.
- Modeling was to be pursued on a best-effort basis.

The distribution of work as actually executed was somewhat different. When we reached our first serious attempt at TRIR testing, we found that performing a TRIR “pump-probe” experiment with an arc as a probe is not a simple task for a number of reasons, with two especially dominant.

The first major obstacle was throughput. For the arc characterization work, the brightness of the source meant that there was a good correspondence between a single arc pulse and a useful data point. While the holder and coupon setup (described later) had drawbacks, the necessary data was obtainable. However, for TRIR experiments, many more shots are required to obtain a single data point. The signal into the detector is not the strong output from the arc, but the transmitted spectral density from the laser source. Averaging over a number of shots at the same point in time are typically required. On top of that, the precise timing of the probe light relative to the arc cannot be controlled precisely because of the way the pulser and the laser system are triggered; so dialing in the same time at which to take data does not necessarily mean the data is acquired at the desired time, and even more shots are required. The original coupon/holder system was not adequate to achieve anywhere near the required testing throughput, and had to go through a major re-design in the middle of the project, introducing a delay.

The second major obstacle was electrical noise. The pulser is a fast, high-current electrical device and produces considerable electromagnetic radiation. The IR detector array is a sensitive piece of equipment whose electronics, and particularly the grounding scheme, were not accessible to us. The pulser could be modified and wrapped in a number of ways, but there is ultimately no way to deal with the exposed portion of the circuit that is required to drive current along the HE film surface and “pump” the experiment. Considerable time and effort was invested to reduce the noise levels, although we were never successful in getting those levels low enough that data could be taken at “early” times when any substantial arc current was still flowing.

The time invested in overcoming these obstacles pushed the main TRIR experimental campaign into the third year, at which point a radically different and much more serious obstacle was encountered: failure of the femtosecond laser system that provides the broadband IR probe pulse. This failure ultimately proved fatal to the experiment since it was not possible to extend the LDRD beyond 36 months (we did make a request) while we waited for repairs. More detail on the failure is given in Section 4.

Thus, relative to the planned scope, the executed scope did not include more than the preliminary round of TRIR experiments, where the throughput and noise issues were first identified. However, the down-time during the coupon/holder redesign period through the wait for attempted TRIR repair was used to boost other areas. Significant progress was made in modeling, and at the end of the project, a brief attempt was made to take some data comparing the response of PETN and TATB to arc insults.

## 1.2. Layout of this document

The remainder of this document provides specific details on all the activities performed during the Arc Initiation LDRD, by either direct description or by pointing to other existing documents that were produced along the way.

Section 2 discusses the design and characterization of the pulser, which was the workhorse arc source for the project. Section 3 provides just a brief summary of the work done to study surface discharges over thin films, then points the interested reader to the more extensive descriptions that have been (or soon will be) published in the peer-reviewed literature. Section 4 describes the TRIR campaign to the extent we were able to take it, including a description of the hardware failure that eventually killed it. Section 5 describes the Pumped Convective Burn model, which may prove to be a solid first-principles foundation for the response of HEs to arc initiation and other fast thermal insults; the steady PCB wave derived from the model appears to be a newly identified phenomenon. Finally, a set of appendices provides detail on software tools and hardware design.

## 2. Pulser Design and Operation

Even under ideal conditions, the signal-to-noise level of TRIR data is not ideal and we were advised from prior efforts that the data from many, many shots would have to be averaged to produce a usable result. In addition, the characterization of the temperature and other properties of the discharges used to pump the HE films was not a simple measurement and, from the beginning, we had planned a separate measurement campaign to characterize the arc plasmas.

Thus, with such a large number of shots required to ultimately obtain our desired data, it was key to have a “workhorse” source of the desired arcs. We had extensive prior experience with the sources used in NSR&D-sponsored threshold measurements and knew that a highly controlled, repeatable arc is obtainable. However, because the NSR&D experiments use more significant quantities of HE, resulting in a certain amount of consumables per shot along with shot-rate limitations imposed by operational safety, the arc source could have some limitations that were not rate-limiting in the NSR&D context but were unacceptable for the LDRD, given the much greater throughput required.

The requirements for the new source were as follows:

- Repeatable arc characteristics, including a well-defined path and only a single branch.
- A triggered spark-gap for the switch, to provide a lifetime of thousands of shots.
- An operating voltage of order 10 kV.
- The minimum possible source inductance and resistance.
- High reliability.

These requirements were met with high success by the “pulser” (capacitive discharge unit) described in the following sections. It proved to be an integral component in the characterization shots, the TRIR shots, and the capillary shots carried out by this LDRD, and also ended up being copied for use in the Nuclear Forensics SI, 10-SI-016.

### 2.1. Pulser Design

Figure 2.1 summarizes the arc pulser and the first load geometry (described in more detail in Section 2.2). The arc pulser consists primarily of a high voltage fast capacitor switched by a triggered spark gap. Currently, a fast low inductance 100 kV General Atomics 35436M capacitor with 8 nF is used along with a Perkin-Elmer GP-20B spark gap switch capable of triggered operation up to 11 kV. The 100 kV capacitor was used to ensure robustness of the system to voltage overshoots and when operated at ~10-20 kV has an essentially infinite shot-lifetime. Voltages greater than 11 kV can be achieved via installation of a different switch, up to the limit of flashover breakdown inside the pulser. The spark gap is triggered by a MOSFET-switched TR-180B transformer, driven by a 200 V 1  $\mu$ F capacitor; the transformer trigger circuit produces up to 18 kV on a  $\mu$ s time-scale to trigger the spark gap. A current viewing resistor (CVR) on the ground return with resistance of 140 m $\Omega$  is used to measure the current. The components sit on a printed circuit board, shown in Figure 2.2, with most of the connections made on the board itself. The circuit board contains wide conducting planes and allows a direct connection to the load in order to minimize system inductance.

The pulser was designed to trigger as quickly as possible to minimize jitter. Figure 2.3 shows the planned typical control and timing scheme for pulser operation. By using a very fast, high power MOSFET to drive the trigger and by loading the trigger transformer with the highest operating voltage (200V), we expected the pulser to commutate its load in approximately 580 ns. This was borne out by experiments as shown by the typical trace in Figure 2.6. The jitter in the system, as discussed in Section 2.3, at start of operations was characterized to be as low as +/- 13 ns but settled to typically +/-30 to 40 ns for the shots discussed in this report.

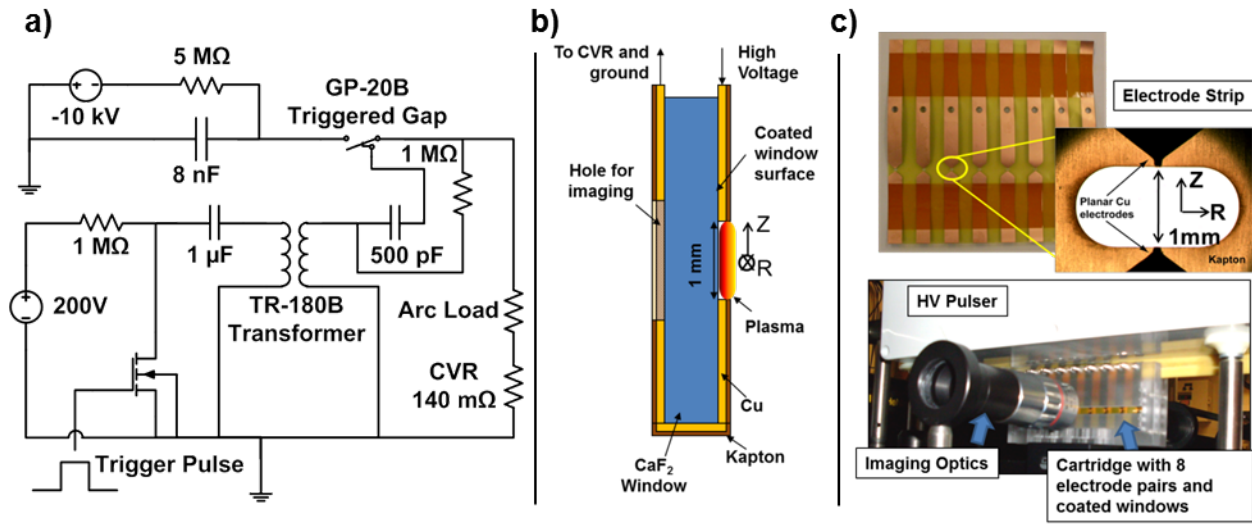
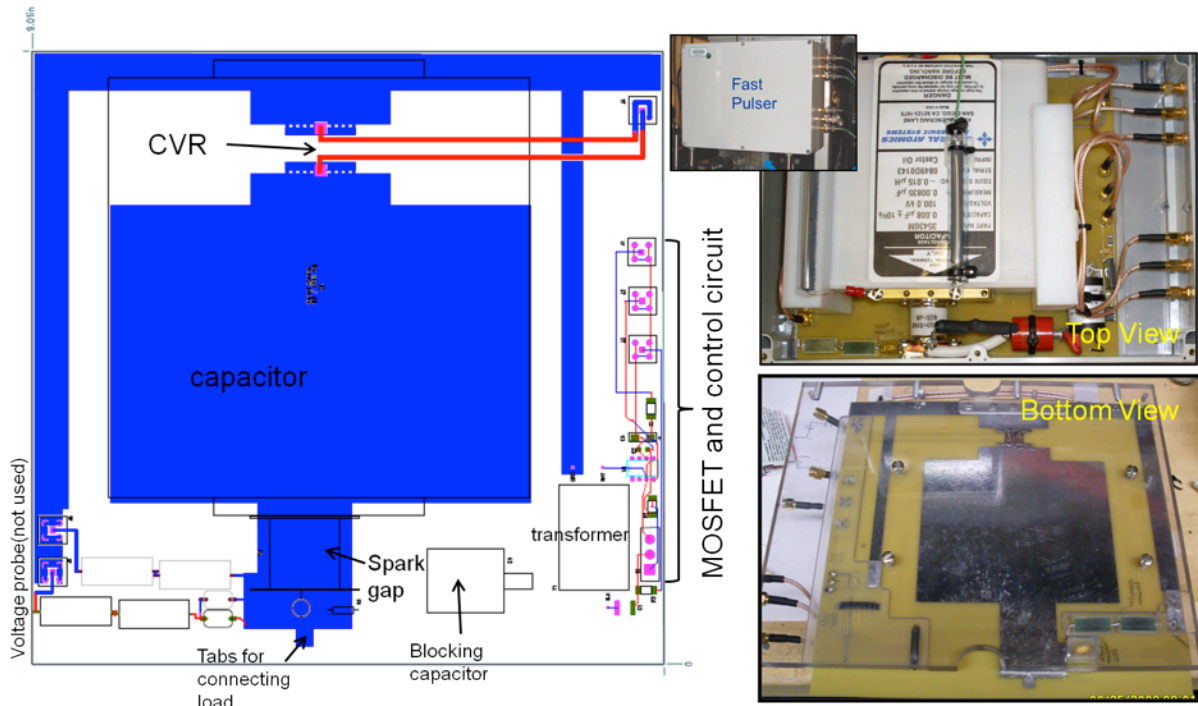
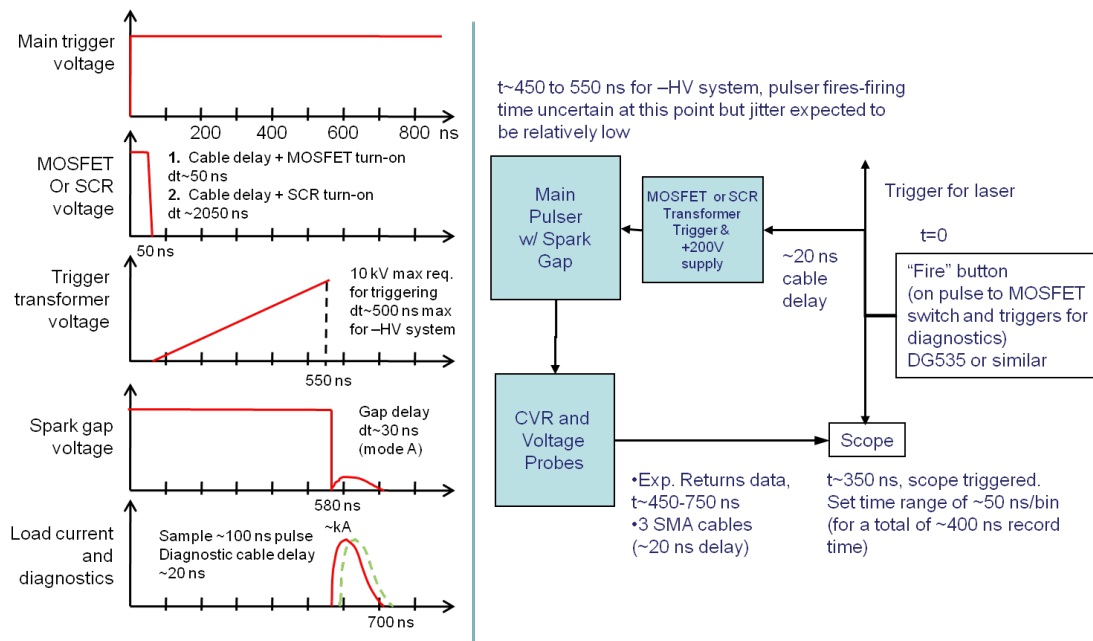


Fig. 2.1: a) Simplified circuit diagram of the high-voltage pulser. b) Diagram of the electrode coupon, which consists of a 17 μm thick Cu strip deposited onto 25 μm thick Kapton. The discharge flashes over the 1 mm long gap and coated film. c-Top) A backlit planar photographic view of the electrodes is shown. The Cu electrodes are 6.3 mm wide but narrow to ~75 μm to form an approximate point-to-point breakdown gap of 1 mm. The white space in the graphic is the transparent CaF<sub>2</sub> window material. There is a clear optical path to collect both fast gated images and make spectroscopic measurements. c-bottom) View of the clamp cartridge mated to the HV pulser. In this setup, there are 8 electrode pairs in the cartridge. After a shot, the cartridge is slid along so that a fresh pair of electrodes can be mated to the pulser terminals for the next shot.



**Figure 2.2: Layout of the pulser circuit board along with top and bottom view of the assembled pulser inside its enclosure. The pulser circuit board and its components are supported inside the enclosure by the lexan backplate that is clearly visible in the bottom view.**



**Figure 2.3: Planned timing and control scheme for the arc initiation pulser.**

For the majority of the experimental campaign, the pulser was operated at  $-10$  kV corresponding to a stored energy in the capacitor of  $418$  mJ. Fitting the CVR waveform data to that of a basic RLC circuit allows us to infer the total time-averaged system inductance,  $L$ , and resistance,  $R$ ,



for each shot. We note that constant (in time) values of L and R are able to match the data well over multiple oscillations. These data along with measurements from baseline shots from a shorted load are used to estimate the power and energy deposited to the load (i.e. electrodes, plasma, and surface). Quantitative specifics are given in Section 2.3.

## 2.2. Coupon and Holder Design (For Plasma Characterization)

The first coupon and holder was designed as a cartridge of 8 electrodes as shown in Figure 2.1(b) and (c). The concept of the design was to allow relatively rapid switching and securing of new electrodes onto the pulser for multiple single-shot experiments. In actual practice a shot rate of 5-6 shots an hour could be achieved, with the majority of the effort going to precise alignment of each new electrode. This allowed us to use this holder for characterizing the plasma, but as discussed, a different design with significantly faster shot rate was ultimately used for the TRIR shots.

The clamp consists of two Lexan pieces with grooves that allow either one or two substrate windows to be clamped to the electrode sheets; this allows the plasma to be either confined or unconfined. Figure 2.1(b) shows the setup for one window. Figure 2.4 provides the schematics. The electrodes on the sheet mated with the pulser tabs using 4-40 set screws along the top of the clamp. For the shots in this report, the substrate window was made from CaF<sub>2</sub> and coated with the desired dielectric material for study.

The coupon and electrode for this clamp design consists of a point-to-point setup with a 1 mm gap, and is made up of 17 μm thick Cu strips with 75 μm wide tips deposited onto 25 μm thick Kapton backing. The low inductance of the design allows the pulser to deliver multi-MW power to the load. Figure 2.5 shows the drawing for the coupon.

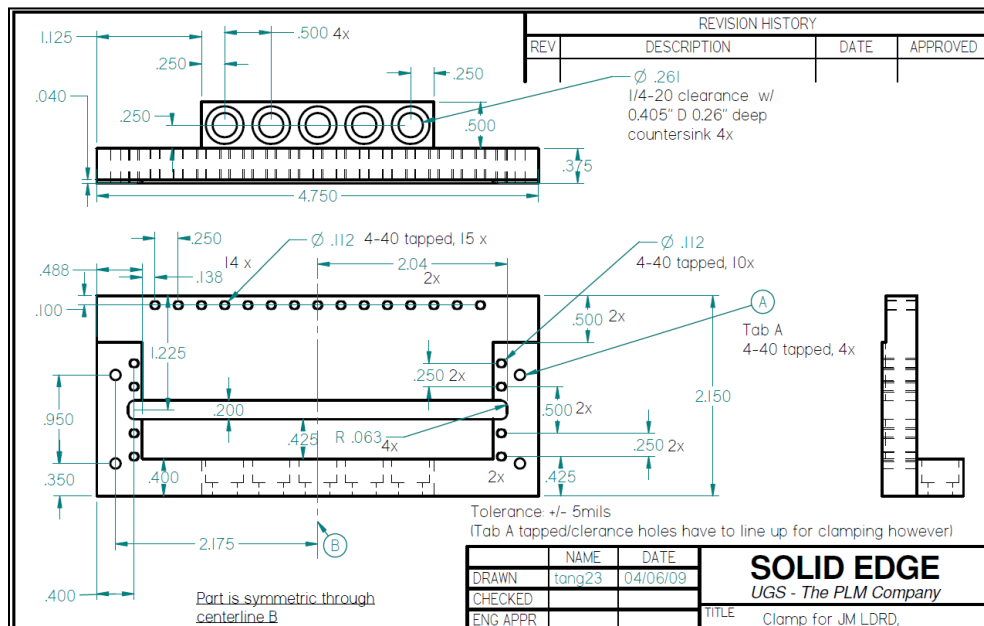
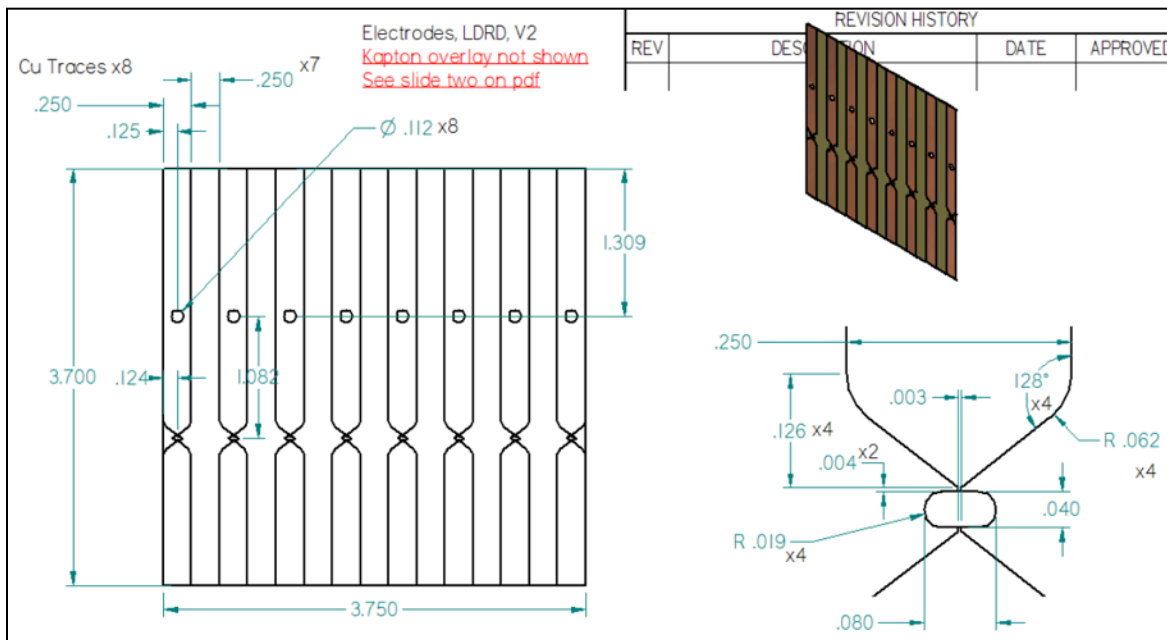


Figure 2.4: Coupon holder design for plasma characterization experiments.

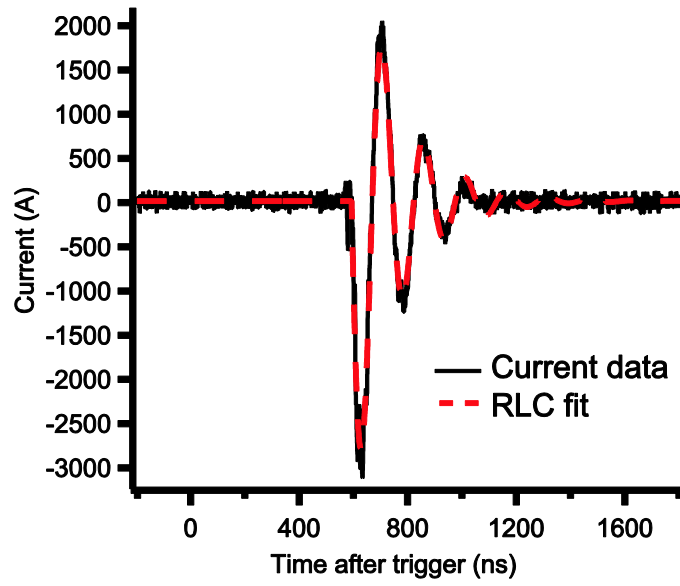


**Figure 2.5: 8-electrode coupon design.** The kapton overlay seen in Figure 2.1(c) is not shown here but was applied to increase flashover holdoff near the top of the substrate window.

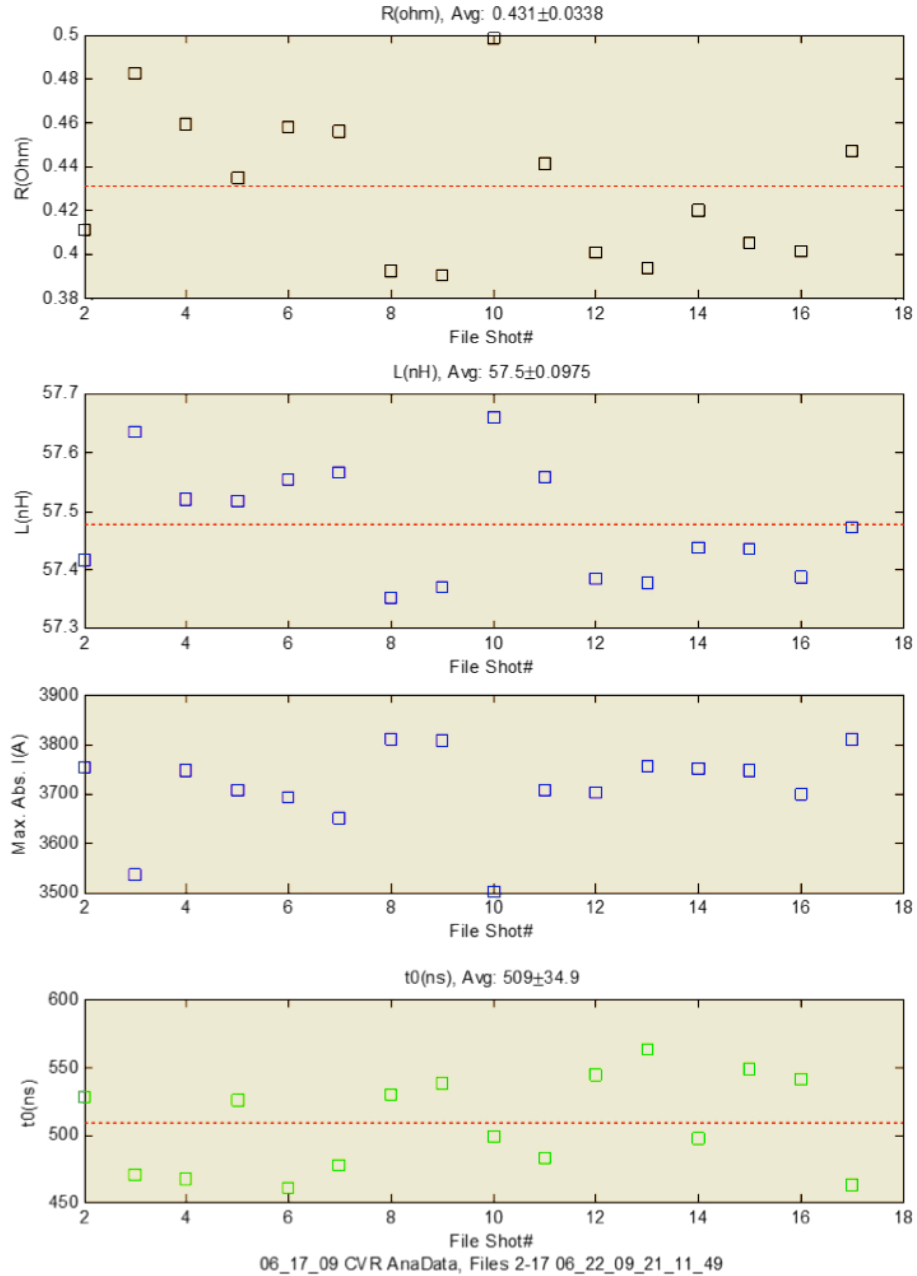
### 2.3. Pulser Output Characterization

Figure 2.6 shows a typical current trace using our pulser along with an RLC fit, assuming constant in time R, L, and C, for a typical unconfined PETN shot using the electrode strip system in Figure 2.1(c). The time delay in current flow is due to switching time inside the pulser. A system inductance of  $68.5 \pm 1.8$  nH and resistance of  $0.74 \pm 0.05$   $\Omega$  was found for unconfined PMMA experiments over 29 independent experiments. The timing jitter for current flow after trigger is significant at  $\pm 44.5$  ns and can make specifying an observation time smaller than this in a single shot difficult; the initial jitter in the system was as low as  $\pm 13$  ns over a series of 30 shots but has grown and settled larger possibly due to erosion in the spark gap. When the pulser terminals were shorted, the resistance was  $0.43 \pm 0.03$   $\Omega$  with inductance of  $57.5 \pm 0.1$  nH over a sample of 16 experiments. By comparing the plasma measurements with the shorted loads, we estimate the average resistance of the arc load was  $0.3 \pm .08$   $\Omega$  and the average inductance was  $11 \pm 1.9$  nH. We thus estimate the total energy deposited to the plasma, electrodes, and surface typically to be  $174 \pm 21$  mJ out of a total available energy of 418 mJ, with peak powers greater than 1 MW. For unconfined PETN experiments, a system inductance of  $69.1 \pm 0.6$  nH and resistance of  $0.74 \pm 0.07$   $\Omega$  was found over 30 replicates. The estimated deposited energy into the PETN loads was thus the same as the energy deposited into the PMMA shots. Figure 2.7 shows a sample series of shorted load data used for the above characterization.

Overall, the electrical shot characteristics was unaffected by the type of film, either PMMA or PETN, for the flashover arc. Approximately 40% of the pulser energy was delivered to the load for both PMMA and PETN films over a current pulse width of  $\sim 500$  ns.



**Fig. 2.6:** Arc source current measurement (solid black line) with corresponding RLC fit (dashed red line) for an unconfined PETN surface flashover.



**Figure 2.7: RLC fits of a sample series of pulser test shots with a shorted load. The resistance, inductance, maximum current, and firing times are plotted.**

#### 2.4. Revised Holder Design (For TRIR)

After characterizing the plasmas produced by our fast pulser using the 8-electrode cartridge holder and performing proof-of-principle TRIR experiments, we started work on a more sophisticated load setup that increased the shot rate significantly. The concept behind this “Revised Holder” was to employ a register-able and very long electrode strip, made up of 10’s to 100 of single-shot point-to-point electrodes with the same tip geometry as shown in Figure 2.5, in a holder that resembled a film camera. After each shot, the electrode strip is advanced easily

by rotatable knobs on the holder and registered using the predefined holes in between each pair of electrodes in the strip. Permanent electrodes in the holder are press-fitted to the electrodes on the strip for electrical contact. The substrate window is also press-fitted to the strip on the opposite side and slid down a rail to allow a fresh coating after each shot; the hole in between each pair of electrodes allows the flashover to occur over the substrate window. A  $\text{CaF}_2$  reaction chamber, or liner, 2 mm x 2 mm x 1 mm in dimension was incorporated for confined shots. Figures 2.8 and 2.9 illustrate the concept schematically along with the implementation. Alternatively, the holder could also be operated with just the permanent electrodes without the electrode strip. The complete drawings are available in Appendix F.

During testing with the electrode strip we were able to achieve shot rates of ~30 shots an hour, with the electrodes automatically achieving alignment to the TRIR system better than 0.15 mm due to the use of the precise registration holes in between the electrodes tips on the strip. The discharges were point-to-point single filament and reproducible; the main difference in these arcs versus the ones in the clamp load is the liner which provides some confinement. The  $\text{CaF}_2$  liner showed little to no damage after repeated shots. In this setup, the arc plasma temperatures and densities were measured simultaneously with the TRIR measurements. The arc plasma temperatures and densities were similar as shown and discussed in the following Chapters. The electrical parameters from the RLC fits were similar also. A system inductance of  $71 \pm 0.4$  nH, resistance of  $0.728 \pm 0.07$   $\Omega$ , and an averaged peak current of 3.26 kA was found over 22 replicates. The system inductance is approximately 2 nH higher than in the clamp load due likely to the longer transmission line used.

This rapid single-shot load concept is unique for arc discharges and represents a significant engineering advancement in this area.

We additionally tested the holder with just the round permanent electrodes and also a set of “ninja star” electrodes made of tungsten copper with rotatable sharp tips; the purpose of these tests were to see if we could use them for repeatable arcs without the single-shot electrode strip. Figure 2.11 shows typical multiple filament arcs with the round electrodes that were not viable for our experiments (contrast with the point-to-point arcs shown in Figure 2.12). Although the “ninja star” electrodes were better in terms of shot reproducibility and producing single filament arcs, we ultimately could not get reliable Cu line data needed for temperature and density measurements due likely to both the doubling of the arc length (from 1 mm to 2 mm) and the reduction in electrode ablation from the harder tungsten copper alloy. Because of time constraints we were not able to investigate these issues fully.

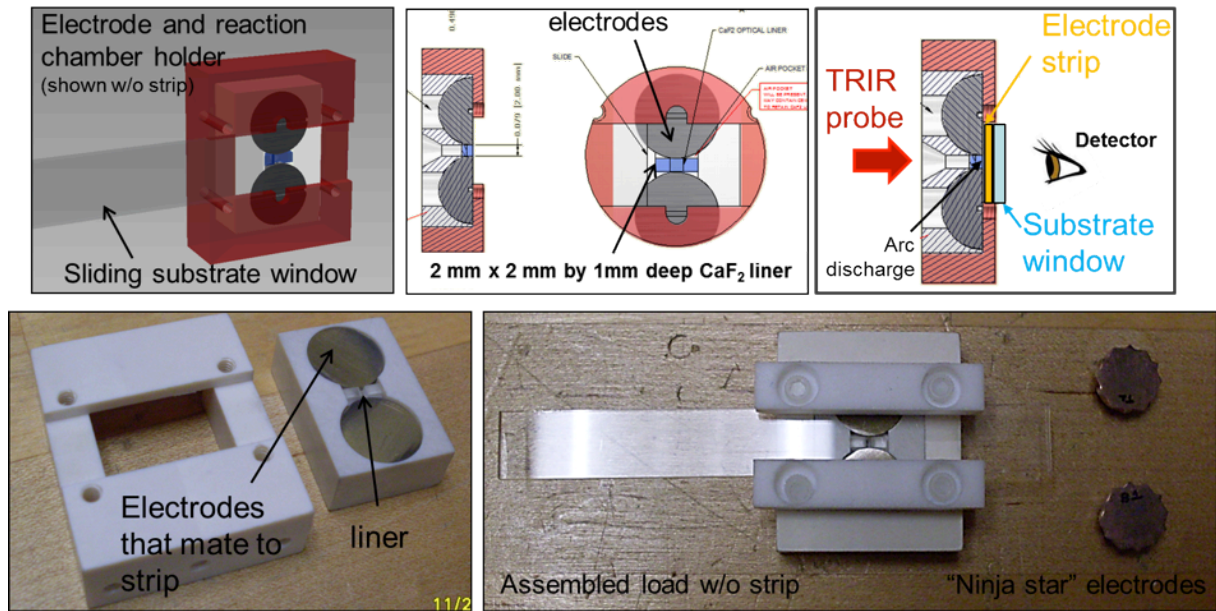


Figure 2.8: Schematic and implementation of the electrode and reaction chamber for the Revised Holder design.

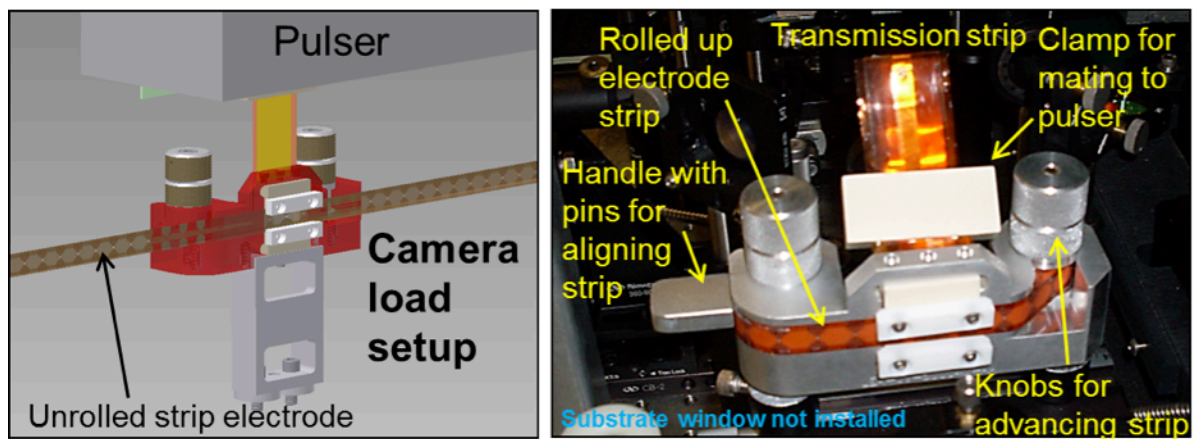
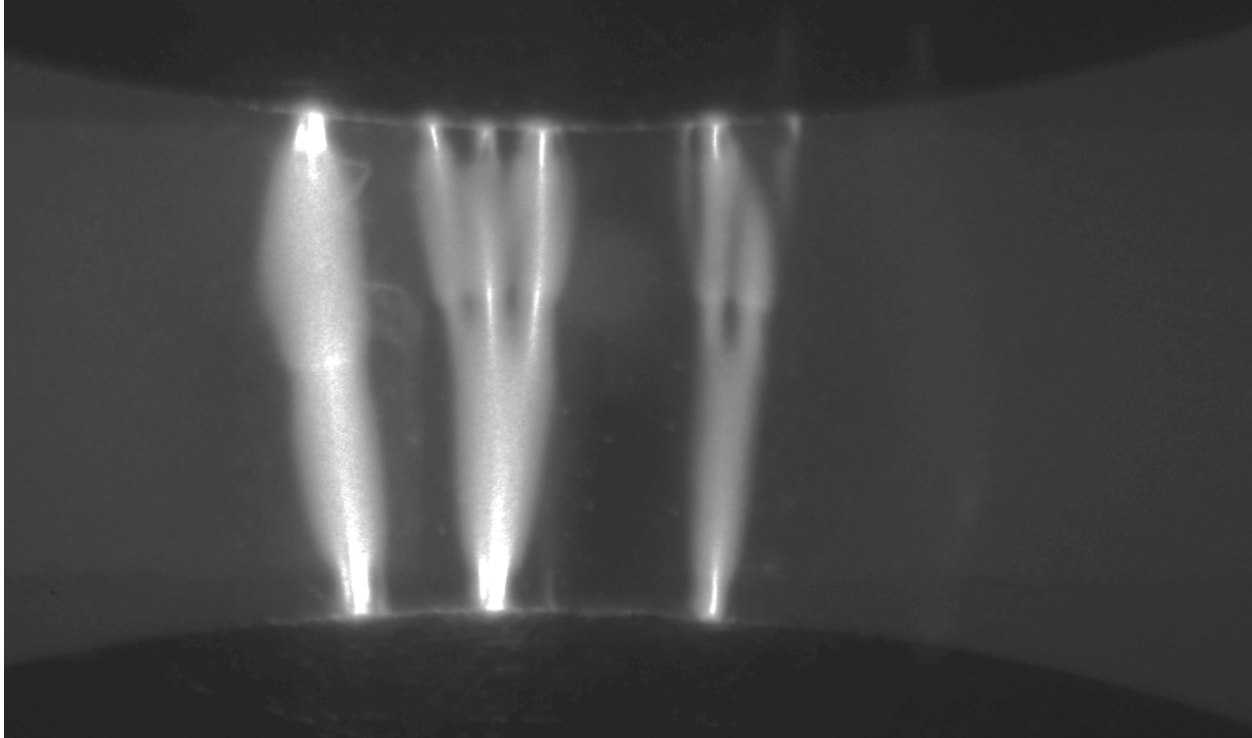
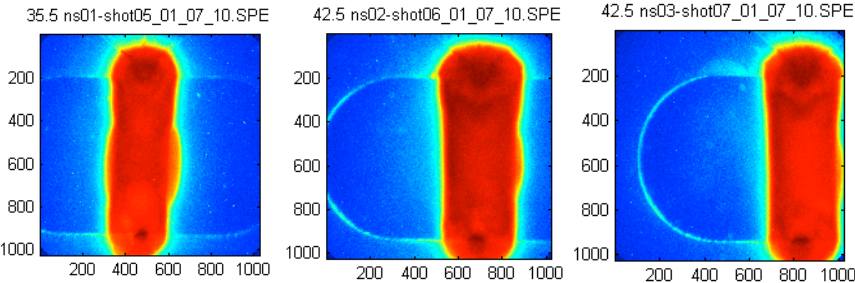


Figure 2.9: "Film Camera" setup for interfacing a long single-shot electrode strip with the reaction chamber in Figure 2-8 and allowing for rapid switching of single-shot electrodes during experiments.



**Figure 2.11: Typical multi-filament arc discharge using round electrodes without the single-shot point-to-point electrode strip. The faint outlines of the  $\text{CaF}_2$  liner can also be seen.**



**Figure 2.12. Highly repeatable, well-defined arcs produced by the point-to-point single-shot electrodes made from coupons of copper-coated kapton.**

### 3. Discharge Characterization with Energetic and Inert Thin Films

This section is meant to provide a “quick reference” of the characterization work performed on the discharges over thin films of PETN and PMMA. The characterization work is a fundamental ingredient in understanding the stimulus received by the materials of interest and was intended to provide the information necessary to unfold the kinetic data data obtained via TRIR. Even without the eventual coupling to TRIR, however, the characterization work by itself provided some key insights into the arc/HE interaction.

For full details, we refer the reader to the following publications:

- “Towards the Understanding of PETN Initiation by a Fast, High-Power Arc Source,” by Chris Grant, Vincent Tang, Elizabeth Glascoe, and James McCarrick was published in the peer-reviewed venue of the 14<sup>th</sup> International Symposium on Detonation, April 2010, pp. 543-551. This is also available through IMS as LLNL-CONF-425208.
- “Spatiotemporal Temperature and Density Characterization of High Power Atmospheric Flashover Discharges Over Inert PMMA and Energetic PETN Dielectric Surfaces,” by Vincent Tang, Chris Grant, James McCarrick, Elizabeth Glascoe, and Han Wang, published in the Journal of Applied Physics (J. Appl. Phys. 111, 053303 2012). It is also available through IMS as LLNL-JRNL-505792.

#### 3.1. Summary of Diagnostics

Film preparation: The thin films prepared on CaF<sub>2</sub> windows were studied using DekTak profilometry to measure thickness and uniformity, and also FTIR to determine the pre-shot absorbance spectra of the films.

During energy input from the pulser: A current-viewing resistor (CVR) was used to measure the output waveform from the pulser. By comparing the shape of this curve to those produced in shorted configurations, we can estimate the power and energy delivered to the discharge.

During and after energy input: A gated spectrometer was used to perform time-resolved emission spectroscopy, in the region of Cu I lines. Copper enters the discharge via ablation of the electrodes; Cu-doped films were also tried. The relative intensity of the Cu I series can be used to determine temperature, and the line shape can determine electron density. A gated intensified camera was also used to take visible-light images of the discharge and subsequent plasma motion. The sharp boundaries of the expanding plasma can be used to determine the expansion speed.

Post shot: DekTak profilometry and FTIR were again employed to determine the end-state of the thin films after being subjected to a discharge.

Finally, a one-D hydrodynamic model was used to simulate the behavior of the discharge, taking advantage of the fact that the reactive contribution to the energy is small and therefore not required in the simulation.



### 3.2. Summary of Major Results

Comparison of pre- and post-shot FTIR spectra shows about a  $\sim 300$  nm depletion in all PETN vibrational modes in the portion of the film subjected to the discharge. Visible inspection shows the extent of the region affected; there is no self-sustained propagation. The  $\sim 300$  nm value appears to be independent of film thickness, as we measure  $\sim 30\%$  absorbance change in 1 micron films and  $\sim 60\%$  change in 500 nm films. This implies the current channel does not form in a breakdown of the solid material, but rather is carried in the air above the film.

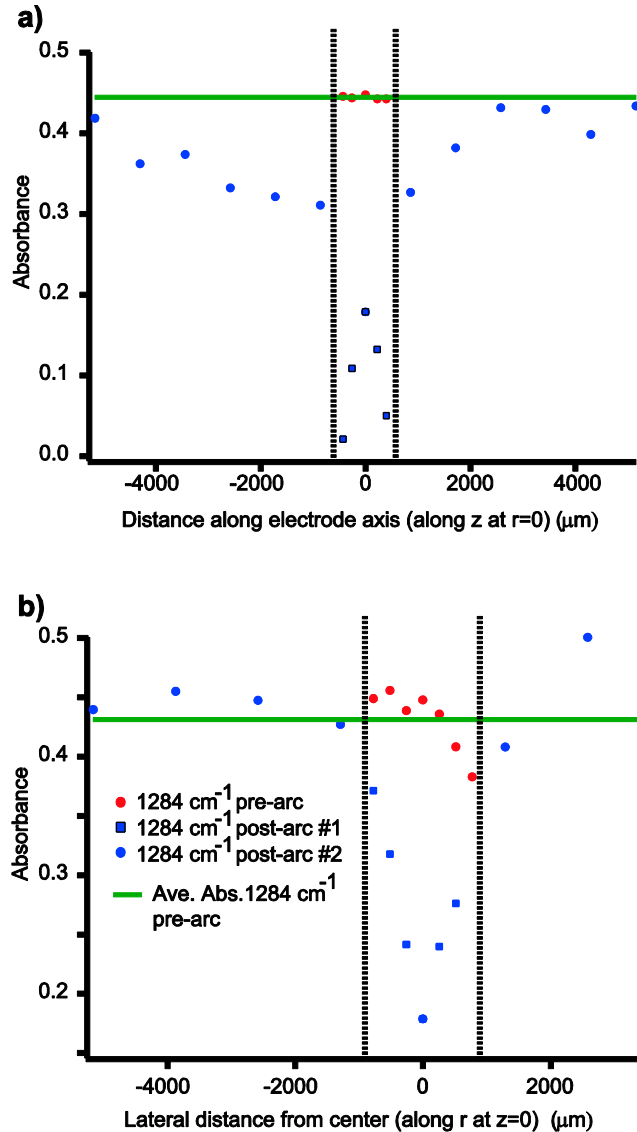


Figure 3.1. Post-shot FTIR analysis of PETN films, both along the r and the z-axis, using the  $\text{NO}_2$  symmetric stretch + CH bend + C5 skeletal combination mode. Approximately 60% of the material is depleted in the  $\sim 1$  mm x  $\sim 1$  mm plasma region corresponding to  $\sim 300$  nm of PETN material.

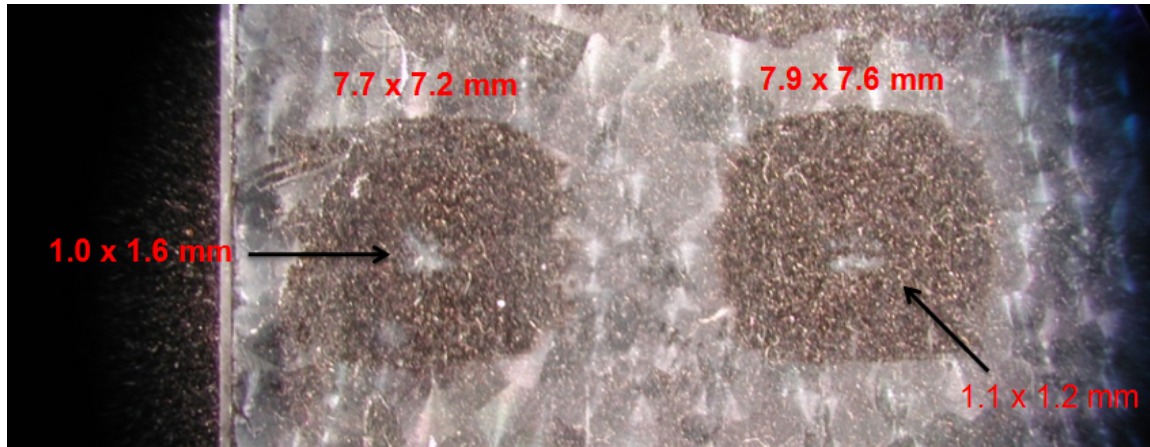


Figure 3.2. Post-shot images of the film coatings.

Determination of the time-resolved temperature finds a quick rise to a temperature of several eV, which decays over several microseconds. An 0.5-1 eV “tail” persists out beyond 10 microseconds. The peak electron densities approach  $10^{18}$  /cc, with a temporal decay similar to the temperature. Densities of order  $10^{17}$  persist beyond 10 microseconds.

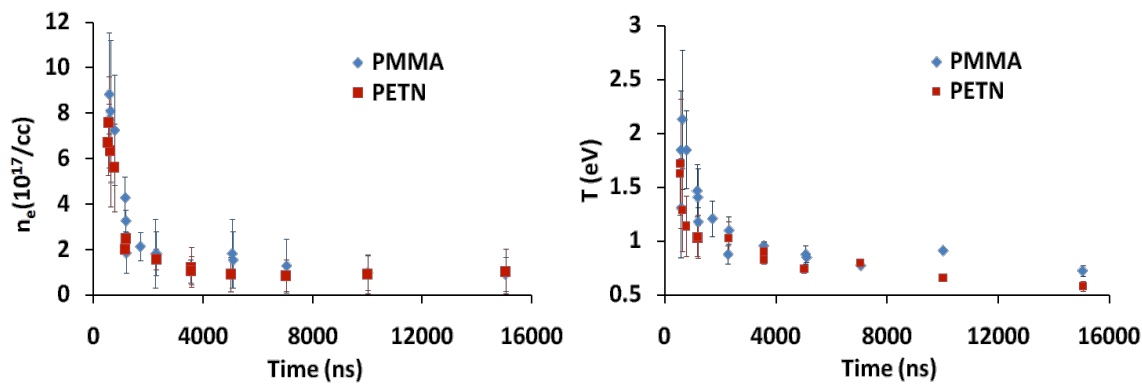


Figure 3.3. Time dependence of the electron density (left) and ion temperature (right), at the center of the discharge.

Gated images of the visible light emission show a sharp expansion front that persists until the plasma radius exceeds the electrode spacing. The initial streamer is straight (no branches or kinks) and of the same order as the electrode tips in size.

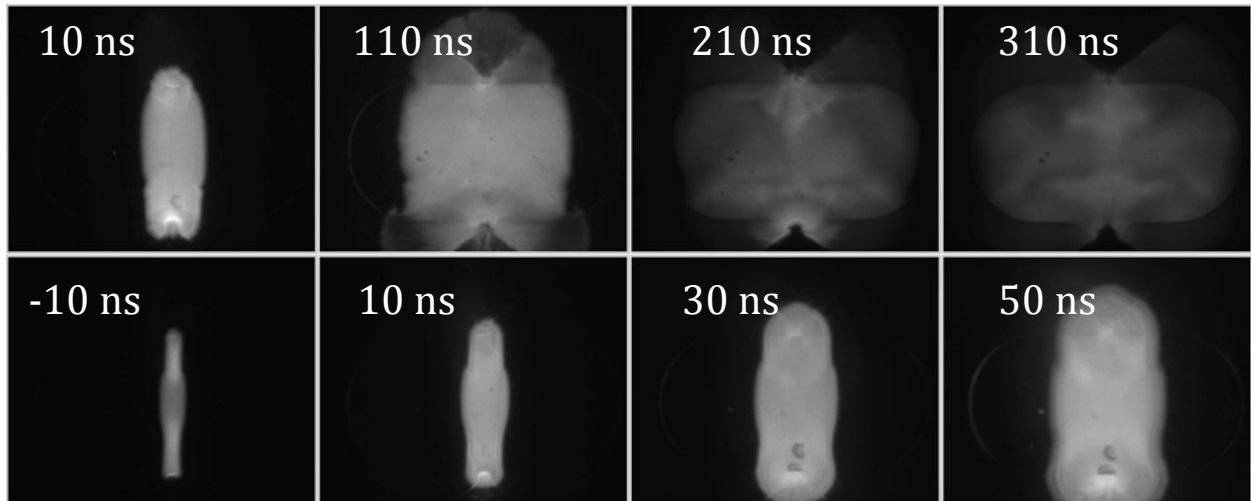


Figure 3.4. Visible light images of the discharge, taken with a 3 ns gate.

Performing measurements at fixed time but at different radii shows that, behind the expansion front, the spatial profile of temperature and density are relative flat.

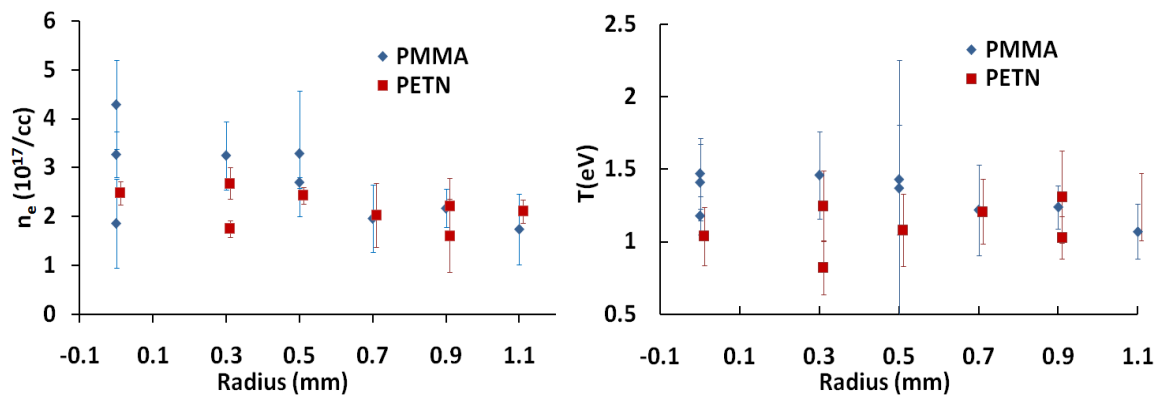


Figure 3.5. Spatial profiles, using data taken at the same times during discharge evolution.

Simulations of a 1-d cylindrical expansion are able to closely reproduce the motion defined by the sharp edge of the visible emission. The EOS is ideal but joule heating, radiation emission and loss are included.

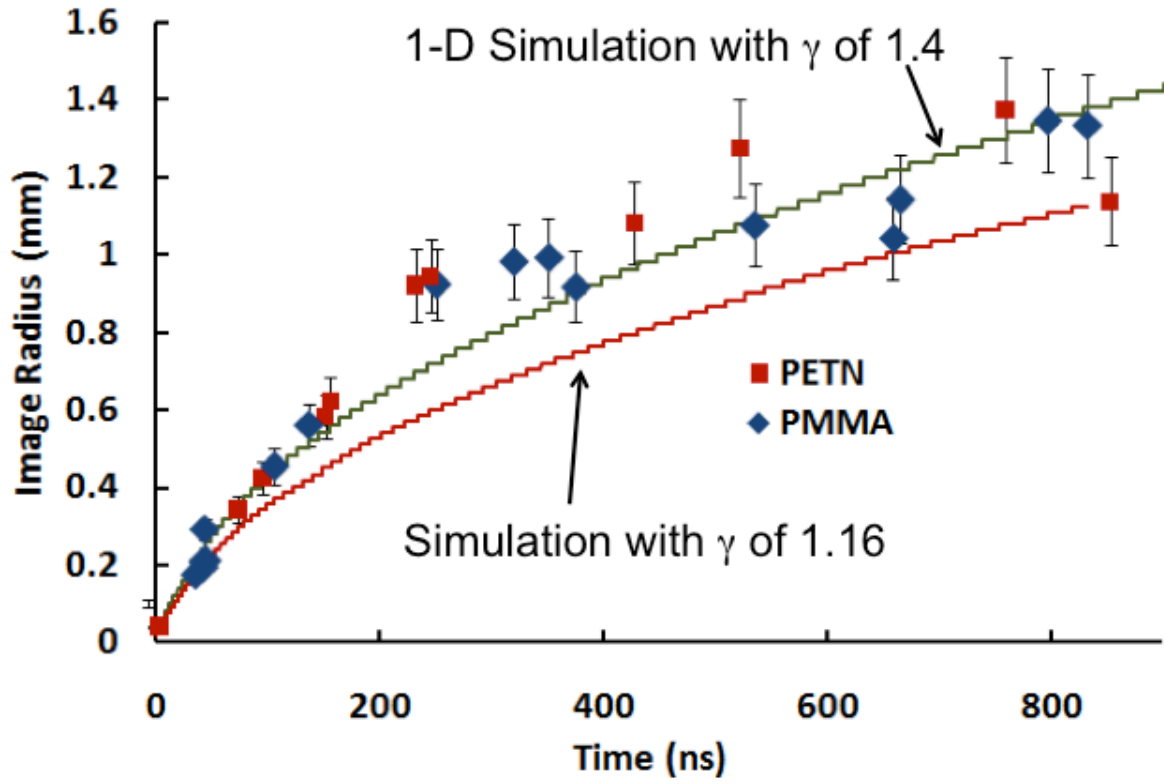


Figure 3.6. Comparison of the edge radius over time with a 1-d cylindrical hydro model.

## 4. Time-Resolved Infrared Spectroscopy of Thin Films

### 4.1. Methodology

The chosen technique for following high-temperature chemistry of high explosive molecules induced by an arc discharge was time-resolved infrared spectroscopy (TRIR). This technique can monitor specific chemical bonds potentially allowing for the determination of the chemical reaction pathways and their associated time scales for formation/depletion. TRIR has been used to monitor TATB deflagration chemistry and was reported previously [Glascoe, JPCA, 2009]. Here we attempt to apply TRIR to help elucidate surface flashed-PETN chemistry. A schematic is shown in Fig. 4.1 while a photograph of the optical table is shown in Fig. 4.2.

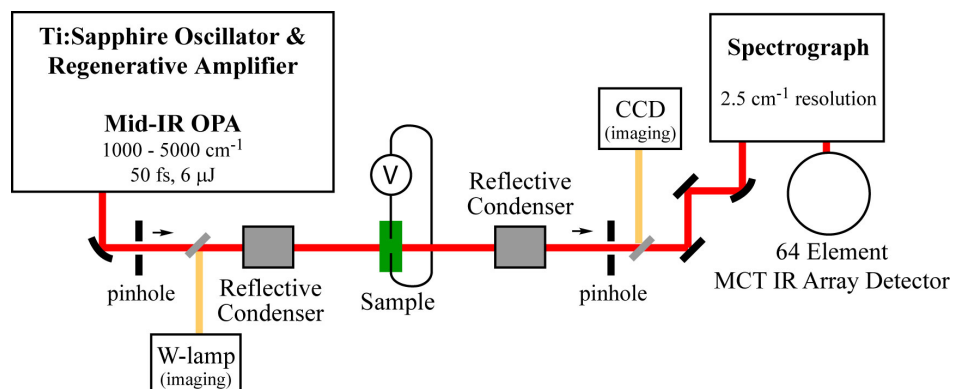
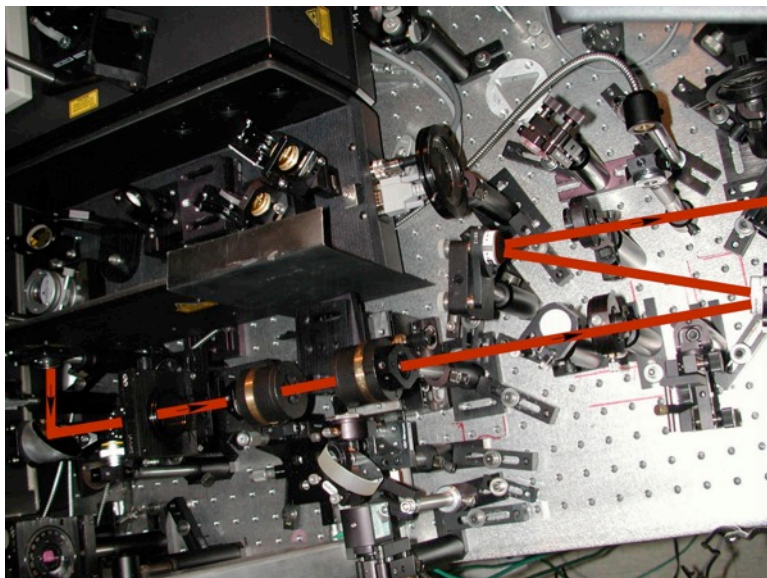


Figure 4.1. Schematic of the TRIR system.

Briefly, 50 fs pulses of mid-IR light (1000-5000 cm<sup>-1</sup>) are generated by an optical parametric amplifier (Coherent, Opera) pumped by the output of a Ti-Sapphire regenerative amplifier (Coherent, Legend) that is seeded by a Ti-Sapphire oscillator (Coherent, Mira). IR pulses are focused through an alignment iris by a gold-coated off-axis optical parametric mirror and directed into a Cassegrain objective. This objective refocuses the IR beam to a ~20 μm beam diameter. Another identical Cassegrain objective collects the transmitted light and focuses it through a second spatial alignment iris. Finally, the beam is focused via a gold-coated off-axis optical parametric mirror into a spectrograph (Jobin Yvon, iHR320) and detected using a 64-element liquid nitrogen cooled HgCdTe (MCT) infrared-array detector (InfraRed Associates, Inc.) coupled to a high-speed signal acquisition system (Infrared Systems Development Corp.). The spatial resolution of the spectrometer, using a 58 grooves/mm grating, is 3 cm<sup>-1</sup>/pixel at 3000 cm<sup>-1</sup> and 0.5 cm<sup>-1</sup>/pixel at 1400 cm<sup>-1</sup>. For these inherently single-shot experiments, a digital delay system synchronizes the IR pulse and the arc pulser with the detector electronics.



**Figure 4.2. Photograph of the optical system showing the direction of the laser light from the mid-IR OPA system (top left) towards the MCT detector (not pictured to the right).**

#### 4.2. Results, First Campaign

The first TRIR campaign used the initial eight-electrode coupon variant of the clamp system discussed previously. This clamp was attached to a rail which itself was affixed to a X-Y translation stage that allowed for positioning of the HE sample relative to the fixed laser beam. Visualization of the sample/electrode area was accomplished using a CCD based imaging system (see Fig. 4.1). The sample was positioned so that the laser beam was approximately 500  $\mu\text{m}$  from either electrode and along the electrode centerline. The strip line would then be clamped to the pulser via set screws just prior to functioning of the pulser. After the sample was arc insulated, the clamp was moved along the rail to the next fresh electrode and the process was repeated till all eight electrodes had been used at which point a new film/electrode coupon assembly would be built and mounted.

The duty cycle to function eight shots varied, but, on average, eight fresh shots could take approximately 4 hours to collect. This was mainly due to the constraints inherent in the design of the coupon/clamp/pulser interface that was driven initially by the need to keep inductance low in order to deliver the necessary amount of energy to the arc and HE surface on the shortest time scale as possible. This ultimately meant the pulser and clamp were very closely coupled spatially. That constraint along with the positioning of various optics made working conditions cramped.

All spectra were collected in the following manner. A background spectrum was collected usually averaging 100-1000 laser shots in the absence of any laser illumination that was then stored in the LabView data collection program. A reference transmission spectrum on an uncoated  $\text{CaF}_2$  window was collected also averaged over 100-1000 laser shots and saved for post data collection processing. A pre-sparked film spectrum was collected using 100 averaged spectra while the transient was a single spectrum. For comparison between with pre- and transiently sparked films, a spectrum was also collected post-sparked insult and again averaged

over 100 shots. All spectra were transformed into absorbance before analysis. Pre- and transiently sparked spectra were fit to Gaussian profiles and background subtracted to determine peak areas.

Timing was selected by using a digital delay generator and varied when the arc pulser fired relative to when the laser pulse arrived. Output from a single pixel on the MCT IR detector was routed into an oscilloscope along with the CVR output from the pulser. The difference between the start of current flow and the arrival of the laser pulse yields the actual time delay for any given shots. The type of data is illustrated in Fig 4.3. Also illustrated is the amount of signal induced by the high power arc pulser in the IR MCT detector that lasts out to approximately 3  $\mu\text{s}$ . This result was typical from shot to shot. It is evident that the relative amount of noise induced by the pulser is much larger than what the detector sees from the actual laser pulse. This amount of noise made data collection at times relative to pulser current flow earlier than  $\sim 2 \mu\text{s}$  impossible. However, even at later delay times, pulser induced noise in the IR detector was persistent even though this did not manifest itself in the IR MCT pixel readout. Another interesting observation about the noise inducing or broadcasting nature of the high power arc pulser is the fact that on multiple occasions the IR spectrometer's grating moved immediately after functioning the pulser. These incidents happened with enough frequency that after the spectrometer was moved to the appropriate wavelength for data collection, the spectrometer was powered down to prevent any subsequent grating movement during data collection.

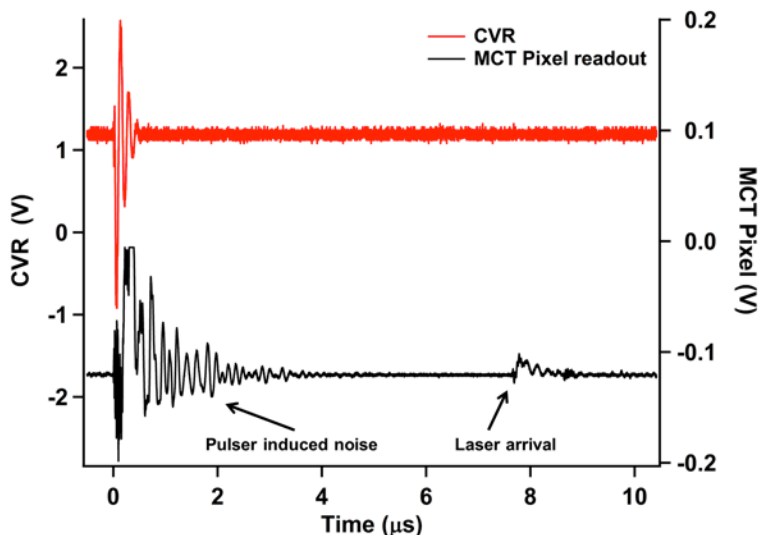


**Figure 4.3.** Waveform traces from the arc pulser CVR and from one of the IR MCT detector pixels. The timing for the TRIR is determined from the start of current flow from the pulser and the rise in current from the arrival of the IR laser pulse. In this case, the delay is  $\sim 8 \mu\text{s}$ . Also of interest is the amount of noise induced in the IR detector by the current flow in the arc pulser. Traces are offset from each other for clarity.

Nevertheless, in spite of these constraints we were still able to collect some usable data from our first campaign by avoiding the first few  $\mu\text{s}$ , but it took approximately 20 shots to gain only three usable time points. In any case, in Figure 4.4a, we present preliminary time-resolved IR absorption spectra (difference between the pre-sparked film and the transient) of an unconfined PETN film for three different time delays relative to plasma development plus an infinite time delay spectrum using the  $\text{NO}_2$  asymmetric stretching vibrational modes around  $1650 \text{ cm}^{-1}$

[Gruzdkov, JPCA, 2004; Folz, 10<sup>th</sup> Det. Symp., 1996]. These particular modes were chosen because they are the most intense IR modes for PETN and also because reactions of nitrate esters typically involve the NO<sub>2</sub> moiety - e.g., the dominant reaction under ambient conditions is the homolysis of the O-NO<sub>2</sub> bond while under high pressure or shock loading heterolysis forming the carbocation and the nitrate ion is observed [Davis, JPC, 1996; Dreger, JPCB, 2002; Hiskey, JPC, 1991; Naud, J Org Chem, 1992]. The infinite time delay spectrum was taken at least several seconds after the sample was sparked. At 2  $\mu\text{s}$ , we observe  $\sim 0.2$  O.D. depletion of PETN while the change in absorption at 6  $\mu\text{s}$  and 8  $\mu\text{s}$  are nearly identical and almost overlay with the infinite time delay spectrum. If we compare the normalized change in absorption versus time as displayed in Figure 4.4b and make the very simple assumption of first order kinetics, we can estimate a  $1/e$  time constant of  $\sim 2 \mu\text{s}$ .

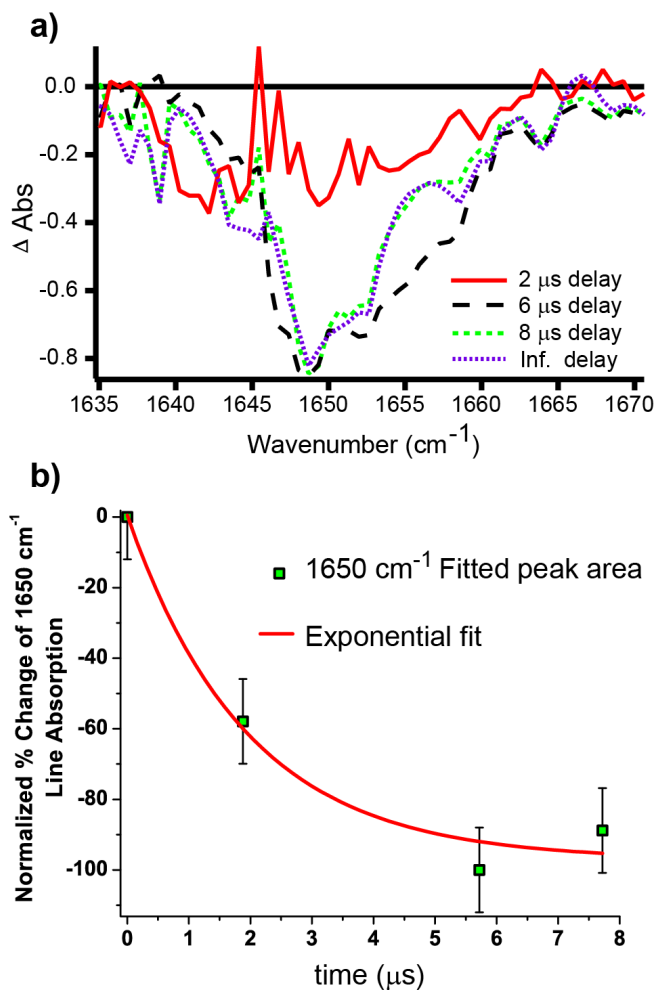


Figure 4.4. a) Time-resolved IR difference spectra between the pre-sparked film and the transient of an unconfined PETN film for three different time delays relative to plasma development plus an infinite time delay spectrum using the asymmetric NO<sub>2</sub> stretching mode region. b) Normalized % change showing the dynamics of PETN depletion. Assuming simplistic first order kinetics an exponential fit yields a decay constant of  $\sim 2 \mu\text{s}$  which sets a time scale for the reaction/depletion of the energetic material.



### 4.3. Preliminary results, second campaign: noise issues

Prior to the start of the second campaign, the TRIR system was redesigned to improve laser as well as overall shot throughput. Images of the redesigned system are shown in Fig. 4.5. This redesign included removal of the Cassegrain optics and replaced with CaF<sub>2</sub> lens to focus the IR light through the sample chamber. This had the effect of increasing the laser spot size by a factor of approximately 10 from ~20-50 μm to ~400 μm. The redesign also utilized the new coupon clamp system termed the “camera clamp”, which has been described in detail previously in this document and provided a much higher shot-to-shot throughput than the previous eight electrode coupon clamp design. Further, an optical path was built so as to pick off some of the arc light using a CaF<sub>2</sub> window and directed to the Andor spectrometer to collect Cu atomic emission for temperature determination. The surface of the CaF<sub>2</sub> window was sputter coated with Al making a highly mirrored finish. However, the center of the aluminized window was etched away to allow IR light pass into the TRIR spectrometer. This redesign allowed simultaneous measurement of both atomic emission for temperature determination and time-resolved infrared data to monitor chemical dynamics.

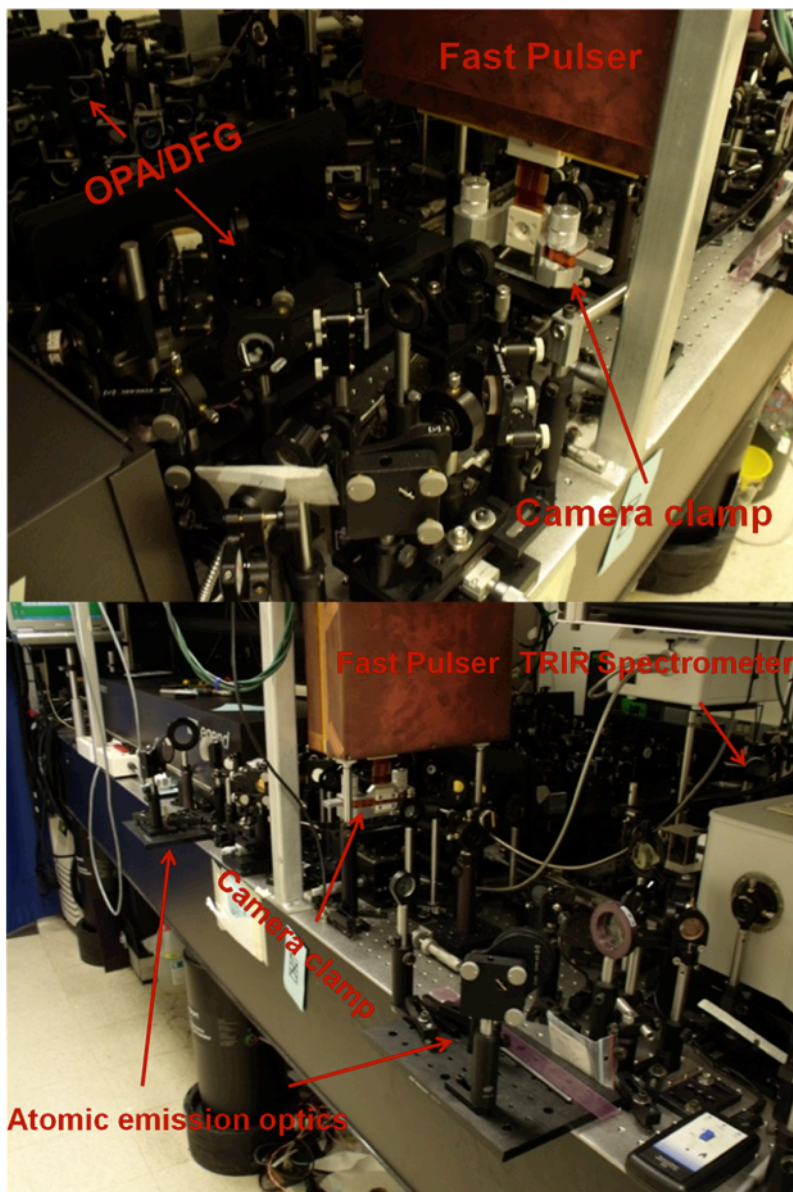
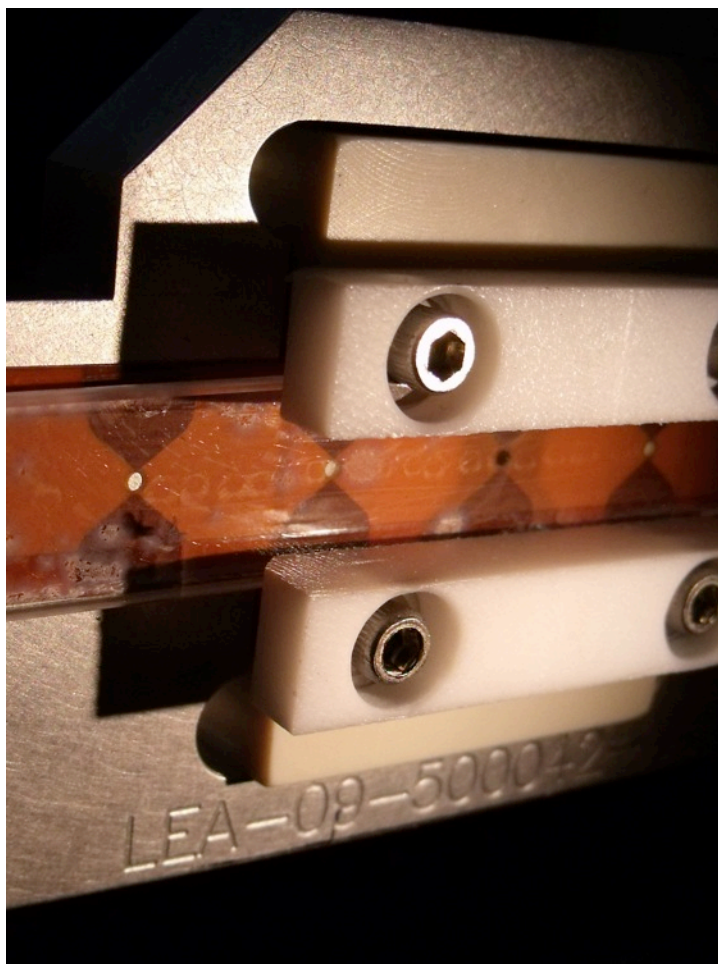


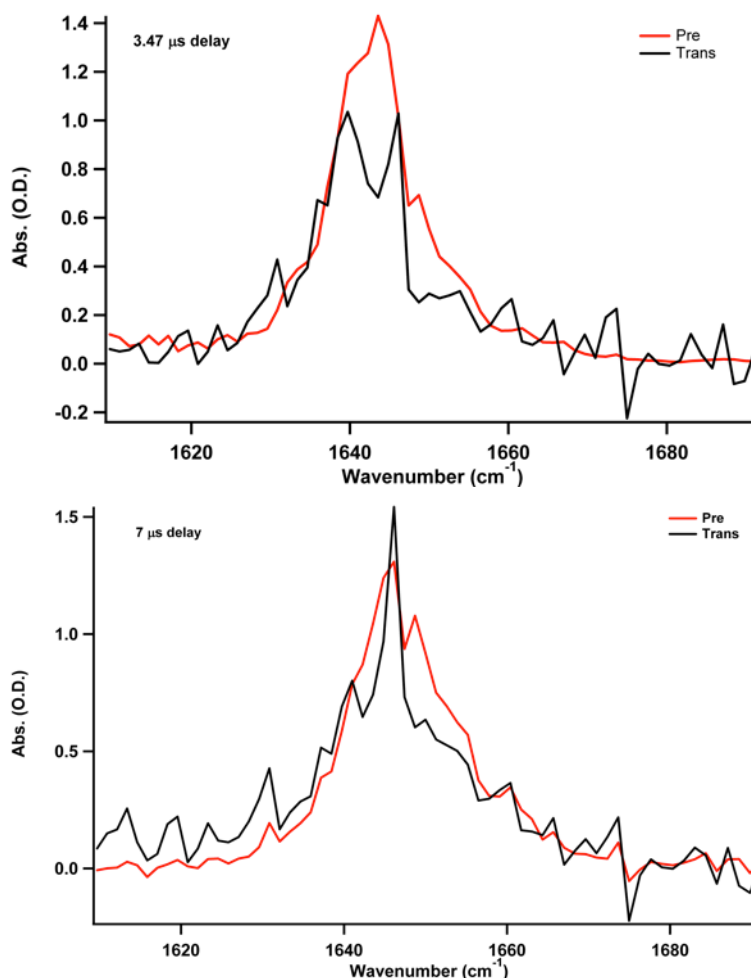
Figure 4.5. The redesigned TRIR system showing the various optical and electrical components. Mid-IR laser pulses are directed from the OPA/DFG system (left to right in both images) through the camera clamp and into the TRIR spectrometer. The atomic emission optics direct part of the arc plasma light down the optical bench to a fast gated detector for collection.

Figure 4.6 shows a close up image of the camera clamp containing a PETN thin film sample. It is clearly evident in the photograph round spots that are the result of HE being ablated or otherwise reacted in response to the arc discharge. This was convenient in that it allowed the operator a visual mark with which to move to an undamaged part of the film for the next experiment. The new clamp design was a success in that it greatly increased the shot throughput by a factor of at least 3. More than 20 shots could be completed within just a couple hours versus 8-10 shots over ~4 hours with the previous clamp system.



**Figure 4.6. Photograph of the camera clamp with a PETN film in place. The round discolored spots are where HE has been reacted/ablated; these spots line up with the circular openings that correspond to the electrodes.**

Figure 4.7 shows sample TRIR spectra for two time delays relative to plasma development. It shows both pre- and transient spectra illustrating the time dependent change in area and intensity. Both transient spectra show an overall peak area decrease relative to and are noisier than the pre-spark spectra. One reason that pre-spark spectra are cleaner is due to averaging while the transients consist of only one spectrum. However, in the  $7 \mu\text{s}$  delay data there is a clear spike that is likely due to electrical noise introduced by the high power arc pulser. The noise issue will be discussed more below.



**Figure 4.7. Pre- and transiently sparked IR spectra at two different time delays relative to plasma development.**

For the second TRIR campaign, 42 data points were taken at different time delays typically with three replicates at each delay. All pre- and transient data were fit to Gaussian lines; the resulting difference in peak areas are averaged and plotted in the top panel of Figure 4.8. There is a fair amount of spread in the data though there is a clear trend as a function of time. If we make the overly simple assumption of first order kinetics like was made previously, an exponential fit yields a time constant of  $1.7 \mu\text{s}$ , which is in agreement with what was observed for a much smaller number of points from the first TRIR campaign. These data combined with what was obtained in the first campaign sets an approximate time scale for the ablation/reaction of the thin HE film.

In addition, temperature measurements were simultaneously collected during the TRIR shots and the average for each time delay are presented in the bottom panel of Figure 4.8. The temperature ranged from 1.3 eV at  $\sim 2 \mu\text{s}$  delay to 0.5 eV at  $\sim 8 \mu\text{s}$ . At time delays greater than  $8 \mu\text{s}$  from plasma development, there was not enough signal intensity from Cu atomic emission to make a reliable temperature determination. However, we have successfully demonstrated that we are able to monitor chemical decomposition as well as temperature in a time-resolved manner (bearing in mind the limitations of the TRIR system), which in and of itself is an achievement.

To our knowledge, no simultaneous measurements of this type have been reported in the open literature, and we do plan on publishing our results as soon as possible.

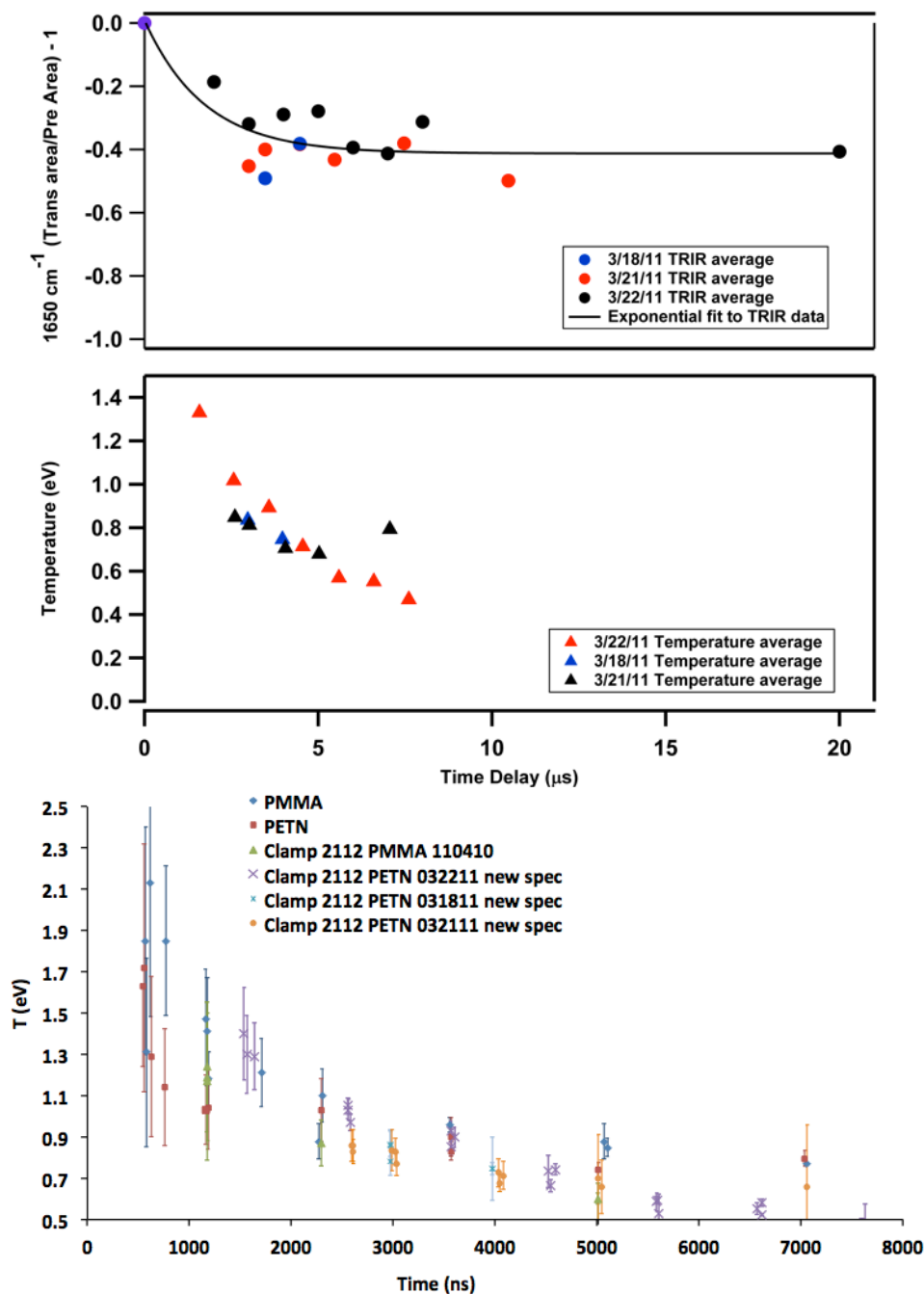
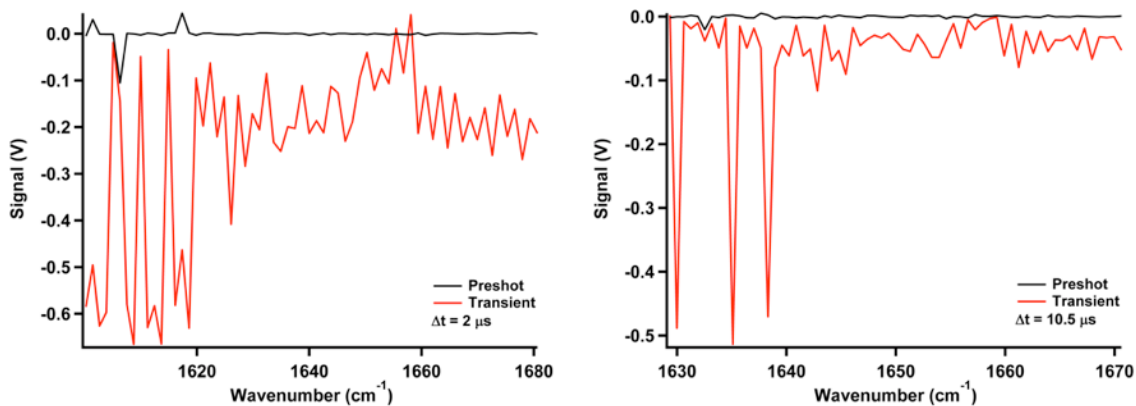


Figure 4.8. Top: Summary of TRIR 2<sup>nd</sup> campaign data. The changes in peak area between pre- and transiently sparked spectra have been average for each time delay. The number of total shots that make up this figure is 42. Making the overly simple assumption of first order kinetics an exponential fit to this data yields a time constant of 1.7  $\mu\text{s}$  which is consistent with the previous results from the 1<sup>st</sup> campaign. Middle: Summary of temperature data simultaneously obtained with the TRIR measurements. Temperature data presented are average for each time point. Beyond 8  $\mu\text{s}$ , Cu lines were not observed with enough intensity to make temperature determination. The total number of data points that have been reduced to make the bottom panel is 40. Bottom: Temperature points before time-averaging.

As was briefly touched upon in the previous section, the arc pulser induces noise in the MCT IR detector (see MCT pixel readout in Fig. 4.3) at early times relative to plasma development ( $< 3 \mu\text{s}$ ) and is larger than the signal from the arrival of the laser pulse. However, even at later delay times noise still plagues the TRIR detector. For example, presented in Figure 4.9 is a comparison of the noise at two different delays (2 and  $10.5 \mu\text{s}$ ) relative to plasma development for pre-spark and transient spark. The noise assessment was made in the absence of laser light, i.e. the input to the IR spectrometer was blocked. This allowed us to make certain that the noise issue was independent of plasma development, e.g. absorption of the IR light by the plasma. What is clearly evident is that there is very little noise in the pre-shot data while the transient data contain a significant amount. At  $2 \mu\text{s}$ , there is more noise in the transient than there is at  $10.5 \mu\text{s}$ . This is consistent with the MCT readout shown in Fig. 4.3. Of major importance is that the signal is negative for the transients. Under normal experimental conditions, the MCT detector registers a positive voltage from laser irradiation. A smaller voltage usually translates into less transmission. For example, thicker PETN films attenuate the laser light more dramatically than thinner films thus leading to smaller voltages. Normally, a larger positive voltage would be observed in the absence of this induced noise because the film is ablating/reacting and becoming thinner (hence, more transmission or less absorbing) in response to the arc impulse. However, because the pulser is inducing a negative voltage bias into the detector during operation this makes the voltage less positive thereby indicating less transmission or more absorption than what is physically possible given post-shot analysis of the films, i.e.  $\sim 300 \text{ nm}$  of material is ablated/reacted. This induced noise is the likely reason that there is so much variation in the TRIR data (Fig. 4.8)



**Figure 4.9. Comparison of noise intensity between pre- and transient signal at two different time delays in the MCT IR detector. At early delay time relative to plasma development the noise in the transient signal is much larger than at later delay time. However, the noise level for both delay times when compared to the preshot signal is actually significant.**

Several attempts were made to mitigate the noise issue. The solutions mostly involved shielding the IR detector or the pulser or trying to reduce ground loops or limiting cabling that could act as antennae. Shielding ultimately only had a minor effect, but was implemented nonetheless. In addition, we performed a careful analysis on some of the raw transmission data by varying the delay time as well as the detector gating while keeping the film thicknesses constant. Figure

4.10 shows three different raw transmission spectra that consist of pre-, transient, and post-spark data. The top and middle panels are for a delay time of 2  $\mu\text{s}$  but have 500 and 1000 ns IR detector gate widths, respectively. The bottom panel has a delay time of 5  $\mu\text{s}$  and a gate width of 1000 ns. The 2  $\mu\text{s}$  delays are “worst” case scenarios in terms of noise contamination from the arc pulser. First, there is more transmission post-spark than pre-spark, which is consistent with less material remaining after a spark insult. However, what is evident between both 2  $\mu\text{s}$  cases is that the 1000 ns gate has more noise contamination from the pulser in the transiently sparked spectrum that manifests in the signal as actually reading a negative voltage, which is physically impossible as described earlier. When comparing the 500 ns gate, 2  $\mu\text{s}$  delay to the 1000 ns gate, 5  $\mu\text{s}$  delay the magnitude of the noise is less with the 500 ns gate versus the 1000 ns gate where the 1000 ns spectrum shows a smaller positive voltage than the pre-spark spectrum. It should be pointed out that the 500 ns gate, 2  $\mu\text{s}$  transient spectrum shows a similar transmission to the pre-spark, which is likely not possible. In any case, the conclusion that we drew from this more detailed analysis was that we should use a shorter gate width whenever possible to limit the noise pollution from the arc pulser.

Further, we also concluded that the PETN films were likely too thick. For a sample thickness of  $\sim 1 \mu\text{m}$ , the optical density was approximately 2. This translates approximately to a transmission of  $\sim 1\%$ . The voltage that corresponds to a transmission of 1% is on the order 100 mV. A negative voltage of that order can be induced by the pulser (see Figure 4.9). To mitigate any negative voltages in the raw data, thinner HE films of approximately 500 nm were spun coated.

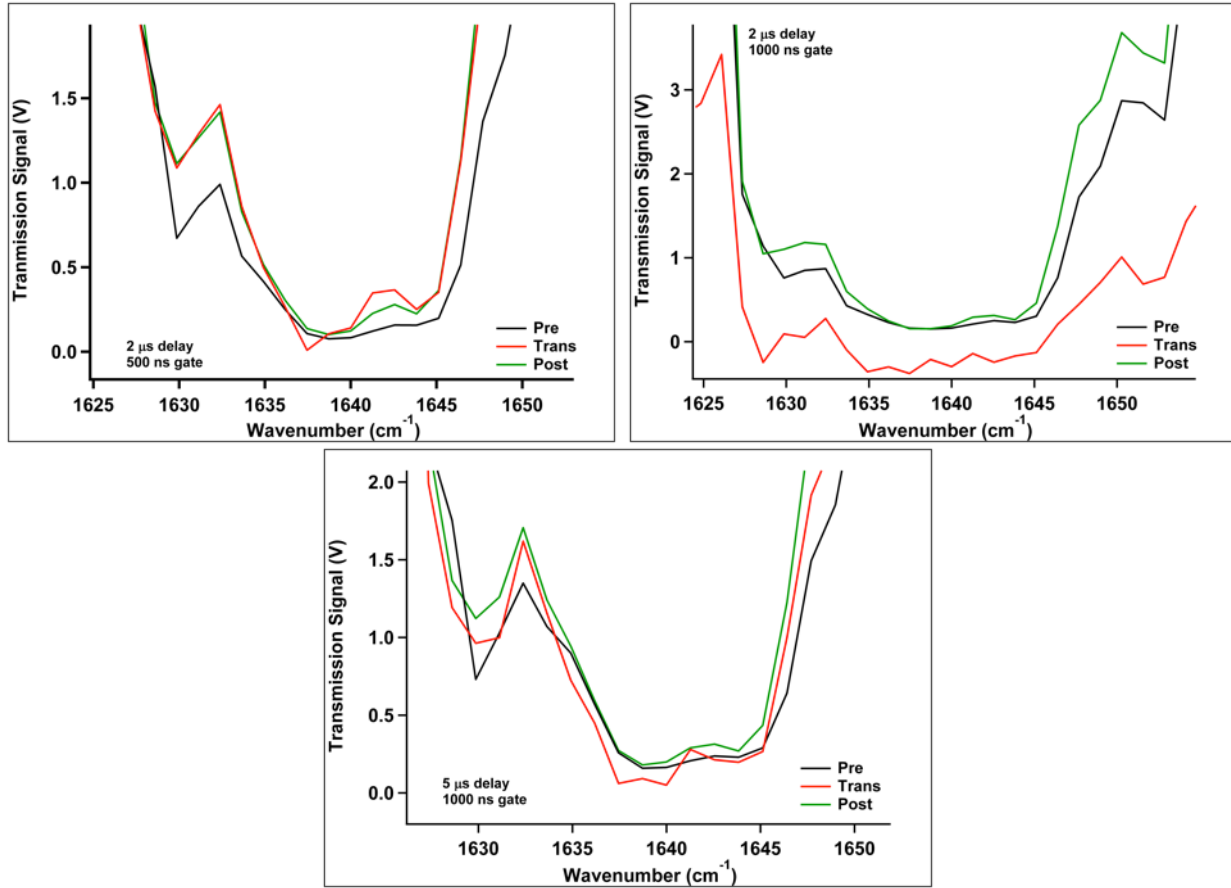


Figure 4.10. Three different raw transmission spectra that consist of pre-, transient, and post-spark data for a PETN thin film of approximately 1  $\mu\text{m}$ .

#### 4.3. Hardware failure and attempted recovery

On 4/13/11, there was a catastrophic failure of the initial pump laser that drives the fs IR system. Initially the diagnosis was that the diodes on the Verdi laser failed. However, after replacing the diodes it was determined that the laser head was the actual component that had failed. All in all, it took more than 8 weeks from initial failure to final repair on 6/16/11 thus jeopardizing finishing the TRIR work by the end of the LDRD project. This 8-week downtime from the failure of the Verdi laser was compounded by other downstream laser problems. We have noticed in the past that when the fs mid-IR system sits idle on the order of weeks to months the optical alignment changes detrimentally. Hence, the OPA/DFG system that generated the mid-IR pulses was not operational after repair of the Verdi laser and needed to be realigned.

We encountered several additional problems during realignment. We noticed soon after sufficient alignment to generate IR pulses was accomplished that the energy/pulse was low. After careful examination, it was determined that, for reasons unknown, the pump beam from the fs amplifier was focusing in the OPA/DFG. This had the effect of burning several mirrors in the OPA and DFG that lead to the decline in power. These mirrors were replaced. Further, the beam qualities in the OPA over the various optical paths were poor and had to be repaired and required a general realignment of the entire OPA/DFG system from first-principles. All of these



additional problems took approximately another month to remedy to the point that new data could be collected.

Several data points were collected and Figure 4.11 shows a sample TRIR spectrum for one time delay. The transient data illustrates the continuing noise issue that has plagued all TRIR measurements. The spikes that are evident in the transient data (and also in the transient difference spectra) make the data unusable and were evident in nearly all data taken in the last TRIR campaign. Even using thinner films combined with a shorter gate width (500 ns) as was determined from the 2<sup>nd</sup> TRIR campaign did not fully mitigate the noise issue.

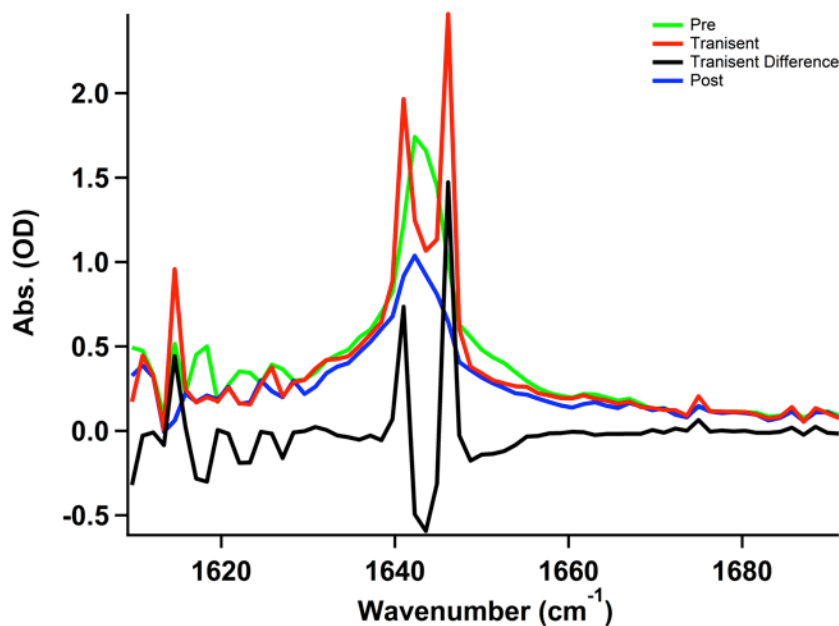


Figure 4.11. Pre-, transient, post-, and transient difference TRIR spectra for a time delay of 10  $\mu$ s from the development of the plasma.

## 5. Pumped Convective Burn

NOTE: The first few subsections (5.1-5.5) were also included in CODT-2010-1816, an internal annual report for NSR&D activities, because it was also of interest to that community.

In this section, we will present a model referred to as “pumped convective burn” (PCB), which shows promising signs of reproducing observed ESD threshold behavior. We emphasize that this work is still in its early stages, and either data acquired in the near future or corrections to the model and its numerical implementation could quickly invalidate it.

This section is rather long and so we provide a breakdown of the subsections in it. Subsection 5.1 gives background on the observations and assumptions that drive the model. Subsection 5.2 gives a physical picture of the process and subsection 5.3 presents a mathematical model for it. Subsection 5.4 discusses the choices for a number of physical parameters in the model, and specifically motivates the values chosen for the numerical study described in subsection 5.5. Subsection 5.6 further pursues the important topic of the burn rate of the HE grains, from a temperature-based perspective. Subsection 5.7 presents the derivation of a steady PCB wave, which can release energy from the HE on fast time scales and short length scales without requiring shock compression of the solid-phase HE (as would occur in a detonation) or compaction of low-density material (as would occur in a deflagration-to-detonation transition, or DDT). We believe this is the first such derivation of this type of wave, which may be important in our understanding of low-density HE initiation and the general response of HE to fast thermal insults. Subsection 5.8 summarizes the steady-wave work, and 5.9 lists the references particular to this section.

### 5.1. Background

The focus of this LDRD was intended to be on the high-temperature kinetics of arc-driven HE, and therefore the experimental configuration is not directly pertinent to pin-to-case discharges in macroscopic (~1 gram as opposed to < 10 mg) HE samples; however, two particular results from the LDRD characterization work have provided what may be key insights into the initiation of detonator-size quantities of low-density HE. The test configuration referred to in the bullets below is shown in Figure 5.1.1.

- The discharge in the LDRD experiments is between two thin electrodes pressed against a thin film of solid PETN. The properties of the discharge are very repeatable and it is observed to occur in the air above film, not through the film itself.
- Only a fraction of the film’s thickness is reacted or at least vaporized as the discharge evolves hydrodynamically against the surface; the volume of material that is removed is quantitatively consistent with what would be expected from rapid ablation (see the reference for a bit more detail). In other words, an initially heated and vaporized volume is quickly convected away from the free surface before any other transport mechanism can heat more of the interior volume of the film.

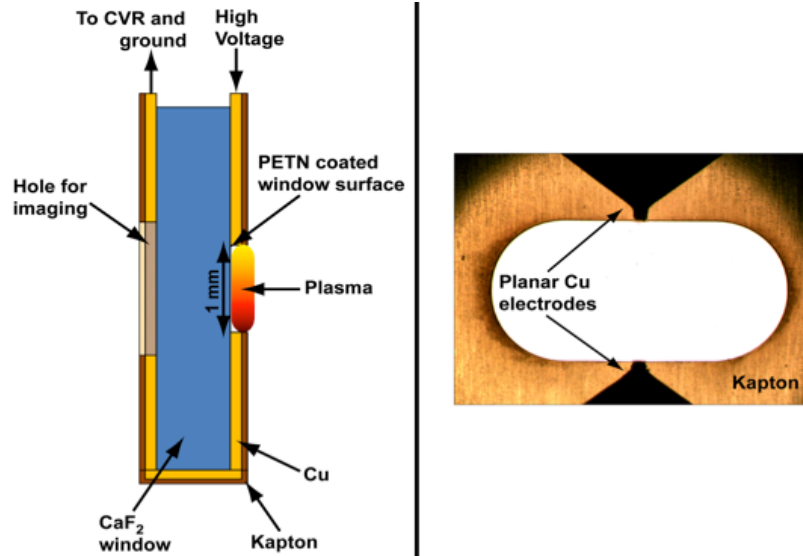


Figure 5.1.1. Reminder of the test configuration for the arc characterization experiments.

In a pin-to-case discharge in a detonator configuration, the discharge is either at an interface between a solid surface and a low-density pressing of HE, or through the low-density volume itself. By “low density” we mean about half of theoretical maximum density (TMD) of the HE in question. In other words, half of the region in question is in fact air-filled void space. Thus, we map the two observations above to the following two assumptions about a macroscopic low-density volume:

- The discharge occurs through the air in the voids, not through the solid HE grains. This means that the resistive heat from the discharge is not directly heating solid HE.
- The subsequent energy transport during and after the discharge is *convection dominated*. Flow through the voids will be an influence on behavior that is at least comparable if not greater than transverse interactions between the heated voids and the grains.

Even if we temporarily ignore the energetic behavior of the HE, the two points above imply a system whose detailed behavior is taking place on the very small and geometrically complex scale of individual HE grains. To maintain tractability, we would nevertheless like to work with a continuum model. In order to do so, certain constraints must be satisfied:

- By the first assumption, the fluid in the voids and the HE grains are *not* in thermal equilibrium. A continuum model must follow two distinct temperature fields.
- To model the behavior described by the second assumption, we will bring to bear some of the machinery developed in the field of flow in *porous media*. While this is a heavily studied area, to this day it remains true that tractable porous media models must invoke some empirical ingredients. We will discuss this in more detail in the next section.

## 5.2. Physical Model

Let us introduce some relevant time and length scales. For simplicity, material properties are assumed to be constants.

We characterize the input electrical source as a roughly cylindrical discharge with an initial radial size scale of  $r_s \sim 0.125$  mm and a length  $L_s$  of 2.5 mm. It deposits a total energy  $E_s \sim 100$  mJ over a time  $t_s \sim 100$  ns.

The HE grains have a size scale  $r_{HE} \sim 10$  mm, a solid density  $\rho_{HE} \sim 1800$  kg/m<sup>3</sup>, a specific heat  $C_{HE} \sim 1100$  J/kg-K, and a thermal conductivity  $\kappa_{HE} \sim 0.25$  W/m-K. They are also characterized by a specific surface area  $s_{HE} \sim 700$  m/kg, which is considerably higher than the spherical value of  $3/\rho_{HE}r_{HE} = 167$  m/kg; the grains are quite irregular in shape. They are initially at room temperature,  $T_i = 300$  K. The only information about its energetic nature that we invoke at this stage is that a self-sustaining detonation wave would travel through bulk solid material at a speed  $c_{HE} \sim 7$  mm/ms.

The void space is initially filled with an ideal stand-in for air, with initial density  $\rho_i = 1.2$  kg/m<sup>3</sup> and in thermal equilibrium with the HE at temperature  $T_i$ . The molecular weight is assumed to be 28 and the equation of state is that of an ideal low-temperature diatomic gas with ratio of specific heats  $\gamma = 7/5$ . For purposes of estimating a Reynolds number, we use a viscosity  $\mu$  of  $1.8 \times 10^{-5}$  kg/m-s.

The overall macroscopic volume of the system has a length scale  $L \sim 1$  cm.

We now have enough information to begin drawing some interesting conclusions about the system behavior. For grains packed into the volume at half of the bulk density, the characteristic void diameter  $d$  will be on the order of the grain diameter,  $\sim 20$   $\mu$ m;  $d/L \ll 1$  and so a continuum porous media model should be feasible.

On the timescale of the input pulse, the characteristic thermal diffusion length into the HE (if it were to remain inert) is:

$$l_{conduct} \sim \sqrt{\frac{\kappa_{HE} t_s}{\rho_{HE} C_{HE}}} \sim 0.1 \mu m$$

and so  $l_{conduct}/r_{HE} \ll 1$ . Thus, not only are the fluid in the void and the HE not going to remain in thermal equilibrium, but there will be significant temperature gradients within an individual grain.

Conductive heat transport through the grains but parallel to the flow direction has a different length scale that is imposed by the scale of the problem—it is  $L$ , the system scale. Even if we assume the grains were a continuous medium, the thermal diffusion time is quite long:

$$t_{parallel} \sim \rho_{HE} C_{HE} L^2 / \kappa_{HE} \sim 1000s$$

Thus, along the flow direction, the dominant coupling mechanism grain to grain is via the convective heat transfer to and from the fluid. Thermal conduction parallel to the flow can be ignored.

If we take the extreme case where all of the input energy goes into the air with no convection, conduction, or other losses, the peak pressure would be:

$$P \sim \frac{2(\gamma - 1)E_s}{\pi r_s^2 L_s} \sim 6.5 \times 10^8 Pa$$

and in actual model results will tend to be less than  $10^8$  Pa, or an order of magnitude too low to be relevant for shock initiation over the run distance  $L$  and certainly far too low for shock-based detonation of individual grains in the early stages of the initiation process. Instead, the individual grains are initially consumed via a conductive burn wave, much slower than a shock wave. However, we posit that in the regime of interest the wave speed  $v_{\text{burn}} \sim 10$  m/s, significantly faster than what would be encountered in an unconfined, slow “cookoff” type of experiment. Such a burn wave would consume an individual grain in a time  $r_{\text{HE}}/v_{\text{burn}} \sim 1$  ms.

Finally, given  $P/P_i \gg 1$  where  $P_i$  is the initial (ambient) pressure, we expect that the peak fluid velocity  $v$  will be on the order of the sound speed  $c$ :

$$v \sim c \sim \sqrt{\frac{\gamma P}{\rho}} \sim 10 \text{ mm}/\mu\text{s}$$

Thus, even though the flow is through a porous media, it will remain compressible. In spite of the small void size, the high velocity gives a Reynolds number  $Re = \rho v d/\mu \sim 10^4$  and the flow will also be turbulent. Turbulence-enhanced heat transfer and shear viscosity must be taken into account. Enhancement of normal viscosity will also occur but not to the extent of smearing out normal gradients enough to avoid numerical treatment of shocks. Whether such shock fronts would remain stable in the porous context is beyond the authors’ current level of understanding.

If the fluid velocity were sustained at these levels, then observe that the transit time through the detonator volume,  $t_{\text{trans}} = L/v$ , is  $\sim 1$   $\mu\text{s}$  and is of the same order as the burn time for an individual grain. Thus a possible physical picture of arc initiation begins to emerge: a high-velocity flow of high temperature fluid in the void space ignites the surface of the HE grains throughout the entire volume in a short time. Then a thermal burn wave rapidly releases energy from the grains. Thus, energy is released from the entire volume within a few microseconds, even though a traditional shock-based detonation never takes place. Grain compaction, which plays a fundamental role in deflagration-to-detonation transition (DDT) in larger samples (typically tens of cm are studied in experiments) [9; 7, Ch. 8], may occur but is not required and in fact will be neglected in what follows (really without much justification at this point).

We refer to this picture as “pumped convective burn” because the high input power from the arc bootstraps the process, and the high temperatures achieved can sustain a faster than typical thermal burn wave which in turn continues to drive the convective flow in a self-sustaining pumping process. The pumped convective burn regime is characterized by the two properties:

$$t_{trans} \sim 1\mu s$$

$$\frac{Lv_{burn}}{r_{HEV}} \sim 1$$

which must be justified in what follows. Note that what is achieved in this regime is not a detonation in the strict sense, but may be more than sufficient to drive (for example) an output pellet in a detonator in the intended mode.

### 5.3. Mathematical Model

The mathematical model used to study pumped convective burn is based on one used with much success on a problem in a completely different area but which has many similarities: propagation of a quench front in cable-in-conduit type superconductors (CICCs). CICCs consist of bundles of superconducting strands with copper cladding, packed into a conduit. The strands are kept in the superconducting state by flowing cryogenic helium through the conduit. If an off-normal occurrence causes a local region of the strands to heat and transition to a resistive phase, the current transfers from the (no longer) superconducting material in the core of the strands to the copper cladding; however, the current density in the copper and the resistivity of the copper are still sufficiently high that rapid Joule heating occurs in the strands and the heat is quickly transferred to the surrounding helium. The hot helium then convects to a larger region, heating an increasing volume of the cable in a runaway event called a “quench.” The tight packing of the strands in the conduit produces a porous-media type of flow environment, with a characteristic void dimension on the order of 1 mm in cables that are tens of meters in overall length.

Details of a successful thermal hydraulic model of CICCs can be found in a series of papers by Shajii and Freidberg [1, 2, 3] and the doctoral thesis of A. Shajii, available from the MIT Plasma Science and Fusion Center [4]. This model will be adopted here without repeating the full derivation, and with some important modifications:

- In a quench, once the Joule heating source turns on, it remains on for a long time scale (in actual operation, the electrical current is dumped from the cable when a quench is detected, but this takes time). In pumped convective burn, the heating from burning HE is transient and an appropriate reactive model must be included.
- CICC quench falls into a unique flow regime called “low Mach number compressible flow,” which as the name implies means the flow retains significant compressibility even though the flow velocity remains highly subsonic. This occurs because frictional forces from the small void diameter can, over tens of meters of flow length, support enough of a pressure gradient to dominate inertial effects. This is not the case in pumped convective burn and the inertial terms in the model must be retained.

The turbulent correlations used in CICC modeling for heat transfer and friction from viscous shear are adopted in our pumped convective burn model without rigorous investigation into their applicability. Given that such empirical correlations are highly dependent on surface characteristics and geometric details, it is likely that these choices are not appropriate and this will have to be addressed in future work.

The model treats a one-dimensional cylindrically symmetric flow geometry, compounded with a locally transverse direction “into” the HE grains. The radial coordinate  $r$  denotes distance from the center of the original electrostatic discharge; the ratio of discharge radius to length is considered small enough that we neglect axial dependence. The coordinate  $x$  denotes distance from the center of any given HE grain. For now, the grains are treated as uniform in size and shape, with the actual complex shape represented by using a ratio of wetted perimeter to flow area that is weighted by the measured specific surface area (more detail will be given later). Figure 5.3.1 shows a somewhat more realistic picture of the physical situation, while Figure 5.3.2 shows that the mathematical equivalent resembles a cylindrical flow (through the pores) between closely spaced, uniform radial slabs (represented the HE grains).

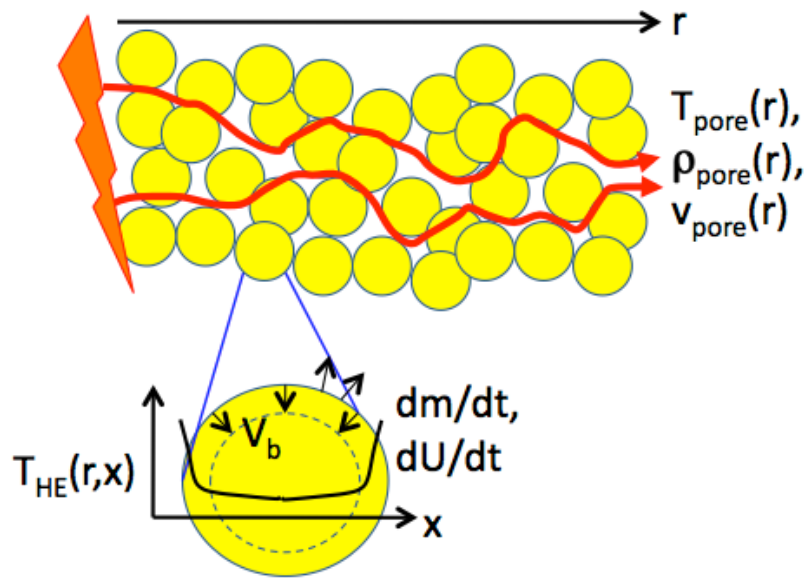


Figure 5.3.1. Schematic of flow through the pores and temperature gradient across individual grains.

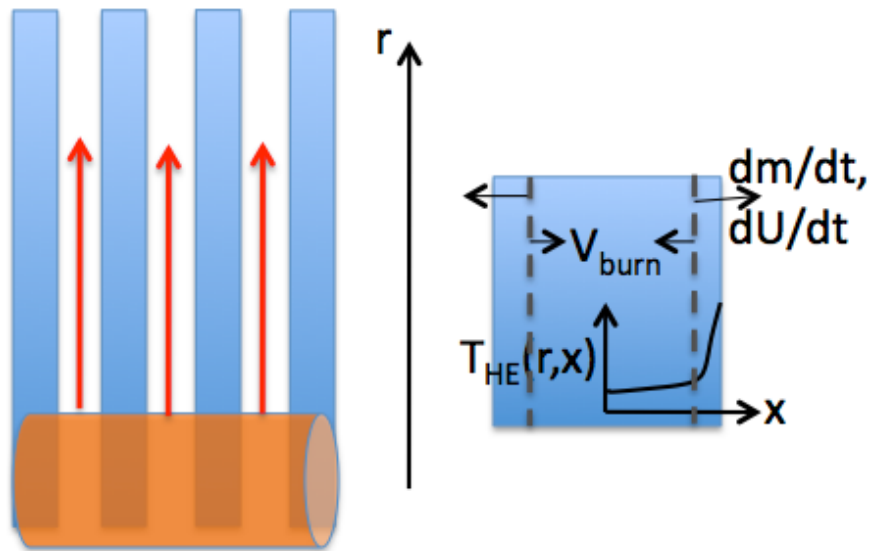


Figure 5.3.2. Schematic of the system as represented by the mathematical model. Note that there are significant gradients across the HE (now represented as slabs) but not across the channels representing the pores.

The system of equations consists of conservation of mass, momentum, and energy in the fluid and energy conservation in the grains. A reaction model for the grains must also be included but is not written explicitly below as a variety of models can be used; specific examples will be presented later.

The notation:

r	radial distance from the center of a cylindrically symmetric arc
t	time
x	local coordinate across the HE grains
$\rho$	fluid density
v	fluid velocity
P	fluid pressure
T	fluid temperature
U	fluid internal energy per unit volume ( <i>not</i> specific!)
E	total fluid energy per unit volume; $E = U + \rho v^2/2$
m	average molecular mass of the fluid
$k_B$	Boltzmann's constant
$\gamma$	ratio of specific heats in ideal EOS
d	hydraulic diameter of the pores
h	heat transfer coefficient (usually turbulent) between the fluid and HE
f	friction factor (usually turbulent) to represent viscous shear in the pores
S	production rate of reaction products entering the flow in the pores
$Q_{ext}$	input heating term from the arc
$P_w, A_w$	wetted perimeter and area, respectively; this is an accounting of the irregular grain shape
$S_{HE}$	specific surface area of the HE grains
$\rho_{HE}$	density of solid HE (the density of an individual grain; not a packing density)
C	specific heat of solid HE
$T_{HE}$	HE temperature
$Q_{HE}$	energy release in the reacting HE
$U_{HE}$	internal energy of reacted material as it flows into the pores from the grains
$\kappa_{HE}$	thermal conductivity of the HE
$f_{HE}$	fraction of HE still in the unreacted state

The system of equations is:

$$\frac{\partial \rho}{\partial t} + \frac{1}{r} \frac{\partial}{\partial r} (r \rho v) = \rho_{HE} S(f_{HE}, t)$$

$$\frac{\partial \rho v}{\partial t} + \frac{1}{r} \frac{\partial}{\partial r} (r \rho v^2) = -\frac{\partial P}{\partial r} - \frac{f \rho v |v|}{2d}$$

$$\frac{\partial E}{\partial t} + \frac{1}{r} \frac{\partial}{\partial r} (r v (E + P)) = Q_{ext}(r, t) + U_{HE} S(f_{HE}, t) - \frac{h P_w}{A_w} (T - T_{HE}) + \frac{f \rho v^2 |v|}{2d}$$



$$\rho_{HE} C \frac{\partial T_{HE}}{\partial t} = \kappa_{HE} \frac{\partial^2 T_{HE}}{\partial x^2} + Q_{HE}(r, x, t)$$

$$\text{subject to } -\kappa_{HE} \frac{\partial T_{HE}}{\partial x} \Big|_{edge} = h(T - T_{HE})$$

$$\text{and } -\kappa_{HE} \frac{\partial T_{HE}}{\partial x} \Big|_0 = 0 \quad (\text{symmetry at the grain center})$$

$$\frac{\partial f_{HE}}{\partial t} = \dots \quad (\text{various kinetic models})$$

Finally, the system is closed by the definition:

$$E = U + \frac{1}{2} \rho v^2$$

and the ideal state equations

$$P = (\gamma - 1)U \quad \text{and} \quad T = \frac{(\gamma - 1)m}{k_B} U / \rho$$

#### 5.4. Various Empirical Choices

In this section we present the choices made for specific values or models used to calculate some parameters in the above system.

##### 5.4.1. Heat Transfer and Viscous Shear

It is very instructive to explore the effects of heat transfer and viscous drag by doing parametric studies across various constant values of  $h$  and  $f$ . However, since in many cases the flow does not fully develop until the input energy from the arc has been turned off, a more realistic bootstrapping of pumped convective burn should take into account the transition from lower (more laminar) to higher (turbulent) flow velocity. As mentioned above, we have explored the effect of some empirical correlations for  $h$  and  $f$ , albeit without much study on whether the chosen correlations are the most appropriate.

For the heat transfer coefficient, we use the same approach as in the references. Defining the heat transfer coefficient in terms of the Nusselt number,  $N$ , fluid thermal conductivity  $\kappa$ , and hydraulic diameter  $d$ :

$$h \equiv \frac{\kappa N}{d}$$

For laminar flow, we use  $N = N_l = 4$ . For turbulent flow,  $N = N_t$ , we use the Dittus-Boelter correlation but keep the Prandtl number  $Pr$  fixed at 1:

$$N_t = 0.026 Re^{0.8} Pr^{0.4} (T/T_{HE})^{0.716}$$

where  $Re$  denotes the Reynolds number,  $\rho v d / \mu$ . To create a single, continuous function, we blend the two so that they transition at about  $Re = 5000$ :

$$N = N_l + N_t e^{-(5000/Re)^2}$$

The friction factor is usually held constant at 0.01, but when a Reynolds number dependent form is desired we again take directly from the references,

$$f = 0.184/Re^{0.2}$$

where, due to lack of any real data for this configuration, we have dropped a leading scaling coefficient of order unity which attempts to account for surface roughness.

The meaning of  $P_w/A_w$  is another open question. Because of the continuous nature of the strands in CICC, the wetted perimeter and area are well-defined quantities. In the packed-powder geometry, it is apparent that a re-derivation of the approximation of turbulent heat transfer should be performed and we have not (yet) done so. Two possible choices of force-fitting this factor in the current model are to use the ratio of the surface area to the grain volume, or the square-root of the surface area to the grain cross-sectional area:

$$P_w/A_w \sim \rho_{HE} s_{HE} \quad \text{or} \quad \sim \sqrt{4\rho_{HE} s_{HE}/3\pi r_{HE}}$$

Because the magnitude of the heat transfer is important to reaching the pumped convective burn regime, we do not want to artificially boost the heat transfer too much and perhaps deceive ourselves into the existence of the pumping mechanism. Thus, until the matter can be investigated with more rigor, we choose the square-root form. (Writing  $s_{HE}$  in the form of a multiplicative factor over the spherical value shows that, for the typical measured values of  $s_{HE}$ , the square-root form is indeed smaller.)

#### 5.4.2. External Heating

Framing camera images of the discharge between the electrodes show that the initial streamer is very well defined by the electrode geometry—i.e., there is a single streamer spanning the gap, whose diameter matches the electrode width. In threshold testing experiments performed under the Nuclear Safety R&D portfolio, whose thresholds are what we ultimately want to predict, the discharge is between two 10-mil (about 250 microns) wide copper electrodes separated by a gap of 100 mils (about 2.5 mm). In the model we wish to work with a smooth distribution and so we represent the source as having a Gaussian profile in  $r$ , with a characteristic radius of 125 microns. The total source energy is in the range 10-100 mJ and thus the 2.5 mm arc length in the NSR&D configuration specifies the input energy density. The temporal profile is taken to be constant over a specified pulse length, typically 100 ns; this specifies the input power density.

Data from the experiments shows that the arc does evolve hydrodynamically while energy is still being input; we do not yet take this into account. In other words, even though the model does convect the heated fluid during the pulse, the heating is still deposited over a fixed profile in the Eulerian frame.

As stated earlier, the initial fluid in the pores is idealized air, at a density of  $1.2 \text{ kg/m}^3$  and temperature of  $300 \text{ K}$ , with a corresponding initial pressure close to  $1 \text{ atm}$ . The molecular weight  $m$  is taken to be  $28$  and the ratio of specific heats  $\gamma$  to be  $7/5$ . When required to evaluate  $h$  and  $f$ , the thermal conductivity is taken to be  $0.024 \text{ W/m-K}$  and the viscosity is  $1.8 \times 10^{-5} \text{ kg/m-s}$ .

### 5.4.3. Burn Model

The details of the grain-level burn model are critical to pumped convective burn, because the speed at which an HE grain is consumed by a conductive burn wave is a key contributor to the overall physics. There are numerous models in the literature [5, 6] but none of those examined thus far meet the correct requirements. Some features that typically result in a mismatch include lack of reactant depletion, an assumed high activation energy limit, or boundary conditions for the flow that do not apply to our conditions (for example, a constant external pressure, with negligible convective effects, is often used).

At this time, we have not developed what we feel to be a fully consistent model. We will describe some simple cases that are easy to implement and then present two limiting calculations that show how the burn rate can be very sensitive to model assumptions.

The speed of the burn wave in a grain is the desired output of the burn model. If the average molecular weight of the fully reacted products is not too different from air, then even at a relatively low product temperature of  $1000 \text{ K}$  we get a thermal speed of about  $500 \text{ m/s}$ . The corresponding transverse transit time (across the void space) for a  $10\text{-micron}$  void is about  $20 \text{ ns}$ , fast compared to the overall timescales of interest (hundreds of  $\text{ns}$  to microseconds). Therefore, we convert the transverse flux of mass and energy to a volumetric source within the voids by means of the source rate  $S = 2v_{\text{burn}}(r,t)/d$ , where the factor of two appears because opposing faces of grains will be contributing to the same void.

In the simplest test case, we use a simple threshold model to represent the burning of the HE. While the grain surface is below a critical temperature, the grain is inert. Above that temperature,  $v_{\text{burn}}$  is taken to be constant until a time  $r_{\text{HE}}/v_{\text{burn}}$  has past, at which point the grain is considered consumed. The parameter  $v_{\text{burn}}$  is a knob but we tend to focus on a value of about  $10 \text{ m/s}$ , at which level interesting behavior is observed.

The HE we try to represent is PETN. We use a solid density of  $1800 \text{ kg/m}^3$ , a specific heat of  $1100 \text{ J/kg-K}$ , and a thermal conductivity of  $0.25 \text{ W/m-K}$ . For the threshold model, we assume that the reaction rate has become fast relative to any other timescale by a temperature of  $1000 \text{ K}$ . For a single-step Arrhenius model, we use parameters similar to those of the final step of the four-step Tarver/Tran/Whipple model [8], with a rate constant of  $1.e14 \text{ s}^{-1}$  and an activation energy of  $145 \text{ kJ/mol}$  (somewhat higher than the fourth-step value, but lower than earlier steps) which maps to a temperature of  $17400 \text{ K}$  ( $1.5 \text{ eV}$ ). The net energy release is taken to be  $6 \text{ MJ/kg}$ , meaning the model parameter  $U_{\text{HE}}$  is given by  $\rho_{\text{HE}}(CT_i + 6 \text{ MJ/kg})$ . Ideally, we would like to incorporate a full multi-step model, including endothermic steps; we expect the latter to have a significant effect, particularly when looking ahead to studying highly insensitive TATB.

### 5.4.3.1. Hard-threshold Limit

Let us consider the hard-threshold model, where the HE is inert below some critical temperature  $T_{crit}$ , then reacts instantly above that threshold. We assume that the reacted material is mixed into the void space on a fast time scale and is the dominant contribution to the volumetric energy density in the voids. We further assume that variation of the temperature of the reacted fluid in the void, as well as acceleration of that fluid, occurs on a slow time scale. Thus we expect the fluid in the void to act as a thermal reservoir at a temperature of order  $U_{HE}/\rho_{HE}C$ . This is not a great assumption since the total thermal mass in the void space will in general be less than that of the grains and thus heat loss into the burning grain is not negligible. However, the idealized limit we are taking will already produce a result that does not attain the burn velocity required to support the pumping mechanism.

We slightly modify the coordinate convention used previously. Consider a steady burn wave moving in the positive  $x$  direction, which is now taken to be moving into a grain. The wave position is defined to be  $x = 0$  in a frame moving at  $v_{burn}$ . Ahead of the wave, the HE is below  $T_{crit}$  and therefore inert. Energy is transported into the inert material via thermal conduction. Far ahead of the wave, the grain is assumed to be at its initial, ambient value  $T_i$ . Behind the wave, we assume heat transfer is taking place from the hot, fully reacted fluid filling the void space; the fluid is at some constant, specified temperature  $T_{fluid} > T_{crit}$ .

The resulting model is a single ODE which is the steady-state heat conduction equation in the moving frame:

$$-v_{burn} \frac{dT}{dx} - \frac{\kappa_{HE}}{\rho_{HE}C} \frac{d^2T}{dx^2} = 0$$

subject to three boundary conditions:

$$T|_{x=0} = T_{crit}$$

$$-\kappa_{HE} \frac{dT}{dx}|_{x=0} = h(T_{ext} - T) = h(T_{ext} - T_{crit})$$

$$T|_{x \rightarrow \infty} = T_i$$

The appearance of three conditions rather than two is what provides an eigenvalue condition to determine  $v_{burn}$ . Integrating the ODE from 0 to  $x$  and applying the initial conditions, we get (using a prime to denote differentiation and dropping the “burn” subscript):

$$T' + \frac{\rho_{HE}Cv}{\kappa_{HE}}T = T'|_0 + \frac{\rho_{HE}Cv}{\kappa_{HE}}T|_0 = \frac{h}{\kappa_{HE}}(T_{crit} - T_{ext}) + \frac{\rho_{HE}Cv}{\kappa_{HE}}T_{crit}$$

This is easily solved:

$$T(x) = T_{crit}e^{-\rho_{HE}Cvx/\kappa_{HE}} + \frac{(h/\kappa_{HE} + \rho_{HE}Cv/\kappa_{HE})T_{crit} - hT_{ext}/\kappa_{HE}}{\rho_{HE}Cv/\kappa_{HE}}$$

Enforcing the third boundary condition, ahead of the front, means:

$$T_i = \frac{(h/\kappa_{HE} + \rho_{HE}Cv/\kappa_{HE})T_{crit} - hT_{ext}/\kappa_{HE}}{\rho_{HE}Cv/\kappa_{HE}}$$

which can only be true if:

$$v_{burn} = \frac{\frac{h}{\rho_{HE}C}(T_{ext}/T_{crit} - 1)}{1 - T_i/T_{crit}}$$

For a rather extreme case of  $T_{ext}/T_{crit} \sim 5$  and assuming  $T_i/T_{crit} \ll 1$  gives:

$$v_{burn} \approx 0.006N \text{ in m/s}$$

where  $N$  is the Nusselt number and we have assumed a hydraulic diameter of 10 microns and that the thermal conductivity of the reacted-product fluid is the same as air. The latter assumption is weak but a correction to it (which would likely move in a favorable upwards direction) is not useful since the Nusselt number is not likely to be very high; for moderate temperature ratios, the Dittus-Boelter value for  $N$  does not reach  $\sim 100$  until  $Re \sim 10^4$  (in fact, that correlation is not valid much below that range of  $Re$ ).  $N$  is of course clamped on the low end by the laminar limit of 4. Thumbnailing an estimate for the change in thermal conductivity in the void, we might expect a burn velocity that is at best in the range 0.1-1 m/s. Thus in this limit we are left with a burn velocity that is one or possibly even two orders of magnitude too low to support pumped convective burn.

#### 5.4.3.2. Single-step Arrhenius with Constant Heat Flux

There are analytic models in the literature, all the way back to the “classical” Frank-Kamenetskii and Semenov models, which incorporate single-step Arrhenius kinetics with various simplifying assumptions [7, Ch. 4]. However, we have not (at least so far) found the exact calculation given below in the literature. Even if it turns out not to be new, it is worthwhile to show it in some detail so that the assumptions used are (hopefully) clearly stated.

We again start by considering the HE in a limit where convection is not important. This sounds like a strange assumption when considering something called convective burn, but recall that in our pumped convective burn model, the dominant convection is of air and fully reacted products through the voids. Transverse convection from a burning grain into the void space is handled via a boundary interaction; fluid-phase HE is assumed to convect quickly enough into the void space that it is treated as a volume source in the void, rather than following the convection explicitly. There is an implied boundary between fluid-phase and solid-phase material and the burn model applies (thus far) only to the solid phase.

Thus, as presented in Section 5.3, we treat the HE with transverse thermal conduction and a heat source from reacting HE, specified by a first-order Arrhenius term, proportional to an unreacted fraction  $f$ . The evolution of  $f$  itself is governed by the same rate term. (In this section we are referring only to HE and will therefore drop all the “HE” subscripts.)

$$\rho C \frac{\partial T}{\partial t} = \kappa \frac{\partial^2 T}{\partial x^2} + U_o f \nu e^{-T_a/T}$$

$$\frac{\partial f}{\partial t} = -f \nu e^{-T_a/T}$$

where  $\nu$  is the rate constant,  $T_a$  is the activation temperature, and  $U_o$  is the net energy release per unit volume of HE.

If we change to a new x-coordinate moving with a fixed speed  $v$  and look for a steady-state burn solution in this frame, we get:

$$-\rho C v \frac{dT}{dx} = \kappa \frac{d^2 T}{dx^2} + U_o f \nu e^{-T_a/T}$$

$$-v \frac{df}{dx} = -f \nu e^{-T_a/T}$$

Exploiting the presence of the same combination of factors in right-hand sides of both equations, we can write the conduction equation in the form:

$$-\rho C v \frac{dT}{dx} = \kappa \frac{d^2 T}{dx^2} + U_o v \frac{df}{dx}$$

which can be integrated from some point  $x$  to positive infinity (representing an undisturbed physical location far ahead of the burn front) where  $f = 1$ ,  $T = T_i$ , and  $dT/dx$  approaches 0:

$$\frac{\kappa}{U_o v} \frac{dT}{dx} = 1 - f - \frac{\rho C}{U_o} (T - T_i) \quad (a)$$

The system is autonomous and  $f$  has a very well defined range from 0 to 1, so we eliminate  $x$  and switch to  $f$  as the independent variable, leaving a single ODE:

$$\frac{\kappa}{U_o v^2} \frac{dT}{df} = \frac{1 - f - \frac{\rho C}{U_o} (T - T_i)}{f \nu e^{-T_a/T}}$$

In the case where the domain of interest for  $x$  extended to negative infinity, we would expect  $dT/dx$  to approach zero along with  $f$ ; by inspecting the equation labeled (a), we can see that  $(T - T_i)\rho C/U_o$  must go to 1 in the same limit. This introduces a useful scale temperature that we use to define several normalized quantities:

$$\hat{T} \equiv (T - T_i)\rho C/U_o \quad \hat{T}_a \equiv T_a \rho C/U_o$$

$$\hat{T}_i \equiv T_i \rho C/U_o \quad V^2 \equiv \frac{\rho C v^2}{\kappa \nu} e^{\hat{T}_a/(1+\hat{T}_i)}$$

Over a broad range of applications, the normalized activation temperature is greater than 1 and the normalized initial temperature is  $\ll 1$ . Introducing these into the ODE yields the final form:

$$\frac{d\hat{T}}{df} = V^2 \frac{1 - f - \hat{T}}{f} e^{\hat{T}_a \left( \frac{1}{\hat{T} + \hat{T}_i} - \frac{1}{1 + \hat{T}_i} \right)}$$

Let us start by considering the full-domain case where  $x$  ranges from negative to positive infinity and  $f$  ranges from 0 to 1. Physically this is “perfect confinement,” with no transverse convection and no heat flux entering or leaving the system behind the burn wave. In this case, the first-order ODE must satisfy two constraints, namely that the normalized temperature asymptote to 0 far ahead of the wave and asymptote to 1 behind it. The only way to satisfy both constraints with a first-order system is to allow  $V$  to be an eigenvalue in the problem, which is what will determine the burn velocity.

Hunt and peck with a simple spreadsheet calculation (where it is numerically more friendly to work in terms of  $df/dT$  than  $dT/df$ ) enables a fairly quick estimate for the eigenvalue  $V$  for various values of normalized  $T_a$ . Figure 5.4.1 shows some sample curves of normalized temperature versus  $f$ , and Figure 5.4.2 shows the resulting estimated eigenvalues. For all cases, the normalized initial temperature is fixed at 0.05.

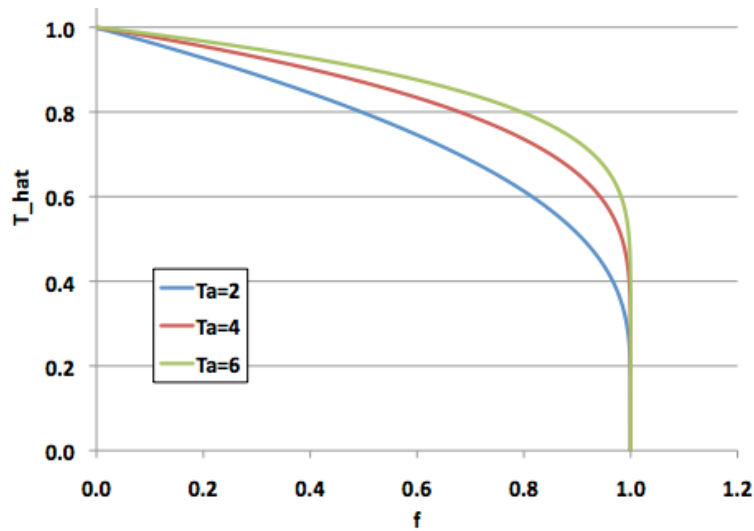


**Figure 5.4.1. Plots of normalized temperature versus  $f$  for three values of normalized activation temperature, in the “perfect confinement” limit.**

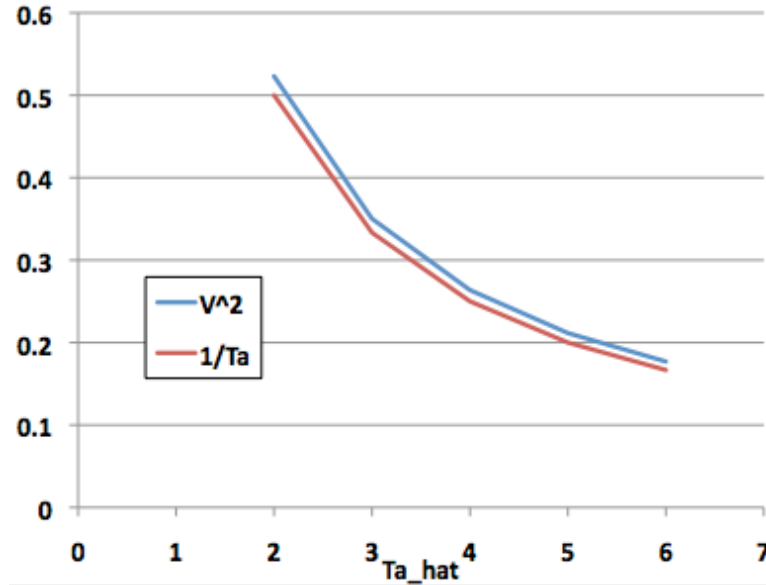


**Figure 5.4.2. Estimated eigenvalues, as a function of normalized activation temperature. Also shown is a comparison to the fit  $V^2 \sim 1/T_a$ .**

Using the fit  $V^2 \sim 1/T_a$  (normalized), the burn velocity can be calculated from the eigenvalue by:

$$v = \sqrt{\frac{\kappa \nu e^{-\hat{T}_a}}{\rho C \hat{T}_a}}, \text{ in m/s}$$

A sample table of values is shown below, using the nominal HE parameters given previously.

Normalized $T_a$	$v$ (m/s)
2	924
3	458
4	240
5	130
6	72

For the model parameters given earlier, the normalized  $T_a$  is about 3, but even at 5 we see that the burn rate is an order of magnitude higher than what we claim is sufficient for pumped convective burn. However, the “perfect confinement” case is not (of course) the whole story.

Let us now consider more realistic confinement. Inspection of the original model shows that the single-step, first-order Arrhenius model cannot completely consume the reactant in finite time. This means in the steady-wave case, the material behind the wave is not burned in a finite length of space. Thus we must choose a location (and corresponding non-zero value of  $f$ ) that we define to be the “edge” of the burning HE. Upstream of that edge is fluid-phase material in the voids; downstream is (mostly) solid grain material. There is no clear choice of the correct value for  $f$  at this location and we can only hope there is a range where the answer is otherwise relatively insensitive to it. We will denote this value by  $f_0$ .



The only change to the formulation already given is that at the edge, there is heat flux into or out of the volume by means of convective heat transfer with the void. We replace the condition that the normalized  $T = 1$  at  $f = 0$  with:

$$-\kappa \frac{dT}{dx} \Big|_{x=x(f_o)} = h(T_{ext} - T)$$

Introducing this condition into equation (a) above and defining a normalized external temperature:

$$\hat{T}_{ext} \equiv (T_{ext} - T_i)\rho C/U_o$$

produces the desired result:

$$\hat{T}|_{f_o} = \frac{(\rho C v/h)(1 - f_o) + \hat{T}_{ext}}{1 + \rho C v/h}$$

For reasonable ranges of parameters,  $\rho C v/h \gg 1$  which means the leading-order behavior of the boundary condition is:

$$\hat{T}|_{f_o} \approx 1 - f_o$$

which is curiously insensitive to the external temperature. If  $f_o$  is chosen to be at a location where the HE is mostly burned, then we do achieve relative insensitivity to the precise value since “mostly burned” means  $f_o \ll 1$ . This returns us to the normalized  $T = 1$  condition, except it is imposed at a non-zero value of  $f$ . Note, however, that the corrections to these approximate forms need to be included when calculating the initial *slope*, due to cancellation of the leading-order terms.

Figure 5.4.3 shows how the peak temperature degrades as the boundary is moved closer to the burn front. Figure 5.4.4 shows how the burn velocity is affected. For all results shown, the ratio  $\rho C v/h$  is fixed at 1000. (Note that the boundary condition is itself actually a function of the burn velocity; however, since the leading-order behavior of  $v$  does not vary tremendously, the uncertainty in the true value of  $h$  enables us to pretend the ratio constant.)

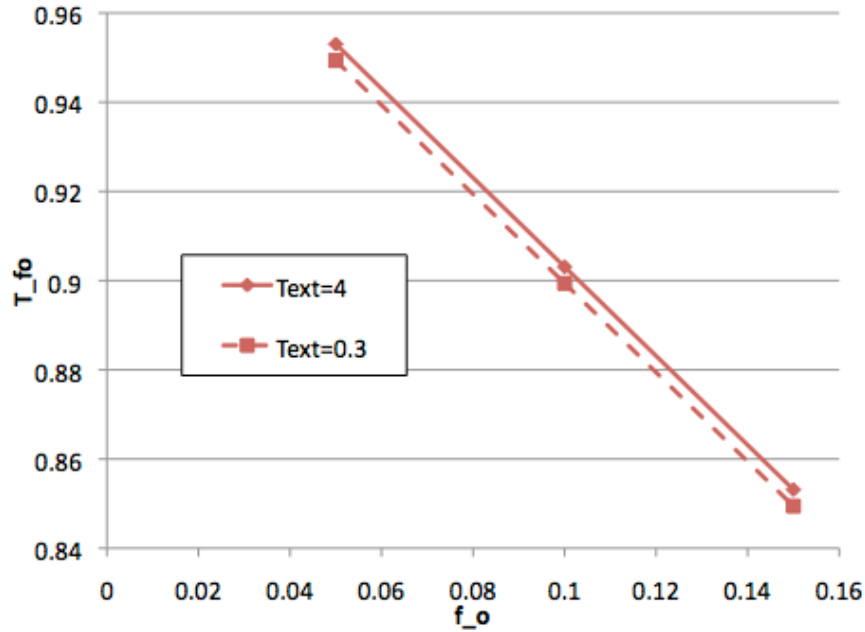


Figure 5.4.3. Change in peak normalized temperature as the finite heat flux boundary is moved into the reaction zone of the grain (increasing  $f_o$ ).

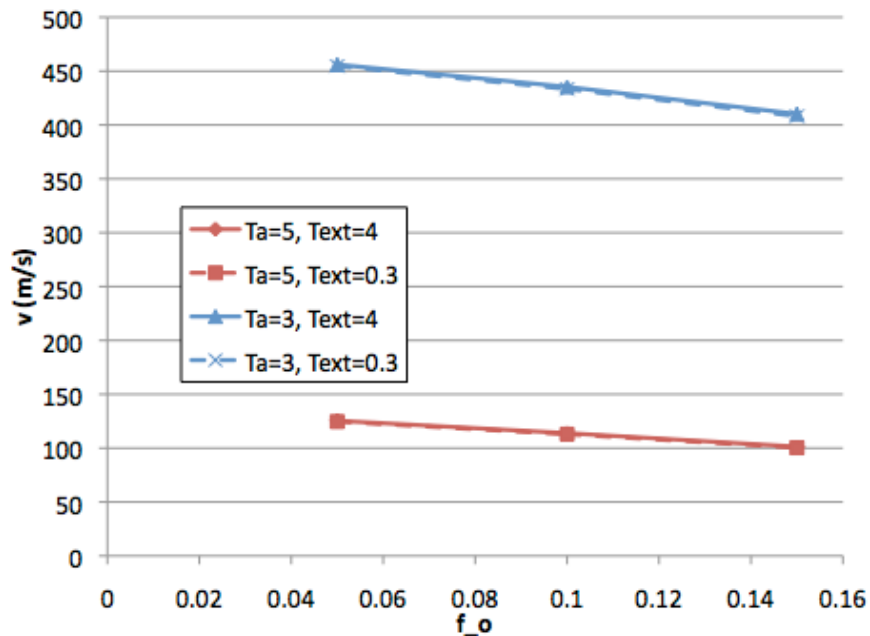


Figure 5.4.4. Dependence of the burn velocity on other parameters in the finite heat-flux case.

### 5.4.3.3. Concluding Remarks on Burn Velocity

We have presented two models that make very different assumptions about a burn wave propagating through an individual grain. In one limit, a very slow velocity of the order 0.1-1 m/s results; in the other, numbers more on the order of 100-500 m/s result. It seems reasonable to choose a middle-of-the-road value such as 10 m/s for further exploration, as will be done in the

next section. However, a better model of grain consumption, that actually treats the transverse convection into the void space, is clearly the direction that must be taken in future work. Section 5.6 takes up the question of endothermic effects by way of multi-step models.

### 5.5. Some Cylindrical Time-Dependent Threshold Results

Given a convective burn model that operates in terms of a constant burn velocity in the grains, and having spent considerable effort justifying what is still a tentative estimate for what a typical velocity might be, we finally present some results of the complete model from Section 5.3. The C++ code used to produce these results is listed in Appendix A.

The following results use the hybrid (constant Prandtl number) Dittus-Boelter heat transfer model discussed earlier, and a hard-threshold HE model where no reaction takes place until the edge temperature exceeds 1000 K, at which point mass and internal energy are released into the void at a constant rate until the grain is consumed in a time  $t_{HE}/v_{burn}$ . Many combinations of parameters could be investigated; only a few are presented here.

First, we do a simple threshold study of input energy. We compare an input of 75 and 88 mJ (over a 100-mil arc length) in the following series of figures. Figure 5.5.1 compares the temperature in the void space (labeled “pore” in the figures). The scale of the figures is set by the peak heating of the source, which is tens of eV; it therefore looks counterintuitive that the temperature drops quickly in time in the higher-energy 88 mJ case. However, this is because the reacted HE is cooler than the low-density air plasma it displaces as the HE burns; it is nevertheless still several thousand degrees. In the 75 mJ case, the cooler products are never introduced into the void space and the temperature stays higher longer. Note that this is the first reasonably first-principles model to predict ESD threshold anywhere in the ballpark observed experimentally; past attempts have generally resulted in extremely tiny values.

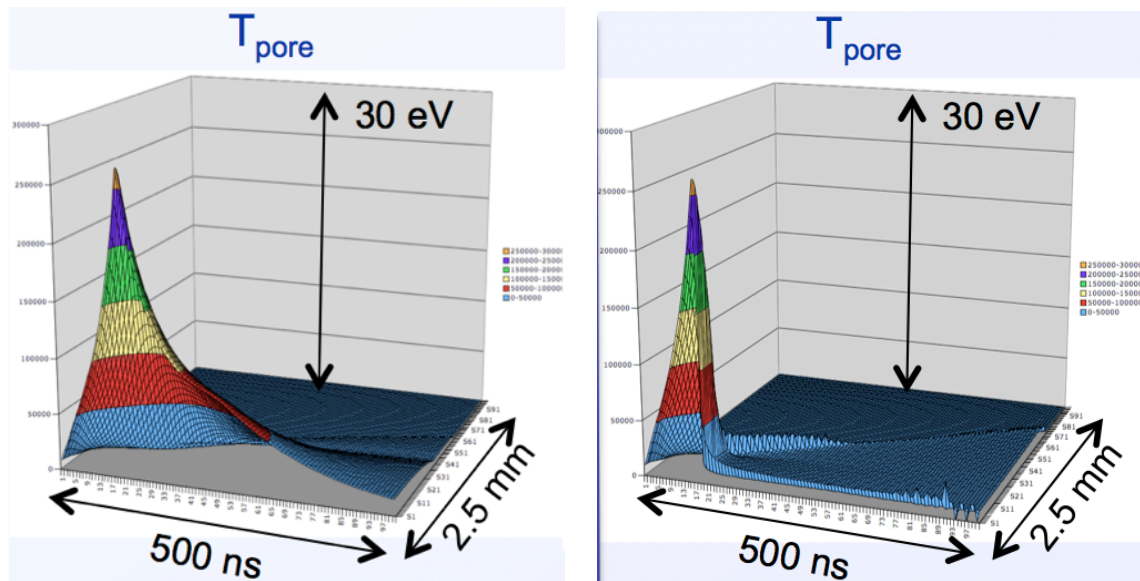


Figure 5.5.1. Temperature of the fluid in the void space below (left, 75 mJ input) and above (right, 88 mJ input) a calculated threshold.

Figure 5.5.2 compares the edge temperature of the HE grains, and here it is clear why a distinct response threshold exists: it is a direct reflection of the hard ignition threshold in the grains. The 75 mJ case never exceeds 1000 K at the grain surface. Obviously it is important future work to see what behavior arises with a “softer” initiation model.

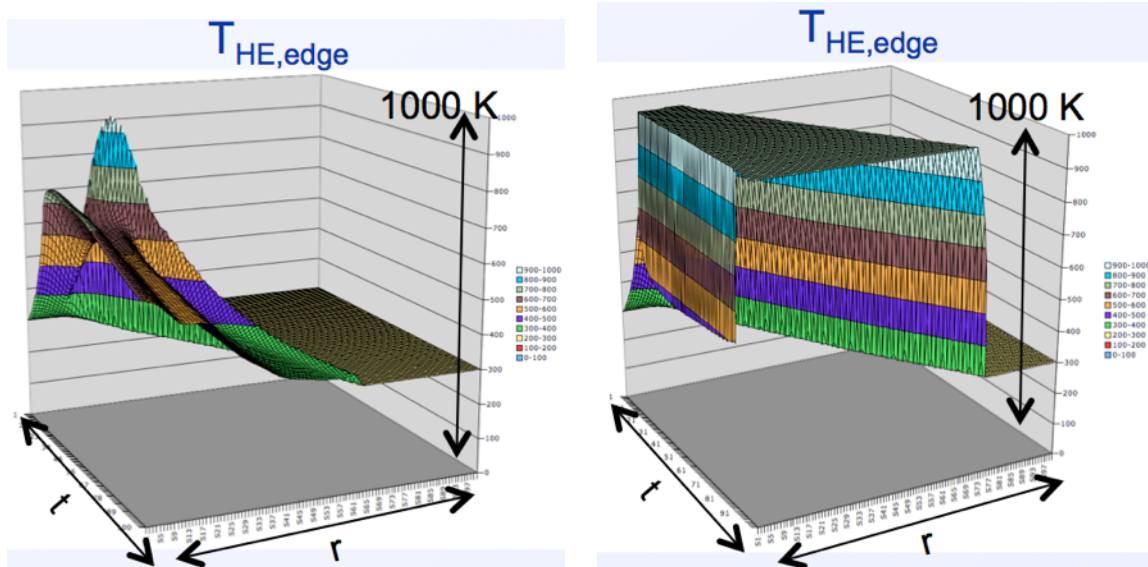


Figure 5.5.2. The edge temperature of the HE grains. The below-threshold case (left, 75 mJ input) never exceeds 1000 K, whereas the above threshold case (right, 88 mJ) does.

Figure 5.5.3 shows the most visibly obvious difference in the output data. Once the HE ignites given the higher input energy, reaction products are injected into the void space, driving the average density much higher than the initial value. In the ideal gas model used, the density gradient in turn produces a pressure gradient that drives the convection through the pores.

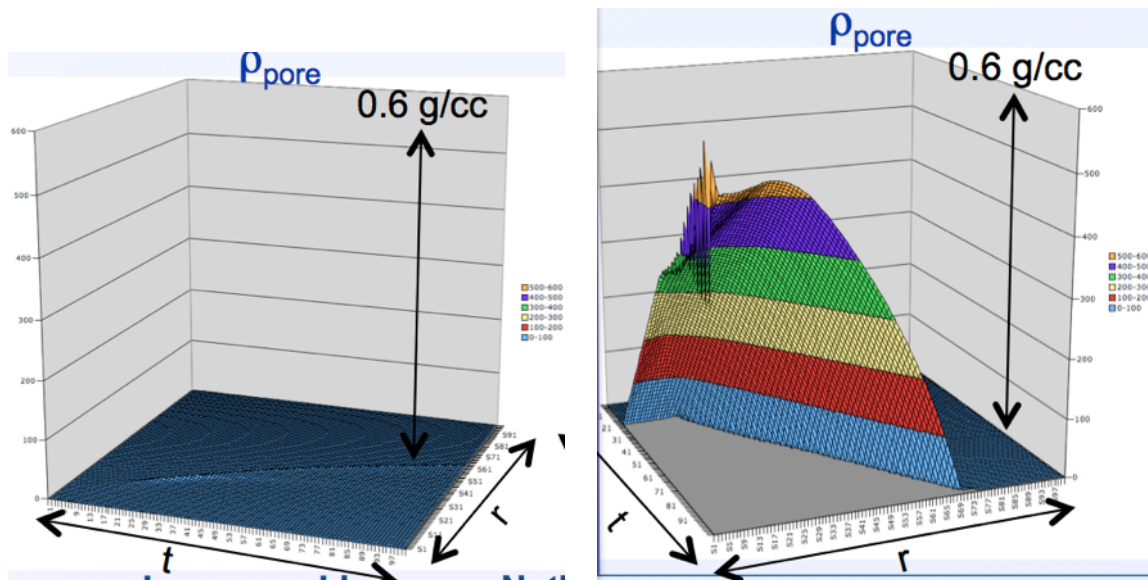
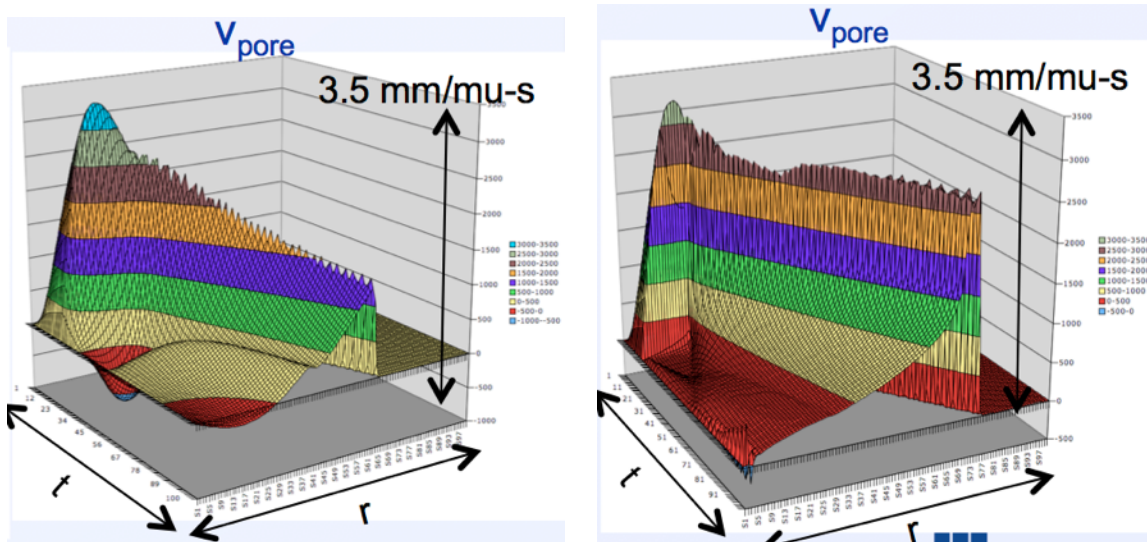


Figure 5.5.3. The fluid density in the void space, showing the clear difference in behavior between the below-threshold case (left, 75 mJ input) where there is only air plasma from the

**initial discharge, and the above-threshold case (right, 88 mJ input) where significant mass is injected into the voids.**

Figure 5.5.4 compares the flow velocity through the void space and is the most interesting from a phenomenological point of view. In the below-threshold case, the flow velocity starts high but decays once the input source is turned off. In the above-threshold case, the velocity stays high and roughly constant, and is clearly sufficient to traverse a detonator-sized volume in 2-3 microseconds.



**Figure 5.5.4. Fluid velocity in the void space, showing the decay following the initial 75 mJ input (left) compared to the sustained propagation in the above-threshold 88 mJ input case (right).**

Figure 5.5.5 shows the thresholds obtained from the model at different pulse lengths (at fixed input energy, a shorter pulse length corresponds to a higher input power). It is interesting to see that the model does indeed show a power-dependent threshold in the regime of interest, which was indicated by early experiments and then not observed in later ones. This remains an open question.

Finally, Figure 5.5.6 shows a variation as the void and grain size are simultaneously varied. This is not exactly analogous to varying the specific surface area, since the latter appears only in the heat transfer term but the void and grain sizes appear in other terms. Nevertheless, the threshold does decrease as the grain decreases, which would imply an increase in surface area; this increase has been observed experimentally.

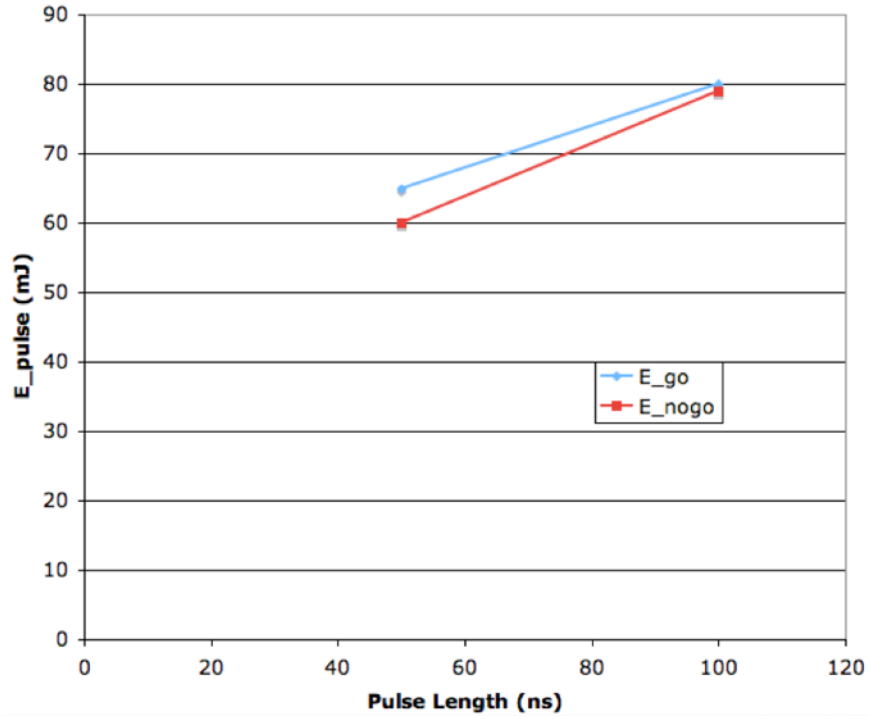


Figure 5.5.5. Effect of varying the pulse length, which varies the input power. A numerical threshold dependence is observed. The experimental results to date are not clear.

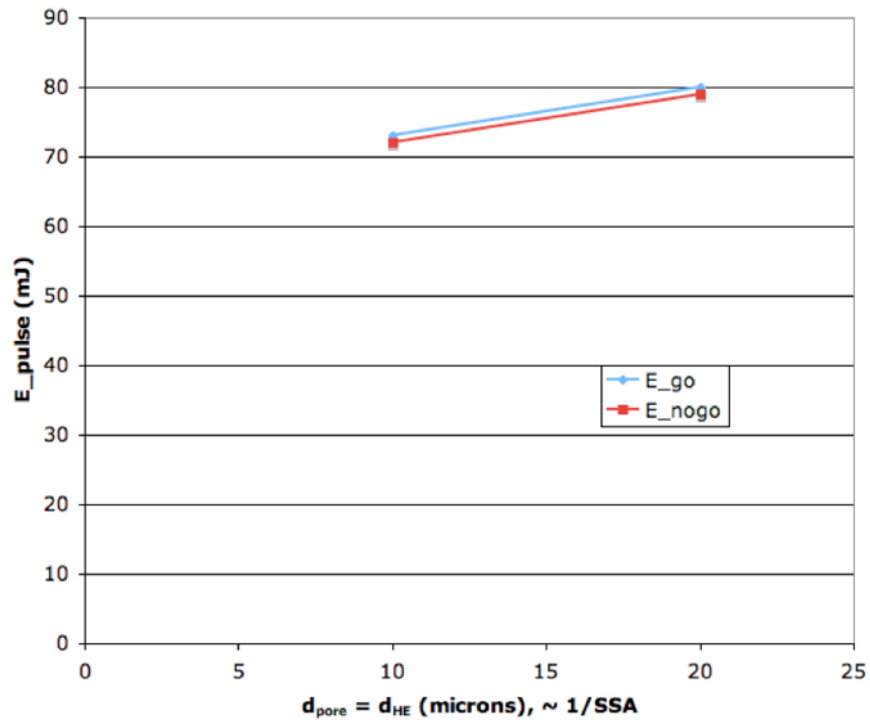


Figure 5.5.6. Effect of varying the grain and void size (which are kept equal to each other).

## 5.6. Burn Rates from Multi-Step Models

The rate at which an individual HE grain burns is an important parameter with respect to being able to sustain a PCB wave (the quantitative role is explored in subsection 5.7). In the broader literature on convective burn of HE, good empirical correlations have been established for the burn rates [10]. However, these correlations are pressure-based and therefore lack connection to the underlying kinetics of the HE. It is also desirable to link the behavior of the burn rate to very specific HE properties such as endothermic barriers, and thus be able to make quantitative statements about the safety-relevant HE behavior.

To that end, in this subsection we explore calculations similar to those introduced in subsection 5.4.3, but for multi-step kinetics models that are intended to provide better-calibrated descriptions of real HEs. While the models themselves are still highly reduced relative to the full, complex reactions chains, much accumulated evidence shows that “binning” similar reactions into a smaller set of steps still does a very good job at reproducing observed behavior.

We will also compare the burn rates that result from such calculations with existing data.

### 5.6.1. Eigenvalue Calculations with Existing Multi-Step Models

The first multi-step model we consider is the Tran/Tarver/Whipple four-step model for PETN [8]. Using the same constant-property assumptions as in 5.4.3 and starting with the equations already moved to the frame of a steady burn wave moving at speed  $v_b$ , the desired system is:

$$\begin{aligned} -v_b \frac{df_1}{dx} &= -f_1 \nu_1 e^{-T_1/T} - \frac{1}{2} f_1 f_2 \nu_2 e^{-T_2/T} \\ -v_b \frac{df_2}{dx} &= +f_1 \nu_1 e^{-T_1/T} - \frac{1}{2} f_1 f_2 \nu_2 e^{-T_2/T} - f_2^2 \nu_3 e^{-T_3/T} \\ -v_b \frac{df_3}{dx} &= +f_1 f_2 \nu_2 e^{-T_2/T} + f_2^2 \nu_3 e^{-T_3/T} - f_3^2 \nu_4 e^{-T_4/T} \\ -v_b \rho_o C \frac{dT}{dx} &= \kappa \frac{d^2 T}{dx^2} + Q_1 f_1 \nu_1 e^{-T_1/T} + Q_2 f_1 f_2 \nu_2 e^{-T_2/T} + Q_3 f_2^2 \nu_3 e^{-T_3/T} + Q_4 f_3^2 \nu_4 e^{-T_4/T} \end{aligned}$$

Table 5.6.1 shows the model parameters; a positive sign on the reaction energy  $Q$  corresponds to an exothermic energy release. The first reaction is from pristine PETN (denoted with mass fraction  $f_1$ ) to solid-phase intermediates ( $f_2$ ). The second has PETN reacting with the solid-phase intermediates to form gaseous intermediates ( $f_3$ ). The third is direct decomposition of the solid-phase intermediates to gaseous intermediates. The last step takes the gaseous intermediates to the final gaseous end products ( $f_4=1-f_1-f_2-f_3$ ).

i	T <sub>i</sub> (K)	v <sub>i</sub> (s <sup>-1</sup> )	Q <sub>i</sub> /ρ <sub>o</sub> (MJ/kg)
1	23645	6.3e19	-0.209
2	21444	1.65e18	0.523
3	18000	4.3e15	0.627
4	15250	7.9e13	5.44

**Table 5.6.1. Model parameters for four-step Arrhenius kinetics for PETN [8]. The specific heat is 1100 J/kg-K, density is 1760 kg/m<sup>3</sup>, and thermal conductivity is 0.25 W/m-K.**

As  $x$  goes to positive infinity, we must have  $f_1=1$ ,  $f_2=0$ ,  $f_3=0$ , and  $T=T_i=300$  K. If we introduce a fictitious mass fraction  $f_0$  which satisfies:

$$-v_b \frac{df_0}{dx} = -f_1 \nu_1 e^{-T_1/T}$$

and  $f_0=f_1$  at positive infinity, it then happens that the individual reaction terms on the right-hand sides of the reaction rate equations form an invertible system from which we can express the reaction rate terms in the temperature equation entirely in terms of combinations of the various  $df_i/dx$ ,  $i=0\dots3$ . Combining this property with the boundary condition at positive infinity allows us to integrate the temperature equation once:

$$\frac{\kappa}{v_b \rho C} \frac{dT}{dx} = T_i - T + \frac{Q_1 + Q_3 + Q_4}{\rho C} - \frac{1}{\rho C} (f_0(Q_1 - 2Q_2 + 2Q_3) + f_1(2Q_2 - Q_3 + Q_4) + f_2(Q_3 + Q_4) + f_3Q_4)$$

This leaves an autonomous first-order system that becomes amenable to solution with spreadsheet-level tools by transforming the independent variable from  $x$  to  $T$ :

$$\frac{df_0}{dT} = f_1 \nu_1 e^{-T_1/T} / (v_b dT/dx)$$

$$\frac{df_1}{dT} = (f_1 \nu_1 e^{-T_1/T} + \frac{1}{2} f_1 f_2 \nu_2 e^{-T_2/T}) / (v_b dT/dx)$$

$$\frac{df_2}{dT} = \frac{f_2^2 \nu_3 e^{-T_3/T} - f_1 \nu_1 e^{-T_1/T} + \frac{1}{2} f_1 f_2 \nu_2 e^{-T_2/T}}{v_b dT/dx}$$

$$\frac{df_3}{dT} = \frac{f_3^2 \nu_4 e^{-T_4/T} - f_2^2 \nu_3 e^{-T_3/T} - f_1 f_2 \nu_2 e^{-T_2/T}}{v_b dT/dx}$$

In practice, to avoid having  $dT/dx$  identically zero at positive infinity, we cheat ever so slightly by setting  $f_1=1-\epsilon$  there, where the final answer turns out not to be sensitive to the value of  $\epsilon$ . We used  $10^{-6}$ . The question is, what is the range of  $T$ ? And under what circumstances does it remain monotonic? The answer to these questions is tied to the ‘‘cold boundary problem,’’ defined by Penner [11] and studied at least as far back as von Karman [see the references within 11]. In short, there is no physical realization of the assumption that the steady wave is actually



established all the way back to negative infinity. The physical solution must be tied to the hydrodynamics of boundary conditions that remain coupled to the burning of the grain over all time scales relevant to the burning; this is why pressure-based correlations work, because the pressure of the larger-scale flow field remains coupled to the problem.

For this level of calculation, however, we solve the cold boundary problem by assuming the upstream material remains motionless. This could only be true if the burn rate was fast compared to the inertial time scales of the motion (and it most certainly is not), or if confinement of the reaction products is extremely strong. We will compare the results to a case where the requisite high pressures can be maintained, namely in a diamond anvil cell (DAC).

With perfect confinement, the temperature will increase monotonically until all steps of the reaction are complete and a limit of zero heat flux is reached. From the integrated form of the temperature equation:

$$T_{-\infty} = T_i + \frac{Q_1 + Q_3 + Q_4 + 2Q_2f_0}{\rho C}$$

Using an a priori assumption that  $f_0$  becomes small, this ideal zero heat flux limit is reached at about  $T=5650$  K. (At the end of the calculations,  $f_0$  asymptotes to about 0.025, justifying the initial assumption.)

With the range of  $T$  established, the burn rate becomes an eigenvalue which at which the reacted fractions reach their steady value of  $f_1=0$ ,  $f_2=0$ ,  $f_3=0$ ,  $f_4=1$  just as  $dT/dx$  is reaching 0. Figure 5.6.1 shows the resulting profiles of reacted fraction as a function of temperature over the desired range, for PETN. The resulting burn rate is 334 m/s. Under the perfect-confinement assumption for material starting at atmospheric pressure, the fully reacted material ends up at pressure of roughly 2-3 GPa if one were to assume an ideal equation of state and an average molecular weight of products between 18 and 44 (water to  $\text{CO}_2$ ). Note that even under these idealized confinement conditions, the pressure is well below the  $\sim 30$  GPa Chapman-Jouguet pressure of detonating PETN.

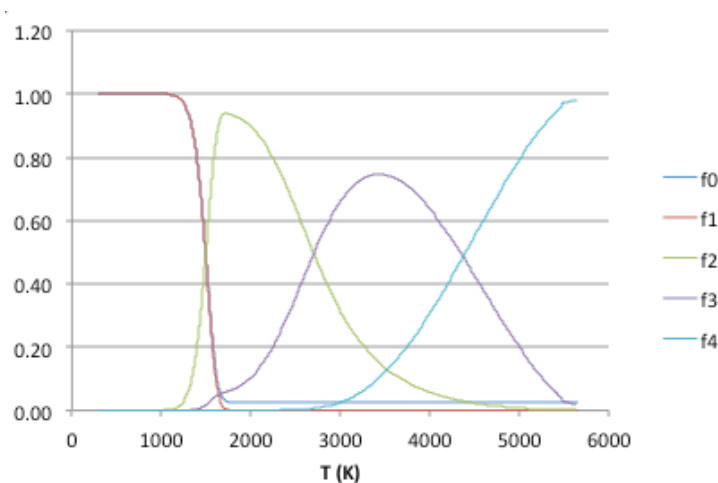


**Figure 5.6.1. Steady-burn-wave profiles of reacting mass fractions versus temperature, based on a four-step Arrhenius model for PETN, assuming idealized confinement. The burn velocity eigenvalue is 334 m/s.**

We also consider the same calculation done on the three-step model of Tarver/Chidester/Nichols for TATB [14]. This model is a serial evolution from TATB to a first solid intermediate (first order), from the first to a second solid intermediate (first order), and then from the second intermediate to gaseous end products (second order). Because of this serial structure, no additional quantities equivalent to  $f_0$  for PETN need to be introduced prior to inverting the rates and integrating the temperature equation. The first two steps are endothermic and the temperature of the end state is much lower,  $T=2580$  K. Table 5.6.2 shows the model parameters and Figure 5.6.2 shows the results of the eigenvalue calculation for the burn rate, yielding a value of 1.7 m/s.

i	$T_i$ (K)	$\nu_i$ ( $s^{-1}$ )	$Q_i/\rho_o$ (MJ/kg)
1	30188	7.e20	-0.209
2	21131	8.75e12	-0.209
3	17000	4.36e11	2.93

**Table 5.6.2. Model parameters for three-step Arrhenius kinetics for TATB [14]. The specific heat is 1100 J/kg-K, density is 1800 kg/m<sup>3</sup>, and thermal conductivity is 0.25 W/m-K.**

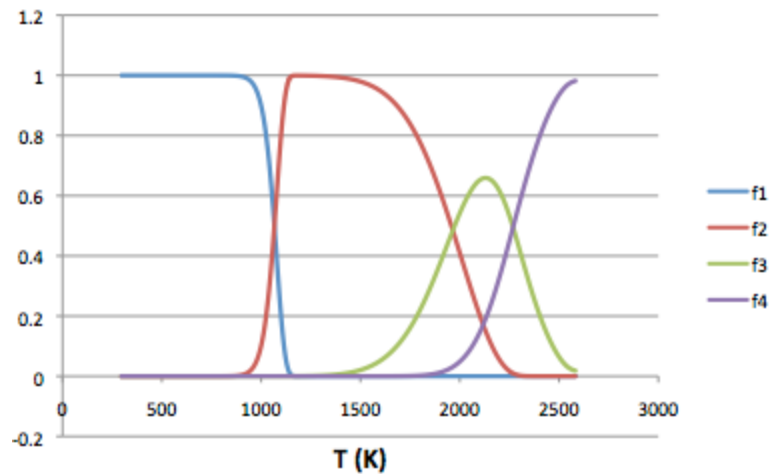


**Figure 5.6.2. Steady-burn-wave profiles of reacting mass fractions versus temperature, based on a three-step Arrhenius model for TATB, assuming idealized confinement. The burn velocity eigenvalue is 1.7 m/s.**

As simple as these models are, it is interesting to note how the values bracket the numerically estimated threshold of roughly 10 m/s for sustaining the PCB phenomenon. TATB, of course, has well-documented insensitivity to anything other than mechanical shock – including to electrical insults.

### 5.6.2. Comparison with DAC Data

One experimental regime where confinement pressures of order of our highly idealized picture can actually occur is with a diamond anvil cell (DAC). Let us assume that as we increase pressure at fixed temperature, the corresponding increase in material density will scale the reaction rates for anything other than simple first-order decomposition, since the corresponding collision rates will increase. Consideration of how the mass fractions emerge from rate equations

based on number density shows that the rates should scale with the square of ratio of compressed to nominal density. When we compare to the DAC results, we assume the density ratio is equal to the ratio of the test pressure to the baseline pressures reached in the results of the previous section.

The DAC data in question is for PETN [12] and TATB [13]. Figure 5.6.3 below shows the comparison of predicted and measured burn rates for PETN, and Figure 5.6.4 for TATB. The ellipses span the range of unknown molecular weight of the final products, from 18 to 44. Each HE type compares well in one aspect and not in another. In the case of PETN, the predicted rates are offset from the measured values by roughly 250 m/s. However, the linear slope of the trend with increasing pressure appears to match very well. For TATB, we see the opposite result: the burn velocity is certainly within the ballpark, but the trend with pressure is incorrect; the model appears to predict a roll-over that does not actually occur. However, given all of the other assumptions in the model (constant properties, no thermal conduction losses to sidewalls, etc.), the half-matches are intriguing.

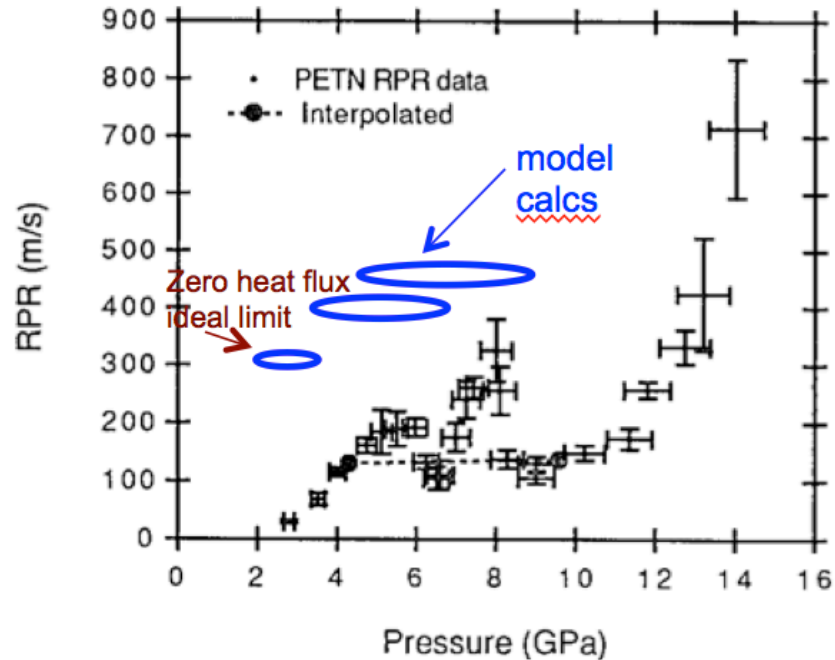


Figure 5.6.3. Measured reaction propagation rates (RPR) versus DAC pressure, for PETN. Data from Foltz, et al (1993) is in black, the modeled results are the blue ellipses where the elongation spans the unknown average molecular weight of reaction products (the ends span 18 to 44).

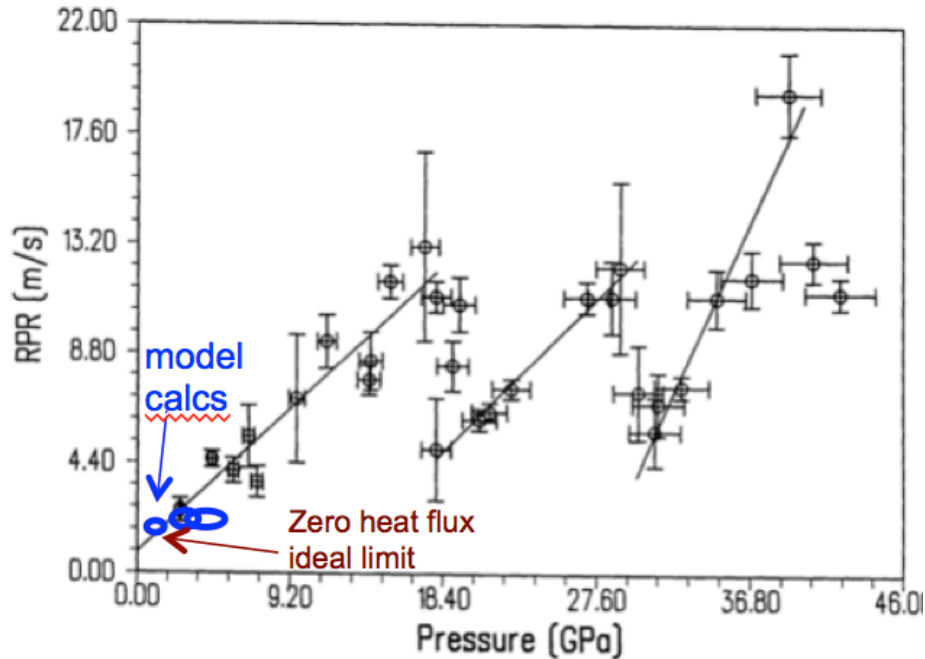


Figure 5.6.4. Measured reaction propagation rates (RPR) versus DAC pressure, for TATB. Data from Foltz, et al (1991) is in black, the modeled results are the blue ellipses where the elongation spans the unknown average molecular weight of reaction products (the ends span 18 to 44).

### 5.7. Derivation of a Steady PCB Wave

The simulations shown in subsection 5.5 are time-dependent, following the evolution of the PCB model starting with an input pulse into a quiescent system. Something resembling a steady wave appears to have formed by the end of the simulation. It is certainly possible that the numerical robustness and accuracy of the simulation are not yet up to par and that these results are artifacts of some sort; the simulation uses artificially large viscosity and thermal conduction coefficients and may well drive the results into a regime determined more by diffusive transport across a shock. It would be desirable to have some other means of studying and confirming such a wave.

In the limit of a hard-threshold HE model with a constant grain burn rate once reaction has commenced – the same limit used in the simulations – it is in fact possible to analytically derive the existence of a steady plane wave (the previous simulation was cylindrical) in the pumped convective burn regime. Separate numerical simulations employing a planar geometry, no thermal conduction, and an artificial viscosity that does not dominate in any region of interest have also been performed and match the analytic results fairly well. This wave has some unique properties:

- The underlying burning of the HE does not assume or require shock compression of solid-phase material. The burn wave in the solid grains is a *conductive* burn wave.
- Compaction of low-density material is not required and not included in the model. (Again, whether compaction can or does actually occur over real-world timescales in a small, detonator-sized volume of HE is a separate question. It is not required to support this steady PCB wave.)

- For typical parameters in something like half-dense PETN, the plane wave speed is slower than a detonation wave by a factor of 3-4 but much faster than any traditional convective burning scenario.

Understanding of this wave is not very deep at this time. Open questions for future pursuit pertain to the wave stability (especially in more realistic non-planar geometries) and the ability to couple to this wave in under- and over-driven scenarios. The latter question is especially intriguing in the context of the role of endothermic barriers. For example, quantitative proof that the properties of TATB result in a fundamental inability to DDT would be a valuable addition to our knowledge.

We break the remainder of this topic into three further subsections. Subsection 5.7.1 shows results of planar, time-dependent simulations. Subsection 5.7.2 is the mathematical derivation of the steady wave; it is certainly important from the perspective of maintaining a record of the method and assumptions, but can be safely skipped by those who find such mechanics uninteresting. Subsection 5.7.3 discusses some properties of the results.

### 5.7.1. Planar Time-Dependent Simulations

The planar model is not unlike that shown previously for the cylindrical case:

$$\begin{aligned} \frac{\partial \rho}{\partial t} + \frac{\partial}{\partial x} \rho v &= \frac{2\rho_H v_b}{d} H(T_H - T_{crit}) H\left(\frac{d_H}{2v_b} - t_{burn}\right) \\ \frac{\partial}{\partial t} \rho v + \frac{\partial}{\partial x} (P + \rho v^2) &= -\frac{f\rho v^2}{2d} H(T_{crit} - T_H) \\ \frac{\partial}{\partial t} \left(\frac{P}{\gamma - 1} + \rho v^2 / 2\right) + \frac{\partial}{\partial x} \left(\frac{\gamma P}{\gamma - 1} + \rho v^2\right) &= \frac{2U_H v_b}{d} H(T_H - T_{crit}) H\left(\frac{d_H}{2v_b} - t_{burn}\right) \\ &\quad + \frac{h}{d} (T_H - T) H(T_{crit} - T_H) + Q_{ext}(x, t) \\ \frac{\partial t_{burn}}{\partial t} &= H(T_H - T_{crit}) \\ \rho_H C_H \frac{\partial T_H}{\partial t} &= \frac{h}{d_{eff}} (T - T_H) \end{aligned}$$

A subscript of H refers to a solid-phase property of the HE. We relate the gas-phase pressure P, internal energy per unit volume U, and temperature T by:

$$U = \frac{P}{\gamma - 1}; \quad P = \frac{\rho k_b T}{m}$$

There are several other simplifying assumptions:

- Material properties, include the friction factor and heat transfer coefficient, are all constant.
- Heat transfer and frictional drag between the solid and gas phases must drop to zero by the time the solid phase has completely burned; here, we set these terms to zero as soon as burning begins.
- Burning is assumed to occur at a constant rate, as if the grains themselves had a planar form (transverse to the flow direction). Thus, a burn front of speed  $v_b$  is propagating in from either “side” of a planar grain of size  $d_H$ , consuming it in a time  $d_H/2v_b$ .
- The characteristic void size  $d$  and grain size  $d_H$  do not vary in time, even when burning is taking place.
- The relevant heating of a grain prior to the onset of burning is assumed to take place uniformly in a thin layer of size  $d_{\text{eff}} < d_H$ .
- For ease of bookkeeping, we enforce continuity of air, solid HE, and reaction products by assuming the initial “air” and the reaction products have the same molecular weight  $m$ , and furthermore that that weight is chosen such that  $C_H = k_b/(\gamma-1)m$ . This yields  $m = 19 m_p$  where  $m_p$  is the mass of a proton, for  $C_H = 1100 \text{ J/K}\cdot\text{kg}$ .
- As a result of the previous assumption and keeping the initial “air” density at the nominal value of  $1.2 \text{ kg/m}^3$ , the initial pressure is about 50% higher than standard conditions.

The quantity  $U_H$  is the internal energy that would be released from a constant-volume burn of the HE; in our idealized constant-property model, we estimate it by using the form:

$$U_H = \rho_H C_H T_{\text{react}}$$

where  $T_{\text{react}}$  is some peak HE-dependent temperature.  $T_{\text{crit}}$  is the hard-threshold temperature at which the HE begins to burn with a fixed burn front speed of  $v_b$  into the grain.

For the results shown below, our baseline parameter set is:

Initial conditions (at  $t=0$ ):

$$\rho = 1.2 \text{ kg/m}^3$$

$$v = 0 \text{ m/s}$$

$$T = 300 \text{ K}$$

$$T_H = 300 \text{ K}$$

$$t_{\text{burn}} = 0 \text{ (note this is a function of } x \text{)}$$

Parameters:

$$\gamma = 1.4$$

$$m = 19 \times 1.67 \times 10^{-27} \text{ kg}$$

$$f = 0.1$$

$$d = 1.e-5 \text{ m}$$

$$d_H = 1.e-5 \text{ m}$$

$$d_{\text{eff}} = 0.1 d_H = 1.e-7 \text{ m}$$

$$\kappa_{\text{air}} = 0.024 \text{ W/m}\cdot\text{K}$$

$$h = \text{Nu } \kappa_{\text{air}}/d, \text{ Nu}=16$$

$$v_b = 100 \text{ m/s}$$

$$\begin{aligned}\rho_H &= 1780 \text{ kg/m}^3 \\ C_H &= 1100 \text{ J/K-kg} \\ T_{\text{react}} &= 5500 \text{ K} \\ T_{\text{crit}} &= 900 \text{ K}\end{aligned}$$

The initial heating is provided by an external source of the form:

$$Q_{\text{ext}} = \frac{E_{\text{tot}}}{t_{\text{pulse}} \pi r_o^2 l} e^{-x^2/r_o^2} H(t_{\text{pulse}} - t)$$

where we chose  $E_{\text{tot}} = 15 \text{ mJ}$ ,  $r_o = 250 \text{ microns}$ ,  $l = 2.5 \text{ mm}$ , and  $t_{\text{pulse}} = 100 \text{ ns}$ .

We enforce a symmetry plane at  $x=0$  and keep conditions at the far end fixed, since it is time-isolated.

Consider the plots below of gas-phase density, velocity, temperature, and pressure, as well as the solid-phase temperature.

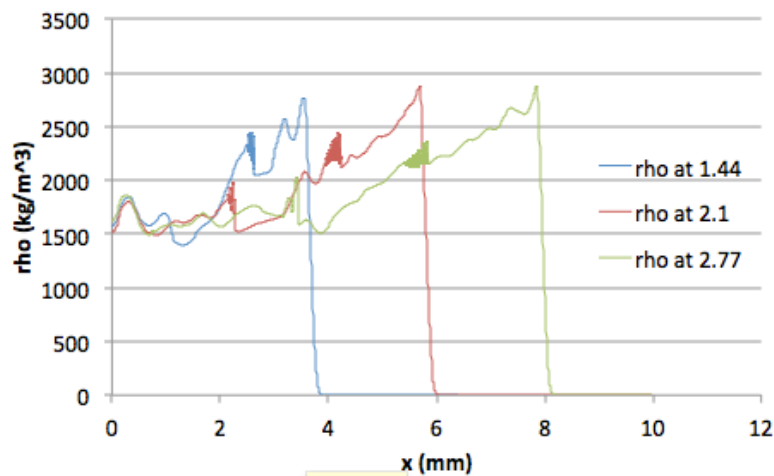


Figure 5.7.1. Gas-phase density at 1.44, 2.1, and 2.77 microseconds.

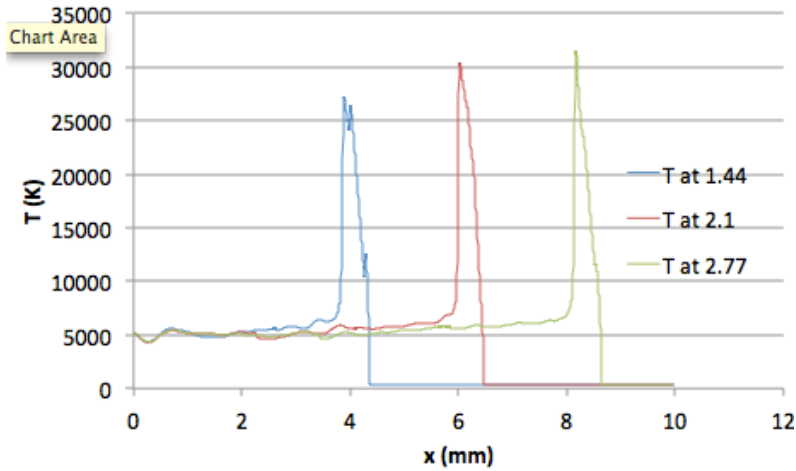


Figure 5.7.2. Fluid velocity at 1.44, 2.1, and 2.77 microseconds.

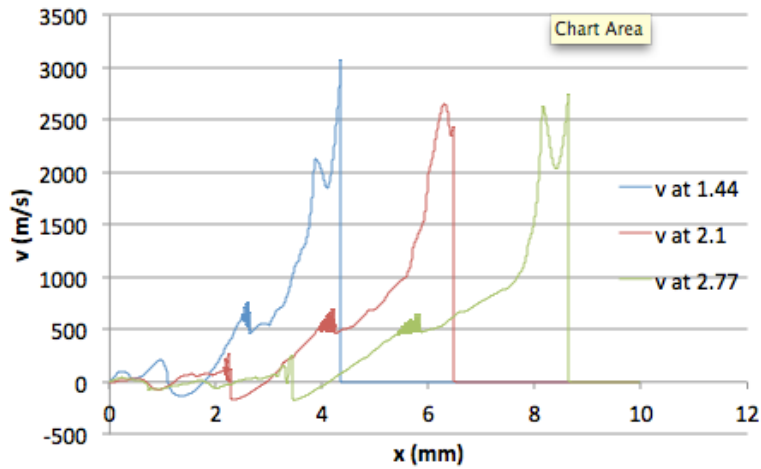


Figure 5.7.3. Gas-phase temperature at 1.44, 2.1, and 2.77 microseconds.

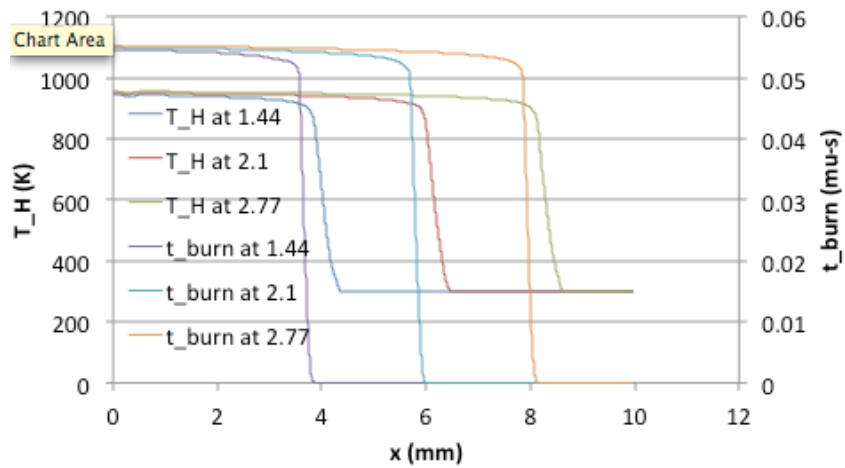
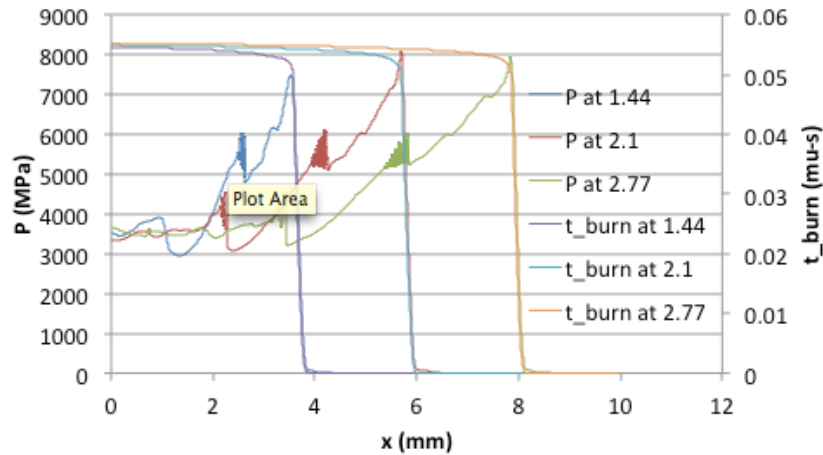


Figure 5.7.4. Solid-phase temperature at 1.44, 2.1, and 2.77 microseconds. Overlaid is the amount of time for which the HE has been burning, showing the spatial shift between the burning region and the heating region ahead of it.





**Figure 5.7.5. Gas-phase pressure at 1.44, 2.1, and 2.77 microseconds. Overlaid is the amount of time for which the HE has been burning, showing coincidence with the main pressure rise *after* burning has already commenced. The initial pressure rise leading to the onset of burn is almost invisible on this scale.**

These plots make clear that a steady front has indeed evolved from the initial quiescent state. Two traits of PCB are evident: the front is moving quite fast, supersonic relative to the air in front of it, at about 3.2 mm/ $\mu$ s. The pressure at the burn front, while significantly elevated above background, is well below shock initiation levels; the burning is driven by the high temperature and not by pressure.

Some other properties of the PCB wave are easier to see if we map the velocities at three different times onto each other in the following way: all points from the upstream end of the burn to the downstream end are shifted proportional to time, as would be expected for a steady-wave structure. All points from the upstream end of the burn to the symmetry plane are scaled linearly so that the end of burn is aligned. What is revealed is a remarkably self-similar structure with relatively small unsteady perturbations added on top. Figure 5.7.6 shows this, along with the solid-phase temperature and the burn time in the burning region; the velocity has been scaled to the unperturbed sound speed and the temperature to the unperturbed value so that they can be displayed on the same scale. The spatial coordinate is plotted in units of  $d$ , the pore size, to confirm that the salient features are indeed much larger than the grain structure, justifying the continuum approach.

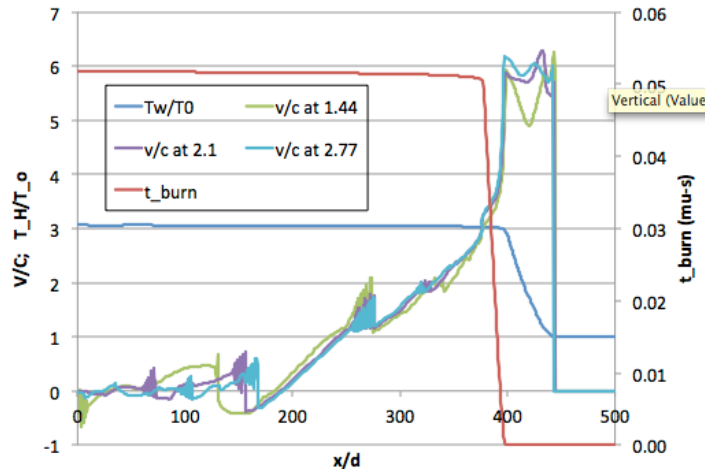


**Figure 5.7.6. Overlay of the velocities from 1.44, 2.1, and 2.77 microseconds, where the portion of the curves from the burn region downstream are shifted proportional to time, and the portion upstream is scaled in a self-similar mapping. A solid-phase temperature profile and the burn time at each point are also shown.**

With these quantities overlaid, other interesting features can be seen. The shock in the gas phase produces heating in a layer of (idealized) zero thickness, but the solid-phase temperature is continuous (which can easily be proven by considering the jump conditions of the starting model). Moving from downstream to upstream, there is a finite-thickness region where the solid-phase heating occurs, until the burn front begins. The shock front and the burn front move at the same constant speed, in spite of the physical separation. Furthermore, since the material velocity upstream of the shock is always less than that of the shock front, and therefore less than the burn front, this implies that, in the frame of the burn front, *the convective flow that drives the burn is actually coming in from the non-burning side.*

We pinpoint this trait as the defining characteristic of “pumped” convective burn. In a typical convective burn, the hot reaction products flow forward to propagate the burn. Here, shock-compressed air convects backwards through the (non-shock-compressed) solid to propagate the burn.

Conditions upstream of the burn region are subsonic with respect to the fully reacted material. Thus, the wave cannot become isolated from the upstream boundary in finite time and is therefore not truly a steady wave. However, a self-similar character clearly sets in, in a way made somewhat more precise in the mathematical analysis of the next section.

Since the boundary is therefore important, the choice of physical boundary condition will matter. We have chosen a symmetry plane since our context is a spark channel through the HE, which would define a center from which the wave will propagate.

### 5.7.2. Details of the Derivation

As described in the previous section, the PCB wave is “quasi-steady,” composed of some approximately steady sections that connect continuously to a self-similar piece. The procedure we follow to analyze the wave is to treat one section at a time, and show that sewing them together requires a particular propagation speed that matches the planar time-dependent

simulations. Even though it is a slight misnomer, we will refer to these results as the steady-wave solution. With a few reasonable assumptions, it is also possible to derive a completely analytic expression for the wave speed that appears to be good to about 10%.

From the upstream end of the burn region forward (downstream), a steady-wave formulation of the planar model given in the previous section is used. In terms of a steady-wave speed  $v_s$ , we change coordinates according to  $x' = x - v_s t$ ,  $t' = t$ , and assume that in this frame there is no variation with respect to  $t'$ . Furthermore, we introduce the following normalizations:

$$\begin{aligned} y &= x'/d \\ \hat{v} &= v/v_s \\ \hat{\rho} &= \rho/\rho_o \\ \hat{T} &= T/T_o \\ \hat{T}_H &= T_H/T_o \\ \hat{T}_{crit} &= T_{crit}/T_o \\ \hat{P} &= P/P_o = \hat{\rho}\hat{T} \end{aligned}$$

and we introduce an eigenvalue-like quantity involving the wave speed, not quite equal to the square of the Mach number:

$$\lambda \equiv \frac{\rho_o v_s^2}{P_o}$$

We expect  $\lambda \gg 1$ . The resulting model is:

$$\frac{d}{dy} \hat{\rho}(1 - \hat{v}) = -\frac{2\rho_H v_b}{\rho_o v_s} H(-y) H\left(y + \frac{d_H v_s}{2v_b d}\right)$$

$$\frac{d}{dy} (\hat{P} - \hat{\rho}(1 - \hat{v})\lambda\hat{v}) = -\frac{\lambda f \hat{v}^2}{2(1 - \hat{v})} \hat{\rho}(1 - \hat{v}) H(y)$$

$$\frac{d}{dy} \left( (\gamma\hat{v} - 1) \frac{\hat{P}}{\gamma - 1} - \hat{\rho}(1 - \hat{v}) \frac{\lambda\hat{v}^2}{2} - U_o \hat{T}_H \right) = \frac{2U_H v_b}{P_o v_s} H(-y) H\left(y + \frac{d_H v_s}{2v_b d}\right)$$

$$\frac{d\hat{T}_H}{dy} = \frac{H}{\sqrt{\lambda}} (\hat{T}_H - \hat{T})$$

We have defined the start of the burn region (the downstream end) to be  $y=0$ . The last equation has been used to move the heat transfer term into the derivative in the gas-phase energy equation; we have not included any special notation to indicate this is only in the region where  $y > 0$ . Finally, we have introduced two dimensionless parameters:

$$U_o \equiv \frac{\rho_H C_H T_o d_{eff}}{P_o d} \quad H \equiv \sqrt{\frac{\rho_o}{P_o}} \frac{hd}{\rho_H C_H d_{eff}}$$

In the region ahead of the shock, the conditions are ambient:

$$\hat{\rho} = \hat{P} = \hat{T}_H = 1; \hat{v} = 0$$

### 5.7.2.1. The Heating Region, $0 < y < y_s$

In the heating region between the shock and the onset of burn, the mass and energy source terms are zero, making it easy to integrate the equations from a location  $0 < y < y_s$  to positive infinity. The position of the shock front,  $y_s$ , is as yet unknown. The results are:

$$\hat{\rho}(1 - \hat{v}) = 1, y > 0$$

$$\frac{-1}{\gamma - 1} - \frac{\gamma \hat{v} - 1}{\gamma - 1} \hat{P} + \frac{\lambda \hat{v}^2}{2} + U_o(\hat{T}_H - 1) = 0, y > 0$$

The momentum equation and solid-phase energy equation take the form:

$$\frac{d}{dy}(\hat{P} - \lambda \hat{v}) = -\frac{\lambda f \hat{v}^2}{2(1 - \hat{v})}, 0 < y < y_s$$

$$\frac{d\hat{T}_H}{dy} = \frac{H}{\sqrt{\lambda}}(\hat{T}_H - \hat{P}(1 - \hat{v})), 0 < y < y_s$$

On the upstream side of the shock, conditions are no longer ambient. The jump conditions across the shock yield:

$$\hat{\rho}_{up} = \frac{1}{1 - \hat{v}_{up}}$$

$$\hat{v}_{up} = \frac{2}{\gamma + 1}(1 - \gamma/\lambda)$$

$$\hat{P}_{up} = \frac{\hat{T}_{up}}{1 - \hat{v}_{up}} = 1 + \frac{2\lambda}{\gamma + 1}(1 - \gamma/\lambda)$$

$$\hat{T}_{H,up} = 1$$

We make up for not knowing  $y_s$  by the fact that the system is autonomous in  $y$  and that we have two conditions on the normalized HE temperature: 1 at  $y=y_s$  and  $T_{crit}$  at  $y=0$ . We therefore switch to  $T_H$  as the independent variable:

$$\frac{d}{d\hat{T}_H}(\hat{P} - \lambda\hat{v}) = \frac{\lambda^{3/2} f \hat{v}^2}{2H(1 - \hat{v})(\hat{T}_H - \hat{P}(1 - \hat{v}))}$$

From the energy equation we note that:

$$\frac{d\hat{P}}{d\hat{T}_H} = \frac{\partial\hat{P}}{\partial\hat{T}_H} + \frac{\partial\hat{P}}{\partial\hat{v}} \frac{d\hat{v}}{d\hat{T}_H}$$

where:

$$\frac{\partial\hat{P}}{\partial\hat{T}_H} = \frac{U_o(\gamma - 1)}{\gamma\hat{v} - 1}, \quad \frac{\partial\hat{P}}{\partial\hat{v}} = \frac{\lambda(\gamma - 1)\hat{v}}{\gamma\hat{v} - 1} - \frac{\gamma\hat{P}}{\gamma\hat{v} - 1}$$

Thus the final equation is for v as a function of T<sub>H</sub>:

$$\left(\frac{\partial\hat{P}}{\partial\hat{v}} - \lambda\right) \frac{d\hat{v}}{d\hat{T}_H} = -\frac{\lambda^{3/2} f \hat{v}^2}{2H(1 - \hat{v})(\hat{T}_H - \frac{1-\hat{v}}{\gamma\hat{v}-1}((\gamma - 1)(\frac{\lambda\hat{v}^2}{2} + U_o(\hat{T}_H - 1)) - 1))} - \frac{U_o(\gamma - 1)}{\gamma\hat{v} - 1}$$

This equation looks unwieldy but is easily solvable on a spreadsheet or any other ODE-capable tool. The initial condition is v=v<sub>up</sub> at T<sub>H</sub>=1. One can simultaneously integrate:

$$y_s - 0 = \int_{T_{crit}}^1 \frac{\sqrt{\lambda}}{H} \frac{1}{\hat{T}_H - \hat{P}(1 - \hat{v})} d\hat{T}_H$$

Which gives the thickness of the heating region.

Inspection of these equations reveals some additional information. Since we expect  $\lambda \gg 1$ , we note that  $v_{up} \sim 2/\gamma+1$ . The momentum equation constrains the normalized velocity to be less than 1. In order for the pressure to remain finite everywhere, v must also be greater than 1/γ. This is a very narrow window and we might reasonably expect that  $v \sim v_{up}$  is a good starting approximation for any term not explicitly involving 1-v or γv-1. Furthermore, since v is so tightly constrained, we might expect that solving for dv/dT<sub>H</sub>=0 is a means of improving the estimate.

We take exactly this approach, with the further assumption, based on the numerical results, that P(1-v) >> T<sub>H</sub> across the range of interest. If we define a constant:

$$K_o \equiv \frac{\lambda^{3/2} f \hat{v}_{up}^2}{2HU_o(\gamma - 1)}$$

And a function of T<sub>H</sub>:

$$K_1(\hat{T}_H) \equiv (\gamma - 1) \left( \frac{\lambda \hat{v}_{up}^2}{2} + U_o(\hat{T}_H - 1) \right) - 1$$

The resulting equation is a simple quadratic:

$$K_1(\hat{T}_H)(1 - \hat{v})^2 - K_o(\gamma \hat{v} - 1)^2 = 0$$

Whose square root can be taken right away:

$$\frac{\gamma \hat{v} - 1}{1 - \hat{v}} = \sqrt{\frac{K_1}{K_o}}$$

With solution:

$$\hat{v} = \frac{1 + \sqrt{\frac{K_1}{K_o}}}{\gamma + \sqrt{\frac{K_1}{K_o}}}, \quad \hat{P} \approx \frac{K_1(\hat{T}_H)}{\gamma \hat{v} - 1} \quad (\text{Eqs. 5.7.1})$$

With these simplifications, the expression for the layer thickness becomes:

$$y_s \approx \frac{\sqrt{\lambda}}{H} \int_1^{\hat{T}_{crit}} \frac{\gamma \hat{v} - 1}{1 - \hat{v}} \frac{d\hat{T}_H}{K_1(\hat{T}_H)}$$

Giving a final answer of:

$$y_s \approx \frac{\sqrt{\lambda}}{\sqrt{U_o(\gamma - 1)K_o}H} \int_0^{\hat{T}_{crit}-1} \frac{df}{\sqrt{\frac{\lambda(\gamma-1)\hat{v}_{up}^2/2-1}{U_o(\gamma-1)} + f}} = \sqrt{\frac{4\sqrt{\lambda}}{fHU_o}} \left( \sqrt{1 + \frac{2U_o(\hat{T}_{crit} - 1)}{\lambda \hat{v}_{up}^2}} - 1 \right)$$

#### 5.7.2.2. The Burning Region, $-d_H V_s/2v_b d < y < 0$

In our simple constant-rate burn model, once the HE has ignited it becomes a mass and energy source and the solid phase temperature is no longer relevant. In the steady-wave frame, we have defined the burn front to be at  $y=0$ , and the end of the burn region must take place upstream at at  $y = -y_{end}$ , where we define  $y_{end} = d_H V_s/2v_b d$ . In this range, the source terms in the steady-wave mass and energy equations are simple constants and we can integrate those equations, again from a point towards positive infinity, with the source contributions beginning at  $y=0$ . The results are:

$$\hat{\rho}(1 - \hat{v}) = 1 - R \frac{y}{y_{end}}, \quad -y_{end} < y < 0$$

$$\frac{\lambda(\gamma - 1)\hat{v}^2}{2} \left(1 - R \frac{y}{y_{end}}\right) - (\gamma\hat{v} - 1)\hat{P} + \hat{U}_o + \hat{U}_H \frac{y}{y_{end}} = 0, -y_{end} < y < 0$$

$$\hat{U}_o \equiv (\gamma - 1)U_o(\hat{T}_{crit} - 1) - 1; R \equiv \frac{\rho_H d_H}{\rho_o d}; \hat{U}_H \equiv (\gamma - 1) \frac{U_H d_H}{P_o d}$$

In most applications, we expect  $U_H$  (hat) to be dominated by the product  $\rho_H T_{react}/\rho_o T_o$  buried within it.  $U_o$  contains  $\rho_H d_{eff}/\rho_o d$ . This produces a typical hierarchy of:

$$\hat{U}_H \gg R \gg \hat{U}_o \gg 1$$

Note that since the original heat transfer term in the energy equation is assumed to drop to zero at  $y=0$ , the term involving  $T_H$  is referenced to 1 at infinity and then completes its contribution at  $T_H=T_{crit}$ .

In this region, we assume frictional drag is unimportant and so we can also integrate the momentum equation; however, the downstream reference point must be  $y=0$ . Let us define  $v_i$  and  $P_i$  to be the normalized velocity and pressure at  $y=0$ , which come from Eqs. 5.7.1 with  $T_H=T_{crit}$ . Then the steady-wave momentum equation integrates to:

$$\hat{P}_i - \lambda\hat{v}_i - \hat{P} + \lambda\hat{v} \left(1 - R \frac{y}{y_{end}}\right) = 0$$

Thus we're left with an algebraic system, which we solve for  $v$ . Defining a shorthand:

$$K_y = 1 - \frac{\gamma(\hat{P}_i - \lambda\hat{v}_i)}{\lambda(1 - Ry/y_{end})}$$

The final result is:

$$\hat{v} = \frac{1}{\gamma + 1} \left( K_y + \sqrt{K_y^2 + \frac{2(\gamma + 1)}{\lambda(1 - Ry/y_{end})} (\hat{U}_H y/y_{end} + \hat{U}_o + (\hat{P}_i - \lambda\hat{v}_i))} \right)$$

### 5.7.2.3. The Self-Similar region, $y < -d_H v_s/2v_{bd}$

The self-similar region extends from the symmetry plane out to the upstream end of the burn region. We return momentarily to the time-dependent model and the original  $x$  coordinate. There are no source terms in this region, and we expect continuous behavior, so it will be useful to switch from flux-conservative to the more traditional Eulerian form of the fluid equations:

$$\frac{\partial \rho}{\partial t} + \frac{\partial}{\partial x} \rho v = 0$$

$$\frac{\partial v}{\partial t} + v \frac{\partial v}{\partial x} + \frac{1}{\rho} \frac{\partial P}{\partial x} = 0$$

$$\frac{\partial P}{\partial t} + v \frac{\partial P}{\partial x} + \gamma P \frac{\partial v}{\partial x} = 0$$

We transform to new coordinates  $(z, t')$ , where  $z$  is normalized between 0 and 1 and “stretches” in time so that 1 is always at the interface between the self-similar and steady-wave regions:

$$z = \frac{x}{x_i + v_s t}, \quad t' = t$$

The reference size  $x_i$  is assumed to become small relative to  $v_s t$  for any time of interest and will not play a role in what follows. The derivatives transform according to:

$$\frac{\partial}{\partial t} = \frac{\partial}{\partial t'} - \frac{v_s z}{x_i + v_s t'} \frac{\partial}{\partial z}$$

$$\frac{\partial}{\partial x} = \frac{1}{x_i + v_s t'} \frac{\partial}{\partial z}$$

Leading to the new system:

$$(x_i/v_s + t') \frac{\partial \rho}{\partial t'} + \left(\frac{v}{v_s} - z\right) \frac{\partial \rho}{\partial z} + \frac{\rho}{v_s} \frac{\partial v}{\partial z} = 0$$

$$(x_i/v_s + t') \frac{\partial v}{\partial t'} + \left(\frac{v}{v_s} - z\right) \frac{\partial v}{\partial z} + \frac{1}{\rho v_s} \frac{\partial P}{\partial z} = 0$$

$$(x_i/v_s + t') \frac{\partial P}{\partial t'} + \left(\frac{v}{v_s} - z\right) \frac{\partial P}{\partial z} + \frac{\gamma P}{v_s} \frac{\partial v}{\partial z} = 0$$

It takes an exponentially large number of transit times before one could rigorously claim the system had evolved into a steady flow. However, we observe from the simulations that the transients that are present are not large compared to the emerging steady structure. We further observe that the density and pressure do not vary by large amounts upstream of the completed burn. Therefore, we proceed by assuming a steady self-similar flow and linearizing  $\rho$  and  $P$  about their values at the interface,  $z=1$ , which are the solutions at  $y/y_{\text{end}} = -1$  from the previous section. We denote the interface values by  $\rho_{\text{int}}$ ,  $v_{\text{int}}$ , and  $P_{\text{int}}$ . The velocity  $v$  will not be linearized and we normalize it not to the interface value but, consistent with the previous sections, to the front speed  $v_s$ :

$$\rho \approx \rho_{\text{int}}(1 + \hat{\rho}_1)$$



$$P \approx P_{int}(1 + \hat{P}_1)$$

$$(\hat{v} - z) \frac{d\hat{\rho}_1}{dz} + \frac{d\hat{v}}{dz} = 0$$

$$(\hat{v} - z) \frac{d\hat{v}}{dz} + \frac{\hat{P}_{int}}{\hat{\rho}_{int}\lambda} \frac{d\hat{P}_1}{dz} = 0$$

$$(\hat{v} - z) \frac{d\hat{P}_1}{dz} + \gamma \frac{d\hat{v}}{dz} = 0$$

The equation for the density is decoupled from the last two. The latter are homogeneous equations that are satisfied either by constant velocity and pressure, or if the determinant can be made to vanish:

$$(\hat{v} - z)^2 - \frac{\gamma \hat{P}_{int}}{\hat{\rho}_{int}\lambda} = 0$$

This occurs if:

$$\hat{v} = z - \sqrt{\frac{\gamma \hat{P}_{int}}{\hat{\rho}_{int}\lambda}}$$

where we've chosen the sign to enable achieving  $v=0$  at the boundary, as described below. The other two quantities are given by:

$$\hat{P}_1 = \sqrt{\frac{\gamma \hat{\rho}_{int}\lambda}{\hat{P}_{int}}}(z - 1) \quad \hat{\rho}_1 = \sqrt{\frac{\hat{\rho}_{int}\lambda}{\gamma \hat{P}_{int}}}(z - 1)$$

The unknown steady-wave speed, buried in  $\lambda$ , is finally revealed by requiring  $v=v_{int}$  at  $z=1$ :

$$\hat{v}_{int} = 1 - \sqrt{\frac{\gamma \hat{P}_{int}}{\hat{\rho}_{int}\lambda}}$$

We discuss this condition shortly. We note that at  $z=(\gamma P_{int}/\rho_{int}\lambda)^{1/2}$  (hatted),  $v$  crosses zero. At this point, we join this solution to the other option, constant velocity and pressure. The solution  $v=0$  is consistent with the boundary condition required by the symmetry axis.

Returning to the pseudo-eigenvalue condition for  $\lambda$ , let us consider the limit where  $U_H \gg P_i$ , a reasonable assumption since  $P_i$  is proportional to the internal energy of the gas after shock heating but before any contribution from burning HE, which should be dominant. Based on the parameter hierarchy given earlier, we also expect  $\lambda R \gg P_i$ . Under these circumstances,

$$\hat{P}_{int} \approx \lambda \hat{v}_{int} R$$

$$\hat{\rho}_{int} \approx \frac{R}{1 - \hat{v}_{int}}$$

which reduces the eigenvalue condition to:

$$\sqrt{\gamma \hat{v}_{int} (1 - \hat{v}_{int})} = 1 - \hat{v}_{int}$$

with solution:

$$\hat{v}_{int} = 1/(\gamma + 1)$$

Applying the same assumptions regarding  $P_i$  in the last expression of section 5.7.2.2, we finally arrive at:

$$\lambda = 2(\gamma + 1)\hat{U}_H/R$$

which, after unraveling several layers of parameter definitions, boils down to:

$$\frac{v_s}{c_o} \approx \sqrt{\frac{2(\gamma + 1)T_{react}}{\gamma T_o}}, \quad c_o^2 \equiv \gamma P_o/\rho_o$$

Our various scaling assumptions have been born out, and all jump and boundary conditions have been met self-consistently. Thus, a steady-wave solution is proven to exist within the PCB model.

### 5.7.3. Discussion of Results

Figure 5.7.7 below repeats the overlay of Figure 5.7.6, but adds the analytic solution and in the heating region also the steady-wave solution calculated with a spreadsheet. The analytic solution does not capture the boundary layer where the velocity drops from  $v_{up}$  to the equilibrium trajectory, but otherwise captures the shape of the heating region fairly well. The spreadsheet solution captures the boundary layer. Neither solution, of course, can reproduce the superimposed unsteady content seen in the time-dependent simulations. The error in the location of where the self-similar region crosses the  $v=0$  axis may be due to neglect of secondary shocks that appear to be in the numerical results; it may also be due to the fact that those shocks are clearly poorly resolved, with obvious spurious ringing, and thus that the error is in the numerical simulation.

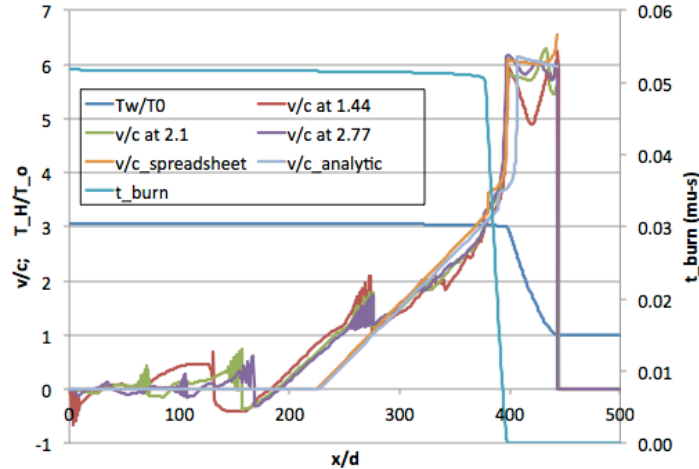


Figure 5.7.7. Overlay of the previous time-dependent solution with the steady-wave solution, shown calculated in the heating region by spreadsheet and also by the stand-alone analytic expressions.

Table 5.7.1 compares the analytic expression for  $v_s/c$  to results from the time-dependent simulation. The comparison is quite good, matching the dependence on  $T_{\text{react}}$  and confirming the weak dependence on solid-phase density.

$T_{\text{react}}$ (K)	$\rho_{\text{HE}}$ (kg/m <sup>3</sup> )	$v_s/c$ , simulated	$v_s/c$ , analytic
4500	1780	7.0	7.2
5000	1780	7.4	7.6
5500	1780	7.8	7.9
5500	1500	7.8	7.9
5500	2000	8.0	7.9

Table 5.7.1. Comparison of analytic and numerical results for the PCB wave speed (normalized to the unperturbed sound speed).

It is noteworthy that the final expression for  $v_s$  is dependent only on the temperature of the reacted HE, without revealing any other conditions required to support a steady wave. These other conditions are buried in the assumptions made at the end regarding the relative magnitude of  $P_i$ ; these assumptions can be violated by varying either the friction factor  $f$  or the heat transfer coefficient  $h$  (clearly, in the limit of no heat transfer from gas to solid, the solid could never burn). We have not explored these other conditions at this time.

## 5.8. Concluding Comments

Pumped convective burn is a physical model that may provide predictive capability for ESD in low-density HE. So far, the work has shown the following promising signs:

- Threshold predictions of the same order as those observed experimentally—as compared to all prior attempts which were off by orders of magnitude;
- Dependence on parameters such as grain size or specific surface area that at least point in the same direction as those observed experimentally;

- Power dependence, which has turned out to be difficult to pin down experimentally (to put it mildly);
- A physical picture of fast thermal initiation as something different than transition to shock propagation but nevertheless capable of fast energy release;
- Identification of a new type of steady wave through low-density energetic materials.

Along with the positive, of course, comes a list of things that require further investigation:

- A better model for the ignition and transverse convection at the grain scale
- More robust numerics for Arrhenius kinetics and shock resolution
- Educated selection of correlations for turbulent viscosity and heat transfer
- Is compaction really negligible on this scale?
- Is the fast energy release “fast enough” to drive an adjacent HE (such as a detonator output pellet) into a violent reaction?

And as with all conclusions drawn from a model, experimental confirmation, at a level of detail beyond simple thresholds, will be required.

### 5.9. Selected References

- [1] Shajii, A., Freidberg J. P. “Quench in superconducting magnets. I. Model and numerical implementation.” *J. Applied Physics* vol. 76 #5, pp 3149-3158, September, 1994.
- [2] Shajii, A., Freidberg J. P. “Quench in superconducting magnets. II. Analytic solution.” *J. Applied Physics* vol. 76 #5, pp 3159-3171, September, 1994.
- [3] Shajii, A., Freidberg J. P. “Theory of low Mach number compressible flow in a channel.” *J. Fluid Mech.* vol. 313, pp 131-145, 1996.
- [4] Shajii, A. “Theory and modeling of quench in cable-in-conduit superconducting magnets.” Ph.D. thesis, Plasma Fusion Center, Massachusetts Institute of Technology, Cambridge, MA, 1994.
- [5] Asay, B., Son, S., Bdzil, J. “The role of gas permeation in convective burning.” *Int. J. Multiphase Flow*, vol. 22, #5, pp. 923-952, 1996.
- [6] Ward, M., Son, S., Brewster, M. “Steady deflagration of HMX with simple kinetics: a gas phase chain reaction model.” *Combustion and Flame*, vol. 114, pp. 556-568, 1998.
- [7] Asay, B. (Ed.). Non-Shock Initiation of Explosives (Shock Wave Science and Technology Reference Library, Vol. 5). Springer, 2010. ISBN 978-3-540-87952-7.
- [8] Tarver, C., Tran, T., Whipple, R. “Thermal decomposition of pentaerythritol tetranitrate.” *Propellants, Explosives, Pyrotechnics*, vol. 28 #4, pp. 189-193, 2003.
- [9] Gifford, M., Luebecke, P., Field, J. “A new mechanism for deflagration to detonation in porous granular explosives.” *J. Applied Physics* vol. 86 #3, pp. 1749-1753, August 1999.

- [10] Son, S., Berghout, C., Bolme, A., Chavez, D., Naud, D., Hiskey, M. "Burn Rate Measurements of HMX, TATB, DHT, DAAF, and BTATz." Proceedings of the Combustion Institute, Volume 28, pp. 919-924, 2000.
- [11] Penner, S., Williams, F. "The Theory of Steady, One-dimension, Laminar Flame Propagation for One-Step Chemical Reactions." *Astronautica Acta*, Vol. 7, pp. 171-189, 1961.
- [12] Foltz, M. F. "Pressure Dependence on the Reaction Propagation Rate of PETN at High Pressure." Proceedings of the 10<sup>th</sup> International Detonation Symposium, Boston, MA, pp. 579-585, July, 1993.
- [13] Foltz, M. F. "Pressure Dependence of the Reaction Propagation Rate of TATB at High Pressure." UCRL-JC-108818, October 1991. Also appearing in *Propellants, Explosives, Pyrotechnics*.
- [14] Tarver, C. M., Chidester, S. K., Nichols III, A. L. "Critical Conditions for Impact and Shock Induced Hot Spots in Solid Explosives." *J. Physical Chemistry*, vol. 100, #14, pp. 5794-5799, 1996.

## 6. Comparative Response of PETN and TATB: A Preliminary Study

A rather obvious consequence of arc initiation should not be overlooked: a purely thermal insult can produce a violent HE response, if that insult is sufficiently fast and strong. Moreover, the high level of violence can apparently be reached in a volume that is small compared to a more traditional picture of a “run to detonation.”

The failure of the TRIR campaign could be re-interpreted as a positive opportunity to include additional experiments in the LDRD, using the remaining resources. Unfortunately, the PI may have waited a bit too long to abandon TRIR, so that the time remaining was short, but we did decide to begin a preliminary study of the violence of response to arc initiation.

The previous comments about not requiring a run distance can be taken to an obvious limit: an experimental configuration where the HE volume and arc volume are the same. This has two advantages. First, due to limitations on the maximum distance over which the 10 kV pulser could form a discharge through packed powder, the total volume is small and the resulting HE mass ends up well under 10 mg, which means experiments could still be easily performed under the B235 R1217 IWS. Second, because we could test powder-filled volumes rather than solid thin films, we could also include TATB (an effort to produce TATB films, outsourced to SNL, never went anywhere). The expectation, of course, is that TATB would retain its usual insensitivity; however, actual tests of this nature have not previously been performed.

A useful application of the test configuration defined below, although not possible with the present pulser design, is to perform threshold testing, since the geometric effects that have caused confusion in ESD testing of larger samples should be minimized.

### 6.1. Description of the Configuration

The test volume is defined by a glass capillary tube of approximately 1 mm inner diameter. The ends of the volume are set by the end positions of solid copper wire closely match to the tube diameter. The volume is hand-loaded with the powder of interest; then lengths of the copper wire are inserted and epoxied in place. The copper wires are then soldered to copper strips used to provide source and return connections to the pulser. The strips are isolated from each other by sheets of Kapton.

The hand-loading process is difficult to control to high precision, but a typical load was between 1.3 and 1.7 mg of powder (each was weighed after loading), packed to roughly 30% of theoretical maximum density. The figures below show various views of the assembled tubes.



**Figure 6.1.** View of a complete capillary tube assembly, showing the powder-filled volume at the very center, the copper wire inserted into both ends of the tube, and the copper foil source strip (top) and return (backplane), with Kapton sheet used as insulation.



**Figure 6.2.** Close-up view of the powder-filled volume. The clear blobs at top and bottom are the epoxy used to hold the copper wire in place.

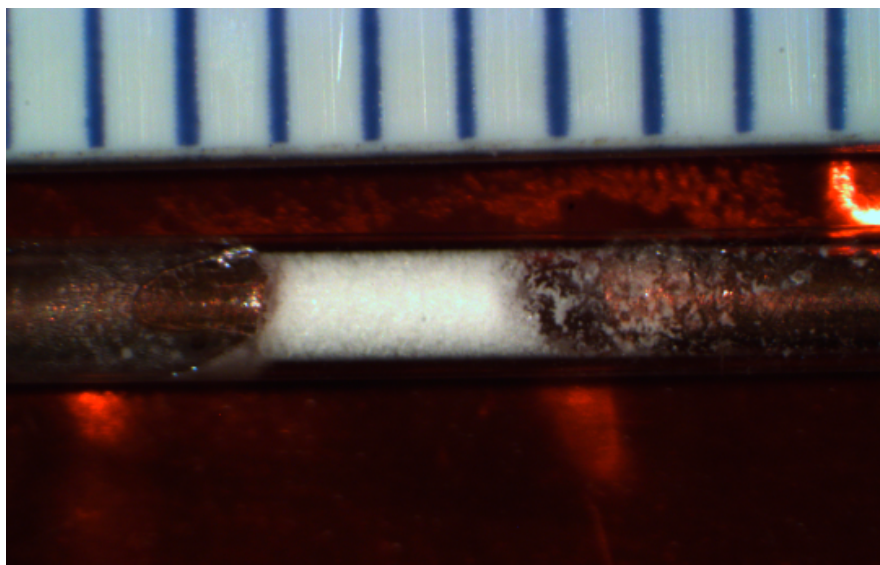


**Figure 6.3.** View of the powder region with a 1 mm ruled reference. Typical loads were between 1.3-1.7 mg at ~30% TMD.

## 6.2. Results

Because of the ad-hoc nature of the assembly, including no easy method for alignment and the lack of a through-hole for line of sight, emission spectroscopy could not be used for these experiments. However, one can easily envision some refinements that would allow the coupling of such a diagnostic. The data acquired for these shots consisted of pre- and post-shot pictures, gated camera images, and video frames taken using the “MIT camera” owned by the HEAF facility. We gratefully acknowledge the assistance provided by Dana Hargrove in the use of the MIT camera.

The test configurations included empty (air-filled) capillaries, and ones loaded with PETN, inert pentaerythritol, and TATB. Empty capillaries typically remained intact following a discharge of the pulser. Capillaries filled with pentaerythritol or TATB would typically crack and also dislocate the copper wire. Much of the powder would burn; some unburned material would be spread locally around the sample area. Figure 6.4 shows a typical post-shot result of TATB. The behavior of TATB and pentaerythritol, at insult levels of approximately 200 mJ, were visually indistinguishable.



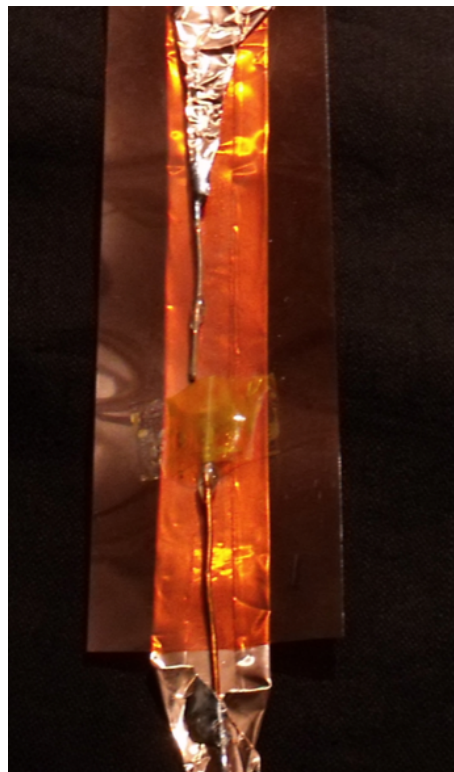


**Figure 6.4. Post-shot image of a TATB-filled capillary. The TATB burns non-violently; the resulting pressure cracks the capillary glass and dislocated the copper wire. Inert pentarerythritol behaves similarly.**

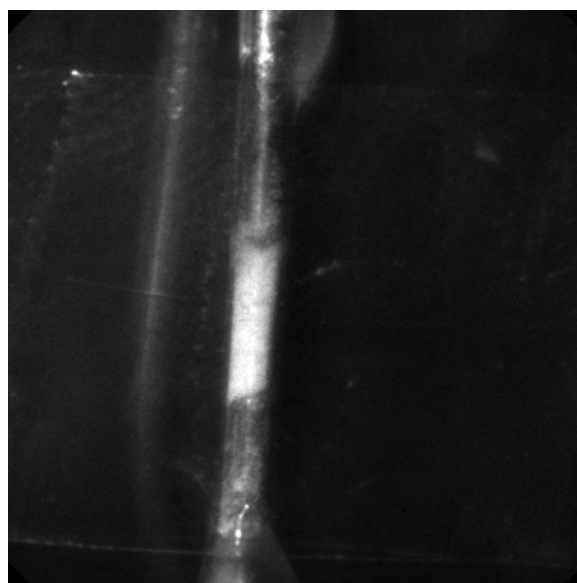


**Figure 6.5. Pre-shot view of a TATB capillary, as seen by the gated camera.**

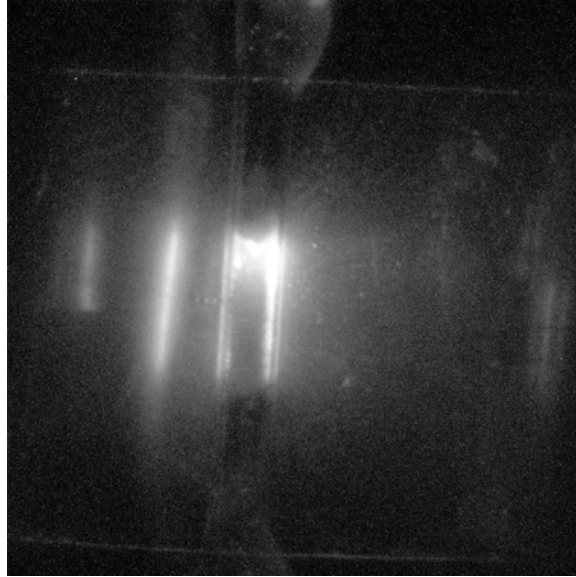


**Figure 6.6. Gated image of a TATB capillary taken 1500 ns into a pulse. The bright region at the top coincides with the slight air gap between the wire and powder as seen in the pre-shot image. The appearance is quite different than PETN imaged at the same time – see Figure 6.8.**

The results of testing PETN were dramatically different. The specimen would react with a surprisingly loud pow for 1.5 mg. As seen in Figure 6.7, the sample would be completely consumed and the capillary completely destroyed. Enough pressure is produced to deform the copper backplane. The discoloration visible in the figure is not powder residue; it is damaged Kapton. Post-shot analysis using Raman spectroscopy found no trace of unreacted PETN.

Figure 6.8 shows frames from video taken using the MIT camera. The expanding front of the exploding capillary can be tracked and yields an estimate of 1.7 mm/microsecond for the speed; this is significantly faster than anything observed in a typical thermal explosion.



**Figure 6.7.** Post-shot photograph of a PETN test, showing destruction of the capillary and deformed of the copper backplane. The white blur in the middle is scoured Kapton, not powder residue; Raman spectroscopy confirmed the absence of PETN.

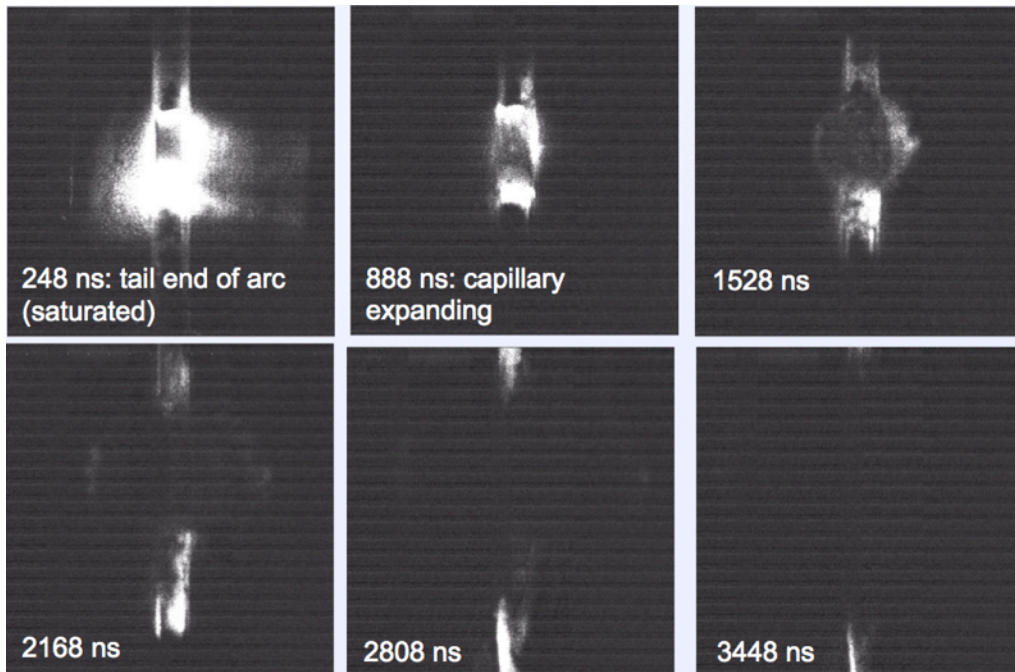


**Figure 6.8.** Frames from a video of the PETN shot. The expansion speed of the front is estimated to be 1.7 mm/microsecond.

### 6.3. Recommendations for Future Capillary Testing

The small footprint of the capillary tests makes them very flexible given the usual limitations on experiments involving high explosives. As this work is transferred to programmatic space, we expect to refine this test by building an improved, standardized holder that can be aligned to within sufficient tolerance to allow use of the imaging spectrometer system. A redesigned pulser that allows tuning of the shot voltage and source energy should be built, to allow true threshold testing and to raise the insult energy to the level of a few joules.

In addition to threshold results, these tests can be used to calibrate a number of assumptions in the PCB model, such as heat transfer.

## Appendix A. Pumped Convective Burn Modeling Tools

Below is a listing of the C++ tool used to study thresholds according to the pumped convective burn model, in a cylindrical geometry, as discussed in Section 5.5, with the hard-threshold model for  $v_{\text{burn}}$ . The “rungekutta.h” header file contains the interface to a standard Runge-Kutta integration routine. The tool uses an explicit time integration with finite-differencing in space and makes use of a numerical viscosity (representing a normal rather than shear effect), scaling with the square of the velocity gradient, to aid in resolving shocks. The planar-geometry tool used to study the evolution of the steady wave follows this listing.

```
#include <iostream>
#include <fstream>
#include "RungeKutta.h"

using namespace ADCGlib;

class GenericChannel {
public:
    virtual ~GenericChannel() { return; }
    virtual f_type get_T(const uint i)
const = 0;
    f_type get_dh()
const { return(dh); }
    virtual f_type get_h(const uint i)
const = 0;
protected:
    GenericChannel(const f_type
dh0):dh(dh0) { return; }
private:
    f_type dh;
};

class FakeChannel:public GenericChannel {
public:
    FakeChannel():GenericChannel(20.e-6)
{ return; }
    f_type get_T(const uint) const {
return(200000.0); }
    f_type get_h(const uint) const {
return(20.0*0.024/20.e-6); }
};
```

```
class GenericWall {
public:
    virtual ~GenericWall() { return; }
    virtual f_type get_T(const uint i)
const = 0;
    virtual f_type get_mdot(const uint i)
const = 0;
    virtual f_type get_udot(const uint i)
const = 0;
    virtual bool not_burned(const uint
i) const = 0;
};

class Wall:public GenericWall, public RKable
{
public:
    Wall(const uint n0, const uint
ndeep0, const f_type tpulse):

        RKable(n0*(ndeep0+1),n(n0),ndeep(ndeep0)
,ntot(n0*ndeep0),ch(0),vb(0),

        xmax(0.0),dx(0.0),dxi2(0.0),rho(0.0),Cp(0
.0),kappa(0.0),r(0.0),
        alpha(0.0),Tcrit(0.0),Ur(0.0) {
        vb = new f_type[n0];
        for(uint i=0; i<n0; ++i) {
            for(uint j=0; j<ndeep; ++j) {
                if (i<20) {
                    f[i*ndeep0+j]
= 300.0;
                    //
                    f[n0*ndeep0+i*ndeep+j]
= 0.0;
                } else {
                    f[i*ndeep0+j]
= 300.0; // K
                    //
                    f[n0*ndeep0+i*ndeep+j]
= 1.0;
                }
            }
        }
        for(uint i=0; i<n0; ++i)
f[ntot+i] = 0.0; // Xb
        rho = 1800.0; // kg/m^3
        Cp = 1100.0; // J/(kg K)
        kappa = 0.25; // W/(m K);
        r = 10.e-6; // m; this is the
particle radius
        Tcrit = 1000.0; // K; ideal
threshold temp // tag
        xmax =
5.0*std::sqrt(kappa*tpulse/(rho*Cp));
        dx = xmax/(ndeep-1);
        dxi2 = 1.0/(dx*dx);
        alpha = kappa*dxi2/(rho*Cp);
        Ur = rho*Cp*6000.0; // J/m^3;
fully reacted energy density
        return; }
    ~Wall() { if (vb!=0) { delete []vb;
```

```

vb=0; } return; }
void link_channel(const
GenericChannel* ch0) { ch=ch0; return; }
f_type get_T(const uint i)
const { return(f[ndeep*i]); }
f_type get_T(const uint i, const uint
j) const { return(f[ndeep*i+j]); }
f_type get_mdot(const uint i)
const { return(2.0*vb[i]*rho/ch->get_dh());
}
f_type get_udot(const uint i)
const { return(2.0*vb[i]*Ur /ch->get_dh());
}
f_type get_Xb(const uint i)
const { return(f[ntot+i]); }
f_type get_Vb(const uint i)
const { return(vb[i]); }
f_type get_y(const uint i)
const { return(i*dx); }
bool not_burned(const uint i)
const { return(f[ntot+i]<r); }
f_type get_f(const uint i)
const { return(f[n*ndeep+i]); }
f_type get_f_front(const uint i)
const {
uint j=0;

/*while((j<ndeep)&&(f[ntot/2+i*ndeep+j]<0
.5)) ++j;*/
return(j*dx); }
void RKable_poststep(const f_type t,
const f_type dt) {
for(uint i=0; i<n; ++i) {
f_type T0=Tcrit;
f_type bccoeff = dx*ch-
>get_h(i)/kappa;
if (fcurl[ndeep*i]<Tcrit) T0 =
(bccoeff*ch-
>get_T(i)+f[ndeep*i+1])/(1.0+bccoeff);
bool crit = (T0<Tcrit);
if ((i!=0)&&(i!=n-1)) crit &=
((fcurl[ndeep*(i-
1)]<Tcrit)||fcurl[ndeep*(i+1)]<Tcrit));
if (crit) f[ndeep*i]=T0; else
f[ndeep*i]=Tcrit;
if (!(crit)&&(f[ntot+i]<r))
vb[i] = 10.0; // tag ch->get_h()*(ch-
>get_T(i)/Tcrit-1.0)/(rho*Cp);
else
vb[i] = 0.0;
}
return; }
void RHS(const f_type t, f_type *rhs)
{
f_type* xr = rhs+ntot;
const f_type* xf = f+ntot;
f_type* Tr = rhs;
f_type* Tf = f;
// f_type* fr = rhs+ntot/2;
// f_type* ff = f +ntot/2;

```

```

const f_type dok = dx/kappa;
for(uint i=0; i<n; ++i) {
f_type bccoeff = dok*ch-
>get_h(i);
if (fcurl[ndeep*i]<Tcrit) *Tf
= (bccoeff*ch-
>get_T(i)+*(Tf+1))/(1.0+bccoeff);
if ((i!=0)&&(i!=n-
1)&&(fcurl[ndeep*(i-
1)]>=Tcrit)&&(fcurl[ndeep*(i+1)]>=Tcrit))
*Tf=Tcrit;
*Tr = 0.0;
// *fr = 0.0; // -
(*ff)*0.25e11*std::exp(-16000.0/(Tf));
if (*Tf<Tcrit) {
++Tf; ++Tr;
// ++ff; ++fr;
for(uint j=1; j<ndeep-1;
++j) {
f_type term = 0.0; //
(*ff)*0.25e11*std::exp(-16000.0/(Tf));
*Tr++ = alpha*(Tf-
1)+*(Tf+1)-2.0*(Tf))+5.e3*term;
// *fr++ = -term;
++Tf; // ++ff;
}
*Tr++ = 0.0; ++Tf; // far
endpoint
// *fr++ = 0.0; ++ff;
*xr++ = 0.0; // position
of burn front
} else {
for(uint j=0; j<ndeep;
++j) {
*Tr++ = 0.0;
// *fr++ = 0.0;
++Tf; //++ff;
}
if (*xf<r) *xr++ = 10.0;
// tag h*(ch->get_T(i)/Tcrit-1.0)/(rho*Cp);
else *xr++ = 0.0;
}
++xf;
}
return; }
private:
const GenericChannel* ch;
f_type *vb;
uint n, ndeep, ntot;
f_type dh, h, xmax, dx, dxi2;
f_type rho, Cp, kappa, r, alpha,
Tcrit, Ur;
};

class Channel:public GenericChannel, public
RKable {
enum { RHO=0, GAM, E };
public:
Channel(const uint n0, const f_type
tp0):

```

```

GenericChannel(20.e-
6),RKable(3*n0),w(0),n(n0),tpulse(tp0),

dx(0.0),dxi(0.0),dxi2(0.0),L(0.0),TpU(0.0
),TpP(0.0),mua(0.0),vpeak(0.0),Xf(0.0) {
L = 0.0025;
dx = L/(n0-1);
dxi = 0.5/dx;
dxi2 = 4.0*dxi*dxi;
TpP = 28.0*1.67e-27/1.38e-23;
TpU = 0.4*TpP;
mua = dxi*dxi*5.e-9;
for(uint i=0; i<n0; ++i) {
f[RHO*n0+i] = 1.2;
f[GAM*n0+i] = 0.0;
f[E*n0+i] =
(300.0*1.2/TpU);
}
return; }
void link_wall(const GenericWall* w0)
{ w=w0; return; }
f_type S(f_type x, const f_type t)
const {
if (t<tpulse) {
const f_type r0 = 125.e-6;
const f_type S0 = 0.05/(2.5e-
3*3.14159*r0*r0); // 73 g at d=10, 80 g at
d=20, all for r=250 mu
x /= r0;
return(S0*exp(-x*x)/tpulse);
} else return(0.0); }
f_type get_T(const uint i) const {
f_type U = get_U(i);
return(TpU*U/f[i]); }
f_type get_rho(const uint i) const {
return(f[i]); }
f_type get_gam(const uint i) const {
return(f[n+i]); }
f_type get_E( const uint i) const {
return(f[2*n+i]); }
f_type get_v( const uint i) const {
return(f[n+i]/f[i]); }
f_type get_U( const uint i) const {
return(f[2*n+i]-0.5*f[n+i]*f[n+i]/f[i]); }
f_type get_PC( const uint i) const {
return(0.4*get_U(i)); }
f_type get_r( const uint i) const {
return(i*dx); }
f_type get_vpeak() const {
return(vpeak); }
f_type get_Xfront() const {
return(Xf); }
f_type get_h(const uint i) const {
// Dittus-Boelter but assumes Pr=1
f_type kappa = 0.024;
if (f[i]>1.2) kappa +=
0.226*(f[i]-1.2)/1800.0; // crude attempt to
mix gas & HE values
f_type mu = 1.8e-5*kappa/0.024;
// similar crude scaling of mixture

```

```

f_type Re = f[n+i]*get_dh()/mu;
f_type Nu = 4.0;
if (Re>1.0) {
f_type Tr =
std::pow(get_T(i)/w->get_T(i),0.716);
Nu +=
0.026*std::pow(Re,0.8)*Tr*std::exp(-
2.5e7/(Re*Re));
}
return(Nu*kappa/get_dh()); }
void RHS(const f_type t, f_type *rhs)
{
const f_type tod = 2.0/get_dh();
f_type hod = tod*get_h(0);
const f_type fod =
0.01*0.5/get_dh();
const f_type *rf = f;
const f_type *gf = f+n;
const f_type *ef = f+2*n;
f_type *rr = rhs;
f_type *gr = rhs+n;
f_type *er = rhs+2*n;
f_type rm = 0.0;
f_type rhim = 1.0/(*rf);
f_type gm = 0.0;
f_type em = *ef;
f_type vm = 0.0;
f_type pm = 0.4*em;
++rf; ++gf; ++ef; // now at index
1
f_type r = dx;
f_type rhi = 1.0/(*rf);
f_type g = *gf;
f_type e = *ef;
f_type v = g*rhi;
f_type p = 0.4*(e-0.5*g*v);
*rr++ = -4.0*dxi*g+w-
>get_mdot(0);
*gr++ = 0.0;
*er = S(0.0,t)+w->get_udot(0)-
4.0*dxi*v*(e+p);
//
+2.0*0.5e2*dxi2*TpP*(p*rhi-p*rhim);
if (w->not_burned(0)) *er +=
hod*(w->get_T(0)-TpP*pm*rhim);
++er;
for(uint i=1; i<n-1; ++i) {
hod = tod*get_h(0);
++rf; ++gf; ++ef; // now at
index i+1
f_type rp = r+dx;
f_type rhip = 1.0/(*rf);
f_type gp = *gf;
f_type ep = *ef;
f_type vp = gp*rhip;
f_type pp = 0.4*(ep-
0.5*gp*vp);
f_type tm = mua*std::fabs(v-
vm)*(v-vm);
f_type tp = mua*std::fabs(vp-

```

```

v)*(vp-v);
    *rr++ = w->get_mdot(i)-
dxi*(gp-gm)-g/r;
    *gr = dxi*(gm*vm-gp*vp+pm-
pp+tp-tm)-g*v/r;
    if (w->not_burned(i)) *gr -=
fod*g*std::fabs(v);
    ++gr;
    *er = S(r,t)+w-
>get_udot(i)-dxi*(vp*(ep+pp)-vm*(em+pm)-
(vp*tp-vm*tm))-v*(e+p)/r;
//
    +0.5e2*dxi2*TpP*(pm*rhim+pp*rhip-
2.0*p*rhi);
    if (w->not_burned(i)) *er +=
hod*(w->get_T(i)-
TpP*p*rhi)+fod*v*v*std::fabs(g);
    ++er;
    rm = r;
    rhim = rhi;
    gm = g;
    em = e;
    pm = p;
    vm = v;
    v = vp;
    r = rp;
    rhi = rhip;
    g = gp;
    e = ep;
    p = pp;
}
hod = tod*get_h(0);
*rr = 2.0*dxi*gm;
*gr = 0.0;
*er = S(L,t)+w->get_udot(n-
1)+2.0*dxi*vm*(em+pm);
    if (w->not_burned(n-1)) *er +=
hod*(w->get_T(n-1)-TpP*p/(r*f));
    return; }
void RKable_poststep(const f_type
t, const f_type dt) {
    vpeak = 0.0;
    Xf = 0.0;
    for(uint i=0; i<n; ++i) {
        f_type tmp =
std::fabs(f[n+i]/f[i]);
        if (tmp>vpeak) vpeak =
tmp;
        if (w->get_mdot(i)!=0.0)
    }
    return; }
private:
    const GenericWall* w;
    uint n;
    f_type tpulse, dx, dxi, dxi2, L, TpP,
TpU, mua, vpeak, Xf;
};

int main (int argc, char * const argv[]) {
    const uint n=600, ndeep=50;
    f_type tpulse = 100.e-9;

    Wall w(n,ndeep,tpulse);
    Channel ch(n,tpulse);
    FakeChannel fch;
    w.link_channel(&ch);
    ch.link_wall(&w);
    MultiRungeKutta RK(2);
    RK.set_block(0,&w);
    RK.set_block(1,&ch);

    uint nstep=10000, csc=nstep/50,
cfile=nstep/100, cend=n/200, cline=n/100;
    if (csc ==0) csc = 1;
    if (cfile==0) cfile = 1;
    if (cend ==0) cend = 1;
    if (cline==0) cline = 1;
    f_type t=0.0, dt=0.01e-9;
    uint count=0;

    std::fstream
vsTime("vsTime.txt",std::fstream::out);
    std::fstream
rhofile("rho.txt",std::fstream::out);
    std::fstream
vfile("v.txt",std::fstream::out);
    std::fstream
Tchfile("Tch.txt",std::fstream::out);
    std::fstream
Twfile("Twtime.txt",std::fstream::out);
    std::fstream
Twfile2("Twaxis.txt",std::fstream::out);

    std::cout << "Step\tTime (mu-s)\tRho
(kg/m^3)\tVpk (m/s)\tT_ch (K)\tT_w
(K)\tFront pos. (m)" << std::endl;
    vsTime << "Step\tTime (mu-s)\tRho
(kg/m^3)\tVpk (m/s)\tT_ch (K)\tT_w
(K)\tFront pos. (m)" << std::endl;
    while(count<nstep) {
        RK.RKstep(t,dt);
        t += dt;
        ++count;
        if (count%csc==0) {
            std::cout << count << "\t" <<
t*1.e6 << "\t" << ch.get_rho(0) << "\t" <<
ch.get_vpeak() <<
"\t" << ch.get_T(0) << "\t"
<< w.get_T(0) << "\t" <<
ch.get_Xfront() << std::endl;
            vsTime << count << "\t" << t*1.e6
<< "\t" << ch.get_rho(0) << "\t" <<
ch.get_vpeak() <<
"\t" << ch.get_T(0) << "\t"
<< w.get_T(0) << "\t" <<
ch.get_Xfront() << std::endl;
        }
        if (count%cfile==0) {

```



```

        for(uint i=0; i<n; i += cline) {
            rhofile << ch.get_rho(i) <<
'\t';
            vfile << ch.get_v(i) <<
'\t';
            Tchfile << ch.get_T(i) <<
'\t';
            Twfile << w.get_T(i) <<
'\t';
        }
        Twfile2 << w.get_T(0,i) << '\t';
        rhofile << std::endl;
        vfile << std::endl;
        Tchfile << std::endl;
        Twfile << std::endl;
        Twfile2 << std::endl;
    }
}

vsTime.close();
rhofile.close();
vfile.close();
Tchfile.close();
Twfile.close();
Twfile2.close();

std::fstream
finals("finals.txt",std::fstream::out);
std::cout << std::endl << "r" << '\t' <<
"rho" << '\t' << "v" << '\t' << "Tch" <<
'\t' << "Pch" << '\t' << "Tw" << '\t'
<< "Vb" << '\t' << "Xb" << std::endl;
finals << std::endl << "r" << '\t' <<
"rho" << '\t' << "v" << '\t' << "Tch" <<
'\t' << "Pch" << '\t' << "Tw" << '\t'
<< "Vb" << '\t' << "Xb" << std::endl;
for(uint i=0; i<n; i += cend) {
    std::cout << ch.get_r(i) << '\t' <<
ch.get_rho(i) << '\t' << ch.get_v(i) <<
'\t' << ch.get_T(i) << '\t' <<
ch.get_P(i) << '\t' << w.get_T(i) << '\t' <<
w.get_Vb(i) <<
'\t' << w.get_Xb(i) << std::endl;
}
for(uint i=0; i<n; ++i) {
    finals << ch.get_r(i) << '\t' <<
ch.get_rho(i) << '\t' << ch.get_v(i) <<
'\t' << ch.get_T(i) << '\t' <<
ch.get_P(i) << '\t' << w.get_T(i) << '\t' <<
w.get_Vb(i) <<
'\t' << w.get_Xb(i) << std::endl;
}
finals.close();

std::cout << std::endl;
for(uint i=0; i<ndeep; ++i) std::cout <<
w.get_y(i) << '\t' <<
w.get_T(0,i) << '\t' << w.get_f(i) <<
std::endl;

```

```

        return 0;
    }

```

The following listing is of the tool used to study the appearance of a steady wave, in a planar geometry. No thermal conduction is used (it is included in the code, but the coefficient is set to zero). A small artificial viscosity is used in order to help follow the fluid-phase shock front, but otherwise viscosity is also not a significant factor. This tool also used the previously described Runge Kutta routines. Also note that the transitions between the heating and burning regions, and then the burning and completed-burn regions, are smoothed slightly. The crude numerics employed could not handle a sharp transition of those effects.

```

#include <iostream>
#include <fstream>
#include <sstream>
#include "RungeKutta.h"

using namespace ADCGlib;

class Stretch:public RungeKutta {
public:
    Stretch(const uint n0, const char*
filename=0):RungeKutta(5*n0),n(n0),f0(0),dy(
1000.0/(n0-1.0)),dyi(0.5/dy) {
        f0 = new f_type[5*n0];
        const f_type vb = 100.0;
        const f_type P0 = 1.2*1.38e-
23*300.0/(19.0*1.67e-27); // 156571 Pa
        const f_type c =
std::sqrt(P0/1.2); // 361 m/s
        const f_type h =
16.0*0.024/1.e-5; // tag, Nu=16
        const f_type rho_HE = 1780.0;
        Sr = 2.0*rho_HE*vb/(1.2*c);
        M = 150.0*2.e-5/(1.e-
5*1.2*c); // tag
        fr = 0.1;
        K = 0.0*0.25*300.0/(P0*1.e-
5*c); // tag
        Su =
2.0*vb*rho_HE*1100.0*4500.0/(P0*c); //
U=68780; Uo=37.5 at deff/d=0.01
        HE = h*300.0/(P0*c);
        HT = h*1.e-
5/(rho_HE*1100.0*c*1.e-7);
        f_type t_pulse = 1.e-7;
        Q0 =

```

```

(0.015/(t_pulse*3.14*2.5e-3*6.25e-8))*(1.e-
5/(P0*c));
    gm1= 0.4;
    tcut = t_pulse*c/1.e-5;
    tmax = (0.5*1.e-5/vb)*(c/1.e-
5);
    Tcrit= 3.0;
    argt = 220.0/tmax; // for use
in smoothing
    if (filename==0) {
        for(uint i=0; i<n0;
        ++i) {
            //Planar
            f0[i] =
            1.0;
            // Cylindrical
            //
            f_type y =
            i*dy;
            //
            f0[i] =
            y;
            f0[n0+i] =
            0.0;
            // Planar
            f0[2*n0+i] =
            1.0/gm1;
            // Cylindrical
            //
            f0[2*n0+i] =
            y/gm1;
            f0[3*n0+i] =
            1.0;
            f0[4*n0+i] =
            0.0;
        }
    } else {
        std::fstream
file(filename, std::ios_base::in);
        for(uint i=0; i<n0;
        ++i) {
            file >> f0[i];
            file >>
            f0[n0+i];
            file >>
            f0[2*n0+i];
            file >>
            f0[3*n0+i];
            file >>
            f0[4*n0+i];
        }
        file.close();
    }
    return; }
~Stretch() {
    if (f0 !=0) { delete []f0;
f0 =0; }
    return; }
    f_type y( const uint i) const
{ return(dy*i); }
// Planar
    f_type rho(const uint i) const
{ return(f0[i]); }

```

```

    f_type P( const uint i) const
{ return(gm1*(f0[2*n+i]-
0.5*f0[n+i]*v(i))); }
    f_type v( const uint i) const
{ return(f0[n+i]/f0[i]); }
    f_type T( const uint i) const
{ return(P(i)/f0[i]); }
    f_type gam(const uint i) const
{ return(f0[n+i]); }
    f_type E( const uint i) const
{ return(f0[2*n+i]); }
    f_type Tw( const uint i) const
{ return(f0[3*n+i]); }
    f_type tau_to_t(const f_type tau)
const { return(tau/(1.e7*tcut)); }
    f_type tb(const uint i) const
{ return(f0[4*n+i]); }
    f_type xmax() const {
        uint imax=n-1;
        f_type vmax=0.0;
        f_type vp = f0[2*n-1]/f0[n-
1];
        for(uint i=n-1; i!=0; --i) {
            f_type v =
            f0[n+i]/f0[i];
            if (v-vp>vmax) { vmax
            = v-vp; imax=i; }
            vp = v;
        }
        return(dy*imax); }
    f_type Qext(const f_type y, const
f_type t) {
        if (t<tcut) {
            f_type r = y*1.e-
5/250.e-6;
            return(Q0*std::exp(-
r*r));
        } else return(0.0); }
    void step(const f_type t, const
f_type dt) { RungeKutta::RKstep(t,dt,f0,f0);
return; }
    f_type smooth(const f_type arg) const
{
        if (arg<-23.0) return(0.0);
        if (arg< 0.0)
return(0.5*std::exp(arg));
        if (arg< 23.0) return(1.0-
0.5*std::exp(-arg));
        return(1.0); }
    void RHS(const f_type t, const
f_type *f, f_type* rhs) {
        f_type vm, v;
        f_type Pm, P;
        f_type Tm, T, Tw = f[3*n];
        f_type rmi=1.0/f[0],
ri=1.0/f[1];
        f_type gm=f[n], g=f[n+1];
        f_type Em=f[2*n], E=f[2*n+1];
        f_type sr = 0.0;
        f_type su = 0.0;

```

```

v = g*ri;
P = gm1*(E-0.5*g*v);
T = P*ri;
vm = 0.0;

// Planar
Pm = gm1*Em;
Tm = Pm*rmi;
f_type rate_fac =
smooth(73.33*(Tw-Tcrit
f_type rate_2 =
rate_fac*smooth(argt*(tmax-f[4*n
sr = Sr*rate_2; su =
Su*rate_2;
// Planar
rhs[0] = sr-2.0*dyi*g;
rhs[n] = 0.0;
rhs[2*n] = su+HE*(Tw-
Tm)*(1.0-
rate_fac)+Qext(0.0,t)+dyi*(4.0*dyi*(2.0*K*(T
-Tm)+M*v*v)-2.0*(P+E)*v);
rhs[3*n] = HT*(Tm-Tw)*(1.0-
rate_fac);
rhs[4*n] = rate_2;
for(uint i=1; i<n-1; ++i) {
f_type rpi =
f_type gp = f[n+i+1];
f_type Ep =
f[2*n+i+1];
Tw = f[3*n+i];
f_type vp = gp*rpi;
f_type Pp = gm1*(Ep-
0.5*vp*gp);
f_type Tp = Pp*rpi;
sr = 0.0;
su = 0.0;
rate_fac =
smooth(73.33*(Tw-Tcrit));
rate_2 =
rate_fac*smooth(argt*(tmax-f[4*n+i]));
sr = Sr*rate_2; su =
Su*rate_2;
// Planar
f_type dmassdy = gp-
gm;
f_type dmomdy = Pp-Pm
+ vp*gp-vm*gm;
f_type dEdy =
vp*(Ep+Pp) - vm*(Em+Pm);
rhs[i] = sr-
dyi*dmassdy;
rhs[n+i] = -
dyi*(dmomdy - 4.0*M*dyi*(vp+vm-2.0*v))-
0.5*std::fabs(v)*g*fr*(1.0-rate_fac);
rhs[2*n+i] =
su+HE*(Tw-T)*(1.0-rate_fac)+Qext(i*dy,t)-
dyi*(dEdy - 4.0*dyi*(K*(Tp+Tm-2.0*T)
+0.5*M*(vm*vm+vp*vp-2.0*v*v)));
rhs[3*n+i] = HT*(T-

```

```

Tw)*(1.0-rate_fac);
rhs[4*n+i] = rate_2;
vm = v; Pm = P; Tm =
T; rmi = ri; gm = g; Em = E;
v = vp; P = Pp; T =
Tp; ri = rpi; g = gp; E = Ep;
}
rhs[n-1] = 0.0;
rhs[2*n-1] = 0.0;
rhs[3*n-1] = 0.0;
rhs[4*n-1] = 0.0;
return; }
void file_dump(const uint nstep,
const uint incr=1) {
std::stringstream ss;
ss << "data" << nstep <<
".txt";
std::fstream
file(ss.str().c_str(),std::ios_base::out);
file <<
"y\rho\tv\tT\tTw\tP\tt\tburn" << std::endl;
for(uint i=0; i<n; i += incr)
{
file << y(i) << '\t'
<< rho(i) << '\t' << v(i) << '\t' << T(i) <<
'\t' << Tw(i)
<< '\t' << P(i) << '\t' << tau_to_t(tb(i))
<< std::endl;
}
file.close();
return; }
void state_dump(const uint nstep) {
std::stringstream ss;
ss << "state" << nstep <<
".txt";
std::fstream
file(ss.str().c_str(),std::ios_base::out);
file.setf(std::ios::scientific,std::ios
::floatfield);
file.precision(16);
for(uint i=0; i<n; ++i) {
if (std::fabs(f0[i])
>1.e-90) file << f0[i] << std::endl;
else file << 0.0 << std::endl;
if (std::fabs(f0[n+i])
>1.e-90) file << f0[n+i] << std::endl;
else file << 0.0 << std::endl;
if
(std::fabs(f0[2*n+i])>1.e-90) file <<
f0[2*n+i] << std::endl; else file << 0.0 <<
std::endl;
if
(std::fabs(f0[3*n+i])>1.e-90) file <<
f0[3*n+i] << std::endl; else file << 0.0 <<
std::endl;
if
(std::fabs(f0[4*n+i])>1.e-90) file <<
f0[4*n+i] << std::endl; else file << 0.0 <<
std::endl;
}
}

```

```

    }
    file.close();
    return; }
private:
    uint n;
    f_type *f0;
    f_type dy, dyi, Sr, M, fr, K, Su, HE,
HT, Q0, gm1, tcut, tmax, Tcrit, argt;
};

int main (int argc, char * const argv[]) {

    const uint n = 20001;
    Stretch stretch(n);
    const f_type dt = 0.001;
    f_type t = dt*0.0;
    uint count = 0;
    std::cout << "Step\tt (mu-s)\tT\tTw" <<
std::endl;
    f_type x52, x76, x100;
    while(count<100000) {
        stretch.step(t,dt);
        t += dt;
        ++count;
        f_type Tw0 = stretch.Tw(0);
        if (count%400==0) std::cout << count
<< '\t' << stretch.tau_to_t(t)*1.e6 <<
        '\t' << stretch.T(0) << '\t'
<< Tw0 << '\t' << stretch.tb(0) <<
std::endl;
        if (count%4000==0)
{ stretch.file_dump(count,10);
stretch.state_dump(count); }
        if (count==52000) x52 =
stretch.xmax();
        if (count==76000) x76 =
stretch.xmax();
        if (count==100000)
x100=stretch.xmax();
    }

    std::cout << std::endl;
/*    std::cout <<
"y\rho\tv\tT\tTw\tP\ttburn" << std::endl;
    for(uint i=0; i<n; i += 5) {
        std::cout << stretch.y(i) << '\t' <<
stretch.rho(i) << '\t' << stretch.v(i) <<
'\t' << stretch.T(i) <<
        '\t' << stretch.Tw(i) << '\t'
<< stretch.P(i) << '\t' <<
stretch.tau_to_t(stretch.tb(i)) <<
std::endl;
    } */

// The following calculates the speed of the
fluid-phase shock front.
    f_type speed1 = (x76-x52)/(76.0-52.0);
// assumes dt = 0.001
    f_type speed2 = (x100-x76)/(100.0-
76.0); // assumes dt = 0.001

    speed2 = 0.5*(speed2+speed1);
    std::cout << "Positions: " << x52 << '
' << x76 << ' ' << x100 << std::endl;
    std::cout << "Estimated lambda: " <<
speed2*speed2 << std::endl;

    return 0;
}

```

## Appendix B. MATLAB Code for RLC Fits to Pulse Waveforms

### RLC fitting routine

```

%use this script to analyze a specific set
of pulser data with RLC model
%V. Tang, 6/22/09, V1.0
%Takes current waveform data in csv form and
fits a RLC model to it using
%fminsearch in Matlab. Plots figure for
each fit, and provides summary
%figures also. Will save all data.
%
%Inputs on top are C, V0, the CVR
attenuation and resistance, and starting
%parameter guesses. Define what you
consider to be t0 in terms of CVR voltage
and program inputs that into starting guess.
%Also, input the file numbers you want to
analyze in filenumrng
%
%12-20-09, V2.0
%edits for trigger, self-determined from
Ch4.
%minor edits for plots
%10-14-10, V3.0
%added in fitting time time
%07-14-11, V4.0 R. Richardson
%change to five parameter fit to data;
%Fits A, tau, w, t0 (firing time), and
Baseline current
%Requires function RLC_Ifit2
%data in TDS3014B csv format; from floppy
%07-14-11, V5.0 , R. Richardson
%modify to read in csv file from OpenChoice
reader with two channel data;
% file name mm_dd_yy_pulser_00n.csv
%08-8-11, V6.0 , R. Richardson
%modify to fit to complex roots ; make
compatible with matlab R13 (2002)
%RLC_Ifit3

clear all;
close all;
clear GLOBAL;

global C_global V0_global
RLC_Ifit_global_curr_out

filenumrng=[1:2];

%User Inputs
C_global=8e-9; %8.35e-9;
V0_global=10e3; %initial voltage in V
CVR_resist=0.0140;
%CVR_resist=0.224;
CVR_atten=1; %133.5; %CVR atten change
7/29/11, was 205;
Rguess= 10;
Lguess= 350e-9; %H
t0guess= 100e-9; %s
alphaguess= Rguess/2/Lguess;
wo=1/sqrt(Lguess*C_global);
wdguess= sqrt(alphaguess^2-wo^2);
Aguess= -(V0_global/wdguess/Lguess);
params_guess=[Aguess alphaguess wdguess
t0guess -.24*CVR_atten/CVR_resist ];

```

```

%amplitude, decay, frequency, firing time,
and scope baseline current
t0V0=-3.5; %voltage value on CVR trace that
defines t0 initial guess
%V2 12-20-09 edits
t0CVR0=1.5; %voltage for trigger pulse for
trigger time

%V3 10-14-10 optional time after, comment
out if don't want
%dtfit=(669-610)*.7; % dt for fit in ns
RLC_Ifit_global_curr_out=0; %switch for RLC
fit function
d=dir; %get names of files
shotnumind=1;
for ii=1:length(d)
    if length(d(ii).name)>2 &
d(ii).name(end-2:end)=='csv'

        %if d(ii).name(20:22)=='Ch1'

temp1=str2num(d(ii).name(16:18));
temp2=find(filenumrng==temp1);
if length(temp2)==1
    RLC_Ifit_global_curr_out=0;

shotnum(shotnumind)=str2num(d(ii).name(16:18
));
    %d(ii).name

S1=csvread(d(ii).name,17,3,[17,3,9999,4]);
%ch1 data; CVR voltage

S4=csvread(d(ii).name,17,9,[17,9,9999,10]);
%ch4 data; camera time
    offset= mean(S1(1:100,2));
%scope offset

%dum=find(S1(:,2)<(t0V0+offset),1);

dum=min(find(S1(:,2)<(t0V0+offset))); % for
old matlab release
    if isempty(dum); dum=1; end
    %10-14-10 added here to to a
dt after shot option
    if exist('dtfit','var') &&
dtfit>0

%dum2=find(S1(:,1)>(S1(dum,1)+dtfit*1e-
9),1);

dum2=min(find(S1(:,1)>(S1(dum,1)+dtfit*1e-
9)));
        S1=S1(1:dum2,:);
        end;
        params_guess(4)=S1(dum,1);
%time in s

params_guess(5)=0;%offset*CVR_atten/CVR_resi
st; %offset current
        t0=S1(1,1)*1e9;
        %t0=S1(1,1)*1e6;
        dt=S1(2,1)*1e9-t0;
        %dt=S1(2,1)*1e6-t0;
        tstart=200; %start time of
fit in ns
        tend=900; %end time of fit
in ns

%dstart=dum-2500;
%dend=10000-6000;d

```

```

dstart= ((tstart-t0)/dt);
dend=((tend-t0)/dt);
%S1=S1(dstart:dend,:); %trim
lead from data

options=optimset('TolX',1e-
5,'Tolfun',1e-5); %, 'PlotFcns',@optimplotx);

[fitdata3(shotnumind,:),fval,exitflag,output
]= ...

fminsearch(@RLC_Ifit3,params_guess,options,S
1(:,1)',S1(:,2)'.*CVR_atten./CVR_resist);

maxabsI(shotnumind)=max(abs(S1(:,2)'.*CVR_att
en./CVR_resist));
disp(d(ii).name);
%

alpha=fitdata3(shotnumind,2);
wd=fitdata3(shotnumind,3);
L= real(1/((-wd^2
+alpha^2)*C_global));
R=real(L*2*alpha);
Amag=
fitdata3(shotnumind,1);
if abs(imag(Amag))>0; Amag=
i*Amag; end
fitdata(shotnumind,:)= [R L
fitdata3(shotnumind,4)
fitdata3(shotnumind,5) Amag];

%V2 edits to get time for
trigger% 12-20-09

%timename=[d(ii).name(1:19),'Ch4',d(ii).name
(23:end)];

%S4=csvread(timename,7,3);
dum2=1;

dum2=min(find(S4(:,2)>t0CV0)); %find point
when V>1 V as trigger time
%
dum2=find(S4(:,2)>t0CV0,1); %find point when
V>1 V as trigger time
if isempty(dum2)
t_trigger=0;
else
t_trigger=S4(dum2,1); %t_trigger in seconds
end
t_trigger=0; % don't use
this now.

t0C(shotnumind)=fitdata3(shotnumind,4)-
t_trigger; %actual shot time on scope

%t0C(shotnumind)=fitdata(shotnumind,3);

%%%%%%%%%%%%%%%%%%%%%%%%%%%%%%%%%%%%%%%%%%%%%%%%%%%%%%%%%%%%%%%%%%%%%%%%

RLC_Ifit_global_curr_out=1;
%V2 edits: deal with record
lengths..%

fitcurrent(shotnumind)={RLC_Ifit3(fitdata3(s
hotnumind,:),S1(:,1)',[])};

```

```

figure;

plot(S1(:,1)*1e9,S1(:,2)*CVR_atten./C
VR_resist,S1(:,1)*1e9,fitcurrent(shotnumind)
);
%
xlabel({'Time (ns)';['CVR R
& Atten:',num2str(CVR_resist),' &
',num2str(CVR_atten),'----
',datestr(now)]});ylabel('Current (A)');
legend('Data','Fit');
shotdate=d(ii).name(1:8);
savetitle=[shotdate ' CVR
AnaData, File
',num2str(shotnum(shotnumind))];
%V2 12-20-09 edits for dt
from scope trigger trace%
title({savetitle;...

['C=',num2str(C_global,3),'
V0=',num2str(V0_global,3),'
R=',num2str(fitdata(shotnumind,1),3),...
',
L(nH)=' ,num2str(fitdata(shotnumind,2)*1e9,3)
',
t0(ns)=' ,num2str(fitdata(shotnumind,3)*1e9,3
),...
',
t0C(ns)=' ,num2str(t0C(shotnumind)*1e9,3),'
V6']],'interpreter','none');
%%%
axis tight; %xlim([300
1400]);

grid on;
%savetitle=[shotdate ' CVR
AnaData, File
',num2str(shotnum(shotnumind)),'
',datestr(now,'mm_dd_yy_HH_MM_SS')];
savetitle=[shotdate ' CVR
AnaData, File
',num2str(shotnum(shotnumind)),'
',datestr(now,30)];
saveas(gcf,savetitle,'png');
saveas(gcf,savetitle,'fig');
shotnumind=shotnumind+1;

end;
%end;
end;
end;

%master data

AverageR=mean(fitdata(:,1)); %average R
Rstdev=std(fitdata(:,1));
disp(['Average R:',num2str(AverageR),'+/-
',num2str(Rstdev)]);

AverageL=mean(fitdata(:,2)); %average L
Lstdev=std(fitdata(:,2));
disp(['Average
L(nH):',num2str(AverageL*1e9),'+/-
',num2str(Lstdev*1e9)]);

Averaget0=mean(fitdata(:,3)); %average t0
t0stdev=std(fitdata(:,3));
disp(['Average t0(ns):
',num2str(Averaget0*1e9),'+/-
',num2str(t0stdev*1e9)]);

```

```

%V2 12-20-09 edits for t0 from trigger%
Averaget0C=mean(t0C); %average t0C
t0Cstddev=std(t0C);
disp(['Average t0C(ns):
',num2str(Averaget0C*1e9),'+/-
',num2str(t0Cstddev*1e9)]);
%
%% Master Plot
skip=1;
save=0;
if skip ==0
    figure; set(gcf,'Position',[100 100 600
900]);
subplot(5,1,1);
plot(shotnum,fitdata(:,1),'ks');ylabel('R(Ohm)');
title(['R(ohm), Avg:
',num2str(AverageR,3),'\pm',num2str(Rstddev,3)
]);
hold on;
YAverageR=AverageR*ones(size(fitdata(:,1)));
plot(shotnum, YAverageR);
%hline(AverageR);
subplot(5,1,2);
plot(shotnum,fitdata(:,2)*1e9,'bs');ylabel('L(nH)');
title(['L(nH), Avg:
',num2str(AverageL*1e9,3),'\pm',num2str(Lstddev*1e9,3)
]);
hold on;
YAverageL=AverageL*1e9*ones(size(fitdata(:,1)
));
plot(shotnum, YAverageL);
%hline(AverageL*1e9);

subplot(5,1,3);
plot(shotnum,maxabsI,'bs');
ylabel('Max. Abs. I(A)');
%hline(mean(maxabsI));
hold on;
YmaxI=mean(maxabsI)*ones(size(fitdata(:,1)
));
plot(shotnum, YmaxI);
title(['Abs. I(A), Avg:
',num2str(mean(maxabsI),3),'\pm',num2str(std(maxabsI),3)
]);

%V2 12-20-09 edits
subplot(5,1,4);
plot(shotnum,t0C(:)*1e9,'gs');ylabel('t0C(ns)');
title(['t0C(ns), Avg:
',num2str(Averaget0C*1e9,3),'\pm',num2str(t0Cstddev*1e9,3)
]);
hold on;
Yt0C=Averaget0C*1e9*ones(size(fitdata(:,1)
));
plot(shotnum, Yt0C);
%hline(Averaget0C*1e9);
%

subplot(5,1,5);
plot(shotnum,fitdata(:,3)*1e9,'gs');ylabel('t0(ns)');
title(['t0(ns), Avg:
',num2str(Averaget0*1e9,3),'\pm',num2str(t0stddev*1e9,3)
]);
hold on;
Yt0=Averaget0*1e9*ones(size(fitdata(:,1)
));
plot(shotnum, Yt0);

%hline(Averaget0*1e9);
%savetitle=[shotdate ' CVR AnaData, Files
',num2str(shotnum(1)),'-
',num2str(shotnum(end)),'
',datestr(now,'mm_dd_yy_HH_MM_SS')];
savetitle=[shotdate ' CVR AnaData, Files
',num2str(shotnum(1)),'-
',num2str(shotnum(end)),'
',datestr(now,30)];
xlabel({'File
Shot#';savetitle},'interpreter','none');
end
%% save files
if save==1
saveas(gcf,savetitle,'png');
saveas(gcf,savetitle,'fig');
%print(gcf,'-dtiff',savetitle);

savedataname=[shotdate ' Analyzed CVR Data
Fnum ',num2str(shotnum(1)),'-
',num2str(shotnum(end)),'
',datestr(now,30)];
%savedataname=[shotdate ' Analyzed CVR Data
Fnum ',num2str(shotnum(1)),'-
',num2str(shotnum(end)),'
',datestr(now,'mm_dd_yy_HH_MM_SS')];
save(savedataname);
end

```

## Appendix C. MATLAB Code for Fitting Temperature and Density

### Spectral fitting routine

#### Call script

```
clear all;
close all;
%script for 1800 grating (shot xx12
13 15 16)
op60s514_1800=csvread('OOLampCalib_0p2s
_25acq_100gain_50slit.asc',0,0,[0 0
2047 1]);
op60s514_1800=csvread('OOLampCalib_0p2s
_25acq_50gain_50slit.asc',0,0,[0 0 2047
1]);
op60s514_1800=csvread('OOLampCalib_0p2s
_25acq_25gain_50slit.asc',0,0,[0 0 2047
1]);
op60s514_1800=csvread('OOLampCalib_0p5s
_25acq_20gain_50slit.asc',0,0,[0 0 2047
1]);
op60s514_1800=csvread('OOLampCalib_0p5s
_25acq_0gain_50slit.asc',0,0,[0 0 2047
1]);
op60s514_1800=csvread('OOLampCalib_0p2s
_25acq_100gain_50slit.asc',0,0,[0 0
2047 1]);
%op60s514_1800=csvread('OOLampCalib_0p2
s_25acq_150gain_50slit.asc',0,0,[0 0
2047 1]);
filestart=40
fileend=22;
fileend=filestart;
in.savedata=1; %0 no save, 1 save
%
%op60ns514_1800=csvread('Lamp_',0,0,
[0 0 2047 1]);
%new correction from 8/3/2011 cal
%wavelength_correction=[1.009592 -
2.67305]; %[1.007578 -1.58970];
wavelength_correction=[1.0090392 -
2.3592]; %new calibration 9_16_11
xnm514=op60s514_1800(:,1)*wavelengt
h_correction(1)+wavelength_correcti
on(2);
load calisrc; %loads LSC1125_CC3
csinterp514=interp1(calisrc(:,1),ca
lisrc(:,2),xnm514,'spline');

in.analysis_shot_ind=[filestart:fil
eend];%[7:22];
in.eff=op60s514_1800(:,2)./csinterp
514;

nlines=3; %3 for 3 line fit, 2 for
2 lines; 4 for 4 lines; 1 for
special
if nlines==4
```

```
in.mainpeaks= [510.55 515.32
521.82 529.2];
in.gafactors=[8e6 2.4e8 4.5e8
8.72e7];
in.Eu=[3.82 6.19 6.19 7.74];
in.man_int_lim=[1.5 1.5;2.5
2.75;2.75 2.5;2.5 2.75];
in.man_int_lim=[1. 1.;1. 1.;1.
1.;1.5 1.4];
%in.man_int_lim=[2 2.;3. 3.;3.
3;1 2];
elseif nlines==2 %first and third
lines.
in.mainpeaks= [510.55
521.82];
in.gafactors=[8e6 4.5e8];
in.Eu=[3.82 6.19];
in.man_int_lim=[1. 1.;.5 1];
elseif nlines==3
in.mainpeaks= [510.55 515.32
521.82];
in.gafactors=[8e6 2.4e8 4.5e8];
in.Eu=[3.82 6.19 6.19];
in.man_int_lim=[1. 1.;3. 3;3
3.];%[1.0 1.0;1 .5;0.8 1];
%in.man_int_lim=[1.5 1.5;2.5
3.;4.5 3.5];%fat lines
elseif nlines==1 %first and fourth
line, shot 12.
in.mainpeaks= [510.55 529.2];
in.gafactors=[8e6 8.72e7];
in.Eu=[3.82 7.74];
in.man_int_lim=[1.5 1.5;.75 1];
end;
in.smoothopt='n';
slitw=200; %slit width of
spectrometer
in.blopts=[2 .09*slitw/50];%[2
.09];
in.shotid='092111r1';
in.wavelength_correction=wavelength
_correction;
in.roi_range_lim=in.man_int_lim;
in.tholdfactor=.7;
in.manual_fit_opt=1;
diary([in.shotid,'_',datestr(now,'m
mddy_HHMMSS'),'_.txt']);

[a032211,d032211,o032211]=main_call
_auto_fit_Vld2_voigt(in);
if in.savedata==1

datatitle=['data_',in.shotid,'_',da
testr(now,'mmddy_HHMMSS')];
save(datatitle);
end;
diary off;
```



```

%close all;

Voigt profile fitting function
function
[a,d,o]=main_call_auto_fit_vld1_voigt(i
n);
%120909--modified for manual peak input
to try to get better result for s3

%020310
%Vld1--checks for if manual peaks are
inputed and then calls auto-fit as
%appropriate--i.e. does both regular
auto_fit call and auto_fit_122909
%Now for Cu also include three points
for Star Brodening, based on JPhys.
%Chem Paper 1990, page 1337. (lines
510, 515.3, 5218.2)
%22310--added linear wavelength
correction
%6-12-10: modified to call voigt
profile fits

disp('Main_call_auto_fit_voigt: Version
1.1');
%readout in structure:
temp=fields(in);
for ii=1:length(temp)

eval([temp{ii}, '=in.', temp{ii}, ',']);
end;
clear temp;
%%%%%%%%%%%%%%%%%%%%%%%%%%%%%%%%%%%%%%%%%%%%%%%%%%%%%%%%%%%%%%%%%%%%%%%%

[d]=read_in_asc;
if savedata==1

sumplot_title=['All_asc ',shotid, '_',da
tetr(now, 'mmdyy_HHMMSS')];
set(gcf, 'PaperPositionMode', 'auto')
saveas(gcf, sumplot_title, 'fig');
print('-dpng', '-
r300', sumplot_title);
end;

ss=1;
for jj=1:length(d)

%d(jj).spec(:,1)=d(jj).spec(:,1)+wavele
ngth_correction;

d(jj).spec(:,1)=d(jj).spec(:,1).*wavele
ngth_correction(1)+wavelength_correctio
n(2);

d(jj).spec(:,2)=d(jj).spec(:,2)./eff;
if sum(jj==analysis_shot_ind)==1
h=figure;
scnsize = get(0, 'ScreenSize');
set(h, 'Position', [50 50
scnsize(3)/2 scnsize(4)*.9])
xnm=d(jj).spec(:,1);
spec=d(jj).spec(:,2);

for kk=1:length(mainpeaks)
subplot(3,2, kk);
roi(kk, :)= [mainpeaks(kk)-
roi_range_lim(1)
mainpeaks(kk)+roi_range_lim(2)];
roiind=find(xnm>=roi(kk,1)
& xnm<=roi(kk,2));

thold=max(spec(roiind))*tholdfactor;
%122909 special--modified
below line
%modified here for vld1
if
exist('manual_fit_opt', 'var') &
manual_fit_opt==1
%mainpeaks exist, doing
manual fit

disp('Main_call_auto_fit_voigt: Manual
line option on, calling auto_fit with
input peaks')

a(ss, kk)=auto_fit(xnm, spec, roi(kk, :), th
old, smoothopt, blopts, man_int_lim, [mainp
eaks(kk)], [d(jj).name, '-', shotid], h);
else

disp('Main_call_auto_fit_voigt: Manual
line option off, calling auto_fit with
auto peak finding');

a(ss, kk)=auto_fit(xnm, spec, roi(kk, :), th
old, smoothopt, blopts, man_int_lim, [], [d(
jj).name, '-', shotid], h);
end;

%%%%%%%%%%%%%%%%%%%%%%%%%%%%%%%%%%%%%%%%%%%%%%%%%%%%%%%%%%%%%%%%%%%%%%%%
%
if
exist('Cu_fit_opt', 'var') &
Cu_fit_opt==0 %2-26-10 option to not do
Cu fits
else

fitlnterm(ss, kk)=log(a(ss, kk).fittedInt
I(1).*a(ss, kk).fittedIntI(2)./gafactors
(kk));

nofitlnterm(ss, kk)=log(a(ss, kk).dataInt
I(1).*a(ss, kk).dataIntI(2)./gafactors(k
k));

end;
end;

if exist('Cu_fit_opt', 'var') &
Cu_fit_opt==0 %2-26-10 option to not do
Cu fits
ss=ss+1;
else

[Tfitparams(ss, :), Tfitererrors(ss, :)] = pol
yfit(Eu, fitlnterm(ss, :), 1);

```

```

TfiteV(ss)=-
1/Tfitparams(ss,1); %now just needs to
functionalize!

[Tnofitparams(ss,:),Tnofiterrors(ss,:)]
=polyfit(Eu,nofitlterm(ss,:),1);
TnofiteV(ss)=-
1/Tnofitparams(ss,1); %now just needs
to functionalize!

[ytemp
deltatemp]=polyval(Tfitparams(ss,:),1e7
,Tfiterrors(ss,:));

TfiteV1std(ss)=abs(deltatemp/ytemp)*1.3
66; %+/- error, 1std dev (for full - to
+ range, 66% confidence)
[ytemp
deltatemp]=polyval(Tnofitparams(ss,:),1
e7,Tnofiterrors(ss,:));

TnofiteV1std(ss)=abs(deltatemp/ytemp)*1
.366;

%Summary of fit
graph%%%%%%%%%%%%%%%%%%%%%%%%%%%%%%%%
subplot(3,2,5)

plot(Eu,fitlterm(ss,),'bs',Eu,nofitlterm(ss,),'rx');
hold on;

plot(Eu,polyval(Tfitparams(ss,:),Eu),'b
-
',Eu,polyval(Tnofitparams(ss,:),Eu),'r-
');

[ytemp
deltatemp]=polyval(Tfitparams(ss,:),Eu,
Tfiterrors(ss,:));
plot(Eu, ytemp
+deltatemp*1.366, 'b:', Eu, ytemp -
deltatemp*1.366, 'b:');
[ytemp
deltatemp]=polyval(Tnofitparams(ss,:),E
u,Tnofiterrors(ss,:));
plot(Eu, ytemp
+deltatemp*1.366, 'r:', Eu, ytemp -
deltatemp*1.366, 'r:');
axis tight
xlabel('eV)--T fits w/1
Sigma'); ylabel('Ln Term');
legend(['F :
T(eV)=' ,num2str(TfiteV(ss),3),'\pm',num
2str(TfiteV1std(ss),3)],...
['NF:
T(eV)=' ,num2str(TnofiteV(ss),3),'\pm',n
um2str(TnofiteV1std(ss),2)]];

%%%%%%%%%%%%%%%%%%%%%%%%%%%%%%%%
% changed 02-03-10 to
accomdate new data for stark brodening

```

```

%Determine density, from
515.32 line for now (index 2)
%
half_width_for_scaling=0.041;
%
density_for_scaling=1e17;
%
density(ss)=a(ss,2).halfwidths(2)./half
_width_for_scaling.*density_for_scaling
;

half_widths_for_scaling=[0.43/2/10
1.90/2/10 2.20/2/10]; %the first dat
apoint I assume should have been 1.43
instad of 0.43...have to check?
density_for_scaling=1e17;
for kk=1:3

all_den(ss, kk)=[a(ss, kk).halfwidths(2)]
./half_widths_for_scaling(kk).*density_
for_scaling;
end;

density(ss)=mean(all_den(ss,:));

density_err(ss)=std(all_den(ss,:));

%Summary of density
graph%%%%%%%%%%%%%%%%%%%%%%%%%%%%%%%% (new section 2-3-10)
subplot(3,2,6)

plot(mainpeaks(1:3),all_den(ss,),'bs')
;
hline(density(ss));

hline((density(ss)+density_err(ss)));
hline((density(ss)-
density_err(ss)));
axis tight
xlabel('Cu Line (nm)');
ylabel('Density(1/cc)');
title(['Density(1e17/cc):
',num2str(density(ss)/1e17,3),'\pm',num
2str(density_err(ss)/1e17,3)]);

%%%%%%%%%%%%%%%%%%%%%%%%%%%%%%%%
%%%%%%%%%%%%%%%%%%%%%%%%%%%%%%%%
ss=ss+1;
if savedata==1

figtitle=[d(jj).name(1:end-
4),'_',shotid,'_',datestr(now,'mmdyy_H
HMMSS')];

set(gcf,'PaperPositionMode','auto')

saveas(gcf,figtitle,'fig');
print('-dpng','-
r300',figtitle);
end;
end;
end;
end;

```

```

end;

%T summary plots
figure; subplot(2,1,1);
% size(analysis_shot_ind)
% size(TfiteV)
% size(TfiteVlstd)
errorbar(analysis_shot_ind,TfiteV,TfiteVlstd,TfiteVlstd,'bs','Markersize',6,'Linewidth',1.5);
hold on;
errorbar(analysis_shot_ind,TnofiteV,TnofiteVlstd,TnofiteVlstd,'rx','Markersize',6,'Linewidth',1.5);
xlim([analysis_shot_ind(1)-1 analysis_shot_ind(end)+1]);
ylabel('T (eV)');
legend('T-F','T-NF');
subplot(2,1,2);
errorbar(analysis_shot_ind,density,density_err,density_err,'bs','Markersize',6,'Linewidth',1.5);
xlabel(['asc file index--',shotid,'-: ',datestr(now,'mmddy_HHMMSS')], 'interpreter','none');
legend('D-515.32');
ylabel('n(1/cc)');
xlim([analysis_shot_ind(1)-1 analysis_shot_ind(end)+1]);
if savedata==1
    figtitle=['T-Den_Sum_',shotid,'_',datestr(now,'mmddy_HHMMSS')];
    set(gcf,'PaperPositionMode','auto')
    saveas(gcf,figtitle,'fig');
    print('-dpng','-r300',figtitle);
end;

```

```

%clear temp variables
clear h jj kk ytemp deltatemp scnsz
spec thold ss
%now read back out.
varnamelist=who;
for ii=1:length(varnamelist)
    if strcmp(varnamelist{ii},'a') |
    strcmp(varnamelist{ii},'d') |
    strcmp(varnamelist{ii},'in')
        else
eval(['o.',varnamelist{ii},'=',varnamelist{ii},';']);
        end;
end;

```

### Auto-fit function

```

function
a=auto_fit(x,s,roi,thold,smoothopt,blots,man_int_lim,varargin)
%This function automatically find peaks with an roi for input wavelength x and %spectra s, using threshold thold

```

```

%To indicate peaks manually, input them into varargin by array
%
%Inputs:
%x: wavelength index
%s: spectra/intensity data for x
%roi: [x1 x2]: region of interest in x
%thold: intensity threshold for peak finding routine
%smoothopt: 'yx' to smooth data for peak finding routine--x is number of %points to use of smooth; 'n' for no smoothing
%blopts: ==1 for line baseline; ==2 for parabolic
%man_int_lim: data integration limits--used to compare integrated %intensities of the data itself with integrated intensities using the %fitted Loreztian.--typically [lim1 lim2] nm with lim1=lim2=1 which gives %+1/-1 nm from peak(if roi allows it--otherwise goes up to roi limit)
%varargin: varargin(1)==[peak wavelengths for peaking] use for manual %indication of peaks, instead of using automatic peak finding routine.
%
%Output:
%a: structure that includes all variables in function, plus a nice summary plot
%
%
%Non-standard Sub_functions required: (does not require any extra toolboxes): %calls peakfinder and lorentz_for_fmin (included)
%calls fminsearchbnd
%calls hline and vline for plots

%V. Tang, V1, 12-25/31-09

Ver=1; %version number
plotsyms='.ox+*sdv^<>ph'; %setup plot symbols and colors
plotcolors='bgrcmyk';

disp(' ');
disp(datestr(now));
disp('-----auto_fit-----');

if nargin==7 | isempty(varargin{1})
    disp('auto_fit: Using automatic peak finding and fitting');
    autopeaks=1;
else
    disp('auto_fit: Fitting to inputed peaks:');
    disp(varargin{1});
    autopeaks=0;
end;

```

```

roiind=find(x>roi(1) & x<roi(2));

sroi=s(roiind);
xroi=x(roiind);
if autopeaks==1
    if smoothopt(1)=='y' %smooths out
spectra here for peak founder so we
don't get too many non-peaks--later
fits using these peaks are not smoothed

peaksfoundind=peakfinder(smooth(sroi,st
r2num(smoothopt(2))),thold);
    elseif smoothopt(1)=='n'; %does no
smoothing as requested

peaksfoundind=peakfinder(sroi,thold);
end;
elseif autopeaks==0
    peaksfoundind=interp1(xroi,
1:length(xroi), [varargin{1}],
'nearest', 'extrap'); %find nearest
indexes to manual peaks
end;
peaksfoundx=xroi(peaksfoundind);
%returns wavelengths for peaks found
using peakfinder in roi region
peaksfoundintensity=sroi(peaksfoundind)
; %found peak intensity for peaks found
using peakfinder in roi region

numpeaks=length(peaksfoundx); %number
of peaks found
disp(['auto_fit: # of peaks
found/inputed: ',num2str(numpeaks)]);
disp(['auto_fit: Peaks found/inputed in
roi: ',num2str(roi),'', with threshold:
',num2str(thold)]);

disp([peaksfoundx
peaksfoundintensity]);
%fitting parameter guess for fit
routines
%setup as
%I1
%I2
%I3
%x01
%x02
%x03, etc.
%gamma
%last 2 are for baseline if line
%last 3 are for baseline if parabolic
if blopts==1
    params_guess=[peaksfoundintensity-
mean(sroi); peaksfoundx;
zeros(numpeaks,1)+.1; 0; 0;];
    pg_LB=[zeros(numpeaks,1);
peaksfoundx-1; zeros(numpeaks,1); -inf;
-inf];
    pg_UB=[ones(numpeaks,1)*inf;
peaksfoundx+1; ones(numpeaks,1)*inf;
inf; inf];

```

```

elseif blopts==2
    params_guess=[peaksfoundintensity-
mean(sroi); peaksfoundx;
zeros(numpeaks,1)+.1; 0; 0;];
    pg_LB=[zeros(numpeaks,1);
peaksfoundx-1; zeros(numpeaks,1); -inf;
-inf; -inf];
    pg_UB=[ones(numpeaks,1)*inf;
peaksfoundx+1; ones(numpeaks,1)*inf;
inf; inf; inf];
end;

%call fitting routine
% options.MaxFunEvals=20000; %maximumn
function evaluations
% options.MaxIter=20000; %maximumn
iterations
%[fitparams,fval,exitflag,output]=fmins
earch(@lorentz_for_fmin,params_guess,op
tions,xroi,sroi,numpeaks,1,blopts);
%determines best fitting parameters
[fitparams,fval,exitflag,output]=fminse
archbnd(@lorentz_for_fmin,params_guess,
pg_LB,pg_UB,[],xroi,sroi,numpeaks,1,blo
pts);
disp('auto_fit: Fminsearchbnd fitting
details:');
disp(output);
fittedspecall=lorentz_for_fmin(fitparam
s,xroi,sroi,numpeaks,2,blopts);
%determines fitted spec for all peaks
combined

if blopts==1 %calc baseline

bl=(fitparams(numpeaks*3+1).*xroi+fitpa
rams(numpeaks*3+2));
elseif blopts==2

bl=(fitparams(numpeaks*3+1).*xroi.^2+fi
tparams(numpeaks*3+2).*xroi+fitparams(n
umpeaks*3+3));
end;

%now plot all fitted curves and also
determine integral of each fitted peak
%in roi

if length(varargin)>2 &
isfloat(varargin{3})
    fitfigurehandle=varargin{3};
    figure(fitfigurehandle);
else
    fitfigurehandle=figure;
end;

plot(x,s,'b-',xroi,fittedspecall,'r--
'); xlim(roi); ylim([0
max(sroi)*2]);hold on; %first plot data
+ combined fit
for ii=1:numpeaks
    if blopts==1

```

```

        tempparams=[fitparams(ii)
fitparams(ii+numpeaks)
fitparams(ii+numpeaks*2)
fitparams(numpeaks*3+1)
fitparams(numpeaks*3+2)];
        elseif blopts==2
            tempparams=[fitparams(ii)
fitparams(ii+numpeaks)
fitparams(ii+numpeaks*2)
fitparams(numpeaks*3+1)
fitparams(numpeaks*3+2)
fitparams(numpeaks*3+3)];
        end;

fittedspec(ii,:)=lorenz_for_fmin(tempparams,xroi,sroi,1,2,blopts); %now also
get spec for each fit

        %determines integral of each I;
first column is peak wavelength, 2nd
column is integrated intensity
        fittedIntI(ii,:)=[tempparams(2)
lorenz_for_fmin(tempparams,xroi,sroi,1
,3,blopts)]; %

        %now plot each one on same curve

plot(xroi,fittedspec(ii,:),[plotcolors(
rem(ii,length(plotcolors))+1)
plotsyms(rem(ii,length(plotsyms))+1)],'
markersize',3);
        %now figure out for integration of
data within specified bounds what
%integrated Idlambda is

man_int_ind=find(xroi>=(tempparams(2)-
man_int_lim(1)) &
xroi<=(tempparams(2)+man_int_lim(2)));

man_int_lim_calc(ii,:)=[xroi(man_int_in
d(1)) xroi(man_int_ind(end))];
        disp(['auto_fit: No-fit integration
limits for peak at
',num2str(tempparams(2),7),' nm:',...

num2str(xroi(man_int_ind(1)),7),' to
',num2str(xroi(man_int_ind(end)),7),'
nm'])
        dataIntI(ii,:)=[tempparams(2)
trapz(xroi(man_int_ind),sroi(man_int_in
d)-bl(man_int_ind))];

        %%%now find half-widths of fits:
%
halfint=(1/2).*max(fittedspec(ii,:)'-
bl);
% halfintx=abs(tempparams(2)-
interp1((fittedspec(ii,:)'-bl),xroi,
halfint));
        halfwidths(ii,:)=[tempparams(2)
tempparams(3)];

```

```

        disp(['auto_fit: fitted half-width
for peak at
',num2str(tempparams(2),7),' nm:',...
num2str(halfwidths(ii,2),4),'
nm']);
end;

%plot baseline
plot(xroi,bl,'r:');
plot(fittedIntI(:,1),fittedIntI(:,2),'k
s','markersize',8,'LineWidth',1.5);
%plotted integrated Idlambda
plot(dataIntI(:,1),dataIntI(:,2),'kx',
'markersize',8,'LineWidth',1.5);
%plotted integrated Idlambda
%rest of plot
legendtxt=[cellstr('Data');cellstr('Fit
-All')];
cellstr(num2str(peaksfoundx,4));cellstr
('BL');cellstr('\intId\lambda-
F');cellstr('\intId\lambda-NF');];
legend(legendtxt,'location','best');
plot(x,s,'b-'); %plot again to put main
curves on top

hold off;
ylabel('I','FontSize',12);
title(['Auto_fit:',datestr(now)],'inter
preter','none');
hline(thold,'k--');
vline(fittedIntI(:,1));
vline(halfwidths(:,2)+halfwidths(:,1));

%set (fitfigurehandle,'FontSize',12);
if length(varargin)>1 &
ischar(varargin{2})
        xlabel(['\lambda (nm) --
',char(varargin{2})]);
else
        xlabel('\lambda (nm)','FontSize',12);
end;

disp('auto_fit: Integrated Intensity
Summary:')
disp('--Lambda (nm) ---w/Fit---w/o Fit---
Fit-1/2wid')
disp([fittedIntI dataIntI(:,2)
halfwidths(:,2)]);

% dataIntI=sortrows(dataIntI,2); %sorts
according to integrated intensity
% fittedIntI=sortrows(fittedIntI,2);
%sorts according to integrated
intensity

%now dump all variables out to
structure
varnamelist=who;
for ii=1:length(varnamelist)

eval(['a.',varnamelist{ii},'=',varnamel
ist{ii},';']);
end;

```

```

function y=peakfinder(vdata,thold)
%function y=peakfinder(vdata,thold)
%John Liptac's peak finding routine
%Version 1.0 Locked 3-16-06
%
%Inputs:
%vdata=voltage data with peaks; peaks
have to be positive!
%thold=threshold voltlage
%
%output:
%Index of peaks above threshold
%
%Version 1.0

sat=find(vdata >=thold);          % subs
above thresh
curve=diff(sign(diff(vdata)));    %
look at curvature of peak, max=-2,
min=2
lmax=find(curve == -2)+1;        %
return the subs of local max
imax=intersect(sat, lmax);       % take
points with right curvature above
threshold
y=imax;

function
sse=lorentz_for_fmin(params,x,spectra,numLor,fitops,blopts)
%let you add up large number of
lorentzians for fitting
%x0=location
%I=height
%gamma=corresponds to width?
%actual output gives errors
%
%numLor=params(1); %number of
lorentzians to fit
%structured like:
%I1
%I2
%I3
%x01
%x02
%x03, etc.
%last one is baseline!
for ii=1:numLor

```

```

        I(ii)=params(ii); %get intensities
end;
%disp(I)
for ii=1:numLor
        x0(ii)=params(ii+numLor); %get x0's
end;
%disp(x0)
for ii=1:numLor
        gamma(ii)=params(ii+numLor*2); %get
gammas's
end;
%disp(gamma)
%now produce lorentzians for input x
y=0;
for ii=1:numLor
        y=I(ii).*gamma(ii).^2./((x-
x0(ii)).^2+gamma(ii).^2)+y;
end;

%now for baseline
%uses blopts to determine if parabolic
baseline is used or not.

if blopts==1 %line
        blx1=params(numLor*3+1);
        blinterp=params(numLor*3+2);
        bl=(blx1.*x+blinterp);
elseif blopts==2 %parabolic
        blx2=params(numLor*3+1);
        blx1=params(numLor*3+2);
        blinterp=params(numLor*3+3);
        bl=(blx2.*x.^2+blx1.*x+blinterp);
end;
y=y+bl;

if fitops==1
        Error_Vector=y-spectra;
        sse=sum(Error_Vector.^2);
%difference in error
elseif fitops==2 %return actual vector,
with baseline
        sse=y;
elseif fitops==3 %returns intergral,
without baseline
        sse=trapz(x,y-bl);
end;

```

## Appendix D. Summer Student Report on Numerical Approach to Hydro Modeling.

### **Modeling Arc Initiation of Pentaerythritol Tetranitrate: Strategies for Tool Development for High Gradient Hyperbolic Partial Differential Equations**

Han Wang, Vincent Tang, James F. McCarrick, and Christian Grant  
Lawrence Livermore National Laboratory

While much research has focused on shock-driven initiation of high explosives (HE) such as pentaerythritol tetranitrate (PETN), few studies have been conducted on prompt thermal initiation from mechanisms such as an electrical arc from electrostatic discharge (ESD). The Weapons Complex Integration (WCI) Arc Initiation Project seeks to understand the reaction mechanisms of arc-initiated HE utilizing computer simulation validated by experimental results. Overall, the simulation model accounts for multispecies convection, interspecies reactions, conduction, radiation cooling, and ohmic heating. MATLAB was chosen as the development tool for its balance of sophistication versus development effort. Optimization was implemented through extensive vectorization and explicit parallelization for multi-core architecture utilizing MATLAB's parallel processing capabilities. Chemical species convections were simulated with a two-dimensional Euler-equation solver based on the MUSCL-Hancock method, and source terms are resolved with the implicit trapezoidal method. This combination yields a second order accurate scheme in space and time. The development phase discovered sensitivity of second order schemes to high gradients, stiff source terms, and grid imprinting. High gradient source terms such as ohmic heating significantly alter the energy landscape in comparison to fluid convection and have to be resolved through a modified use of slope limiters in order to preserve the total variation diminishing (TVD) property of the scheme. In addition, the stiff ordinary differential equations of the chemical reaction rates force the use of multispecies reaction formulas in integral form. Anomalous grid effects, a result of enforcing the Courant–Friedrichs–Lewy (CFL) condition on Cartesian mesh, were also observed and analyzed in the course of code development. The decomposition of PETN into gas is modeled through a two-step consecutive chemical reaction utilizing Arrhenius reaction rates. Hydrodynamic simulations of the plasma used to drive the chemical reactions match experimental observations within error bars of observed data, demonstrating the utility of the developed hydrodynamic code to explore PETN reactions in the high temperature regime. Future work involving higher order solvers and multipath reaction formulas are required to resolve arc-initiation of PETN at high resolution.

## • I. INTRODUCTION

Arc initiation of pentaerythritol tetranitrate (PETN) is of paramount importance due to the subjectivity of PETN combustion to spark input energies of ten millijoules [1].

(general background here)

Section II gives the initial conditions and setup used in the simulation. Section III focuses on basic background in the Riemann problem and Euler equation. Section IV details treatment of the inhomogeneous source terms. Section V concentrates on the numerical methods utilized in this program for the homogeneous portion of the partial differential equations solved. Section VI presents numerical results for test cases and real world simulations and section VII entails conclusions.

## II. Simulation Geometry

In our attempt to study the effects of arc initiation on PETN, we layered PETN film on top of a  $CaF_2$  window. The PETN film was surrounded by a layer of isolating Kapton. Parts of the Kapton was layered with  $Cu$  as an electrode.

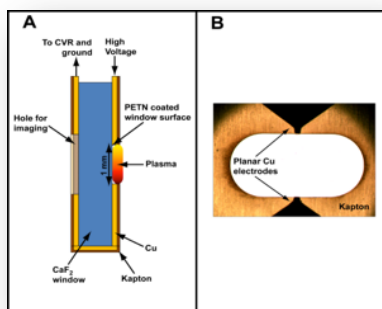


(Figure 1) A. Cutout view of experimental setup, B. View of experimental setup normal to the plane of the electrodes

For the simulation, we modeled the right side of the window in Figure 1A. We ran a two dimensional simulation with the  $y$  axis defined as normal to the plane of the window and the  $x$  axis defined as coplanar to the window and collinear to the electrodes.

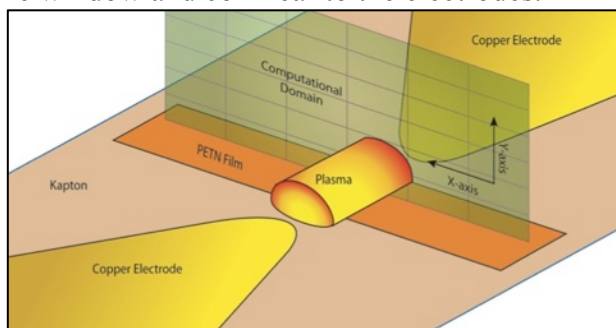


(Figure 2) Placement of the simulation regime in relation to the experimental setup

By our setup, the air and PETN plasma is an expanding half cylinder from the center of the computational domain in  $X$  and bottom of the computational domain in  $Y$ . We discretized the computational domain into  $m$  cells in  $x$  and  $n$  cells in  $y$ . We utilize a uniform grid and so for a computational domain of  $\Delta x_{net} \times \Delta y_{net}$ , each cell is  $\frac{\Delta x_{net}}{m} \times \frac{\Delta y_{net}}{n}$  in size with a net boundary



length of  $2 \frac{\Delta x_{net}}{m} + 2 \frac{\Delta y_{net}}{n}$ . For simplicity, we simplify our notation with  $\Delta x \equiv \frac{\Delta x_{net}}{m}$ , and  $\Delta y \equiv \frac{\Delta y_{net}}{n}$  for the rest of the paper.

In each cell, we track the local density,  $\rho$ , local momentum in  $x$ ,  $\rho u$ , local momentum in  $y$ ,  $\rho v$ , and the local energy density,  $E$ . We define

$$U \equiv \begin{bmatrix} \rho \\ \rho u \\ \rho v \\ E \end{bmatrix},$$

with  $U_{i,j}$  denoting all the tracked variables in cell  $i,j$  st.  $1 \leq i \leq m$ ,  $1 \leq j \leq n$ , and  $i,j \in Z$ . At the edges of the computational domain, we utilize a layer of ghost cells to simulate reflection and transmission at the boundaries. For a reflective ghost cell, such as those at the bottom of the  $y$  axis, we make its orthogonal velocity the negation of its mirror across the computational domain.

$$U_{R,y}^{ghost} = \begin{bmatrix} 1 & 0 & 0 & 0 \\ 0 & 1 & 0 & 0 \\ 0 & 0 & -1 & 0 \\ 0 & 0 & 0 & 1 \end{bmatrix} \times U_{i,j} \quad j \in \{1, n\}$$

For a reflecting cell in  $x$ , we negate the  $u$ , the  $x$  velocity

$$U_{R,x}^{ghost} = \begin{bmatrix} 1 & 0 & 0 & 0 \\ 0 & -1 & 0 & 0 \\ 0 & 0 & 1 & 0 \\ 0 & 0 & 0 & 1 \end{bmatrix} \times U_{i,j} \quad i \in \{1, m\}$$

If we wish to simulate transmission, we make the ghost cell exactly the same as its mirror in the computational domain.

$$U_{T,y}^{ghost} = U_{i,j} \quad j \in \{1, n\}$$

$$U_{T,x}^{ghost} = U_{i,j} \quad i \in \{1, m\}$$

The depth of the ghost cell layer is decided by the order of the numerical scheme. In our second order scheme, we utilize two layers of ghost cells and for the reflective cells at the bottom of the  $y$  axis (Figure 2), they are

$$U_{R,y}^{ghost 1} = \begin{bmatrix} 1 & 0 & 0 & 0 \\ 0 & 1 & 0 & 0 \\ 0 & 0 & -1 & 0 \\ 0 & 0 & 0 & 1 \end{bmatrix} \times U_{i,n}$$

$$U_{R,y}^{ghost 2} = \begin{bmatrix} 1 & 0 & 0 & 0 \\ 0 & 1 & 0 & 0 \\ 0 & 0 & -1 & 0 \\ 0 & 0 & 0 & 1 \end{bmatrix} \times U_{i,n-1}$$

st.  $ghost n$  designates the  $n^{th}$  ghost cell layer. For all ghost cells, transmissive or reflective, their values of  $T, p, \rho, E, a$  and  $\gamma$  are identical to their mirror counterparts.

### III. Background and Equations

The time-dependent Euler equations are a system of non-linear hyperbolic conservation laws which govern the behavior of compressible fluids such as gases. In standard literature, the two-dimensional Euler conservation laws are written in vector form as follows

$$U_t + F(U)_x + G(U)_y = 0, \quad (1)$$

$$U = \begin{bmatrix} \rho \\ \rho u \\ \rho v \\ E \end{bmatrix}, F = \begin{bmatrix} \rho u \\ \rho u^2 + p \\ \rho uv \\ u(E + p) \end{bmatrix}, G = \begin{bmatrix} \rho v \\ \rho uv \\ \rho v^2 + p \\ v(E + p) \end{bmatrix} \quad (2)$$

Here,  $\rho$  is the mass density,  $u$  is the velocity in the  $x$  direction,  $v$  is the velocity in the  $y$  direction,  $p$  is the pressure, and  $E$  is total energy per unit volume. Also,  $U_t$  means the partial derivative of  $U$  with respect to  $t$ .

With the addition of  $n$  equations, the densities of  $n$  chemical species can also be tracked. The modified Euler equations become

$$U_t + F(U)_x + G(U)_y = 0, \quad (3)$$

$$U = \begin{bmatrix} \rho \\ \rho u \\ \rho v \\ E \\ \rho_1 \\ \vdots \\ \rho_n \end{bmatrix}, F = \begin{bmatrix} \rho u \\ \rho u^2 + p \\ \rho uv \\ u(E + p) \\ \rho_1 u \\ \vdots \\ \rho_n u \end{bmatrix}, G = \begin{bmatrix} \rho v \\ \rho uv \\ \rho v^2 + p \\ v(E + p) \\ \rho_1 v \\ \vdots \\ \rho_n v \end{bmatrix} \quad (4)$$

with  $\rho_n$  being the density of chemical species  $n$ . We assume the specie densities to sum to the mass density

$$\sum_i \rho_i = \rho.$$

In the presence of mass, momentum, and energy sinks or sources, the homogenous Euler equations are modified with source terms on the right hand side to model effects other than fluid convection. For arc initiation, we add source terms of conduction, radiation cooling, ohmic heating and chemical reaction.

$$U_t + F(U)_x + G(U)_y = S(U) \quad (5)$$

$$S(U) = \begin{bmatrix} 0 \\ 0 \\ 0 \\ \frac{\partial E_{conduction}}{\partial t} + \frac{\partial E_{radiation}}{\partial t} + \frac{\partial E_{ohmic}}{\partial t} + \frac{\partial E_{chem}}{\partial t} \\ \frac{\partial \rho_1}{\partial t} \\ \vdots \\ \frac{\partial \rho_n}{\partial t} \end{bmatrix}, \quad (6)$$

Since formulas for each source term may vary depending on the physical systems modeled, they are omitted here. However, formulas used for each source term in the arc simulation are given in section IV, with its numerical treatment in section V. These source term differential equations are solved in conjunction with the convection partial differential equations to model the multi-physics evolution of the system through time.

To close the system of equations used for the simulation, an equation of state is needed. For a good balance between accuracy and computational efficiency, we chose the ideal gas equation of state with weighted  $\gamma$  and  $R_{specific}$ . Weighing of  $\gamma$  and  $R_{specific}$  are done on a particle basis

$$\gamma = \frac{\sum_{i=1}^n \frac{\rho_i}{M_i} \gamma_i}{\sum_{i=1}^n \frac{\rho_i}{M_i}}, \quad (7)$$

$$R_{specific} = \frac{\sum_{i=1}^n \rho_i R_i}{\rho}, \quad (8)$$

Where  $\gamma_i$ ,  $M_i$  and  $R_i$  are the ratio of specific heats, molar weight, and specific gas constant for specie  $i$ . More information on our specific EOS can be found in the appendix.

#### IV. Source Terms

Homogenous PDDE's describe only the most idealized physical systems and for most applications, source terms are required in the creation of useful models. For arc initiation of PETN, our choice of the guiding equations of conduction, radiation, and ohmic heating are

$$\frac{\partial E_{conduction}}{\partial t} = k \cdot \nabla^2 T, \quad (9)$$

st.  $k$  is the conduction coefficient,

$$\frac{\partial E_{radiation}}{\partial t} = \frac{8\pi^5 k_b^4}{15c^2 h^3} k_{gas} T^4, \quad (10)$$

st.  $c$  is the speed of light,  $h$  is Plank's constant,  $k_b$  is the Boltzmann constant, and  $k_{gas}$  a normalization factor which accounts for the opacity of the plasma

$$\frac{\partial E_{ohmic}}{\partial t} = \frac{j^2}{\sigma}, \quad (11)$$

st.  $j$  is the current density and sigma is the plasma conductivity.

Also presented in this section is  $\frac{\partial E_{chem}}{\partial t}$ , the energy change due to chemical reactions, and  $\frac{\partial \rho_i}{\partial t}$ , the change in specie density due to reactions. For brevity, the formulas of  $\frac{\partial E_{chem}}{\partial t}$  and  $\frac{\partial \rho_i}{\partial t}$  are omitted until their respective discussions.

These source equations guide the non-convection aspect of our computation domain. To utilize them in our numerical simulations, we need to adapt them to a discrete meshed domain. First, we define our computational domain of  $n$  by  $m$  cell ( $n$  in the  $x$ -direction,  $m$  in the  $y$ -direction).  $U_{i,j}$  designates the  $i^{th}$  cell in  $x$  and the  $j^{th}$  cell in  $y$  (Figure 2).

The discretization of the radiation source term is straightforward. We use  $k_{gas}$  as a normalization constraint used to factor in reabsorption of radiation. Reabsorption in the gas depends on the mean free photon path in the plasma which itself depends on the density of the plasma. Here, we chose  $k_{gas}$  is so that  $(k_{gas} \rho_0)^{-1} = 1 \text{ cm}$  as in [5]. Essentially,  $k_{gas}$  is chosen so that at normal atmosphere density,  $\rho_0$ , photons will travel a mean free path of 1cm. Since local cell density will fluctuate, we use the equation

$$\left( \frac{\partial E_{radiation}}{\partial t} \right)_{i,j} = \frac{8\pi^5 k_b^4}{15c^2 h^3} k_{gas} T_{i,j}^4 \cdot \rho_{i,j} \quad (12)$$

to calculate the power loss due to radiation effects in local cell,  $U_{i,j}$ .

For conduction, we require an estimate of the Laplacian of temperature in every cell. Since we have discrete points of temperature stored at known intervals, we utilize a numerical derivative approximation. We choose a second derivative stencil which is at least second order accurate to maintain the second order spatial accuracy of the entire simulation. A second order centered stencil is

$$\frac{\partial^2 T_{i,j}}{\partial x^2} = \frac{1}{\Delta x^2} (T_{i-1,j} - 2T_{i,j} + T_{i+1,j}) + O(\Delta x^2)$$

s.t.  $\Delta x$  is the L1 distance between cell centers in  $x$ . In  $y$ , the formula becomes

$$\frac{\partial^2 T_{i,j}}{\partial y^2} = \frac{1}{\Delta y^2} (T_{i,j-1} - 2T_{i,j} + T_{i,j+1}) + O(\Delta y^2) \quad (13).$$

Substituting both into the Laplacian and plugging back into (7) we obtain

$$\left(\frac{\partial E_{\text{conduction}}}{\partial t}\right)_{i,j} = k \cdot \left(\frac{1}{\Delta x^2} (T_{i-1,j} - 2T_{i,j} + T_{i+1,j}) + \frac{1}{\Delta y^2} (T_{i,j-1} - 2T_{i,j} + T_{i,j+1})\right) \quad (14).$$

For cell at the edge of the computational domain, we utilize the fact that the ghost cell's temperature is the same as their neighboring cell to reduce the second derivatives (Section II). For  $U_{1,1}$  the stencil becomes

$$\frac{\partial^2 T_{i,j}}{\partial x^2} = \frac{1}{\Delta x^2} (-T_{i,j} + T_{i+1,j}) + O(\Delta x^2) \quad (15)$$

$$\frac{\partial^2 T_{i,j}}{\partial y^2} = \frac{1}{\Delta y^2} (-T_{i,j} + T_{i,j+1}) + O(\Delta y^2) \quad (16).$$

This result can be easily generalized to other corner cells and boundary cells.

For ohmic heating, we assume the user has data of net current through plasma as a function of time. We note that (9) requires the conductance of the plasma. One method of approximating the conductance of air based on its ionization states is

$$\sigma(T, \rho) = \frac{4.173 \times 10^{-10} (A_1 + A_2) T^{-\frac{1}{2}}}{2 \times 10^{-15} (1 - A_1) + A_1 a} \quad (17),$$

$$A_1 = \frac{2}{1 + \sqrt{2B_1 + 1}},$$

$$A = \frac{2}{1 + 2B_2 + \sqrt{1 + 6B_2 + B_2^2}},$$

$$B_1 = \rho T^{-1.5} C_1 \exp\left(\frac{I_1}{2RT}\right),$$

$$B_2 = \rho T^{-1.5} C_2 \exp\left(\frac{I_2}{2RT}\right),$$

here,  $I_1$  and  $I_2$  are the first and second ionization energies of air. While the approximation of the conductance of air is borrowed from a more sophisticated EOS [5], we have hybridized it with our multispecies ideal gas EOS. We recognize the sub optimality of our hybrid approach but since the ionization EOS requires a root finding procedure in its temperature solution, computational tractability necessitates our hybrid approach. To find an approximation of the scalar field of  $\sigma$ , we compute  $\sigma_{i,j}$  for each cell. We now derive  $\frac{\partial E_{\text{ohmic}}}{\partial t}$  as a function of current,  $I$ , and  $\sigma$ . We start with

$$\frac{\partial E(x,y,t)}{\partial t} = \frac{J^2(x,y,t)}{\sigma(x,y,t)},$$

and utilize the identity  $J = \rho\theta$ , st.  $\theta$  is the electric field strength, for a substitution. We now have

$$\frac{\partial E(x,y,t)}{\partial t} = \sigma(x,y,t)\theta^2(t)$$

if we assume uniform Electrical field strength in space and by definition,  $\theta(t) = \frac{V(t)}{l} = \frac{I(t)R(t)}{l}$  st.  $l$  is the distance between the electrodes.

Substituting back into power, we recover

$$\frac{\partial E(x,y,t)}{\partial t} = \sigma(x,y,t) \frac{I^2(t)R^2(t)}{l^2} \quad (18).$$

$R(t)$  is the resistance of the entire plasma at time  $t$ . So to find  $R(t)$  we first assume each cell represents a connection from one electrode to the other with conductivity defined by  $\sigma_{i,j}$ . Each cell now represents a conducting column of plasma connecting the electrodes *in parallel*. We first find the resistance of each cell,

$$R_{i,j} = \rho \cdot \frac{l}{A} = \frac{l}{\sigma_{i,j} \Delta x \Delta y}$$

Since the columns of plasma are essentially resistors in parallel, the net resistance is

$$\frac{1}{R_{net}} = \sum_i \sum_j \frac{1}{R_{i,j}} = \sum_i \sum_j \frac{\sigma_{i,j} \Delta x \Delta y}{l}, \quad (19)$$

$$R = l \left( \sum_i \sum_j \frac{1}{\sigma_{i,j} \Delta x \Delta y} \right) \quad (20).$$

Substitute (20) into (18) and we recover the desired form of the ohmic heating equation [4]

$$\left( \frac{\partial E_{ohmic}}{\partial t} \right)_{i,j}^t = \frac{l^2(t)}{(\sum_i \sum_j \sigma(T_{i,j}^t, \rho_{i,j}^t) \Delta x \Delta y)^2} \sigma(T_{i,j}^t, \rho_{i,j}^t). \quad (21)$$

This equation defines ohmic heating of cell  $U_{i,j}$ .

For the chemistry equations, we started with the differential equations of a consecutive reaction  $[A] \rightarrow [B] \rightarrow [C]$ . This set of reaction equations is based on the simplified assumption of PETN undergoing complete ionization before recombining to form products.

$$\begin{aligned} \frac{d[A]}{dt} &= -k_1[A]_0, \\ \frac{d[B]}{dt} &= k_1[A]_0 - k_2[B]_0, \\ \frac{d[C]}{dt} &= k_2[C]_0. \end{aligned}$$

The discussion about the choice for an Arrhenius model of the rate constant,  $k$ , will be detailed in section IV and will not be repeated here. Now, we propose the solution of the above differential equations in integral form after a time  $t$  has elapsed. They are

$$[A] = [A]_0 e^{-k_1 t}, \quad (22)$$

$$[B] = [A]_0 \frac{k_1}{k_2 - k_1} (e^{-k_1 t} - e^{-k_2 t}) + [B]_0 e^{-k_2 t}, \quad (23)$$

$$[C] = [A]_0 \left( 1 + \frac{k_1 e^{-k_2 t} - k_2 e^{-k_1 t}}{k_2 - k_1} \right) + [B]_0 (1 - e^{-k_2 t}) + [C]_0. \quad (24)$$

Inputting the initial chemical concentrations at the start of the source time step, we chose  $t = \frac{\Delta t}{2}$  (the choice of  $\frac{\Delta t}{2}$  is due to source splitting) and recover a closed form solution of the chemical system at the end of each source step. We define  $[A]_{\frac{\Delta t}{2}}$ ,  $[B]_{\frac{\Delta t}{2}}$ , and  $[C]_{\frac{\Delta t}{2}}$  to designate the chemical concentrations at the end of the source time step. We also define the heat of formation as  $Q_A$ ,  $Q_B$ , and  $Q_C$  for chemical specie  $A$ ,  $B$ , and  $C$ , respectively. Then the integral average of  $\frac{\partial E_{chem}}{\partial t}$ ,

$\frac{\partial \rho_1}{\partial t}$ ,  $\frac{\partial \rho_2}{\partial t}$ , and  $\frac{\partial \rho_3}{\partial t}$  during the source time step becomes

$$\left( \overline{\frac{\partial E_{chem}}{\partial t}} \right)_{i,j}^0 = \frac{2}{\Delta t} \left[ Q_A \left( [A]_{i,j}^{\frac{\Delta t}{2}} - [A]_{i,j}^0 \right) - Q_B \left( [B]_{i,j}^{\frac{\Delta t}{2}} - [B]_{i,j}^0 \right) - Q_C \left( [C]_{i,j}^{\frac{\Delta t}{2}} - [C]_{i,j}^0 \right) \right], \quad (25)$$

$$\left( \overline{\frac{\partial \rho_1}{\partial t}} \right)_{i,j}^0 = \frac{2}{\Delta t} \left( [A]_{i,j}^{\frac{\Delta t}{2}} - [A]_{i,j}^0 \right), \quad (26)$$

$$\left( \overline{\frac{\partial \rho_2}{\partial t}} \right)_{i,j}^0 = \frac{2}{\Delta t} \left( [B]_{i,j}^{\frac{\Delta t}{2}} - [B]_{i,j}^0 \right), \quad (27)$$

$$\left( \overline{\frac{\partial \rho_3}{\partial t}} \right)_{i,j}^0 = \frac{2}{\Delta t} \left( [C]_{i,j}^{\frac{\Delta t}{2}} - [C]_{i,j}^0 \right). \quad (28)$$

Now that we have discrete derivative formulas for each source term, we can combine them into a time stepping scheme that goes from the initial condition to  $\frac{\Delta t}{2}$ . We reformulate the implicit trapezoidal method with chemical source terms as

$$E_{i,j}^0 + \frac{\Delta t}{2} \left( \frac{1}{2} \left[ \left( \frac{\partial E_{ohmic}}{\partial t} \right)_{i,j}^0 + \left( \frac{\partial E_{conduction}}{\partial t} \right)_{i,j}^0 + \left( \frac{\partial E_{radiation}}{\partial t} \right)_{i,j}^0 + \left( \frac{\partial E_{ohmic}}{\partial t} \right)_{i,j}^{\frac{\Delta t}{2}} + \left( \frac{\partial E_{conduction}}{\partial t} \right)_{i,j}^{\frac{\Delta t}{2}} + \left( \frac{\partial E_{radiation}}{\partial t} \right)_{i,j}^{\frac{\Delta t}{2}} \right] + \left( \frac{\partial E_{chem}}{\partial t} \right)_{i,j}^0 \right), \quad (25)$$

$$\rho_{1,i,j}^{\frac{\Delta t}{2}} = \rho_{1,i,j}^0 + \frac{\Delta t}{2} \frac{\partial \rho_1}{\partial t} = [A]_{i,j}^{\frac{\Delta t}{2}}, \quad (29)$$

$$\rho_{2,i,j}^{\frac{\Delta t}{2}} = \rho_{2,i,j}^0 + \frac{\Delta t}{2} \frac{\partial \rho_2}{\partial t} = [B]_{i,j}^{\frac{\Delta t}{2}}, \quad (30)$$

$$\rho_{3,i,j}^{\frac{\Delta t}{2}} = \rho_{3,i,j}^0 + \frac{\Delta t}{2} \frac{\partial \rho_3}{\partial t} = [C]_{i,j}^{\frac{\Delta t}{2}}. \quad (31)$$

A flowchart for our algorithm detailing our implementation of the predictor-corrector method with explicit chemical terms is found in the appendix.

## V. Numerical Methods

In our simulations, we chose numerical schemes based on the finite volume method. Many published literature have shown the superior resolution of finite volume methods for problems involving high gradient shock wave [3]. The finite volume method divides up the computational regime into discrete computational cells. The cell averaged values of the conservative variables are stored in the geometrical center. The inter-cell interactions are then solved through computations of the Riemann problem.

A Riemann problem for the Euler equations is a set of initial conditions which satisfy the follow the requirements

$$U(x, 0) = \begin{cases} U_L & x < 0 \\ U_R & x > 0 \end{cases} \quad (32).$$

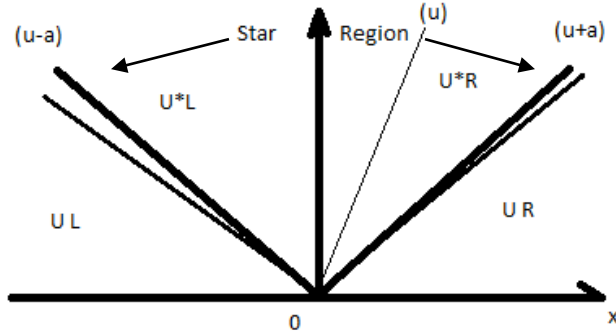


(Figure 3) General solution of the linearized Riemann problem

The Riemann problem yields wave fronts propagating from the inter-cell contact surface. Of the three waves, the outside waves with velocities  $(u - a)$ , and  $(u + a)$  are either rarefaction or shock waves; the center wave is always a contact wave. More information on Riemann wave fronts can be found in [3]. The solution of the Riemann problem also yields the value of the conservative variables in the interwave regions. Since the definition of a cell's conservative variables comes from the integral average through the cell, the wave speeds and interwave values given by the Riemann problem solution allows for an easy and intuitive way to advance the computational domain through time. After the Riemann solution, the wave fronts are advanced  $\Delta t$  in time and the cell average recalculated. Courant showed that as long as  $\Delta t$  is taken small

enough that the leading wave fronts of left and right cells do not interfere, each cell's progression in time can be calculated through its boundary interactions with its neighboring cells, this result is call the Courant–Friedrichs–Lewy condition [3].

$$\Delta t \leq \frac{\Delta x}{u_{max}} \quad (33)$$

Here  $u_{max}$  means the fastest possible wave speed resulting from the solution to the Riemann Problem. Once the solution of the intermediate regions  $U_{i+\frac{1}{2}}$  and  $U_{i-\frac{1}{2}}$  is known, the cell average can be advanced through time by the Godunov method

$$U_i^{n+1} = U_i^n + \frac{\Delta t}{\Delta x} \left[ F \left( U_{i-\frac{1}{2}}^n \right) - F \left( U_{i+\frac{1}{2}}^n \right) \right] \quad (34)$$

The significance of all Riemann solvers is that they incorporate upwind information into the approximation of the inter-cell region  $U_{i+\frac{1}{2}}$  which is more accurate than the simple numerical average of

$$U_{i+\frac{1}{2}} = \frac{1}{2} [U_i + U_{i+1}] \quad (35)$$

However, an exact solution has to be obtained iteratively making the solution very computationally costly. Thus for a solution to the Riemann problem, we forgo the exact Riemann solver for sake of computational efficiency as is typically done [3] and chose the Harten, Lax, van-Leer, and Contact (HLLC) solver. Out of the main Riemann solvers in literature, the Roe Riemann solver and the HLLC solver are the only ones which resolve the intermediate contact wave between cells. However, the HLLC solver is about 40% more computational efficient [6] and because we intend to deploy our code on a desktop computer, we chose the HLLC solver for the additional computational efficiency.

The intercell region for the HLLC solver is defined as

$$U_{i+\frac{1}{2}} = \begin{cases} U_L, & 0 \leq S_L \\ U_{*L}, & S_L \leq 0 \leq S_* \\ U_{*R}, & S_* \leq 0 \leq S_R \\ U_R, & S_R \leq 0 \end{cases} \quad (36)$$

$$U_{*K} = \begin{pmatrix} \rho \\ S_* \\ v_K \\ \left( \frac{S_K - u_K}{S_K - S_*} \right) \frac{E_K}{\rho_K} + (S_* - u_K) \left[ S_* + \frac{p_K}{\rho_K (S_K - u_K)} \right] \\ \rho_1 \\ \vdots \\ \rho_n \end{pmatrix} \quad (37)$$

with  $S_L$  and  $S_R$  being estimates for the wavespeeds of the rightmost and leftmost waves. Instead of utilizing a simple direct estimate for  $S_L$  and  $S_R$  [5], we estimated for the wavespeeds in our program through pressure. Let  $K \in \{L, R\}$  and our estimate for  $S_K$  becomes

$$S_K = u_K - a_K q_K, \quad (38)$$

Where

$$q_K = \begin{cases} 1 & p_* \leq p_K \\ \left[ 1 + \frac{\gamma+1}{2\gamma} \left( \frac{p_*}{p_K} - 1 \right) \right]^{\frac{1}{2}} & p_* > p_K \end{cases} \cdot \quad (39)$$

Notice, we now require an estimate for  $p_*$  (pressure estimate of the intermediate wave region), and we obtain this estimate through the Adaptive Noniterative Riemann Solver (ANRS). This is a primitive variable Riemann Solver which is even more computationally cheap than the HLLC. For brevity, details of the ANRS can be found in [3].

After obtaining  $S_L$  and  $S_R$ , we can now compute  $S_*$  which is used for the piecewise evaluations in (36).

$$S_* = \frac{p_R - p_L + \rho_L u_L (S_L - u_L) - \rho_R u_R (S_R - u_R)}{\rho_L (S_L - u_L) - \rho_R (S_R - u_R)}, \quad (40)$$

Finally, we now evaluate (36) with the calculated  $S_*$  for  $U_{i+\frac{1}{2}}$ . After  $U_{i+\frac{1}{2}}$  is found, we define the HLLC intercellular flux as,

$$F_{i+\frac{1}{2}} = F\left(U_{i+\frac{1}{2}}\right)$$

and return  $F_{i+\frac{1}{2}}$  back to the numerical scheme of choice. In two dimensions, the fluxes are solved via dimensional splitting. Two passes of the HLLC solver are made through the computational domain, the first pass solves for  $F_{i\pm\frac{1}{2},j}$  ( $x$  direction), while the second pass solves for  $F_{i,j\pm\frac{1}{2}}$  ( $y$  direction). When solving for  $U_*$  in the  $y$  direction, the formula changes to

$$U_{*K} = \left( \frac{S_K - v_K}{S_K - S_*} \right) \begin{bmatrix} \rho \\ v_K \\ S_* \\ \rho_1 \\ \vdots \\ \rho_n \end{bmatrix} + (S_* - v_K) \left[ S_* + \frac{p_K}{\rho_K (S_K - v_K)} \right]. \quad (41)$$

Many options exist for a second order total variation diminishing (TVD) scheme [3] and we chose the MUSCL-Hancock method [3]. As a member of the Monotone Upstream-Centered Scheme for Conservation Laws (MUSCL) class methods, MUSCL-Hancock relies on spatial reconstruction of the data inside each computational cell.

MUSCL-Hancock aims to supply more accurate initial conditions to the Riemann Problem. First, linear data reconstruction is done on the interfaces of each cell to find a left and right interface value, namely

$$U_i^L = U_i^n - \frac{1}{2} \Delta i, \quad U_i^R = U_i^n + \frac{1}{2} \Delta i, \quad (42)$$

$$\Delta i = \frac{U_{i+1}^n - U_{i-1}^n}{2}. \quad (43)$$

Then the interface values are evolved in time for  $\frac{1}{2} \Delta t$  according to

$$\bar{U}_i^L = U_i^L + \frac{\Delta t}{2\Delta x} F_{time}, \quad \bar{U}_i^R = U_i^R + \frac{\Delta t}{2\Delta x} F_{time}, \quad (44)$$

$$F_{time} = [F(U_i^L) - F(U_i^R)]. \quad (45)$$

Finally, the values  $\bar{U}_i^L$  and  $\bar{U}_i^R$  are reconstructed from  $U_{i-1}$  and  $U_i$  are used as initial conditions of a piece-wise constant Riemann Problem on the left

$$U(x, 0) = \begin{cases} \bar{U}_i^R, & x < 0 \\ \bar{U}_{i+1}^L, & x > 0 \end{cases}, \quad (46)$$

and the values  $\bar{U}_i^L$  and  $\bar{U}_i^R$  reconstructed from  $U_i$  and  $U_{i+1}$  are used as initial conditions of a piece-wise constant Riemann Problem on the right.



$$U(x, 0) = \begin{cases} \bar{U}_i^L, & x < 0 \\ \bar{U}_{i+1}^R, & x > 0 \end{cases} \quad (47)$$

The solutions obtained from the Riemann Problem is then used to update the cell average of  $U_i$  through

$$U_i^{n+1} = U_i^n + \frac{\Delta t}{\Delta x} \left[ F \left( U_{i-\frac{1}{2}} \right) - F \left( U_{i+\frac{1}{2}} \right) \right]. \quad (48)$$

The MUSCL-Hancock method is analogous to combining two integration rules, the trapezoidal rule in space and the midpoint rule in time. A detailed flowchart of the MUSCL-Hancock method is included in the appendix.

While the MUSCL-Hancock method allows a 2<sup>nd</sup> order accurate solution in space and time, it yields spurious oscillations in the neighborhood of high gradients. Literature advocates the use of limited slopes,  $\bar{\Delta}i$ , to smooth out gradient induced oscillations. Limited slopes are defined as

$$\bar{\Delta}i = \varphi(r) \cdot \Delta i \quad (49)$$

st.  $r \equiv \frac{U_{i+1}^n - U_i^n}{U_i^n - U_{i-1}^n}$ , and  $\varphi(r)$  is the limiter function.

One popular choice for a limiter function which we found to be robust and accurate is SUPERBEE [3]

$$\varphi_{superB}(r) = \begin{cases} 0, & r \leq 0 \\ 2r, & 0 \leq r \leq \frac{1}{2} \\ 1, & \frac{1}{2} \leq r \leq 1 \\ \min \left\{ r, \frac{2}{1+r}, 2 \right\}, & r \geq 1 \end{cases} \quad (50)$$

Nevertheless, even with limited slopes, we still encountered computational failures when high gradient source terms are coupled with the advection PDE's. In our system, the ohmic heating term could increase energy density in certain cells by more than 200% between convection time steps. We experimented with placing the limiter on  $\rho$ ,  $E$ ,  $p$ ,  $\rho u$ , and  $\rho v$  but no matter what variable, conservative or primitive, we chose for the limiter, all simulations would succumb to spurious oscillations.

Acting on the observation that simulation failures for different choices of variables occurred at different times, we reformulated  $r$  as  $r_{min}$ .

$$r_{min} = \min \begin{Bmatrix} r_\rho \\ r_{\rho u} \\ r_E \end{Bmatrix} \quad (51)$$

This simple reformation guarantees the data reconstruction only occurs in regions where *all* conservative variables are smooth. This protects the scheme from succumbing to source terms which make sharp changes to a single conservative variable. Empirically, the use of  $r_{min}$  has led to stability for energy source terms in our simulations.

Treatment of the right hand of (5) is done via source splitting. First, we define  $S^{(t)}$  as the solution operator for the right hand side of (5) and  $C^{(t)}$  as the solution operator for the left hand side of (5). Then source splitting defines the updated full time step as

$$U^{n+1} = S^{(\frac{\Delta t}{2})} \left[ C^{(\Delta t)} \left[ S^{(\frac{\Delta t}{2})}(U^n) \right] \right]. \quad (52)$$

Essentially, the solution to the ODE source problem for  $\frac{1}{2}$  the time step is taken as the initial condition of the convection problem for a full time step. Then the solution of the convection

problem is taken as the initial condition for the source problem for another  $\frac{1}{2}$  time step and the resulting solution taken as the solution for the entire scheme. For our purposes,  $C^{(\Delta t)}$  is the MUSCL-Hancock scheme for  $\Delta t$  and  $S^{(\Delta t)}$  is the implicit trapezoidal method for our chosen source terms (6). Due to our numerical treatment of the source terms (see section III),  $\Delta t$  is only restricted by the CFL condition.

We chose implicit trapezoidal method for most source term calculations because the implicit nature of the method allowed us to avoid making multiple EOS calls per cell, per time step. This is because all explicit methods rely on closed forms of derivatives with respect to time. However, all of our energy source terms (radiation, ohmic, conduction, and chemical reaction) are temperature dependent, forcing us to utilize the chain rule in conjunction with the EOS to obtain a 2<sup>nd</sup> order approximation. While normally the use of the chain rule on the ideal gas EOS does not result in huge overheads, it does in the case of noninvertible EOS's where  $\frac{\partial T}{\partial E}$  has to be approximated numerically with a stencil. This result in a minimum of three EOS calls per time step versus the implicit trapezoidal method's two. Also, implicit trapezoidal is unconditionally A-stable, a feature which any explicit method lacks.

For the chemistry source term, we did not implement the implicit trapezoidal rule. This is because the Arrhenius reaction rates,

$$k = Ae^{-\frac{E}{RT}}, \quad (53)$$

where  $k$  is reaction constant,  $A$  is collision frequency,  $E$  is activation energy and  $R$  is universal gas constant, are exponential with respect to temperature.

While the implicit trapezoidal method works fine for the chemical reactions in differential form, regions in the simulation with high temperatures predicted reaction rates consuming over 20 x the available PETN in the cell in a single time step. This would force the use of a time step about  $\frac{1}{20}$  the size of the required CFL limited time step. This is highly undesirable because it increases computation run time for little to no gain in resolution.

We instead resort to the integral form of the chemical reactions. However, the accuracy of the integral form of chemical reactions depends on the reaction rate supplied as the close formed expression results from the assumption of a constant reaction constant for the time step. In a  $\Delta t$  where the temperature can vary wildly, the integral form will not give a good approximation of the solution. Two solutions to alleviate this problem are take a smaller time step, or find a reaction rate which best represents the chemical system for the entire range of temperatures in the  $\Delta t$ . Since we have already decided that the first solution is computationally infeasible, we utilize solution two. We model the reaction rate,  $k$ , through the Arrhenius model and note that  $k$  is dependent only on temperature. The ideal temperature supplied to the Arrhenius model would be the integral average temperature of the time step,

$$T_{int} = \frac{1}{\Delta t} \int_0^{\Delta t} T(x) dx.$$

However this forces us to obtain the temperature at every intermediate point in the interval  $[0, \Delta t]$ . We instead settle for the 2<sup>nd</sup> order approximation of  $T_{int}$ . First we use the trapezoidal rule on the integral

$$T_{int} = \frac{1}{\Delta t} \left( (\Delta t - 0) \left( \frac{T(0)+T(\Delta t)}{2} \right) + O(\Delta t^2) \right).$$

Then we move the truncation error to the left hand side and simplify. The result,

$$\bar{T} \equiv \frac{T(0)+T(\Delta t)}{2} = T_{int} + O(\Delta t^2),$$

shows that the simple numerical average can be an acceptable approximation for temperature. Because our overall scheme is only 2<sup>nd</sup> order accurate, a finer approximation would only result in higher computation time and no gain of accuracy. Thus, we take the average temperature of the cell within the source time step, to supply a more accurate temperature for Arrhenius model.

$$\bar{T} = \frac{T_0 + T_{\Delta t}}{2} \quad (54)$$

The choice for  $T_0$  as the initial condition temperature is obvious but the choice of  $T_{\Delta t}$  lies open. Our method is to take the temperature computed by the corrector step from the other source terms. Notice this choice does not account for the energy released and/or absorbed by the chemical reaction in *this* time step until the *next* time step. Mathematically, the decoupling of chemical reaction energy until the next time step can be seen in (25). Nevertheless, this problem is much alleviated by the fact that we take two source steps per convection step. A detail treatment of the use of Arrhenius reaction rates is given in Section III, and a flowchart of our algorithmic implementation is given in the appendix.

## VI. Numerical Tests and Results

Our first test is chosen to document the stability of our numerical solver for a purely convection based problem. For the convection benchmark, we took a cylindrical explosion test problem from [3]. In this test, the initial condition is chosen such that a cylinder of high pressure and volume is placed at the center of the computational domain. Mathematically, the setup is

$$\rho = \begin{cases} .125 & r > .4 \\ 1 & r \leq .4 \end{cases},$$

$$p = \begin{cases} .1 & r > .4 \\ 1 & r \leq .4 \end{cases},$$

with  $r$  being the radial distance from the center of the computational domain. We evolved the system for .25 time units and the simulation predicted the following behavior

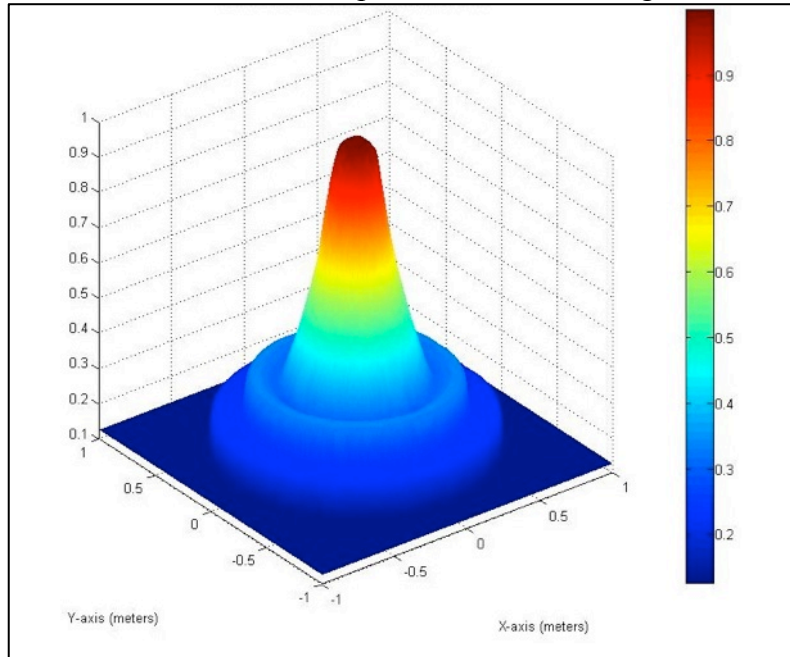


(Figure 4) Convection Test Case after .25 Time Units

We benchmarked the results with our one dimensional solver which is known stable and obtain the following lineout as a comparison.

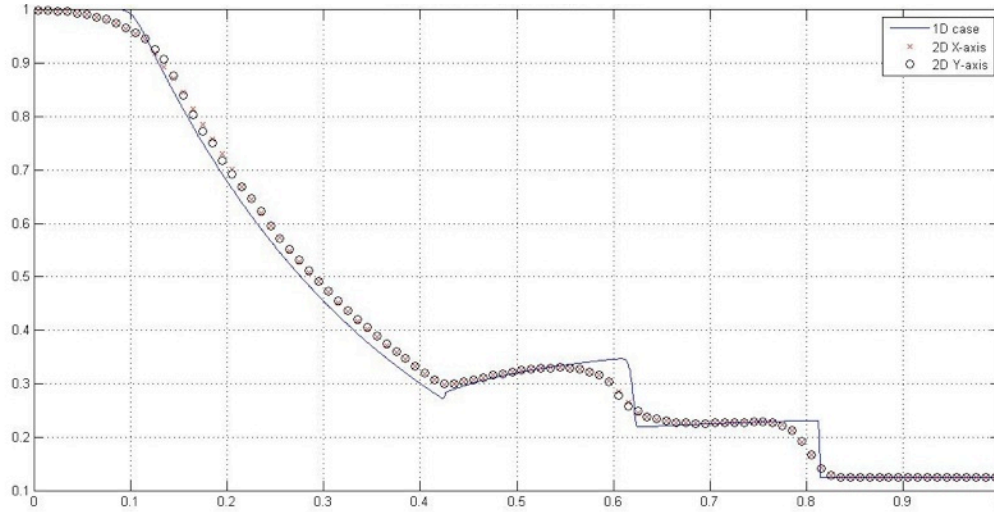


**(Figure 5) Comparison of 2D and 1D solver on convection test case**

The lineout shows good agreement between the two solvers. In an attempt to obtain an exact answer, the one dimensional case is run with 1500 cells. The two dimensional case is run on a mesh of 200x200 cells.

We then proceeded to simulate the setup shown in Figure 2. The initial conditions are

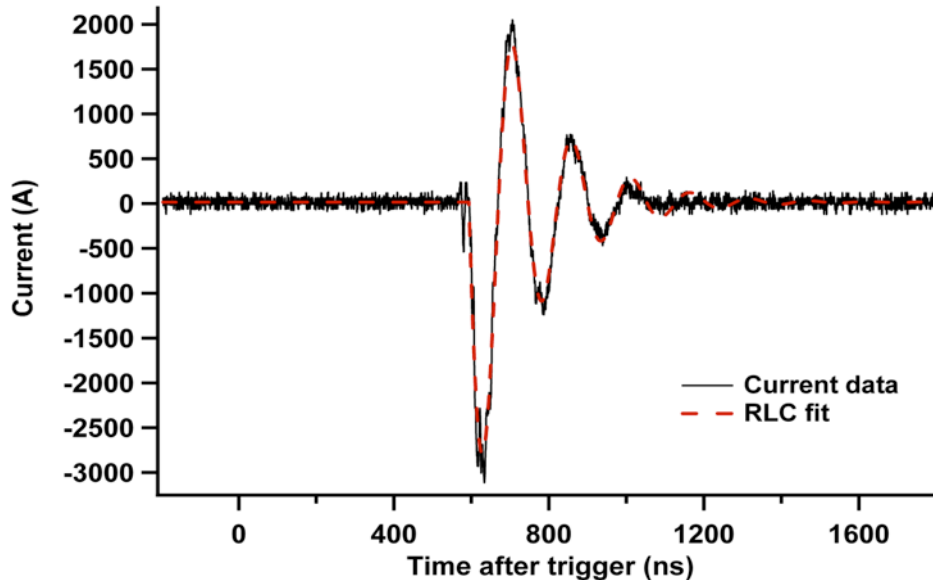
$$\rho_{i,j} = \begin{cases} 1.278 & \forall i, \forall j < n \\ 53.1 & \forall i, \forall j = n \end{cases}$$

$$u_{i,j} = 0 \quad \forall i, j$$

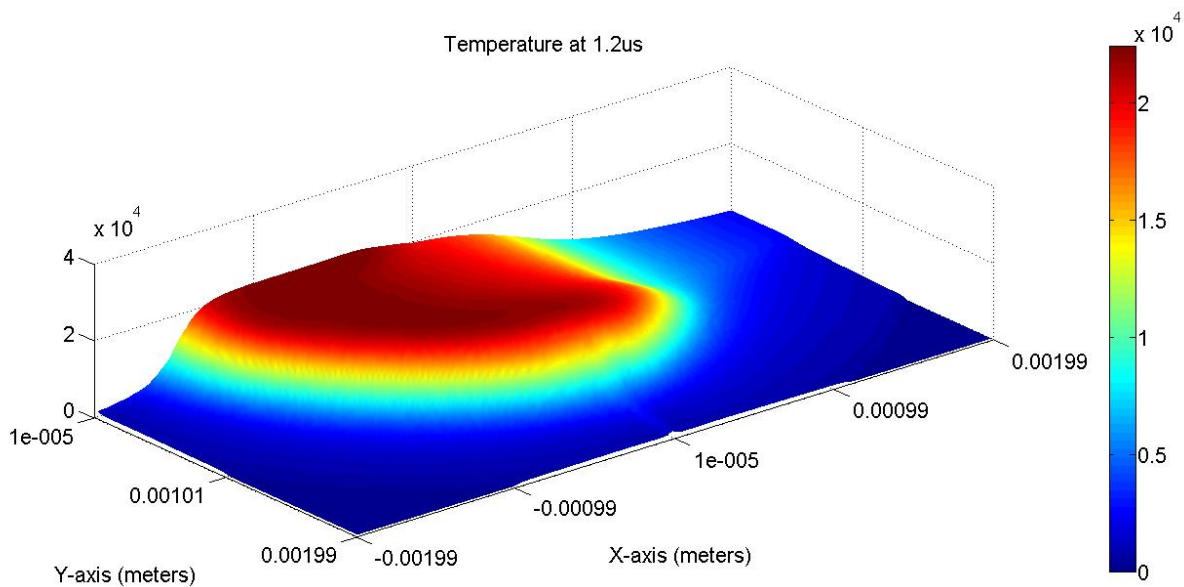
$$v_{i,j} = 0 \quad \forall i, j$$

$$E_{i,j} = (9.06 \times 10^6) \exp\left(-\frac{r_{i,j}^2}{8 \times 10^{-5}}\right) + (1.1 \times 10^5)$$

st.  $r_{i,j}$  is the distance from cell  $i, j$  to the center of the computational domain. The energy initial condition sets up a Gaussian temperature profile in the center of the computational domain and [5] suggested its use as a way to jump start the ohmic heating source term. Throughout the simulation run, ohmic heating was implemented with the following current profile.

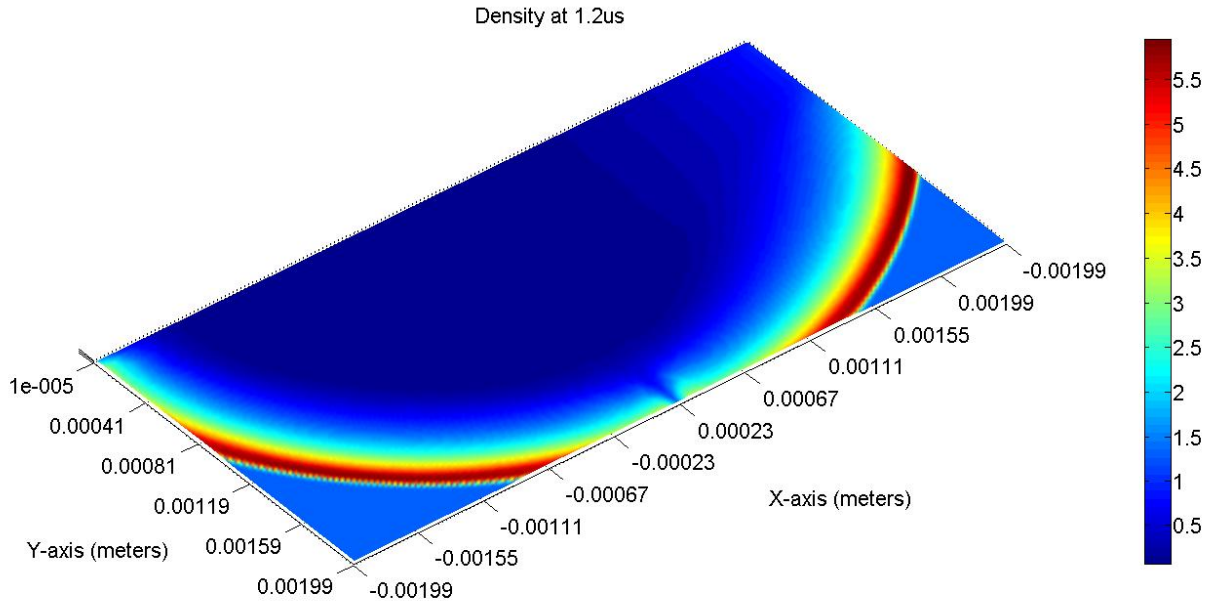


(Figure 6) Current Profile used in ohmic heating source term  
The results for temperature after 1.2 microseconds are shown below.



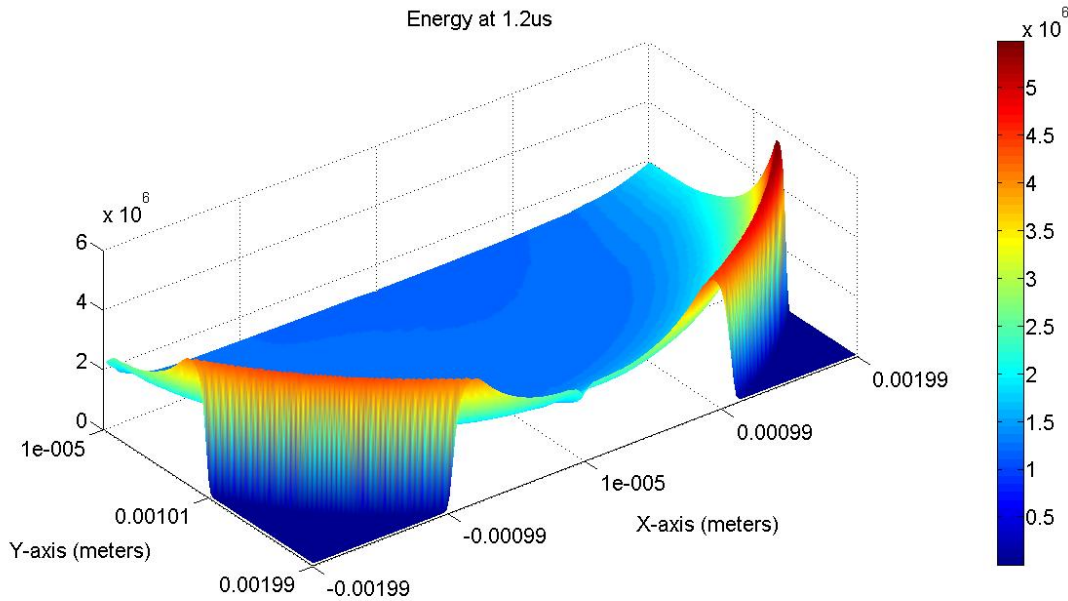
(Figure 5) Temperature Results

The asymmetry of the temperature is caused by the ohmic heating source term, which would allocate more the power to cells that were hotter than their neighbors, resulting in runaway heating of cells which obtained marginally higher temperatures than their neighbors through round off error. However, benchmarking against experimental data shows good agreement even with this numerical artifact.



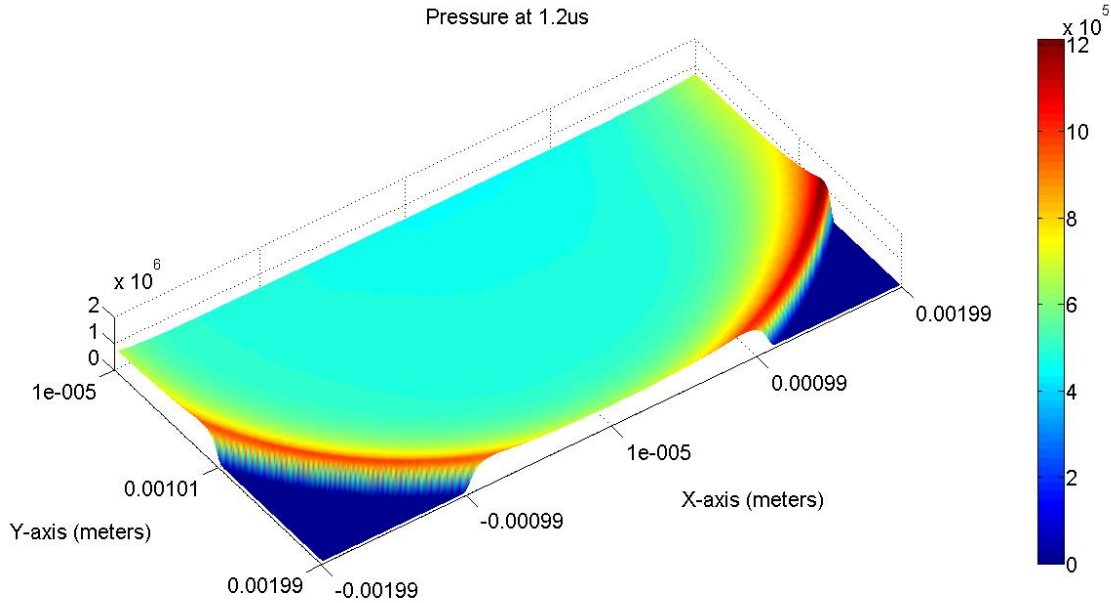
**(Figure 6) Density Results**

The asymmetry of density is the opposite of temperature because given similar energy densities; lower density will exhibit higher temperatures. Figure 6 also shows that the leading edge of the shock wave is much cooler than the center of the shock region.



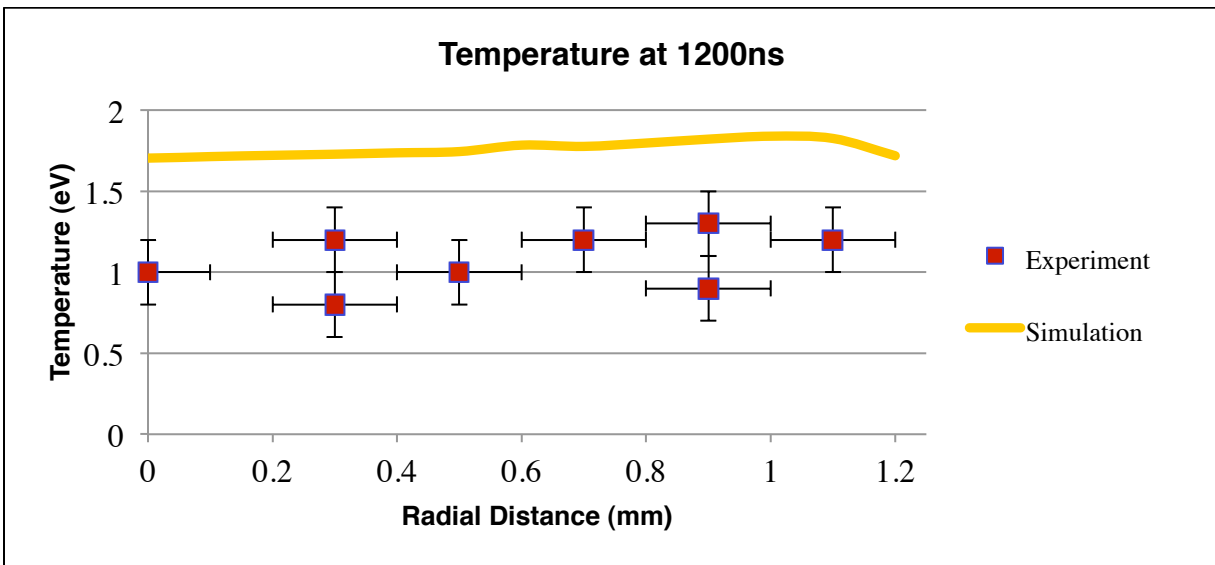
**(Figure 7) Energy Results**

Figure 7 explains the discrepancy between temperature radii and shock radii. While the center of the shock wave has densities roughly one order of magnitude less than the shock edge (Figure 6), their respective energy density is approximately one third as much. This discrepancy leads to particles in the shock center having three times more energy than their counterparts on the shock edge. As expected, the temperature difference in between shock center and edge is roughly a factor of three (Figure 5).



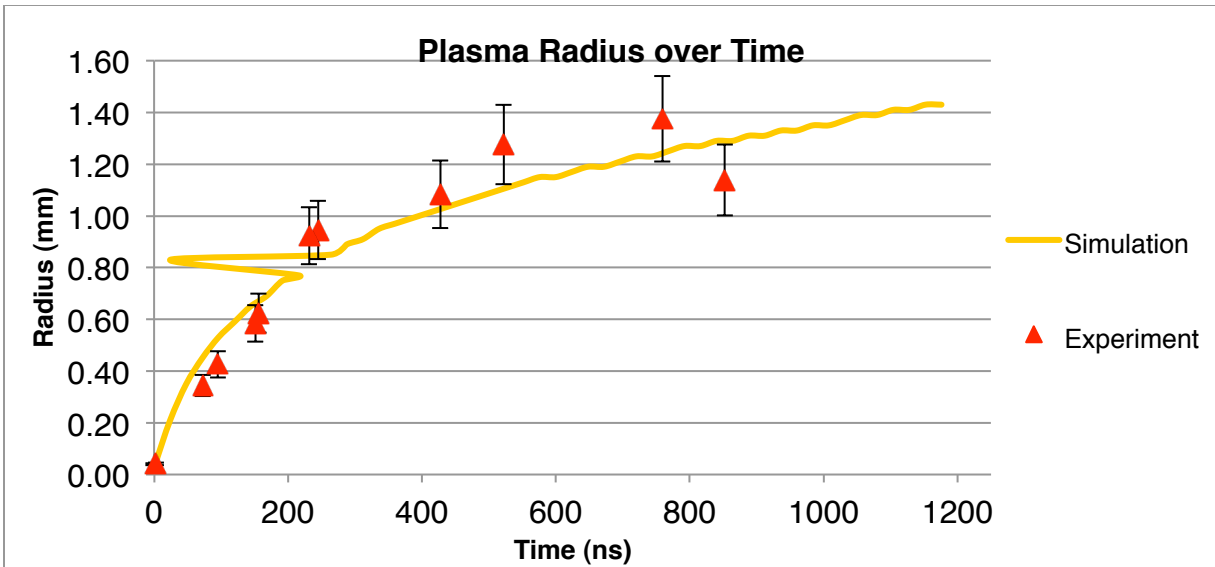
**(Figure 8) Pressure Results**

Figure 8 explains the asymmetry of the temperature and density terms. Since the Riemann problem is essentially pressure driven, two neighboring cells with similar pressures would experience little intercellular flux. As seen by Figure 8, runaway ohmic heating, which increased temperature and decreased density, had negligible effects on pressure. With neighboring cells in the shock center region at the same pressure, the excess energy of ohmic heating could not be dissipated through convection.



**(Figure 9) Simulation vs. Experimental Temperature Lineout**

Since there was asymmetry of temperature in the simulation along the x axis, the lineout for temperature was taken along the y axis. Because the simulation temperature is consistently 0.5 eVs higher than experimental, we believe the excess simulation temperature comes from an EOS issue. We hypothesize that an EOS which factors in the correct degrees of freedom for the fluid particles should reconcile the results.



(Figure 10) Simulation vs. Experimental Radii Lineout

Similar to the temperature lineout, the radius is taken along the y axis. The radius was captured in the experiment through a visible range camera, and in the simulation, it is defined as the cell farthest from the computation domain center with  $T \geq 5000K$ . The value of  $5000K$  is chosen as it represents an approximate temperature where light emission decreases significantly and as a mid-point of the steep outer temperature gradient of the simulation (Figure 6).

Initial conditions for the chemistry is 300nm of PETN in gas form along the bottom of the computational domain in Y, see Figure 2. The interspecies reactions follow (22-24). After  $1.2 \mu s$ , we obtained the resulting specie densities.



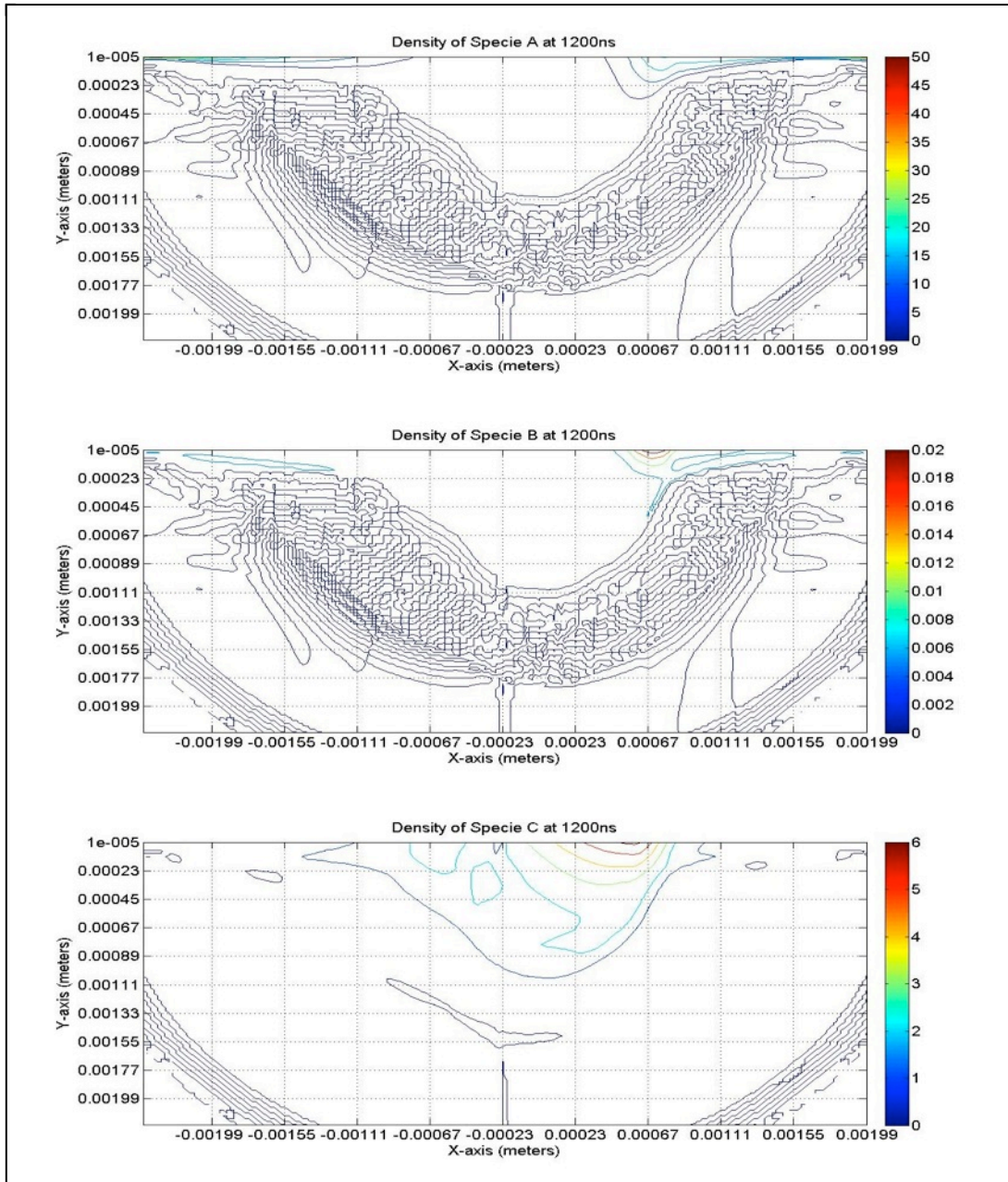


**(Figure 8) Contour plots of chemical species**

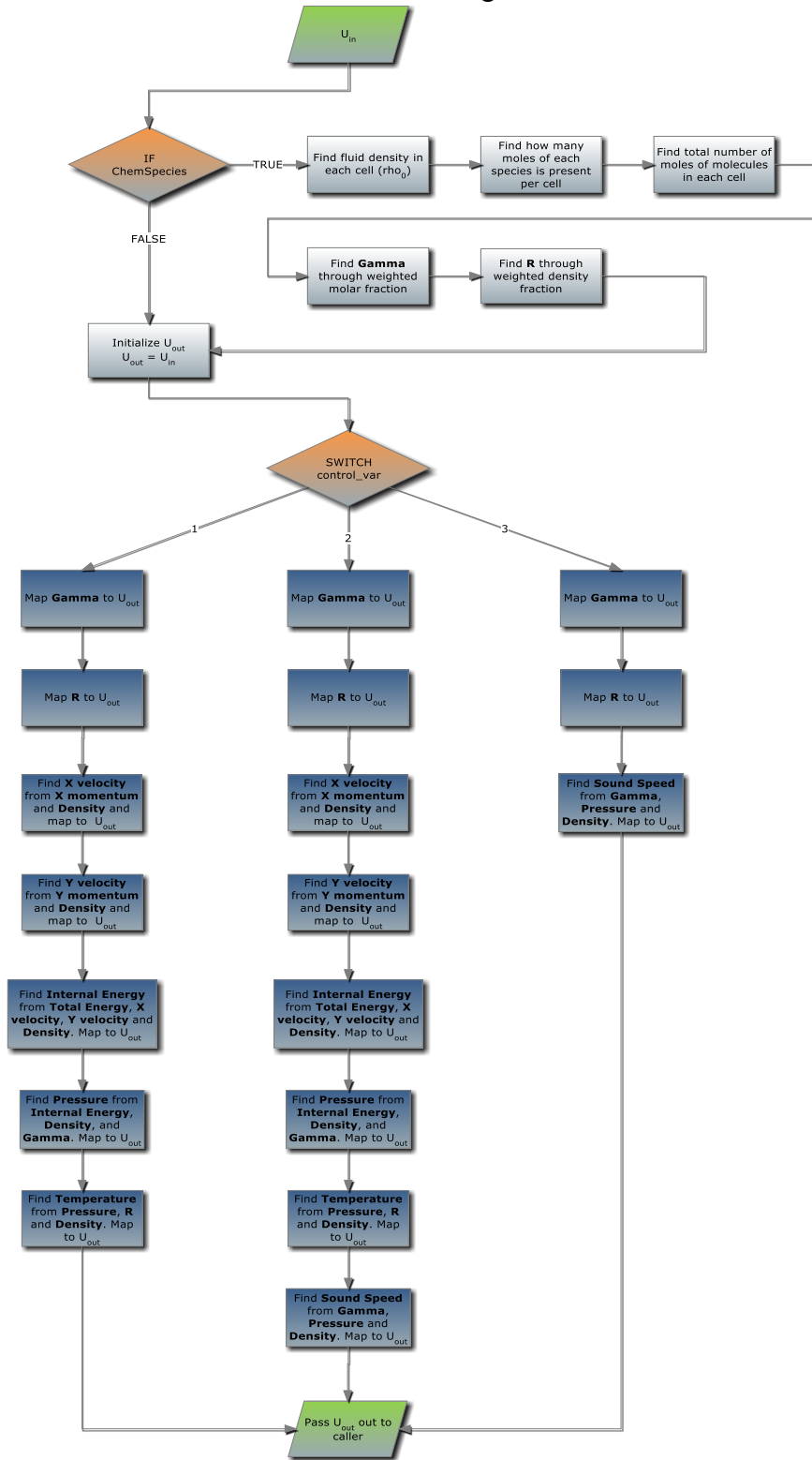
As expected, the individual chemical densities mirror the asymmetry of the net particle density. However, one surprising result of the chemical simulation is the minimal amount of convection of Specie C (PETN products) after their formation. This interesting result will be explored in future studies.

## VII. Conclusions

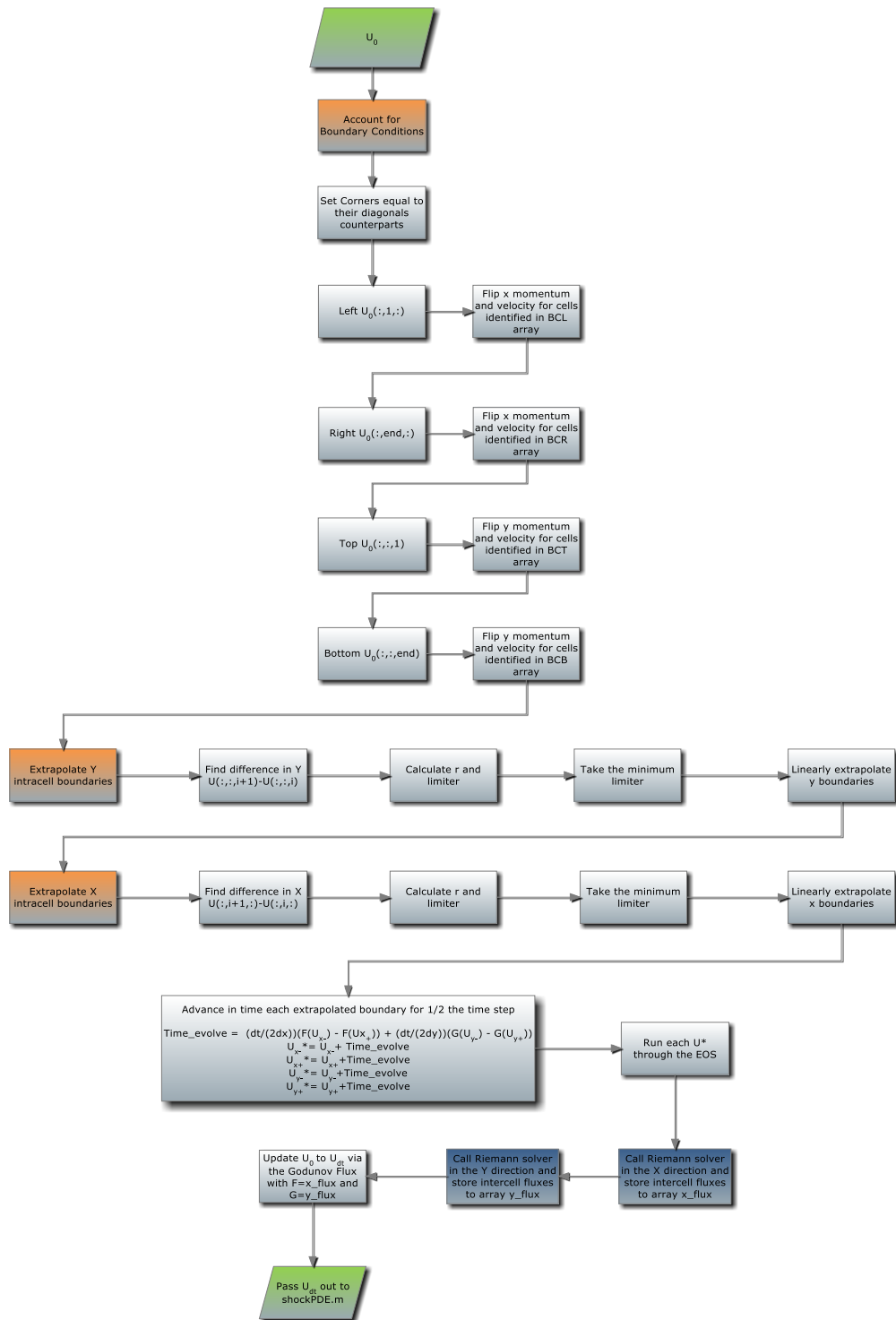
We have detailed methods for constructing a second order TVD scheme for convection equations with high gradient source terms. During development, we devoted much time to discretizing and stabilizing the first principle physics formula for the source terms. For the reader's convenience, we have a fully second order and stable scheme of the source terms including chemical reacting flows. Future work will encompass higher order solvers and even more complex multi-path reactions to simulate the entire system from first principle.



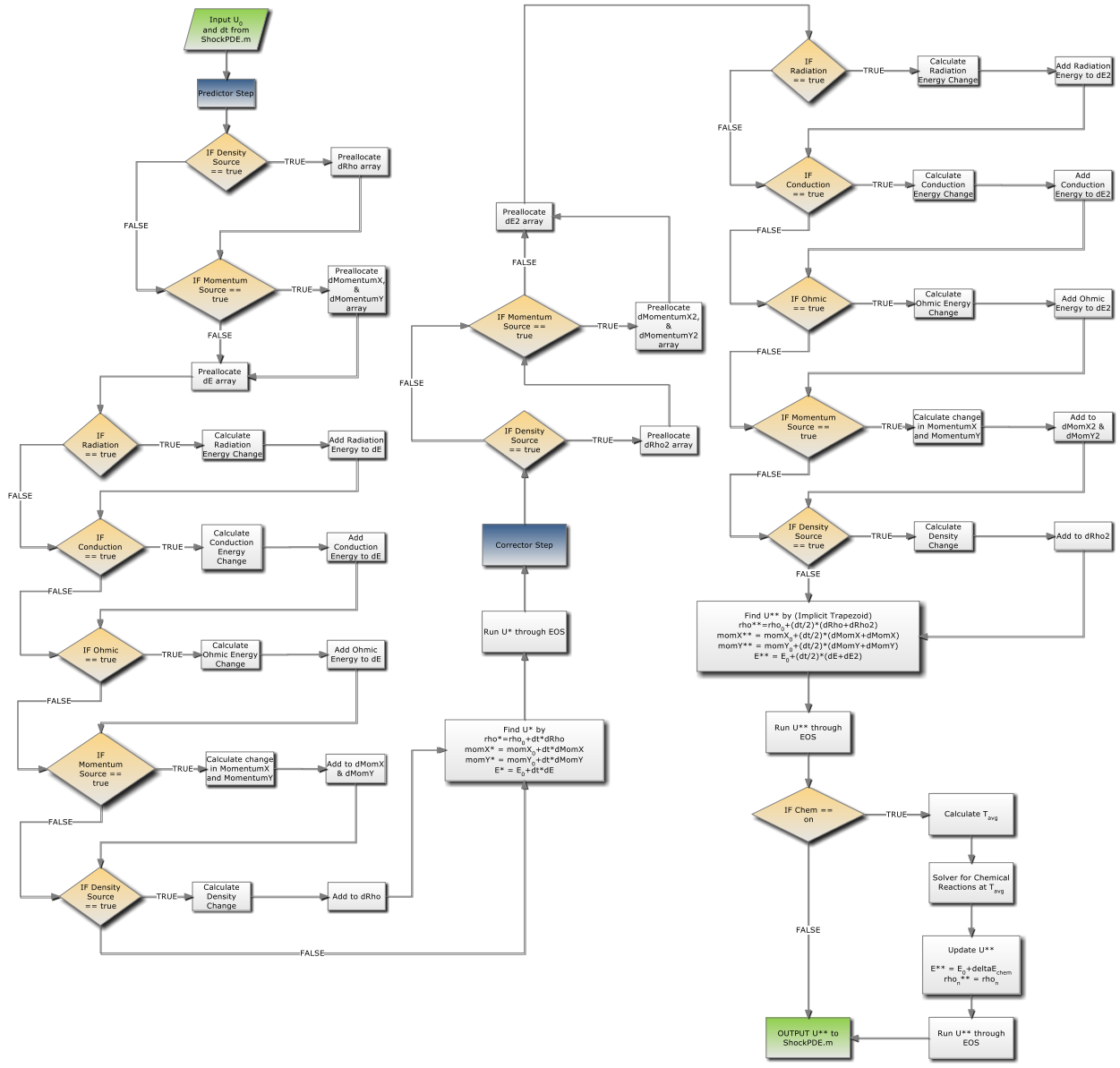
## VII. Appendix Flowchart for Ideal gas EOS



Flowchart for MUSCL-Hancock Scheme



Flow chart for Source term solver



The flowchart illustrates a numerical solver for shock PDEs, consisting of a Predictor Step and a Corrector Step. The Predictor Step begins with inputting initial conditions  $U_0$  and  $dt$  from the file ShockPDE.m. It then checks for various source terms: Density Source, Momentum Source, Radiation, Conduction, Ohmic, and Momentum Source. If any source term is active, it calculates the corresponding energy or momentum change and adds it to the differential equations. The Corrector Step follows, performing a similar set of checks and calculations. The final output is the updated state  $U^{**}$  written to ShockPDE.m.

**Find U\* by**  
 $\rho^* = \rho_0 + dt \cdot d\rho$   
 $momX^* = momX_0 + dt \cdot dMomX$   
 $momY^* = momY_0 + dt \cdot dMomY$   
 $E^* = E_0 + dt \cdot dE$

**Find U\*\* by (Implicit Trapezoid)**  
 $\rho^{**} = \rho_0 + (dt/2) \cdot (d\rho + d\rho2)$   
 $momX^{**} = momX_0 + (dt/2) \cdot (dMomX + dMomX2)$   
 $momY^{**} = momY_0 + (dt/2) \cdot (dMomY + dMomY2)$   
 $E^{**} = E_0 + (dt/2) \cdot (dE + dE2)$

**Update U\*\***  
 $E^{**} = E_0 + \delta E_{chem}$   
 $\rho_0^{**} = \rho_0$

## VII. References

- [1] Tucker, T. Kennedy, J., and Allensworth, D. "Secondary Explosive Spark Detonators"; *Proceedings of the 7<sup>th</sup> Symposium on Explosives and Pyrotechnics*, Philadelphia, PA, 1971.
- [2] Liou, W.; McCarrick, J.F., Hodgins, R., and Phillips, D. "High-Power Electrostatic Discharges in PETN: Threshold and Scaling Experiments", 2010, Coeur D'Alene, IA.
- [3] Toro E. L., *Riemann Solvers and Numerical Methods for Fluid Dynamics : A Practical Introduction*. 3rd. New York: Springer, 2009. 724. Print.
- [4] Akram, M. "Two-Dimensional Model for Spark Discharge Simulation in Air." AMERICAN INST OF AERONAUTICS AND ASTRONAUTICS. 34. (1996): 1835-1842. Print.
- [5] Plooster, Myron. "Numerical Simulation of Spark Discharges in Air." *Physics of Fluids*. 14.10 (1971): 2111-2124. Print.
- [6] Shengtai Li, An HLLC Riemann solver for magneto-hydrodynamics, *Journal of Computational Physics*, v.203 n.1, p.344-357, 10 February 2005

## Appendix E. MATLAB code for processing TRIR data

```
function Process_TRIR_v2
% Process_TRIR_v2
% by J. M. Zaug, LLNL
% Code to batch proces TRIR data at LLNL, B235 R1217B 3_19_2011
%
%This script will take a TRIR reference file (name must be = "ref.txt")
%(air + substrate - electronic background) and compute the optical
%absorption density (O.D.) of a time resolved single-shot IR spectrum. The
%ref.txt file must be in the same directory path as this IR_Process_TRIR_v2
%function. Each series of single shot data must be stored in folder named
%"shot#". Each shot folder must consist of three data files named, "Pre.txt",
%"Trans.txt", and "Post.txt".
%The user is asked to input a folder or range of folders to process. For
%example, enter "0:4" to process folders shot0 to shot4.
%
%Processed results are stored in each selected folder under the name
%"folder_array" -the format is [wavenumber; Pre_OD; Trans_OD; Post_OD]
%The user may upload "complete_array" text files for further analysis.
%In addition, a running total of previous and current folder(s) processed
%data is stored in each folder under the name "total_array". For example,
%if you decide to process shot0 to shot 100 folders, then all of the
%processed data can be found in the shot100 folder in "total_array". Thus,
%all processed results may be uploaded from "total_array" found in the last
%selected folder where the format is (N = shot#)
%[wavenumberN; PreN_OD; TransN_OD; PostN_OD; wavenumberN+1; . . .]
%
%This script will also plot the results of each folder where curves are
%coloured as such, blue=PreShot; red=Transient; green=PostShot. For
%clarity, each dataset is offset in the plot by an O.D. value of 1.00.
%

clear; close all
format long; warning off MATLAB:divideByZero
program_name='Process_TRIR_v2';
Dpath = which(eval(['program_name'])); %Finds the entire path to the current data
ncs=0; % # of characters to the right of the decimal pt.
    %including the decimal pt. (e.g., '.txt.10', ncs = 7)
%Assumes you're running from a directory containing reference spectra
shifter=1.00; %Amount to shift spectra on same plot (units = O.D.)
% cd 'C:\Documents and Settings\zaug1\Application Data\Desktop\IR projects\PETNtrir_2';
% Dpath='C:\Documents and Settings\zaug1\Application Data\Desktop\IR projects\PETNtrir_2';

%Enter in the pot. range of TDIR folders
tdirs={'shot0';'shot1';'shot2';'shot3';'shot4';'shot5';'shot6';'shot7';'shot8';'shot9';'shot10';
```

'shot11';'shot12';'shot13';'shot14';'shot15';'shot16';'shot17';'shot18';'shot19';'shot20';  
'shot21';'shot22';'shot23';'shot24';'shot25';'shot26';'shot27';'shot28';'shot29';'shot30';  
'shot31';'shot32';'shot33';'shot34';'shot35';'shot36';'shot37';'shot38';'shot39';'shot40';  
'shot41';'shot42';'shot43';'shot44';'shot45';'shot46';'shot47';'shot48';'shot49';'shot40';  
'shot51';'shot52';'shot53';'shot54';'shot55';'shot56';'shot57';'shot58';'shot59';'shot60';  
'shot61';'shot62';'shot63';'shot64';'shot65';'shot66';'shot67';'shot68';'shot69';'shot70';  
'shot71';'shot72';'shot73';'shot74';'shot75';'shot76';'shot77';'shot78';'shot79';'shot80';  
'shot81';'shot82';'shot83';'shot84';'shot85';'shot86';'shot87';'shot88';'shot89';'shot90';  
'shot91';'shot92';'shot93';'shot94';'shot95';'shot96';'shot97';'shot98';'shot99';'shot100';

'shot101';'shot102';'shot103';'shot104';'shot105';'shot106';'shot107';'shot108';'shot109';'shot110';  
'shot111';'shot112';'shot113';'shot114';'shot115';'shot116';'shot117';'shot118';'shot119';'shot120';  
'shot121';'shot122';'shot123';'shot124';'shot125';'shot126';'shot127';'shot128';'shot129';'shot130';  
'shot131';'shot132';'shot133';'shot134';'shot135';'shot136';'shot137';'shot138';'shot139';'shot140';  
'shot141';'shot142';'shot143';'shot144';'shot145';'shot146';'shot147';'shot148';'shot149';'shot150';  
'shot151';'shot152';'shot153';'shot154';'shot155';'shot156';'shot157';'shot158';'shot159';'shot160';  
'shot161';'shot162';'shot163';'shot164';'shot165';'shot166';'shot167';'shot168';'shot169';'shot170';  
'shot171';'shot172';'shot173';'shot174';'shot175';'shot176';'shot177';'shot178';'shot179';'shot180';  
'shot181';'shot182';'shot183';'shot184';'shot185';'shot186';'shot187';'shot188';'shot189';'shot190';  
'shot191';'shot192';'shot193';'shot194';'shot195';'shot196';'shot197';'shot198';'shot199';'shot200'};

```
%ltdirs=length(tdirs); % # of TRIR files
%nums=cell(ltdirs,1);
%for p=1:ltdirs  nums{p} = p; end
%ndirectories=[nums tdirs]; %show user all of the entered directories and their assigned #
%%%%%%%%%%
%%%%%%%%%%
ref = 'ref.txt'; % Common name for all TRIR reference data; length of file does not matter
ref_file = load(ref); reference_data=ref_file;
%%%%%%%%%%
%%%%%%%%%%
%Load up n-shots of Ref data and compute the average
[rowr,colr]=size(reference_data);
if colr >= 3
    data_avgr=zeros(rowr,1); %preload data array
    for pdr = 2:1:colr;
        data_pdr=reference_data(:,pdr);
```



```

        data_avgr=[data_avgr + data_pdr]; %add up the n-shots
    end
    REFDATAcol2 = data_avgr / colr; %average over n-shots
end
wavenumber=reference_data(:,1);
REF=REFDATAcol2;
disp(' ')
number=input('Enter Shot Folder(s) to Process " # or #,# or #:# etc. " ');
min_num = min(number)+1; % add one since MatLab vector lengths start at one, not zero!
max_num = max(number)+1;
%up to 3 possible color plots should be a sufficient range.
color=[ 'b' 'r' 'g'];
% color=[color color]; color=[color color]; color=[color color]; color=[color color]; color=[color
color]; color=[color color]; color=[color color]; color=[color color]; color=[color color];
color=[color color];
% color=[color color]; color=[color color]; color=[color color]; color=[color color]; color=[color
color]; color=[color color]; color=[color color]; color=[color color]; color=[color color];
color=[color color];

%Change to Data directory
%Dpath='C:\Documents and Settings\zaug1\Application Data\Desktop\IR projects\PETNtrir';
scrsz = get(0,'ScreenSize');
%(units in pixels) left bottom width height
figure('Position',[1 scrsz(4)/2 scrsz(3)/2 scrsz(4)/2]);
%
total_data=[]; icounter=0;
for j = min_num : 1 : max_num; % Start the process folder data loop
    icounter = icounter + 1; % Loop iteration counter;
    folder_data=[]; % Reset or clear the data array to be saved

    %load the input files;
    program_path = which(eval(['program_name']));lpn=length(program_name)+2;
    folders_path = program_path(1:length(program_path) - lpn);
    pln=j;
    newpath=[folders_path, '\ tdirs {pln}'];
    cd(newpath); %Change the path to the correct shot folder

    load Pre.txt -ASCII; %Ir pre shot data within specified data folder
    load Trans.txt -ASCII; %Ir transient shot data within specified data folder
    load Post.txt -ASCII; %Ir post shot data within specified data folder
    DATA_PRE=Pre; DATA_TRANS=Trans(:,2); DATA_POST=Post; % Fix the trans data to
just the 2nd column
    %Load up n-shots of sample data

[ row_pre,col_pre]=size(DATA_PRE);[row_trans,col_trans]=size(DATA_TRANS);[row_post,col
l_post]=size(DATA_POST);

```

```

% The next
if col_pre >= 3 % Start pre shot data averaging
    data_pre_avg=zeros(row_pre,1); %preload pre data array
    for pd = 2:1:col_pre;
        data_pre_pd=DATA_PRE(:,pd);
        data_pre_avg=[data_pre_avg + data_pre_pd]; %add up the n-shots
    end
    DATA_PRE = data_pre_avg / col_pre; %average over n-shots
end %End pre shot data averaging

if col_post >= 3 % Start post shot data averaging
    data_post_avg=zeros(row_post,1); %preload post data array
    for pd = 2:1:col_post;
        data_post_pd=DATA_POST(:,pd);
        data_post_avg=[data_post_avg + data_post_pd]; %add up the n-shots
    end
    DATA_POST = data_post_avg / col_post; %average over n-shots
end % %End post shot data averaging

% Process data
AB_pre = log10(REF./DATA_PRE);
AB_trans = log10(REF./DATA_TRANS);
AB_post = log10(REF./DATA_POST);

%Plot the results
%if icounter ==1 shifter = 0; end
plot(wavenumber, AB_pre + (shifter +(icounter-2)), 'b'); if icounter ==1 hold; grid; end
plot(wavenumber, AB_trans + (shifter +(icounter-2)), 'r');
plot(wavenumber, AB_post + (shifter +(icounter-2)), 'g');

%Abs = AB;
% _____
% Save routine
%cd(newpath);
folder_data=[folder_data wavenumber AB_pre AB_trans AB_post];
total_data = [total_data folder_data];
save ('folder_array', 'folder_data', '-ASCII')
save ('total_array', 'total_data', '-ASCII')
end % END the process folder data loop
ylabel('ABS O. D. '); xlabel('Wavenumber, cm^-1');
hold off

complete_array=[wavenumber total_data];
[cola, rowa] = size(complete_array);

%%OLD Code for v1 program...NOT USED/REQUIRED in V2 !!!

```

```

%% %% --- These next lines assume multiple data has been loaded e.g. pre trans post --- %% %%

%Here we perform rudimentary analysis and plots; then save all of the results
%           left bottom   width   height
%figure('Position',[600 scrsz(4)/2 scrsz(3)/1.84 scrsz(4)/1.1]);
blank_row=zeros(1,1);% make a row of zeros to demark ABS data (pre, trans, post) by
analysis result rows
if rowa == 4
    %           left bottom   width   height
    figure('Position',[600 scrsz(4)/2 scrsz(3)/1.84 scrsz(4)/1.1]);
    dABS_pre= complete_array(:,2) - complete_array(:,3);    % pre - trans
    subplot(2,2,1); plot(wavenumber, dABS_pre); ylabel('pre - trans'); xlabel('Wavenumber, cm^-
^1'); axis tight

    PreABS_ratio= complete_array(:,3)./complete_array(:,2); % trans / pre
    subplot(2,2,2); plot(wavenumber, PreABS_ratio);ylabel('trans / pre'); xlabel('Wavenumber,
cm^-^1');axis tight

    dABS= complete_array(:,2) - complete_array(:,4);    % pre - post
    subplot(2,2,3); plot(wavenumber, dABS); ylabel('pre - post'); xlabel('Wavenumber, cm^-
^1');axis tight

    PostABS_ratio= complete_array(:,4)./complete_array(:,2); % post / pre
    subplot(2,2,4); plot(wavenumber, PostABS_ratio); ylabel('post / pre'); xlabel('Wavenumber,
cm^-^1');axis tight

    data_diffs_ratios4 = [blank_row dABS_pre PreABS_ratio dABS PostABS_ratio];
    %wavenumber pre trans post zeros pre-trans trans/pre pre-post post/pre
    complete_array=[complete_array data_diffs_ratios4];

elseif rowa == 3
    figure('Position',[600 scrsz(4)/2 scrsz(3)/1.84 scrsz(4)/1.1]);
    dABS_pre= complete_array(:,2) - complete_array(:,3);    % pre - trans
    subplot(2,1,1); plot(wavenumber, dABS_pre); ylabel('pre - trans'); xlabel('Wavenumber, cm^-
^1');axis tight

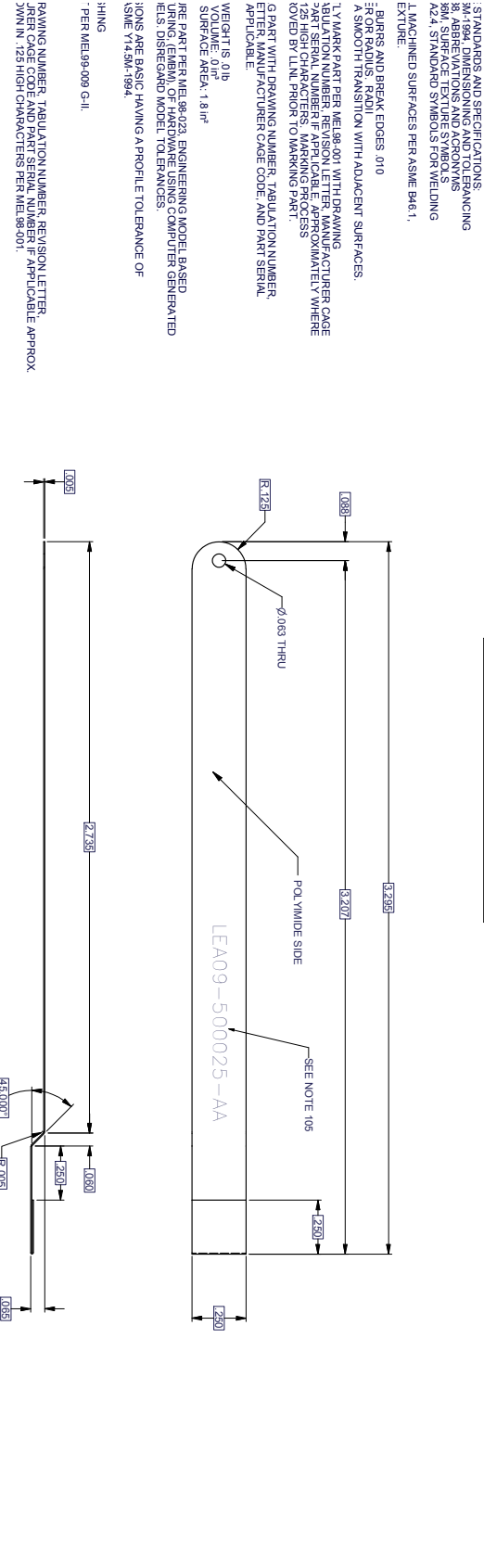
    PreABS_ratio= complete_array(:,3)./complete_array(:,2); % trans / pre
    subplot(2,1,2); plot(wavenumber, PreABS_ratio);ylabel('trans / pre'); xlabel('Wavenumber,
cm^-^1');axis tight

    data_diffs_ratios3 = [blank_row dABS_pre PreABS_ratio];
    %wavenumber pre trans post zeros pre-trans trans/pre
    complete_array=[complete_array data_diffs_ratios3];
end
%save ('complete_array', 'complete_array', '-ASCII')

```

# Appendix F. Drawings of Clamp and Holder Hardware

OTHERWISE SPECIFIED DIMENSIONS ARE IN INCHES.		CLASSIFICATION: UNCLASSIFIED		REVISONS	
STANDARDS AND SPECIFICATIONS: ASME Y14.194, DIMENSIONING AND TOLERANCING		DRAWN HAWKINS		CHECKED TANZOS	
ABBREVIATIONS AND ACRONYMS: A2.4, STANDARD SYMBOLS FOR WELDING		INITIAL RELEASE		APPROVED TM	
E, MACHINED SURFACES PER ASME B46.1, EX TYPICAL.		DESCRIPTION		DATE	
BURRS AND BREAK EDGES: 0.010		LEA09-500025-AA		2	
SURFACES FINISH: A. SMOOTH FINISH WITH ADJACENT SURFACES.		PARTIAL COPPER CLAMP POLYIMIDE LAMINATE SPRING WITH 0.025" TYPICAL APPROXIMATE APPROX		3	
1. MARK PART PER MEL98-001 WITH DRAWING NUMBER AND SERIAL NUMBER APPROXIMATELY WHERE COVERED BY L.N.L. PRIOR TO MARKING PART.		DRAWN		4	
G PART WITH DRAWING NUMBER, TABULATION NUMBER, PART MANUFACTURER CAGE CODE, AND PART SERIAL APPLICABLE.		HAWKINS		5	
WEIGHT IS 0.1b		TANZOS		6	
VOLUME: 0.1r		LEA09-500025-AA		7	
SURFACE AREA: 1.81r <sup>2</sup>		POLYIMIDE SIDE			
PER PART PER MEL98-023, ENGINEERING MODEL BASED DRAWING, (EMBM), OF HARDWARE USING COMPUTER GENERATED DIMENSIONS ARE BASIC HAVING A PROFILE TOLERANCE OF ±0.005		SEE NOTE 105			
DIMENSIONS ARE BASIC HAVING A PROFILE TOLERANCE OF ±0.005		LEA09-500025-AA			
FINISH: - PER MEL99-009 G-II		POLYIMIDE SIDE			
DRAWING NUMBER, TABULATION NUMBER, REVISION LETTER, AND SERIAL NUMBER APPROXIMATELY WHERE COVERED BY L.N.L. PRIOR TO MARKING PART.		COPPER SIDE			
DIMENSIONS ARE BASIC HAVING A PROFILE TOLERANCE OF ±0.005		LEA09-500025-AA			



1		PARTIAL COPPER CLAMP POLYIMIDE LAMINATE SPRING WITH 0.025" TYPICAL APPROXIMATE APPROX		MATERIAL: DESCRIBE IN DETAIL IN LINE	
REV		DESCRIPTION		DATE	
1		PARTIAL COPPER CLAMP POLYIMIDE LAMINATE SPRING WITH 0.025" TYPICAL APPROXIMATE APPROX		2/2009	
CLASSIFICATION: UNCLASSIFIED		DATE		2/2009	
FABRICATION		DATE		2/2009	
INSPECTION		DATE		2/2009	
TESTING		DATE		2/2009	
APPROVAL		DATE		2/2009	
SIGNATURE		DATE		2/2009	
DATE		DATE		2/2009	
DATE		DATE		2/2009	
DATE		DATE		2/2009	
DATE		DATE		2/2009	
DATE		DATE		2/2009	

CLASSIFICATION: UNCLASSIFIED

THIS DRAWING WAS CREATED BY THE LAWRENCE LIVERMORE NATIONAL SECURITY, LLC (LLNS), WHICH OPERATES THE LLNL UNDER CONTRACT NO. DE-AC02-07NA27344 FOR THE U.S. DEPARTMENT OF ENERGY. ANY REPRODUCTION, DISSEMINATION AND/OR FABRICATION IS PROHIBITED WITHOUT THE PERMISSION OF COGNIZANT LLNS PERSONNEL.

DATE: 02/20/09  
 DATE: 02/20/09  
 DATE: 02/20/09  
 DATE: 02/20/09  
 DATE: 02/20/09  
 DATE: 02/20/09  
 DATE: 02/20/09  
 DATE: 02/20/09  
 DATE: 02/20/09  
 DATE: 02/20/09  
 DATE: 02/20/09

INCH  
 THIRD ANGLE PROJECTION

CONTRACTOR: LAWRENCE LIVERMORE NATIONAL SECURITY, LLC  
 CONTRACT NO.: DE-AC02-07NA27344  
 PROJECT NO.: 020100018429  
 DATE: 02/20/09  
 CLASSIFICATION: UNCLASSIFIED

DESIGNED BY: TANZOS  
 DRAWN BY: HAWKINS  
 CHECKED BY: TANZOS  
 APPROVED BY: HAWKINS  
 DATE: 02/20/09  
 DATE: 02/20/09  
 DATE: 02/20/09  
 DATE: 02/20/09  
 DATE: 02/20/09

TITLE: ARC INITIATION EXPER  
 ARC CHAMBER  
 HV LEAD  
 DRAWING NUMBER: LEA09-500025-AA  
 PART NUMBER: LEA09-500025-AA  
 SERIAL NUMBER: 14067  
 DATE: 2/2009

MODEL: LEA09-500025-AA  
 INSERTION: 2011  
 DATE: 07/04/04

not for production

7

6

5

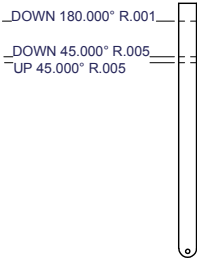
4

3

2

CLASSIFICATION:  
UNCLASSIFIED

UNLIMITED DISTRIBUTION/CLASSIFICATION: UNCLASSIFIED



UNLIMITED DISTRIBUTION/CLASSIFICATION: UNCLASSIFIED

09:16 PM  
MODEL: LEA09-50026.dwg

INVENTOR: 2011

7

6

5

4

3

2

CLASSIFICATION:  
UNCLASSIFIED

CLASSIFICATION: UNCLASSIFIED

**Beam Research**  
VBS

CONTRACT NO.	SIZE	CAD CODE	DRAWING NUMBER
	D	14067	LEA09-50
	SCALE	2:000	



7

6

5

4

3

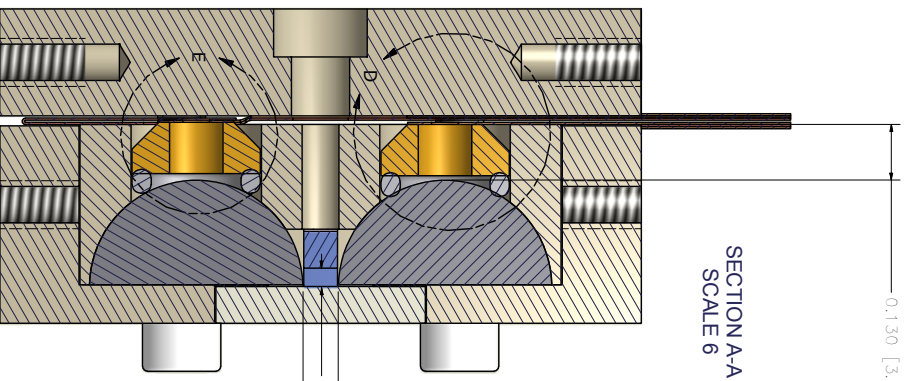
2

CLASSIFICATION:  
UNCLASSIFIED

UNLIMITED DISTRIBUTION/CLASSIFICATION: UNCLASSIFIED

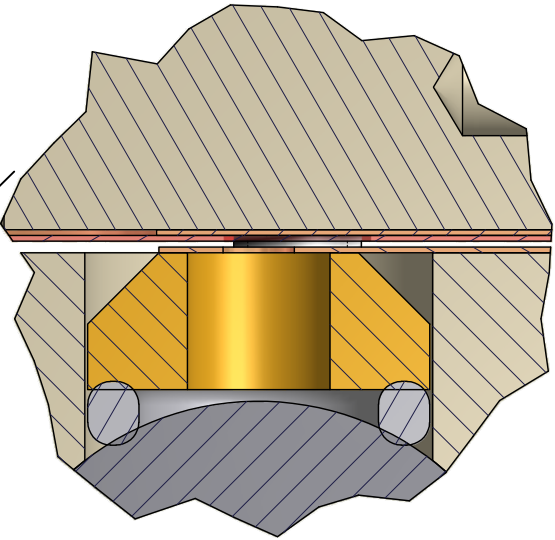
0.130 [3.30 mm]

SECTION A-A  
SCALE 6

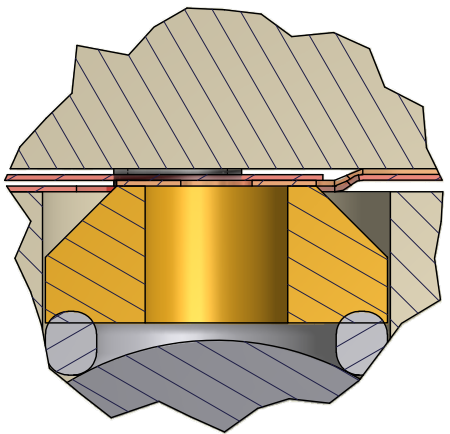


0.046 [1.16 mm]

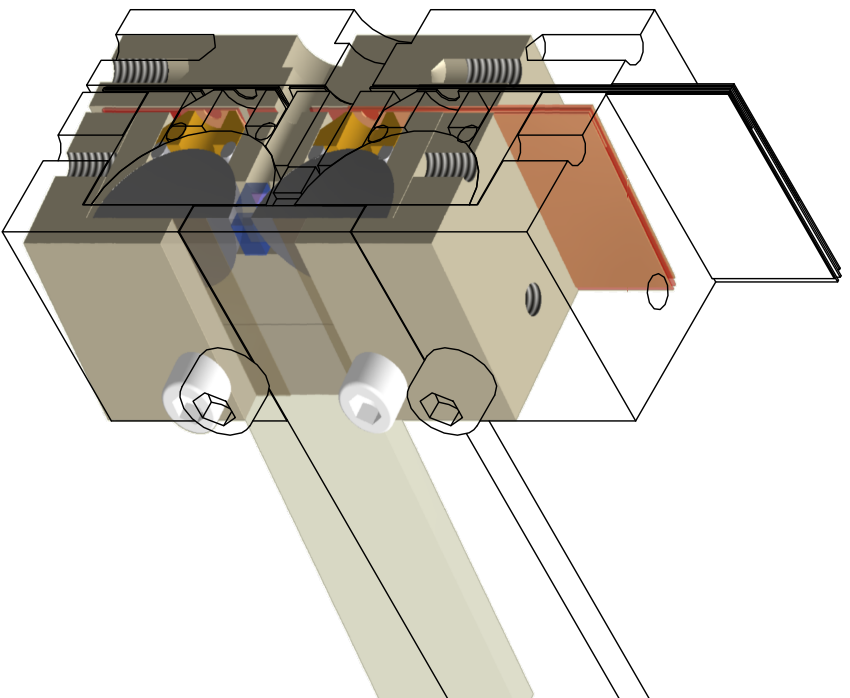
0.082 [2.08 mm]  
ELECTRODE GAP



DETAIL D  
SCALE 16



DETAIL E  
SCALE 16



UNLIMITED DISTRIBUTION/CLASSIFICATION: UNCLASSIFIED

08:52 AM

MODEL: LEA09-50030.0sm

7

INVENTOR: 2011

6

CLASSIFICATION:  
UNCLASSIFIED

5

4

3

2

CLASSIFICATION: UNCLASSIFIED

<b>Beam Research</b>	
WBS	
CONTRACT NO.	DRAWING NUMBER
SIZE	14067 LEA09-50
SCALE	2:00

CLASSIFICATION:  
UNCLASSIFIED

UNLIMITED DISTRIBUTION/CLASSIFICATION:UNCLASSIFIED

SECTION B-B  
SCALE .5

DETAIL C  
SCALE 1:1

UNLIMITED DISTRIBUTION/CLASSIFICATION:UNCLASSIFIED

CLASSIFICATION: UNCLASSIFIED

08:09 PM

MODEL: LEA09-50031 Rev

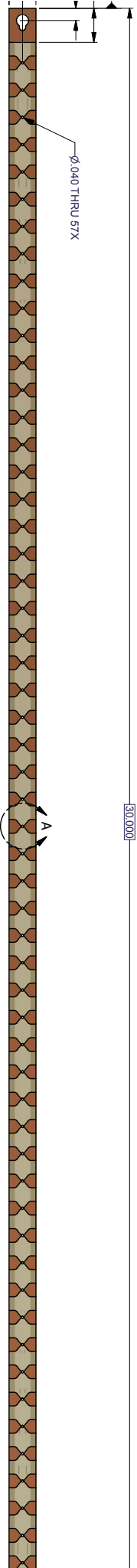
INVENTOR: 2011

CLASSIFICATION:  
UNCLASSIFIED

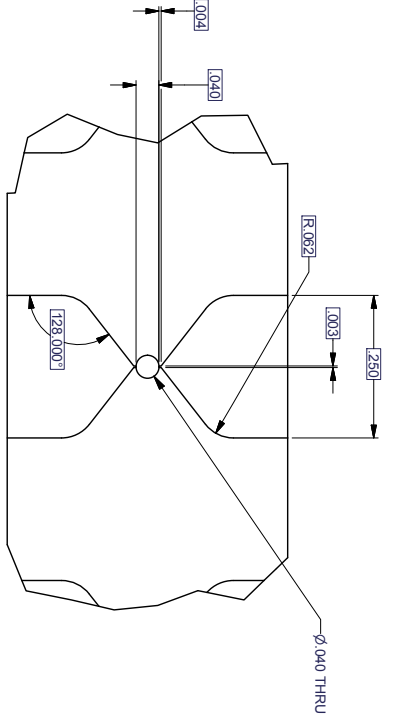
WBS	
CONTRACT NO.	
SIZE	D
CAGE CODE	14067
DRAWING NUMBER	LEA09-50
SCALE	2:00

UNLIMITED DISTRIBUTION UNCLASSIFIED  
UNCLASSIFIED

ZONE	LTR	DESCRIPTION	REVISIONS	DRAWN	CHECKED	APP
/	AA	INITIAL RELEASE	HAWKINS4	TANG23	TAM	

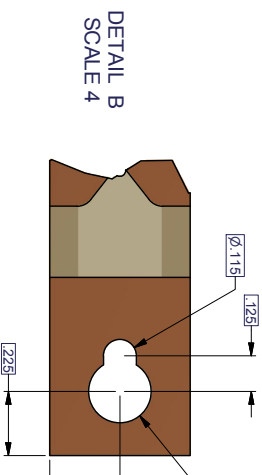


RLAY



DETAIL A  
SCALE 8

- .002 A B C
- ALL FEATURES
- ALL CIRCULAR HOLES: +.002 / -.000
- $\phi$  .002 A B C



DETAIL B  
SCALE 4

**CONSTRUCTION:**  
BASE MATERIAL: POLYIMIDE ADHESIVELESS  
POLYIMIDE THICKNESS: 0.002" (50 UM)  
COPPER THICKNESS: 0.5 OZ (17 UM)  
COVER LAYER: POLYIMIDE ON NON COPPER SIDE ON L.Y.: 0.001" (2 UM)  
SURFACE FINISHES: NONE

OTHERWISE SPECIFIED  
DIMENSIONS ARE IN INCHES.  
STANDARDS AND SPECIFICATIONS:  
ASME Y14.5 DIMENSIONING AND TOLERANCING  
MATERIALS AND FINISHES:  
RMA SURFACE TEXTURE SYMBOLS:  
R2.4 STANDARD SYMBOLS FOR WELDING  
TEXTURE:  
L MACHINED SURFACES PER ASME B46.1.

BURRS AND BREAK EDGES: 010  
R OR RADIUS: RADI  
A SMOOTH TRANSITION WITH ADJACENT SURFACES.  
1 Y MARK PART PER MEL98-001 WITH DRAWING  
TABULATION NUMBER, REVISION LETTER, MANUFACTURER CAGE  
PART SERIAL NUMBER IF APPLICABLE, APPROXIMATELY WHERE  
125 HIGH CHARACTERS, MARKING PROCESS  
OVED BY LINTL PRIOR TO MARKING PART.  
G PART WITH DRAWING NUMBER, TABULATION NUMBER,  
ENTER MANUFACTURER CAGE CODE, AND PART SERIAL  
NUMBER APPLICABLE.

CLASSIFICATION: UNCLASSIFIED  
JTC/JC/CLASSIFICATION UNCLASSIFIED  
1017 AM/04/29 PM

MODEL: LEA09-50M5 9P1	INVENTOR: 20111	DATE: 1/21/2010	SCALE: 2.000
-----------------------	-----------------	-----------------	--------------

Status: **Wincc**  
Fabrication Quantity:  
Project: **Isan Number**

Done: **Due:**

THIS DRAWING WAS CREATED BY THE  
LAWRENCE LIVERMORE NATIONAL SECURITY, LLC  
(LLNS) WHICH OPERATES LAWRENCE  
LIVERMORE NATIONAL LABORATORY (LLNL)  
FOR THE U.S. DEPARTMENT OF ENERGY UNDER  
CONTRACT NO. DE-AC52-07NA27944.

ANY REPRODUCTION, DISSEMINATION AND/OR  
FABRICATION IS PROHIBITED WITHOUT THE  
PERMISSION OF COGNIZANT LLNS PERSONNEL.

INCH		THIRD ANGLE PROJECTION	
CONTRACT NO.	DATE	DESIGNED BY	TITLE
APPROVALS	DATE	CHECKED BY	LAWRENCE LIVERMORE NATIONAL LABORATORY
DESIGNED	DATE	DRAWN BY	LAWRENCE LIVERMORE NATIONAL SECURITY
CHECKED	DATE	CHECKED	
DRAWN	DATE	DATE	
DATE	DATE	DATE	
DATE	DATE	DATE	
DATE	DATE	DATE	
DATE	DATE	DATE	

CLASSIFICATION: UNCLASSIFIED



LAWRENCE LIVERMORE NATIONAL LABORATORY

ARC INITIATION EXPER

ARC CHAMBER

ARC STRIP

14067 LEA09-5C



STANDARDS AND SPECIFICATIONS:  
 M-1994 DIMENSIONING AND TOLERANCING  
 R-ABBREVIATIONS AND ACRONYMS  
 M-1 SURFACE FINISH SYMBOLS  
 A2-4 STANDARD SYMBOLS FOR WELDING  
 L-MACHINED SURFACES PER ASME B46.1, EXTURE.

BURRS AND BREAK EDGES .010  
 R OR RADIUS . RADI  
 A SMOOTH TRANSITION WITH ADJACENT SURFACES.

1.Y MARK PART PER MEL99-001 WITH DRAWING  
 TABULATION NUMBER, REVISION LETTER, MANUFACTURER CAGE  
 PART SERIAL NUMBER IF APPLICABLE, APPROXIMATELY WHERE  
 125 HIGH CHARACTERS. MARKING PROCESS  
 OVED BY L/NL PRIOR TO MARKING PART.

G PART WITH DRAWING NUMBER, TABULATION NUMBER,  
 LETTER, MANUFACTURER CAGE CODE, AND PART SERIAL  
 APPLICABLE.

WEIGHT IS .593 lb  
 VOLUME IS .548 in<sup>3</sup>  
 SURFACE AREA: .39 937 in<sup>2</sup>

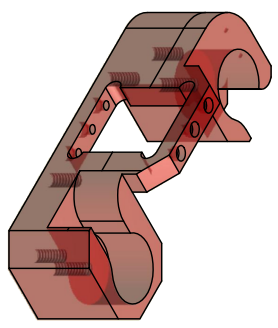
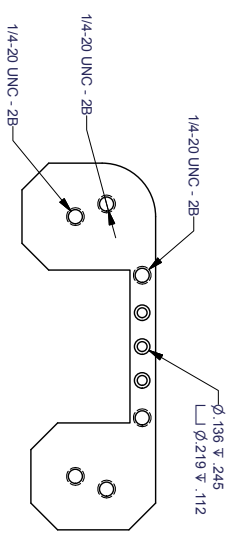
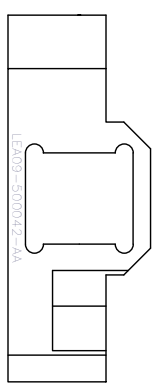
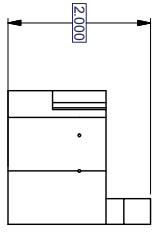
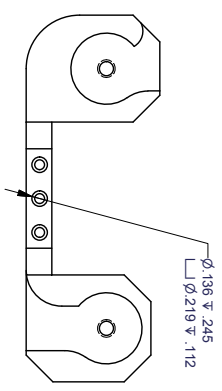
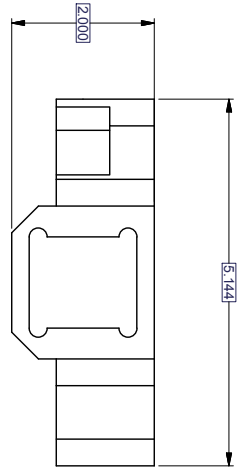
IRE PART PER MEL99-023 ENGINEERING MODEL BASED  
 URING, (EMBM), OF HARDWARE USING COMPUTER GENERATED  
 ELS. DISREGARD MODEL TOLERANCES.

IONS ARE BASIC HAVING A PROFILE TOLERANCE OF  
 ISME Y14.5M-1994.

HING  
 - PER MEL99-009 G-II.

DRAWING NUMBER, TABULATION NUMBER, REVISION LETTER,  
 PART CAGE CODE AND PART SERIAL NUMBER IF APPLICABLE APPROX.  
 20 IN .129 HIGH CHARACTERS PER MEL99-001.

102



**CHECK PRINT**

Status: RELEASED Who: JASON CARROLL  
 Fabrication Quantity: 1 Date: 12/2/2010  
 Project: Task Number: 32900-899629 Due:

THIS DRAWING WAS CREATED BY THE  
 LAWRENCE LIVERMORE NATIONAL SECURITY, LLC  
 (LLNS) WHICH OPERATES LAWRENCE  
 LIVERMORE NATIONAL LABORATORY (LLNL)  
 FOR THE U.S. DEPARTMENT OF ENERGY UNDER  
 CONTRACT NO. DE-AC02-07NA27394.  
 ANY REPRODUCTION, DISSEMINATION AND/OR  
 FABRICATION IS PROHIBITED WITHOUT THE  
 PERMISSION OF COGNIZANT LLNS PERSONNEL.

1	PART OR SERIAL NUMBER	ALUMINUM-6061-T6	
	MATERIAL DESCRIPTION OR NOMENCLATURE		

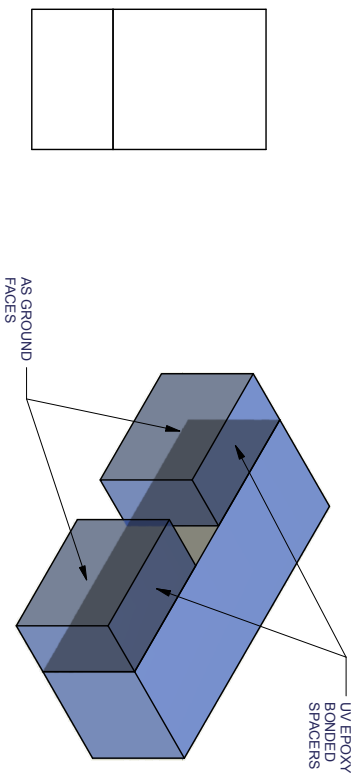
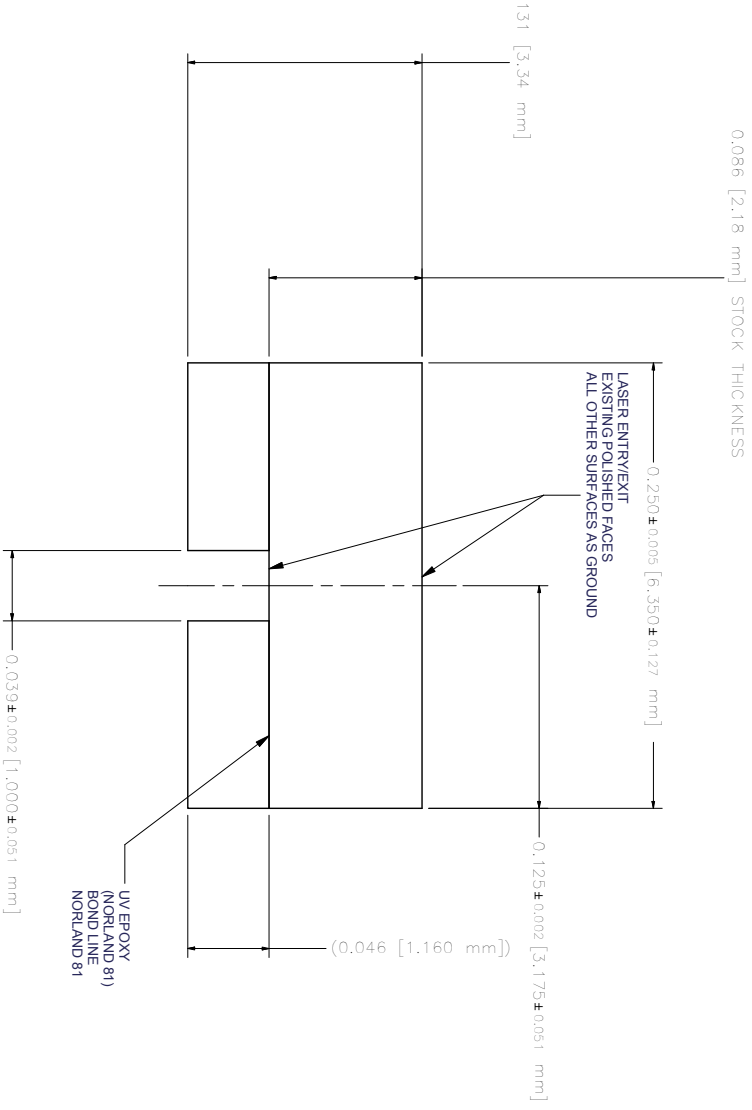
THIRD ANGLE PROJECTION		INCH	
CONTRACT NO	DATE	TITLE	DRAWING NUMBER
Q-15823 BY	11/29/10	ARC INITIATION EXPER	LEA09-56
APPROVALS		ARC CHAMBER	
DESIGNED BY		STRIP HOLDER	
CHECKED BY			
APPROVED BY			
DRAWN BY			
DATE			

UNLESS OTHERWISE SPECIFIED DIMENSIONS IN INCHES TOLERANCES ARE: DECIMALS ± .005 ANGLES ± .1° DIMENSIONS IN PARENTHESES DO NOT SCALE FROM DIMENSIONS	ORGANIZATION LAWRENCE LIVERMORE NATIONAL SECURITY, LLC
--	---

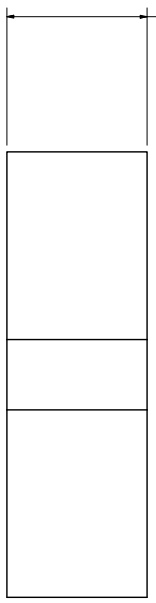
KEY: ASSEMBLY	USED ON	DRAWING LEVEL	SCALE
		D	14067 LEA09-56

7	6	5	4	3	2
CLASSIFICATION: UNCLASSIFIED			REVISIONS		
ZONE	LTR	DESCRIPTION	DRAWN	CHECKED	APP
/	AA	INITIAL RELEASE	HAWKINS4	TANG23	TAM

UNLIMITED DISTRIBUTION/CLASSIFICATION: UNCLASSIFIED



PART MADE FROM  
CALCIUM FLOURIDE  
SLIDE 2MM THICK.  
2 POLISHED FACES  
1.00" WIDE BY 3.75" LONG



UNLIMITED DISTRIBUTION/CLASSIFICATION: UNCLASSIFIED

Status: COMPLETE Who: PETER THELIN  
Fabrication Quantity: 75 Date: 5/11/2010  
Project # Task Number: 25900 899629 Due: 5/11/2010

THIS DRAWING WAS CREATED BY THE LAWRENCE LIVERMORE NATIONAL SECURITY, LLC (LLNS) WHICH OPERATES LAWRENCE LIVERMORE NATIONAL LABORATORY (LLNL) FOR THE U.S. DEPARTMENT OF ENERGY UNDER CONTRACT NO. DE-AC02-07NA47344. ANY REPRODUCTION, DISSEMINATION AND/OR FABRICATION IS PROHIBITED WITHOUT THE PERMISSION OF COGNIZANT LLNS PERSONNEL.

1	QTY	PART OR IDENTIFYING NUMBER	MATERIAL DESCRIPTION OR NOMENCLATURE	REV
CLASSIFICATION: UNCLASSIFIED				

INCH (MM)		THIRD ANGLE PROJECTION	
CONTRACT NO	CLASSIFIED BY	DATE	TITLE
TANG23	TANG23	5/9/2010	ARC INITIATION EXPER
APPROVALS	ORGANIZER	DATE	ARC CHAMBER
	HAWKINS4	5/9/2010	OPTICAL LINER
UNLESS OTHERWISE SPECIFIED DIMENSIONS AND TOLERANCES ARE: DIMS ± .005 ANGLES ± 1° DO NOT SCALE FROM DRAWING	CHECKED	DATE	SIZE
	TANG23	5/9/2010	D
NEXT ASSY	DRAWING NO	SCALE	DRAWING NUMBER
	TANG23	14067	LEA09-5C
USED ON	ED	2	2

MATERIAL DESCRIPTION OR NOMENCLATURE		MATERIAL	
LAWRENCE LIVERMORE NATIONAL LABORATORY		WBS	
DRAWING NUMBER		SCALE	
LEA09-5C		2:000	

7

6

5

4

3

2

CLASSIFICATION:  
UNCLASSIFIED

ZONE	LT/R	DESCRIPTION	REVISIONS	DRAWN	CHECKED	APP
/	AA	INITIAL RELEASE		HAWKINS4	TANG23	TA

UNLIMITED DISTRIBUTION/CLASSIFICATION: UNCLASSIFIED

NOTES: UNLESS OTHERWISE SPECIFIED  
101. ALL DIMENSIONS ARE IN INCHES.

102. APPLICABLE STANDARDS AND SPECIFICATIONS:  
ASME Y14.5M-1994, DIMENSIONING AND TOLERANCING  
ASME Y14.38, ABBREVIATIONS AND ACRONYMS  
ASME Y14.36M, SURFACE TEXTURE SYMBOLS  
ANSI/AWS A2.4, STANDARD SYMBOLS FOR WELDING

103. 63 FINISH ALL MACHINED SURFACES PER ASME B46.1, SURFACE TEXTURE.

104. REMOVE ALL BURS AND BREAK EDGES .010  
.030 CHAMFER OR RADIUS. RADI  
MUST MAKE A SMOOTH TRANSITION WITH ADJACENT SURFACES.

105. PERMANENTLY MARK PART PER MEL99-001 WITH DRAWING NUMBER, TABULATION NUMBER, REVISION LETTER, MANUFACTURER CAGE CODE AND PART SERIAL NUMBER IF APPLICABLE APPROXIMATELY WHERE SHOWN IN THIS DRAWING AND APPROXIMATELY WHERE TO BE APPROVED BY LT/LN, PRIOR TO MARKING PART.

106. BAG AND TAG PART WITH DRAWING NUMBER, TABULATION NUMBER, REVISION LETTER, MANUFACTURER CAGE CODE, AND PART SERIAL NUMBER IF APPLICABLE.

109. ESTIMATED WEIGHT IS 0.1b

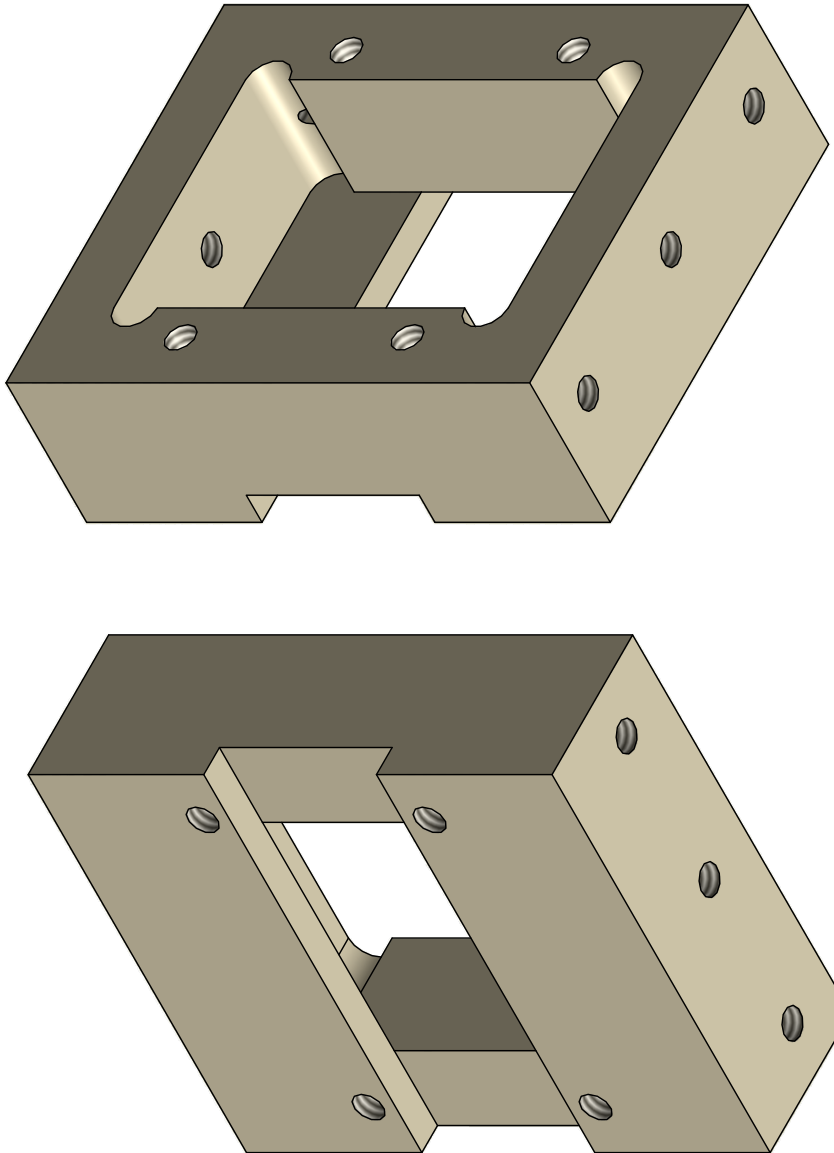
ESTIMATED VOLUME: 5.1in<sup>3</sup>

ESTIMATED SURFACE AREA: 8.0 in<sup>2</sup>

350. CLEAN PART PER MEL99-009 G-11.

IDENTIFICATION

502. ENGRAVE DRAWING NUMBER, TABULATION NUMBER, REVISION LETTER, MANUFACTURER CAGE CODE AND PART SERIAL NUMBER IF APPLICABLE APPROX WHERE SHOWN IN .125 HIGH CHARACTERS PER MEL98-001.



UNLIMITED DISTRIBUTION/CLASSIFICATION: UNCLASSIFIED

07:36 PM

MODEL: LEA09-50019.01

INVENTORY: 2011

CLASSIFICATION:  
UNCLASSIFIED

Status: QUOTATION Who: Done: Due: 5/20/2010  
Fabrication Quantity: 2  
Project / Task Number:

THIS DRAWING WAS CREATED BY THE LAWRENCE LIVERMORE NATIONAL SECURITY, LLC (LLNS) WHICH OPERATES LAWRENCE LIVERMORE NATIONAL LABORATORY (LLNL) FOR THE U.S. DEPARTMENT OF ENERGY UNDER CONTRACT NO. DE-AC02-07NA27344. ANY REPRODUCTION, DISSEMINATION AND/OR FABRICATION IS PROHIBITED WITHOUT THE PERMISSION OF COGNIZANT LLNS PERSONNEL.



THIRD ANGLE PROJECTION

INCH

WBS

Beam Research

CONTRACT NO: LAWRENCE LIVERMORE NATIONAL LABORATORY  
APPROVALS: DATE: TITLE: ARC INITIATION EXPER

UNLESS OTHERWISE SPECIFIED DIMENSIONS AND TOLERANCES ARE: HAWKINS4 5/20/10 5/20/10 ARC CHAMBER

DO NOT SCALE FROM DRAWING TANG23 5/20/10 5/20/10 INSULATOR HOUSING

NEXT ASSY: USED ON: DRAWING NUMBER: LEA09-50019.01

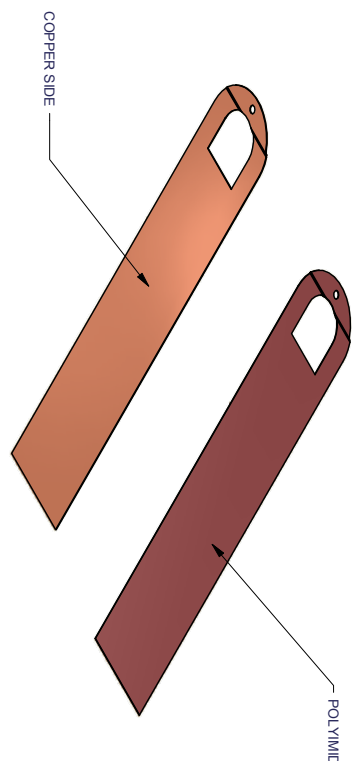
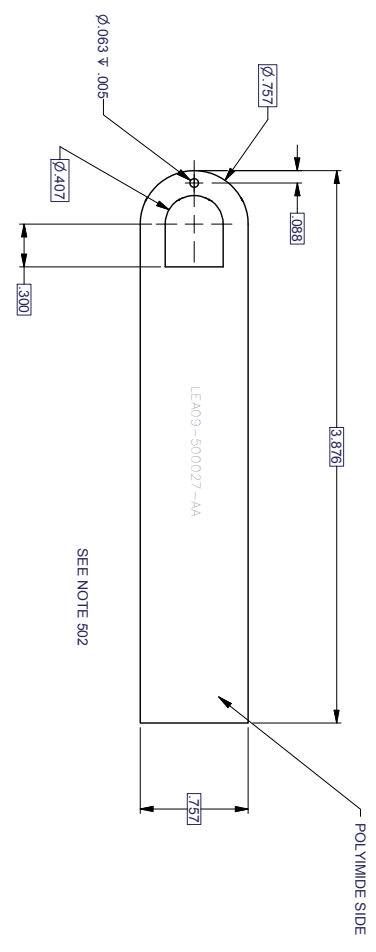
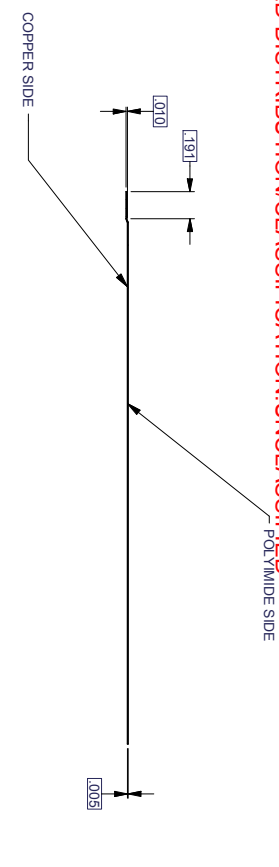
DATE: 5/20/10 SCALE: 2:000

QTY	PART OR IDENTIFYING NUMBER	MATERIAL, DESCRIPTION OR NOMENCLATURE	W
1		PEEK, UNFILLED	

CLASSIFICATION: UNCLASSIFIED

OTHERWISE SPECIFIED	7	6	5	4	3	2
IONS ARE IN INCHES.						
STANDARDS AND SPECIFICATIONS:						
M-1894, DIMENSIONING AND TOLERANCING						
ASME Y14.5, DIMENSIONS AND TOLERANCING						
ASME Y14.9, SURFACE FINISH SYMBOLS						
ASME Y14.12, STANDARD SYMBOLS FOR WELDING						
ASME Y14.13, STANDARD SYMBOLS FOR WELDING						
ASME Y14.18, MACHINED SURFACES PER ASME B46.1, F						
ASME Y14.20, MACHINED SURFACES PER ASME B46.1, F						
BURRS AND BREAK EDGES: 010						
FR OR RADIUS: R010						
A SMOOTH TRANSITION WITH ADJACENT SURFACES.						
1. Y MARK PART PER MEL98-001 WITH DRAWING						
TABULATION NUMBER, REVISION LETTER, MANUFACTURER CAGE						
PART SERIAL NUMBER IF APPLICABLE, APPROXIMATELY WHERE						
125 HIGH CHARACTERS, MARKING PROCESS						
LOVED BY LINTL PRIOR TO MARKING PART.						
G PART WITH DRAWING NUMBER, TABULATION NUMBER,						
LETTER, MANUFACTURER CAGE CODE, AND PART SERIAL						
APPLICABLE.						
WEIGHT IS 0.01 lb						
VOLUME: 0.03 in <sup>3</sup>						
SURFACE AREA: 5.423 in <sup>2</sup>						
RE PART PER MEL98-023, ENGINEERING MODEL BASED						
URING, (EMBM), OF HARDWARE USING COMPUTER GENERATED						
ELS, DISREGARD MODEL TOLERANCES.						
IONS ARE BASIC HAVING A PROFILE TOLERANCE OF						
(SME Y14.5M-1994.						
HING						
- PER MEL99-009 G-II.						
DRAWING NUMBER, TABULATION NUMBER, REVISION LETTER,						
JER CAGE CODE AND PART SERIAL NUMBER IF APPLICABLE APPROX.						
2MM IN .125 HIGH CHARACTERS PER MEL98-001.						

UNLIMITED DISTRIBUTION/CLASSIFICATION: UNCLASSIFIED



UNLIMITED DISTRIBUTION/CLASSIFICATION: UNCLASSIFIED

MODEL: LEA09-500027-4A INVENTOR: 2011

CLASSIFICATION: UNCLASSIFIED	ZONE LTR / AA	DESCRIPTION INITIAL RELEASE	DRAWN hmk/4	CHECKED TANG23	APP'N TM
------------------------------	---------------	-----------------------------	-------------	----------------	----------

1	QTY	PART OR SERIAL NUMBER	DESCRIPTION	MATERIAL	DESCRIPTION/ALTERNATIVE
1			PYRAMID AP COPPER COATED POLYIMIDE LEAD	DOUBLE SIDED, 3MM DIA, 0.063 THK, DUPONT	

Status: RELEASED Who: BRAD HICKMAN Done: Fabrication Quantity: 4 Project: Task Number: 32900/89829 Due: 5/21/2010

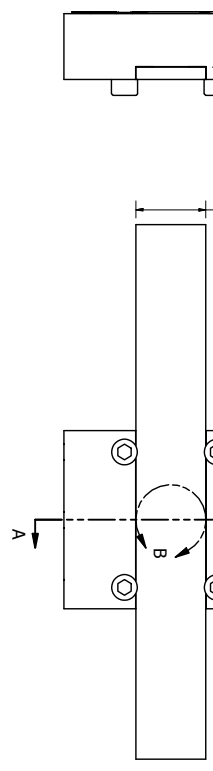
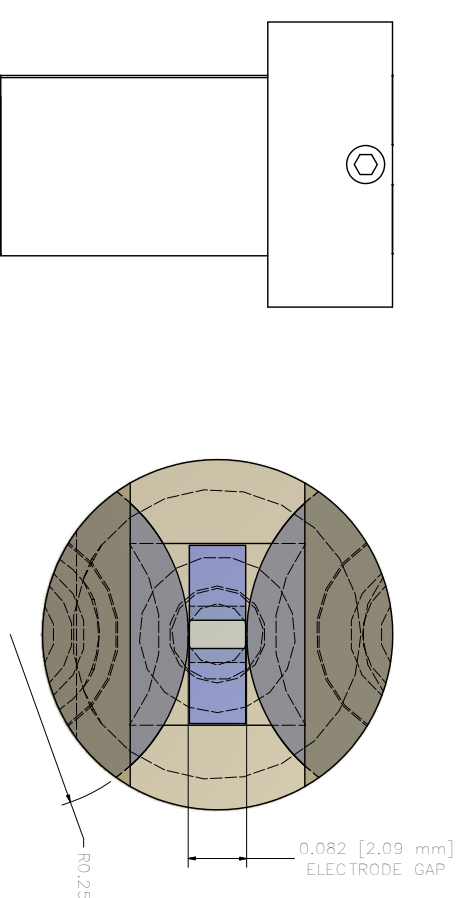
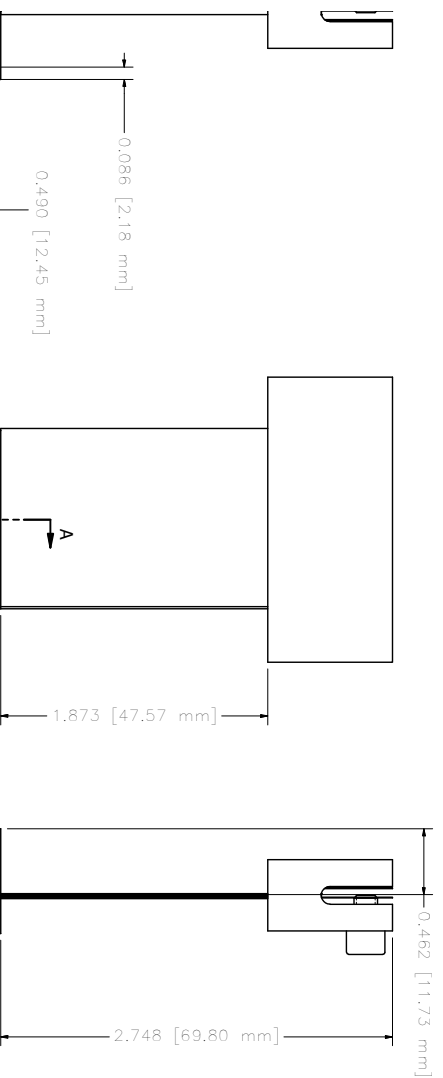
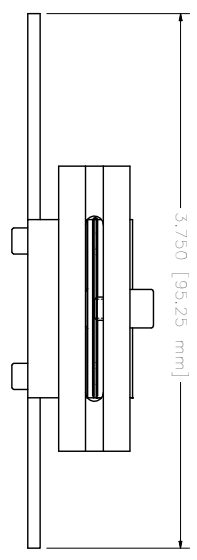
THIS DRAWING WAS CREATED BY THE LAWRENCE LIVERMORE NATIONAL SECURITY, LLC (LLNS) WHICH OPERATES LAWRENCE LIVERMORE NATIONAL LABORATORY (LLNL) FOR THE U.S. DEPARTMENT OF ENERGY UNDER CONTRACT NO. DE-AC02-07NA27344. ANY REPRODUCTION, DISSEMINATION AND/OR FABRICATION IS PROHIBITED WITHOUT THE PERMISSION OF COGNIZANT LLNS PERSONNEL.

THIRD ANGLE PROJECTION	CONTRACT NO	CLASSIFIED BY	DATE	TITLE	ARC INITIATION EXPER
					ARC CHAMBER
					GROUND LEAD

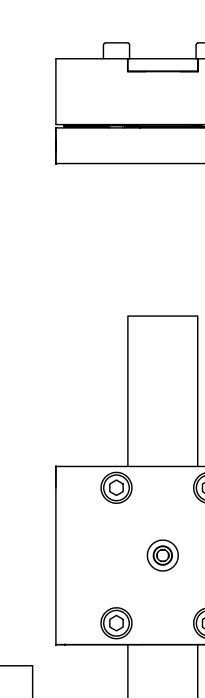
UNLESS OTHERWISE SPECIFIED DIMENSIONS IN THIS DRAWING ARE IN INCHES. TOLERANCES ARE: DIMENALS ± .005 ANGLES ± 1° DO NOT SCALE FROM DRAWING	DATE	SIZE	DRAWING NUMBER
	5/8/2010	D	14067
	5/8/2010		LEA09-500027-4A

7	6	5	4	3	2
CLASSIFICATION: UNCLASSIFIED			REVISIONS		
ZONE	LTR	DESCRIPTION	DRAWN	CHECKED	APP
/	AA	INITIAL RELEASE	HAWKINS4	AKAMAI	TM

UNLIMITED DISTRIBUTION/CLASSIFICATION: UNCLASSIFIED



UNLIMITED DISTRIBUTION/CLASSIFICATION: UNCLASSIFIED



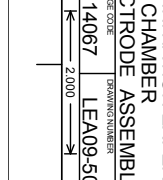
Status: **Wincc**  
Fabrication Quantity:  
Project / Task Number:

Date: **Done:**

THIS DRAWING WAS CREATED BY THE LAWRENCE LIVERMORE NATIONAL SECURITY, LLC (LLNS) WHICH OPERATES LAWRENCE LIVERMORE NATIONAL LABORATORY (LLNL) FOR THE U.S. DEPARTMENT OF ENERGY UNDER CONTRACT NO. DE-AC02-07NA27344. ANY REPRODUCTION, DISSEMINATION AND/OR FABRICATION IS PROHIBITED WITHOUT THE PERMISSION OF COGNIZANT LLNS PERSONNEL.

THIRD ANGLE PROJECTION	INCH	CONTRACT NO	CLASSIFIED BY	APPROVALS	DATE	TITLE	DATE
		6292010	TANCG23	HAWKINS4	5/29/10	ARC INITIATION EXPER	
UNLESS OTHERWISE SPECIFIED DIMENSIONS IN THIS DRAWING ARE IN INCHES. TOLERANCES ARE: DO NOT SCALE FROM DIMENSIONS		ORGANIZATION	DESIGNED	APPROVALS		ARC CHAMBER	
		LAWRENCE LIVERMORE NATIONAL LABORATORY	AKAMAI			ELECTRODE ASSEMBLY	
		LLNS	TANCG23				
			DRIVER/CLIP				
			ETD				

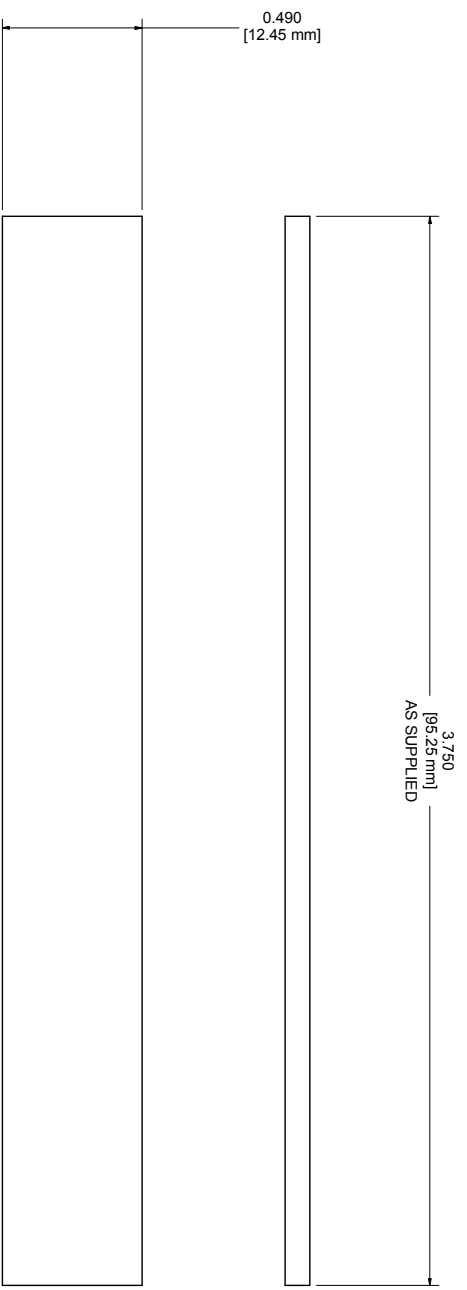
MODEL: LEA09-500303um	INVENTOR: 2011	CLASSIFICATION: UNCLASSIFIED	DATE: 5/29/10	SCALE: 2:000
08:52 AM	7	6	4	3
W				



ZONE		DESCRIPTION		REVISIONS		APP
LTIR	AA	INITIAL RELEASE	DRAWN	CHECKED	DATE	
/	AA		HAWKINS4	TANG23		TM

UNLIMITED DISTRIBUTION/CLASSIFICATION: UNCLASSIFIED

CLASSIFICATION:  
UNCLASSIFIED



PART MADE FROM  
CALCIUM FLOURIDE  
SLIDE 2MM THICK.  
2 POLISHED FACES  
1.00" WIDE BY 3.75" LONG

08:49 AM

MODEL: LEA09-5C0014

INVENTORY: 2011

CLASSIFICATION:  
UNCLASSIFIED

UNLIMITED DISTRIBUTION/CLASSIFICATION: UNCLASSIFIED

Status: IN PROCESS Who: PETER THELIN Done:  
Fabrication Quantity: 20-24 Due: 5/10/2010  
Project Task Number: 35300-939629

THIS DRAWING WAS CREATED BY THE LAWRENCE LIVERMORE NATIONAL SECURITY, LLC (LLNS) WHICH OPERATES LAWRENCE LIVERMORE NATIONAL LABORATORY (LLNL) FOR THE U.S. DEPARTMENT OF ENERGY UNDER CONTRACT NO. DE-AC02-07NA27344. ANY REPRODUCTION, DISSEMINATION AND/OR FABRICATION IS PROHIBITED WITHOUT THE PERMISSION OF COGNIZANT LLNS PERSONNEL.



INCH [MM]

QTY	PART OR IDENTIFYING NUMBER	MATERIAL DESCRIPTION/ABBREVIATURE	W
<b>CLASSIFICATION: UNCLASSIFIED</b>			

**Beam Research**  
WBS

LAWRENCE LIVERMORE NATIONAL LABORATORY  
LAWRENCE LIVERMORE NATIONAL SECURITY

CONTRACT NO	DATE	TITLE	DRAWING NUMBER
592010	5/9/2010	ARC INITIATION EXPER	LEA09-5C
592010	5/9/2010	ARC CHAMBER	
592010	5/9/2010	SAMPLING SLIDE	

SCALE: 2:000

STANDARDS AND SPECIFICATIONS:  
 M-1894, DIMENSIONING AND TOLERANCING  
 18, ABBREVIATIONS AND ACRONYMS  
 604, SURFACE TEXTURES FROM  
 ASME Y14.35, STANDARD SYMBOLS FOR WELDING  
 L MACHINED SURFACES PER ASME B46.1, FINISH  
 EXTURE.

BURRS AND BREAK EDGES .010  
 R OR RADIUS, RADI  
 A SMOOTH TRANSITION WITH ADJACENT SURFACES.

1.Y MARK PART PER MEL 98-001 WITH DRAWING  
 TABULATION NUMBER, REVISION LETTER, MANUFACTURER CAGE  
 PART SERIAL NUMBER IF APPLICABLE, APPROXIMATELY WHERE  
 125 HIGH CHARACTERS, MARKING PROCESS  
 LOVED BY LNL PRIORITY MARKING PART.

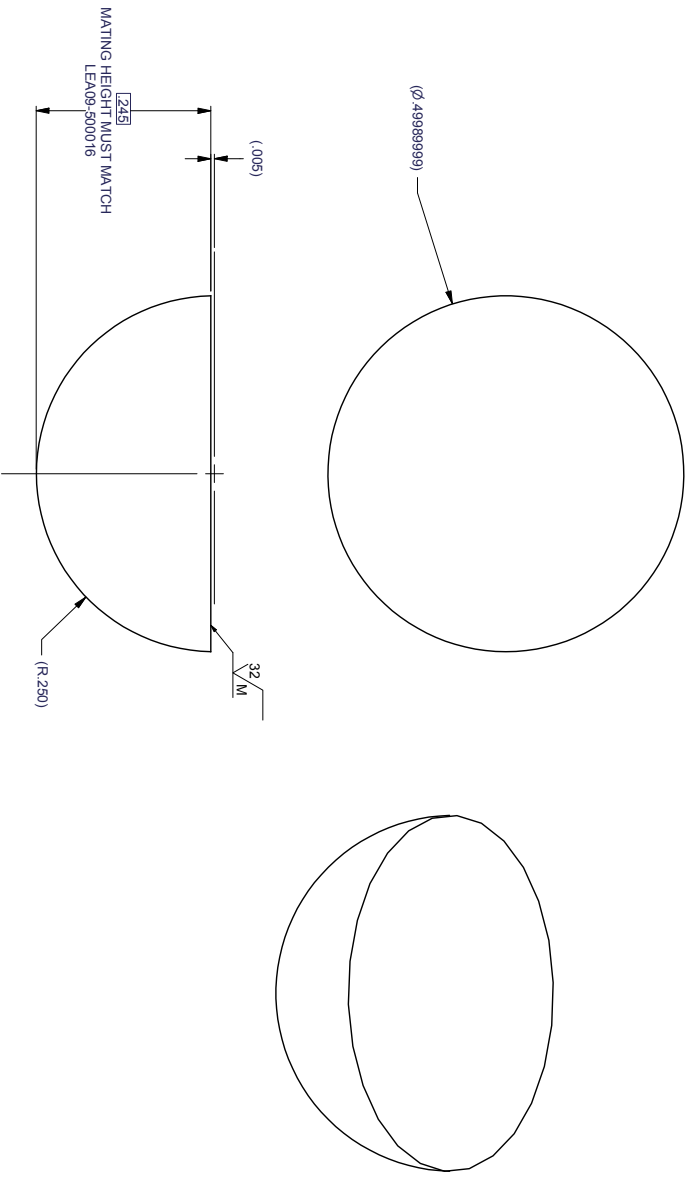
G PART WITH DRAWING NUMBER, TABULATION NUMBER,  
 LETTER, MANUFACTURER CAGE CODE, AND PART SERIAL  
 APPLICABLE.

WEIGHT IS .01b  
 VOLUME IS .01in<sup>3</sup>  
 SURFACE AREA . 6 in<sup>2</sup>

UNLIMITED DISTRIBUTION/CLASSIFICATION: UNCLASSIFIED

CLASSIFICATION:  
 UNCLASSIFIED

ZONE	LTR	DESCRIPTION	REVISIONS	DRAWN	CHECKED	APP
/	AA	INITIAL RELEASE	HAWKINS4	TANG23	TM	



CLASSIFICATION:  
 UNCLASSIFIED

Status: RELEASED Who:  
 Fabrication Quantity: 3 PARTS  
 Project : task Number: Due: 5/19/2010

THIS DRAWING WAS CREATED BY THE  
 LAWRENCE LIVERMORE NATIONAL SECURITY, LLC  
 (LLNS) WHICH OPERATES LAWRENCE  
 LIVERMORE NATIONAL LABORATORY (LLNL)  
 FOR THE U.S. DEPARTMENT OF ENERGY UNDER  
 CONTRACT NO. DE-AC02-07NA27344.  
 ANY REPRODUCTION, DISSEMINATION AND/OR  
 FABRICATION IS PROHIBITED WITHOUT THE  
 PERMISSION OF COGNIZANT LLNS PERSONNEL.

QTY	PART OR SERIAL NUMBER	DESCRIPTION AND QUANTITY	MATERIAL	MM
2	9898K7	TUNGSTEN CARBIDE BALL, GRADE 25, TYPE C1 OR C2 6% COBALT, .500 DIAMETER, +.0001		M

CLASSIFICATION: UNCLASSIFIED



CONTRACT NO  
 CLASSIFIED BY  
 APPROVALS  
 DATE  
 TITLE  
 ARC INITIATION EXPER  
 ARC CHAMBER  
 ELECTRODE  
 DRAWING NUMBER  
 LEA09-56



THIRD ANGLE PROJECTION  
 UNLESS OTHERWISE SPECIFIED  
 DIMENSIONS IN INCHES  
 TOLERANCES ARE:  
 DO NOT SCALE FROM DRAWING  
 NEXT ASSY  
 USED ON  
 ETD

DATE	BY	DESCRIPTION	SCALE
5/20/10	HAWKINS4	ARC INITIATION EXPER	2
5/20/10	TANG23	ARC CHAMBER	2
5/20/10	TANG23	ELECTRODE	2

UNLIMITED DISTRIBUTION/CLASSIFICATION: UNCLASSIFIED

7

6

5

4

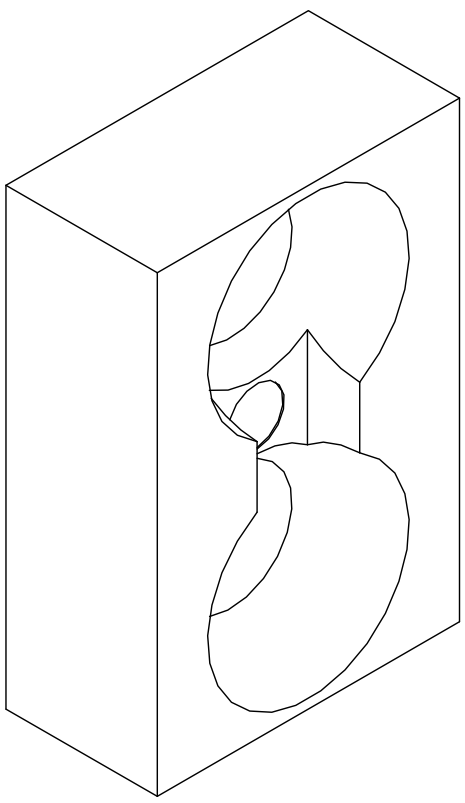
3

2

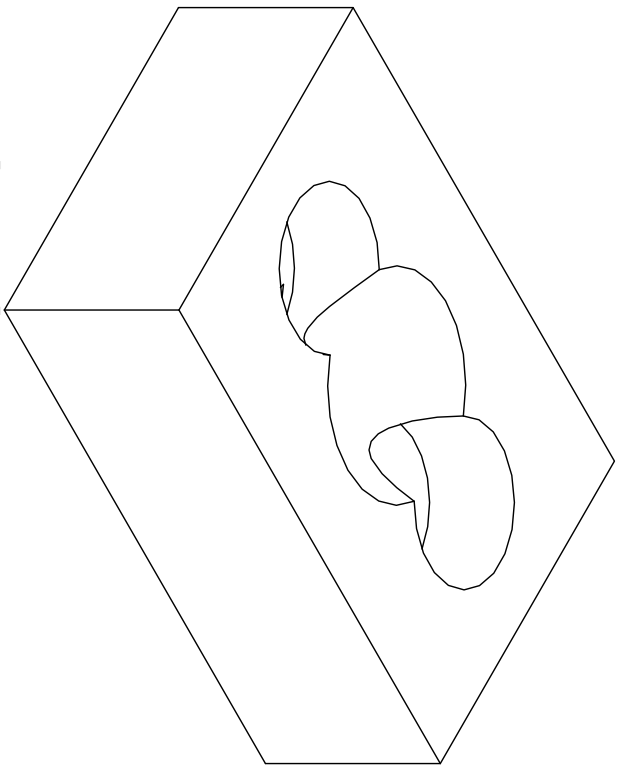
CLASSIFICATION:  
UNCLASSIFIED

ZONE	LTR	DESCRIPTION	REVISIONS	DRAWN	CHECKED	APP
/	AA	INITIAL RELEASE		HAWKINS4	TANG23	TM

UNLIMITED DISTRIBUTION/CLASSIFICATION: UNCLASSIFIED



- NOTES: UNLESS OTHERWISE SPECIFIED  
101. ALL DIMENSIONS ARE IN INCHES.
102. APPLICABLE STANDARDS AND SPECIFICATIONS:  
ASME Y14.5M-1994, DIMENSIONING AND TOLERANCING  
ASME Y14.38, ABBREVIATIONS AND ACRONYMS  
ASME Y14.36M, SURFACE TEXTURE SYMBOLS  
ANSI AWS A2.4, STANDARD SYMBOLS FOR WELDING
103. 63 FINISH ALL MACHINED SURFACES PER ASME B46.1, SURFACE TEXTURE.
104. REMOVE ALL BURRS AND BREAK EDGES. 010 .030 CHAMFER OR RADIUS. RADI MUST MAKE A SMOOTH TRANSITION WITH ADJACENT SURFACES.
105. PERMANENTLY MARK PART PER MEL98-001 WITH DRAWING NUMBER, TABULATION NUMBER, REVISION LETTER, MANUFACTURER CAGE CODE AND PART SERIAL NUMBER IF APPLICABLE. APPROXIMATELY WHERE TO BE APPROVED BY LINE PRIOR TO MARKING PART.
106. BAG AND TAG PART WITH DRAWING NUMBER, TABULATION NUMBER, REVISION LETTER, MANUFACTURER CAGE CODE, AND PART SERIAL NUMBER IF APPLICABLE.
108. ESTIMATED WEIGHT IS .010 LB  
ESTIMATED VOLUME: 2.11 in<sup>3</sup>  
ESTIMATED SURFACE AREA: 3.541 in<sup>2</sup>
- IDENTIFICATION  
502. ENGRAVE DRAWING NUMBER, TABULATION NUMBER, REVISION LETTER, MANUFACTURER CAGE CODE AND PART SERIAL NUMBER IF APPLICABLE. APPROX WHERE SHOWN IN .125 HIGH CHARACTERS PER MEL98-001.



UNLIMITED DISTRIBUTION/CLASSIFICATION: UNCLASSIFIED

08:39 AM

MODEL: LEA09-500016.rvt

INVENTOR: 2011

CLASSIFICATION:  
UNCLASSIFIED

Status: QUOTATION Who:   
Fabrication Quantity: 1 EACH TAB   
Project / Task Number:   
Due: 5/13/2010

THIS DRAWING WAS CREATED BY THE LAWRENCE LIVERMORE NATIONAL SECURITY, LLC (LLNS) WHICH OPERATES LAWRENCE LIVERMORE NATIONAL LABORATORY (LLNL) FOR THE U.S. DEPARTMENT OF ENERGY UNDER CONTRACT NO. DE-AC02-07NA27344. ANY REPRODUCTION, DISSEMINATION AND/OR FABRICATION IS PROHIBITED WITHOUT THE PERMISSION OF COGNIZANT LLNS PERSONNEL.

QTY	PART OR IDENTIFYING NUMBER	MATERIAL DESCRIPTION OR NOMENCLATURE	DATE	TITLE	SCALE
1	LEA09-500016 -02	MACOR	5/8/2010	ARC INITIATION EXPER	2
1	LEA09-500016 -01	PEEK, UNFILLED	5/8/2010	ARC CHAMBER	2
			5/8/2010	HEMI INSULATOR	2

DATE	BY	DESCRIPTION
5/8/2010	TANG23	DESIGN
5/8/2010	TANG23	DESIGN
5/8/2010	TANG23	DESIGN
5/8/2010	TANG23	DESIGN
5/8/2010	TANG23	DESIGN



CONTRACT NO:   
DRAFTER:   
CHECKED BY:   
DATE:   
TITLE:   
SCALE:   
DRAWING NUMBER:   
PROJECT:   
CAGE CODE:   
PART NUMBER:   
REV:   
DATE:   
BY:   
DESCRIPTION:

UNLESS OTHERWISE SPECIFIED DIMENSIONS ARE IN INCHES. TOLERANCES ARE: DECIMALS ± .005 ANGLES ± 1° DO NOT SCALE FROM DRAWING NEXT ASSEMBLY USED ON



LAWRENCE LIVERMORE NATIONAL LABORATORY

LAWRENCE LIVERMORE NATIONAL SECURITY, LLC

UNCLASSIFIED

ARC INITIATION EXPER

ARC CHAMBER

HEMI INSULATOR

DATE: 5/8/2010

BY: TANG23

DESCRIPTION: DESIGN

SCALE: 2:000



7

6

5

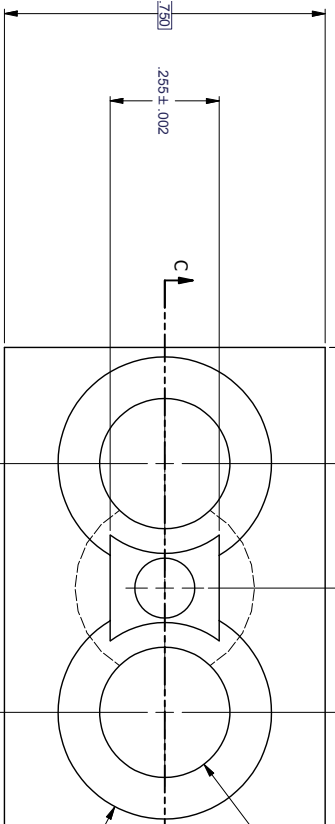
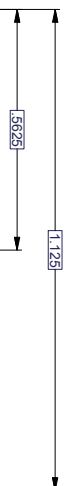
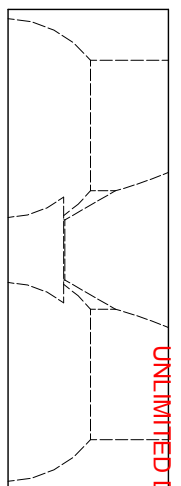
4

3

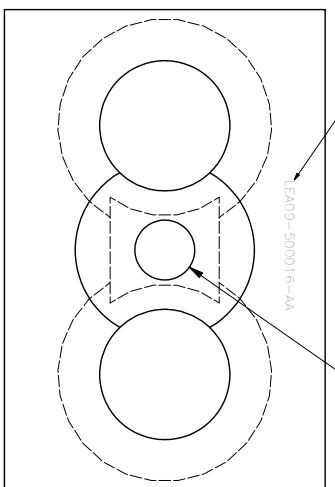
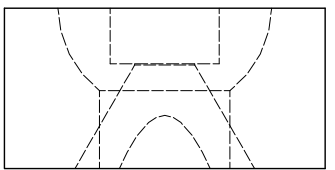
2

CLASSIFICATION:  
UNCLASSIFIED

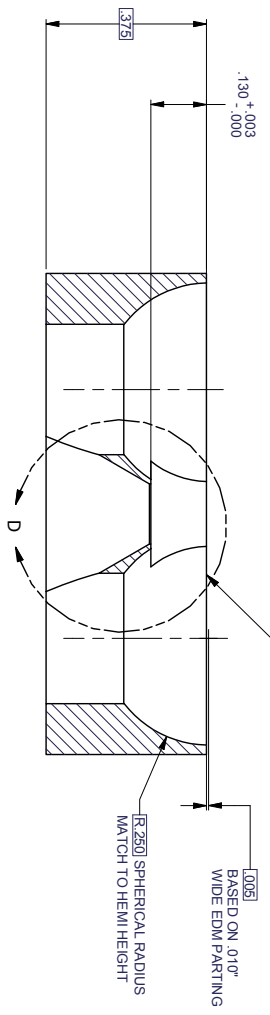
UNLIMITED DISTRIBUTION/CLASSIFICATION: UNCLASSIFIED



Ø.4899  
BASED ON .010"  
WIDE EDM PARTING  
Ø.500 SPHERE



SEE NOTE 502

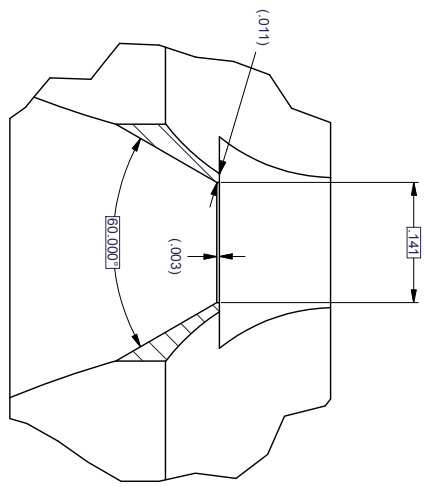


HEMISPHERE SHALL BE FLUSH  
OR .002 MAX. ABOVE FACE

Ø.005  
BASED ON .010"  
WIDE EDM PARTING

R.250 SPHERICAL RADIUS  
MATCH TO HEMI HEIGHT

SECTION C-C  
SCALE 6



DETAIL D  
SCALE 12 : 1

UNLIMITED DISTRIBUTION/CLASSIFICATION: UNCLASSIFIED

CLASSIFICATION: UNCLASSIFIED

09:08 AM

MODEL: LEA09-50016-AA

INVENTOR: 2011

CLASSIFICATION:  
UNCLASSIFIED

CONTRACT NO.		DRAWING NUMBER	
D 14067		LEA09-500016-AA	
SCALE		2.000	
WBS		Beam Research	

7

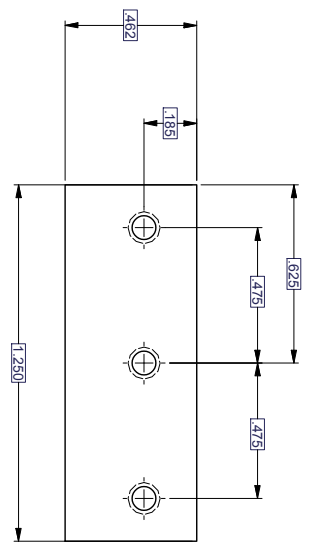
6

5

4

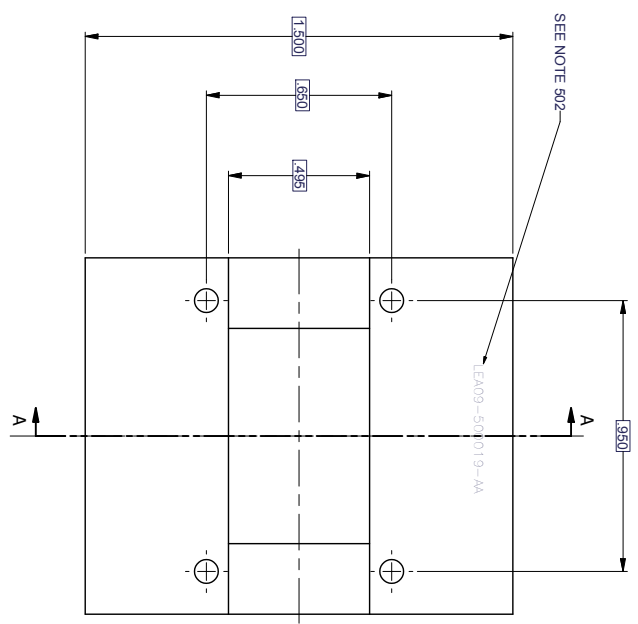
3

2



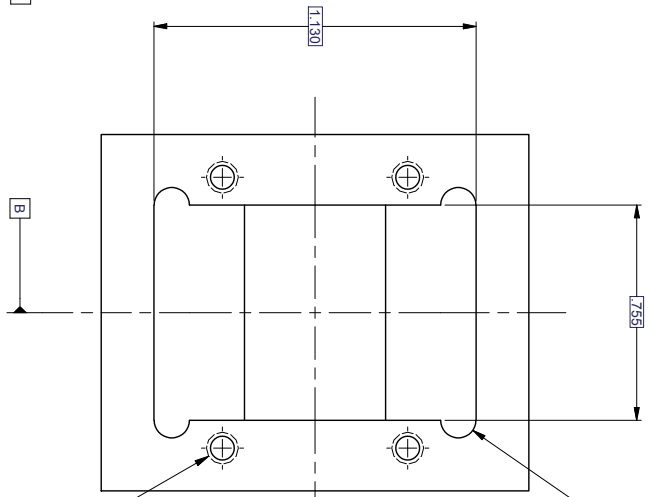
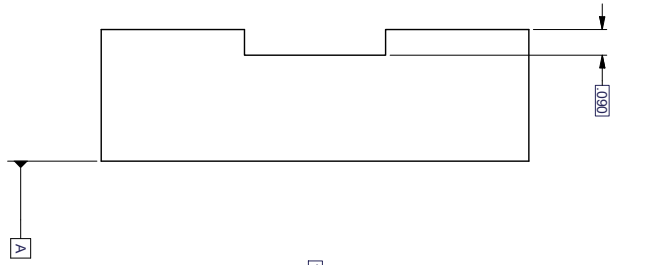
CLASSIFICATION:  
UNCLASSIFIED

UNLIMITED DISTRIBUTION/CLASSIFICATION: UNCLASSIFIED



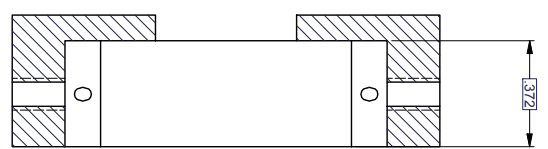
SEE NOTE 502

LEA09-500019-AA

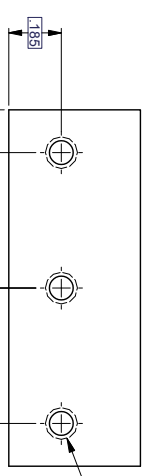


R.0063 MAX  
ZERO RADIUS  
CORNER

4-40 UNC - 2B 4X THRU



SECTION A-A  
SCALE 4



4-40 UNC - 2B T .200 6X

UNLIMITED DISTRIBUTION/CLASSIFICATION: UNCLASSIFIED

ALL MACHINED FEATURES  
0.0025 A B C  
ALL CIRCULAR HOLES: +.010  
-.002 A B C

CLASSIFICATION: UNCLASSIFIED

CONTRACT NO.	WBS
SIZE	DRAWING NUMBER
D	14067 LEA09-50
SCALE	2.000

7

6

5

4

3

2

CLASSIFICATION:  
UNCLASSIFIED

UNLIMITED DISTRIBUTION/CLASSIFICATION: UNCLASSIFIED

QTY	PART NUMBER	DESCRIPTION	ILLN
1	IEA09-500034	OPTICAL LINER ADHESIVE	ILLN
1	ANSI B18.3 - No. 8 - 32 UNC - 1/4 HS NCS	Hexagon Socket Head Cap Screw	ILLN
1	IEA09-500033	GROUND WRAP	ILLN
1	IEA09-500031	GROUND INSULATOR	ILLN
1	IEA09-500029	RIBBON CLAMP	ILLN
1	IEA09-500024	INSULATING SHEET	ILLN
1	IEA09-500028	GROUND LEAD ASSY	ILLN
1	IEA09-500026	HV LEAD ASSEMBLY	ILLN
1	IEA09-500022	CLAMPING PLATE	ILLN
2	Ball Steel X572519	CANTED COIL SPRING, 100MB-(210)-316BRT-SQW-2, 501 X 056 X .007" WIRE	BALL SEA
8	ANSI B18.3 - No. 4 - 40 UNC - 3/8	Hexagon Socket Head Cap Screw	ILLN
2	IEA09-500012	TEFLON TAPE	ILLN
1	IEA09-500014	SAMPLING SLIDE	ILLN
1	IEA09-500019	INSULATOR HOUSING	ILLN
1	IEA09-500017	OPTICAL LINER	ILLN
2	IEA09-500015	ELECTRODE	ILLN
1	IEA09-500018	HEMI INSULATOR	ILLN

UNLIMITED DISTRIBUTION/CLASSIFICATION: UNCLASSIFIED

CLASSIFICATION:  
UNCLASSIFIED

10:46 AM MODEL: LEA09-500030.dwg INVENTOR: 2011

CLASSIFICATION: UNCLASSIFIED

Beam Research

CONTRACT NO. 14067 DRAWING NUMBER LEA09-50

SCALE 2:000

7

6

5

4

3

2

UNLIMITED DISTRIBUTION/CLASSIFICATION: UNCLASSIFIED

UNLIMITED DISTRIBUTION/CLASSIFICATION: UNCLASSIFIED  
for protection

CONTRACT NO		WBS	
SIZE	CODE	SCALE	DRAWING NUMBER
D	14067	2,000	

7

6

5

4

3

2

7

6

5

4

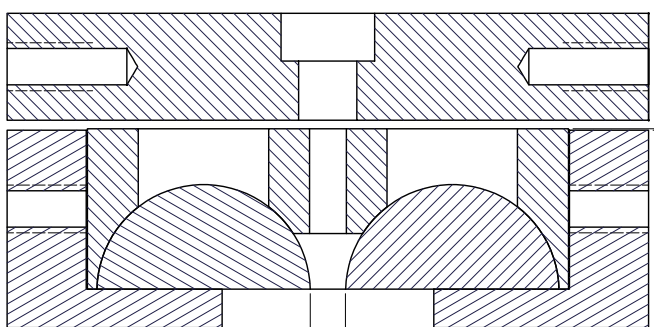
3

2

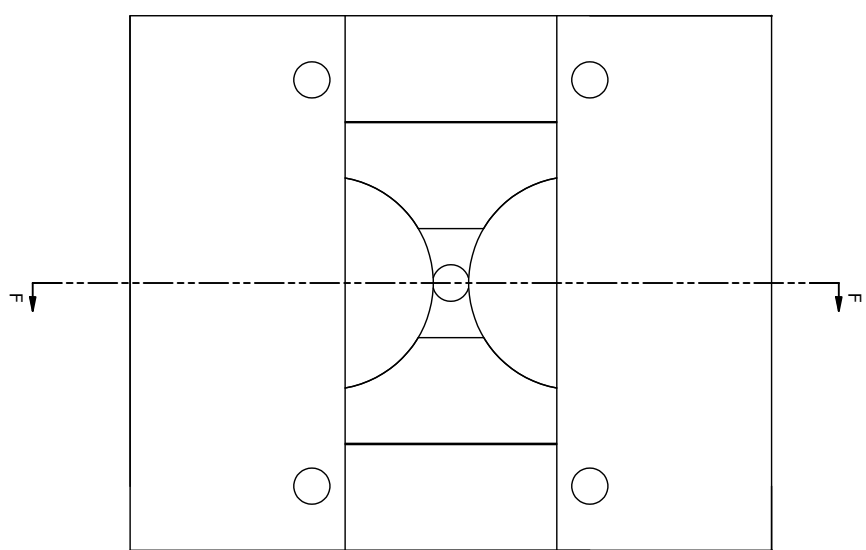
CLASSIFICATION:  
UNCLASSIFIED

UNLIMITED DISTRIBUTION/CLASSIFICATION:UNCLASSIFIED

(.003)  
INSPECT  
CHECK FOR GAP  
MAY BE FLUSH  
OR PROUD BY .005"



SECTION F-F  
SCALE 6



UNLIMITED DISTRIBUTION/CLASSIFICATION:UNCLASSIFIED

CLASSIFICATION: UNCLASSIFIED

08:52 AM  
MODEL: LEA09-50020.0sm  
INVENTOR: 2011

7

6

5

4

3

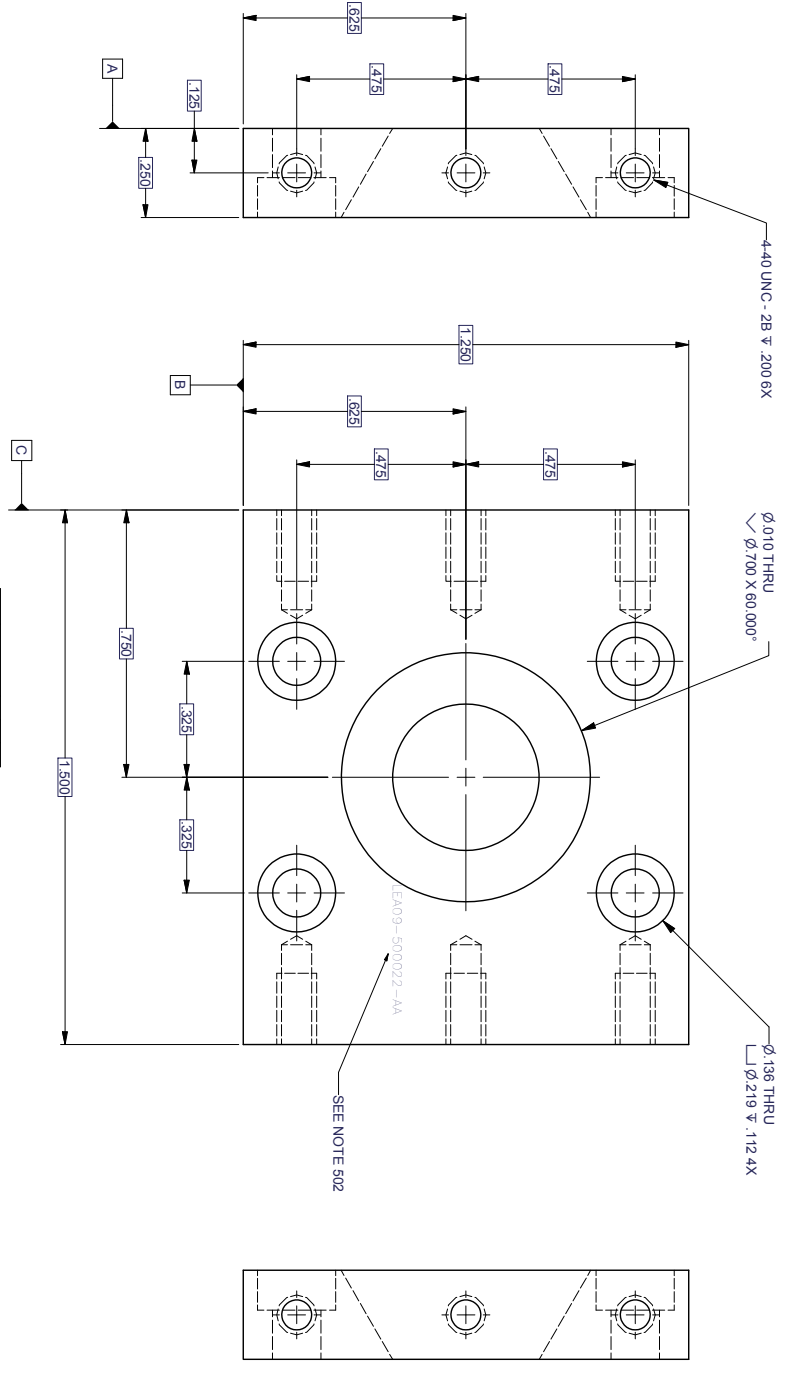
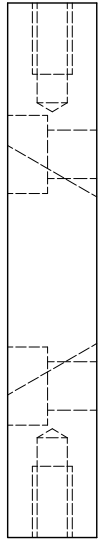
2

CLASSIFICATION:  
UNCLASSIFIED

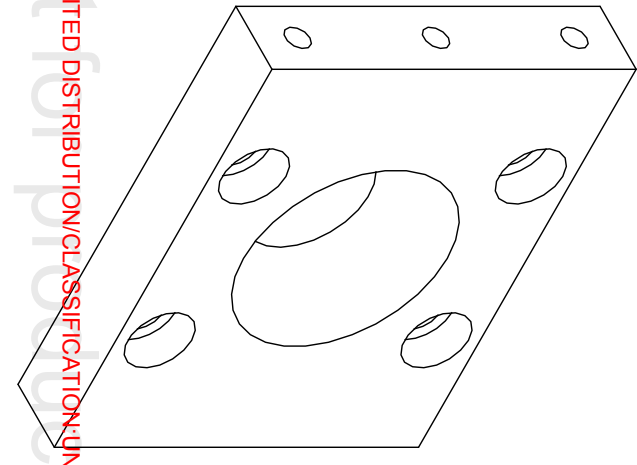
<b>Beam Research</b>	
VBS	
CONTRACT NO.	DRAWING NUMBER
SIZE	DRAWING NUMBER
D	14067 LEA09-50
SCALE	2:000

OTHERWISE SPECIFIED DIMENSIONS ARE IN INCHES.	7	6	5	4	3	2
STANDARDS AND SPECIFICATIONS: M-1994, DIMENSIONING AND TOLERANCING ASME Y14.5-1994, DIMENSIONS AND TOLERANCES MACHINING SURFACES AND FINISHES ASME Y14.4-1994, STANDARD SYMBOLS FOR WELDING MACHINING SURFACES PER ASME B46.1, FINISH TEXTURE.						
BURRS AND BREAK EDGES: 0.010 R OR RADIUS, RADI A SMOOTH TRANSITION WITH ADJACENT SURFACES.						
1. Y MARK PART PER MEL 98-001 WITH DRAWING TABULATION NUMBER, REVISION LETTER, MANUFACTURER CAGE PART SERIAL NUMBER IF APPLICABLE APPROXIMATELY WHERE 125 HIGH CHARACTERS, MARKING PROCESS LOVED BY L1N1 PRIOR TO MARKING PART.						
G PART WITH DRAWING NUMBER, TABULATION NUMBER, LETTER, MANUFACTURER CAGE CODE, AND PART SERIAL APPLICABLE.						
WEIGHT IS: 0.18 lb VOLUME: 0.272 in <sup>3</sup> SURFACE AREA: 5.993 in <sup>2</sup>						
THE PART PER MEL 98-023, ENGINEERING MODEL BASED DRAWING, (EMBM), OF HARDWARE USING COMPUTER GENERATED FILES, DISREGARD MODEL TOLERANCES. DIMENSIONS ARE BASIC HAVING A PROFILE TOLERANCE OF ±0.005 PER ASME Y14.5M-1994.						
HING - PER MEL 99-009 G-II.						
DRAWING NUMBER, TABULATION NUMBER, REVISION LETTER, PART CAGE CODE AND PART SERIAL NUMBER IF APPLICABLE APPROX. DIMENSIONS ARE BASIC HAVING A PROFILE TOLERANCE OF ±0.005 PER ASME Y14.5M-1994.						

UNLIMITED DISTRIBUTION/CLASSIFICATION: UNCLASSIFIED



UNLIMITED DISTRIBUTION/CLASSIFICATION: UNCLASSIFIED



MODEL: LEA09-500022-41  
INVENTOR: 2011  
DATE: 5/13/2010  
DUE: 5/13/2010

CLASSIFICATION: UNCLASSIFIED

STATUS: QUOTATION Who:   
Fabrication Quantity: 1

THIS DRAWING WAS CREATED BY THE LAWRENCE LIVERMORE NATIONAL SECURITY, LLC (LLNS) WHICH OPERATES LAWRENCE LIVERMORE NATIONAL LABORATORY (LLNL) FOR THE U.S. DEPARTMENT OF ENERGY UNDER CONTRACT NO. DE-AC02-07NA27344. ANY REPRODUCTION, DISSEMINATION AND/OR FABRICATION IS PROHIBITED WITHOUT THE PERMISSION OF COGNIZANT LLNS PERSONNEL.

ZONE	LTR	DESCRIPTION	REVISIONS	DATE	BY
1	AA	INITIAL RELEASE	HAWKINS4	TANG23	TA

1	PART OR IDENTIFICATION NUMBER	PEEK, UNFILLED
2	MATERIAL DESCRIPTION OR IDENTIFICATION	

CLASSIFICATION: UNCLASSIFIED

Beam Research WBS

CONTRACT NO	DATE	TITLE
AWARD NO	5/8/2010	ARC INITIATION EXPER
ORGANIZATION	5/8/2010	ARC CHAMBER
AWARD NO	5/8/2010	CLAMPING PLATE
ORGANIZATION	5/8/2010	
AWARD NO	5/8/2010	
ORGANIZATION	5/8/2010	

UNLESS OTHERWISE SPECIFIED DIMENSIONS IN INCHES. TOLERANCES ARE: DIMENALS  $\pm$  .005 ANGLES  $\pm$  1° DO NOT SCALE FROM DRAWING

SCALE: 2.000

OTHERWISE SPECIFIED  
 DIMENSIONS ARE IN INCHES.

STANDARDS AND SPECIFICATIONS:  
 M-1894, DIMENSIONING AND TOLERANCING  
 18, ABBREVIATIONS AND ACRONYMS  
 604, SURFACE FINISH SYMBOLS  
 A2.4, STANDARD SYMBOLS FOR WELDING  
 L MACHINED SURFACES PER ASME B46.1, EXTURE.

BURRS AND BREAK EDGES .010  
 R OR RADIUS . RADI  
 A SMOOTH TRANSITION WITH ADJACENT SURFACES.

1. Y MARK PART PER MEL 98-001 WITH DRAWING  
 TABULATION NUMBER, REVISION LETTER, MANUFACTURER CAGE  
 PART SERIAL NUMBER IF APPLICABLE, APPROXIMATELY WHERE  
 125 HIGH CHARACTERS, MARKING PROCESS  
 OVED BY LNLT PRIOR TO MARKING PART.

G PART WITH DRAWING NUMBER, TABULATION NUMBER,  
 LETTER, MANUFACTURER CAGE CODE, AND PART SERIAL  
 APPLICABLE.

WEIGHT IS .001 LB  
 VOLUME .002 IN<sup>3</sup>  
 SURFACE AREA .10780 IN<sup>2</sup>

IRE PART PER MEL98-023, ENGINEERING MODEL BASED  
 URING, (EMBM), OF HARDWARE USING COMPUTER GENERATED  
 ELS. DISREGARD MODEL TOLERANCES.

IONS ARE BASIC HAVING A PROFILE TOLERANCE OF  
 (SME Y14.5M-1994.

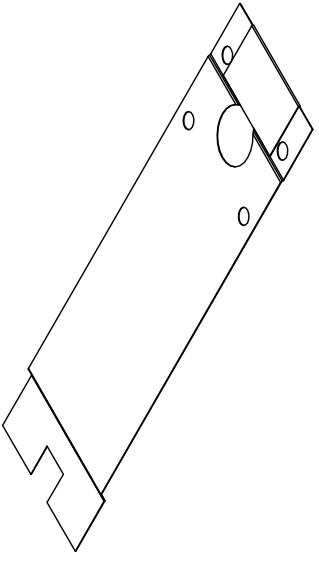
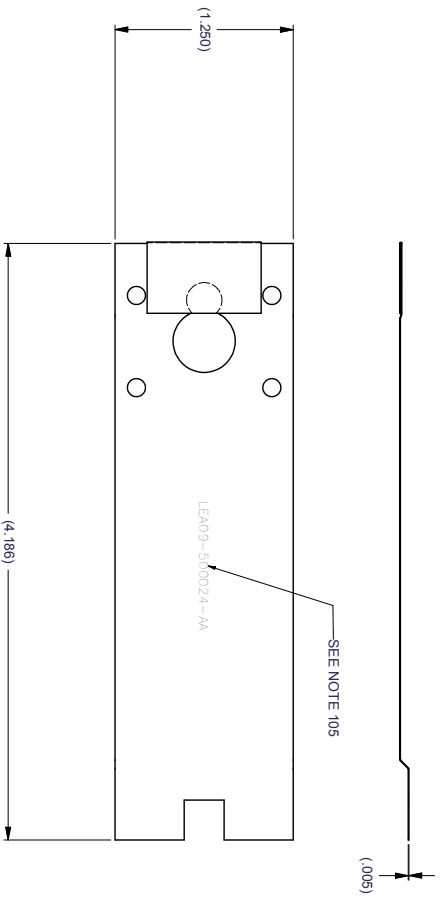
HING  
 - PER MEL99-009 G-II.

DRAWING NUMBER, TABULATION NUMBER, REVISION LETTER,  
 JER CAGE CODE AND PART SERIAL NUMBER IF APPLICABLE APPROX.  
 200 IN .125 HIGH CHARACTERS PER MEL98-001.

CLASSIFICATION:  
 UNCLASSIFIED

UNLIMITED DISTRIBUTION/CLASSIFICATION: UNCLASSIFIED

ZONE	LTR	DESCRIPTION	REVISIONS	DRAWN	CHECKED	APP
/	AA	INITIAL RELEASE		hank4	TANG23	TM



UNLIMITED DISTRIBUTION/CLASSIFICATION: UNCLASSIFIED

CLASSIFICATION:  
 UNCLASSIFIED

Status: RELEASED Who: BRAD HICKMAN  
 Fabrication Quantity: 4 Date: 9/27/2010  
 Project Task Number: 32900/89829 Due: 9/27/2010

THIS DRAWING WAS CREATED BY THE  
 LAWRENCE LIVERMORE NATIONAL SECURITY, LLC  
 (LLNS) WHICH OPERATES LAWRENCE  
 LIVERMORE NATIONAL LABORATORY (LLNL)  
 FOR THE U.S. DEPARTMENT OF ENERGY UNDER  
 CONTRACT NO. DE-AC52-07NA27344.  
 ANY REPRODUCTION, DISSEMINATION AND/OR  
 FABRICATION IS PROHIBITED WITHOUT THE  
 PERMISSION OF COGNIZANT LLNS PERSONNEL.

QTY	PART OR IDENTIFYING NUMBER	POLYIMIDE	MATERIAL DESCRIPTION/DESCRIPTION	W/
1				

CLASSIFICATION: UNCLASSIFIED

THIRD ANGLE PROJECTION	INCH	CONTRACT NO	CLASSIFIED BY	DATE	TITLE	LAWRENCE LIVERMORE NATIONAL LABORATORY
					ARC INITIATION EXPER	

UNLESS OTHERWISE SPECIFIED	ORGANIZATION	DATE	SIZE	DRAWING NUMBER
DIMENSIONS IN INCHES TOLERANCES ARE: DIMENSIONS ± .005 ANGLES ± 1° DO NOT SCALE FROM DRAWING	LLNL	9/27/10	D	LEA09-500024-AA
CHECKED	TANG23	9/27/10		
APPROVED	TANG23	9/27/10		
DATE	9/27/10			
SCALE	14067			
SCALE	2:000			

7

6

5

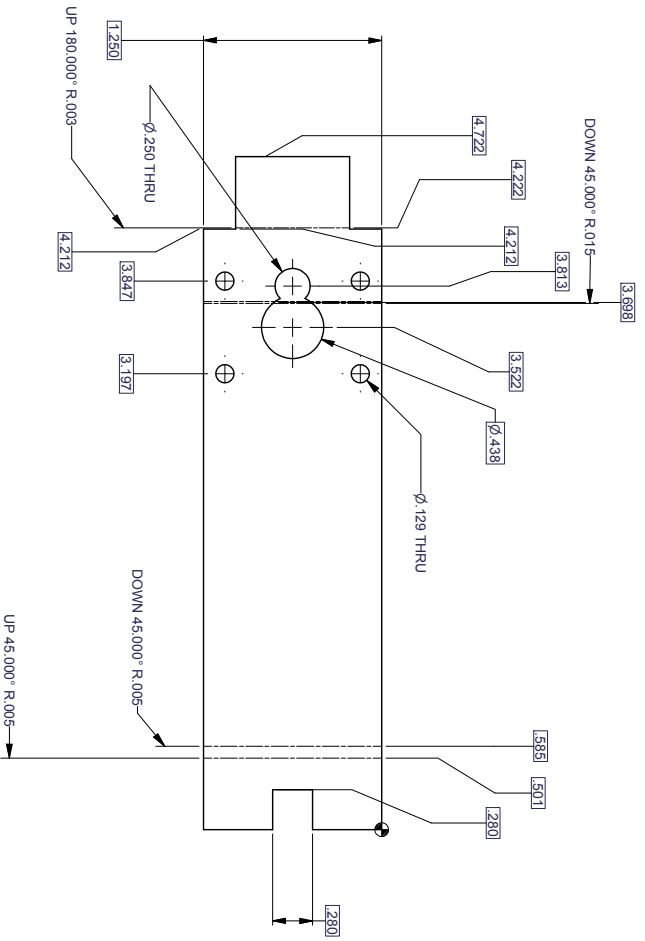
4

3

2

CLASSIFICATION:  
UNCLASSIFIED

UNLIMITED DISTRIBUTION/CLASSIFICATION:UNCLASSIFIED



UNLIMITED DISTRIBUTION/CLASSIFICATION:UNCLASSIFIED



11:58 AM

MODEL: LEA09-50024.dwg

INVENTOR: 2011

7

6

5

4

3

2

CLASSIFICATION:  
UNCLASSIFIED

CLASSIFICATION: UNCLASSIFIED

<b>Beam Research</b>	
VBS	
CONTRACT NO.	DRAWING NUMBER
SIZE	DRAWING NUMBER
D	14067 LEA09-50
SCALE	2.000



7

6

5

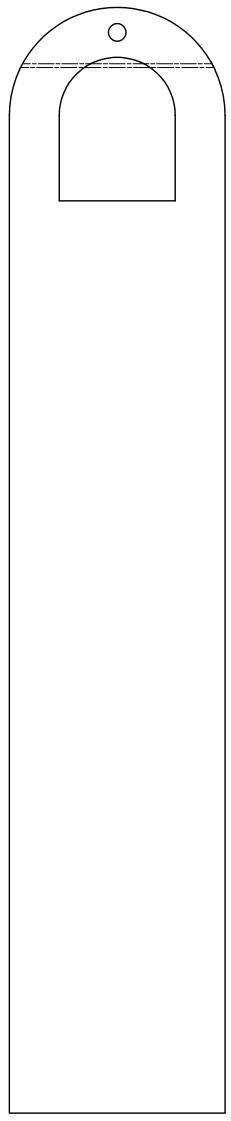
4

3

2

CLASSIFICATION:  
UNCLASSIFIED

UNLIMITED DISTRIBUTION/CLASSIFICATION:UNCLASSIFIED



UNLIMITED DISTRIBUTION/CLASSIFICATION:UNCLASSIFIED

11:18 AM

MODEL: LEA09-50027.dwg

7

INVENTOR: 2011

6

CLASSIFICATION:  
UNCLASSIFIED

5

4

3

2

CLASSIFICATION: UNCLASSIFIED



WBS

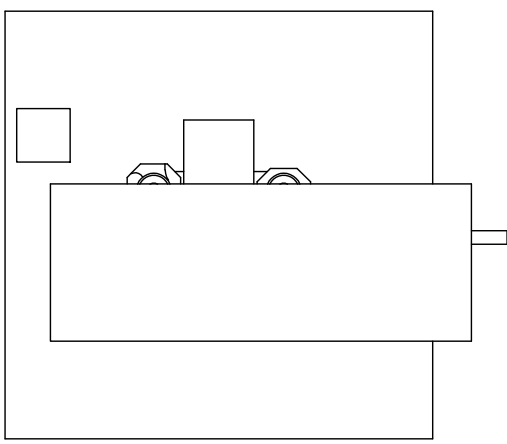
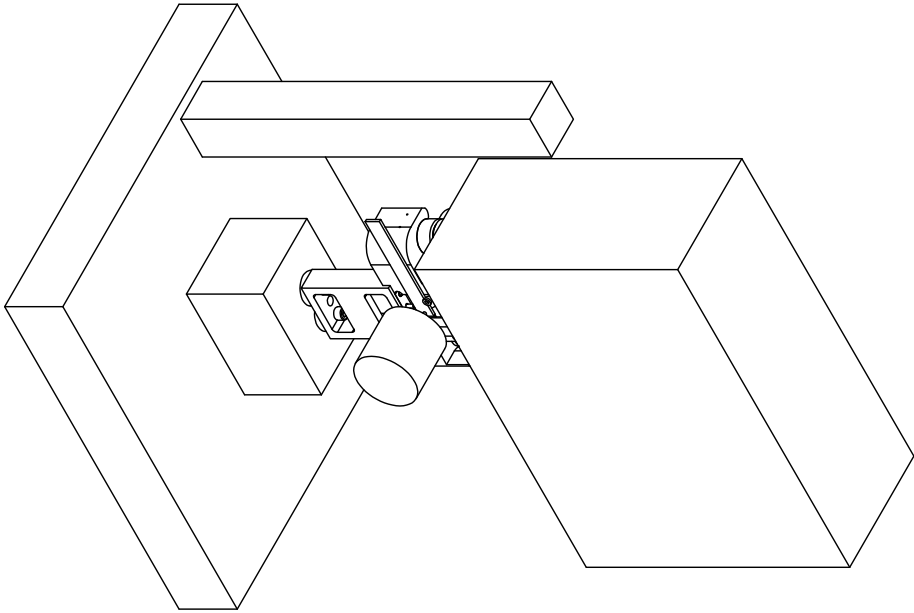
CONTRACT NO.	SIZE	COLOR CODE	DRAWING NUMBER
	D	14067	LEA09-50
	SCALE	2:000	



CLASSIFICATION:  
UNCLASSIFIED

ZONE	LTR	DESCRIPTION	REVISIONS	CHECKED	APP
/	AA	INITIAL RELEASE	HAWKINS4	TANG23	TM

UNLIMITED DISTRIBUTION/CLASSIFICATION: UNCLASSIFIED



QTY	REF DES	PART NUMBER	DESCRIPTION
1		LEA09-500050	BRACKET SPACER
2		ANSI B18.3 - 1/4 - 20	Hexagon Socket Head Cap Screw
3		UNC - 3/4 HS HCS	Hexagon Socket Head Cap Screw
1		ANSI B18.3 - No. 4 - 40	UNC - 1/2 HS HCS
1		LEA09-500035	MOUNTING BRACKET
1		LEA09-500032	POWER SUPPLY
1		LEA09-500020	ARC CHAMBER ASSEMBLY
1		LEA09-500030	EXISTING CONDITIONS
			PARTS LIST

CLASSIFICATION: UNCLASSIFIED

UNLIMITED DISTRIBUTION/CLASSIFICATION: UNCLASSIFIED

02:29 PM  
MODEL: LEA09-500031 Rev  
INVENTOR: 2011

CLASSIFICATION:  
UNCLASSIFIED

Status: Who: Done: Done:  
Fabrication Quantity: Project / Task Number:  
THIS DRAWING WAS CREATED BY THE LAWRENCE LIVERMORE NATIONAL SECURITY, LLC (LLNL) WHICH OPERATES LAWRENCE LIVERMORE NATIONAL LABORATORY (LLNL) FOR THE U.S. DEPARTMENT OF ENERGY UNDER CONTRACT NO. DE-AC02-07NA27344. ANY REPRODUCTION, DISSEMINATION AND/OR FABRICATION IS PROHIBITED WITHOUT THE PERMISSION OF COGNIZANT LLNS PERSONNEL.

THIRD ANGLE PROJECTION	INCH	CONTRACT NO	CLASSIFIED BY	DATE	TITLE
		LEA09-500031	TANG23	5/20/10	ARC INITIATION EXPER
			HAWKINS4	5/20/10	ARC CHAMBER
			TANG23	5/20/10	INSTALLATION DIAGRA
			TANG23	5/20/10	
			DRW/CHK/APP	5/20/10	
			ED	5/20/10	
			USED ON	5/20/10	
			SCALE	D	14067
			SCALE	← 2:000 →	LEA09-50

OTHERWISE SPECIFIED	7	6	5	4	3	2
IONS ARE IN INCHES.						
CLASSIFICATION: UNCLASSIFIED						
ZONE /	LTR	DESCRIPTION	REVISIONS	CHECKED	APP	
AA		INITIAL RELEASE	hank4	TANG23	TM	

UNLIMITED DISTRIBUTION/CLASSIFICATION: UNCLASSIFIED

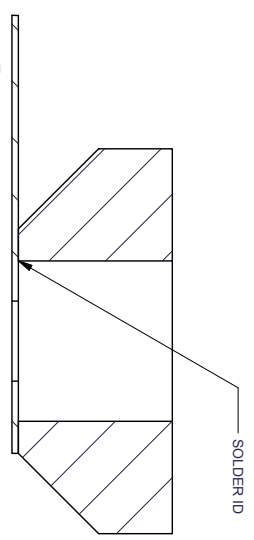
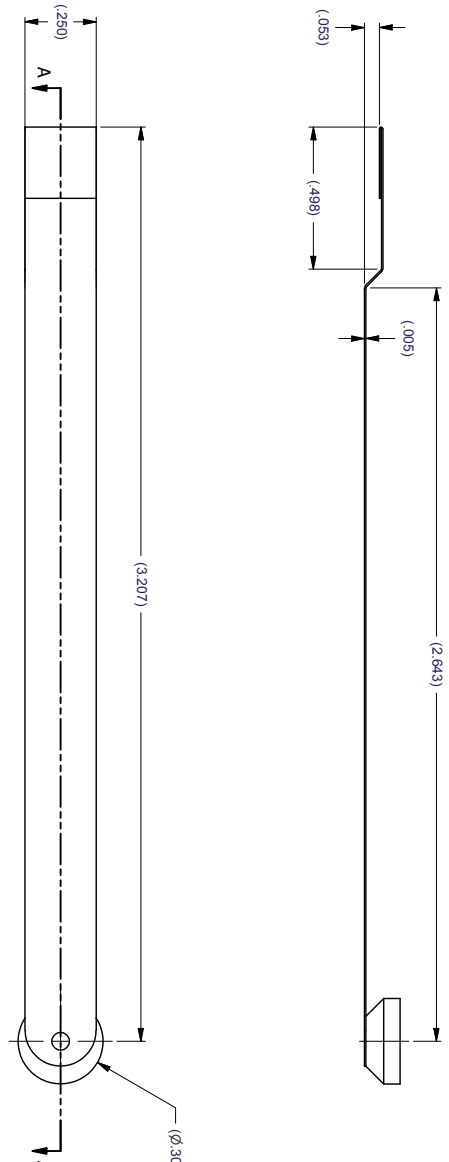
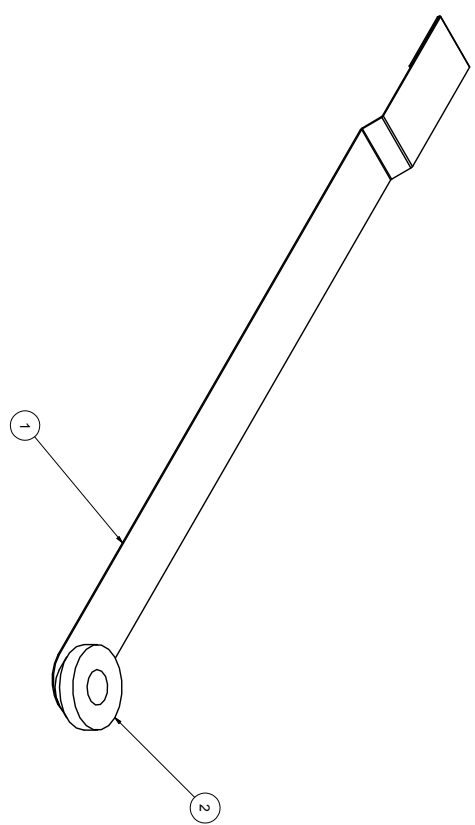
STANDARDS AND SPECIFICATIONS:  
 M-1894, DIMENSIONING AND TOLERANCING  
 18, ABBREVIATIONS AND ACRONYMS  
 10M, SURFACE FINISH SYMBOLS  
 42.4, STANDARD SYMBOLS FOR WELDING  
 L MACHINED SURFACES PER ASME B46.1, EXTURE.

BURRS AND BREAK EDGES .010  
 R OR RADIUS, RADI  
 A SMOOTH TRANSITION WITH ADJACENT SURFACES.

1.Y MARK PART PER MEL 98-001 WITH DRAWING  
 TABULATION NUMBER, REVISION LETTER, MANUFACTURER CAGE  
 PART SERIAL NUMBER IF APPLICABLE, APPROXIMATELY WHERE  
 125 HIGH CHARACTERS, MARKING PROCESS  
 OVED BY L1NL PRIOR TO MARKING PART.

G PART WITH DRAWING NUMBER, TABULATION NUMBER,  
 LETTER, MANUFACTURER CAGE CODE, AND PART SERIAL  
 APPLICABLE.

WEIGHT IS .01b  
 VOLUME IS .01in<sup>3</sup>  
 SURFACE AREA, 2.0 in<sup>2</sup>



UNLIMITED DISTRIBUTION/CLASSIFICATION: UNCLASSIFIED

DETAIL B  
 SCALE 18

CLASSIFICATION:  
 UNCLASSIFIED

Status: RELEASED Who: VINCENT TANG Date: 5/19/2010  
 Fabrication Quantity: 1 Project Task Number:

THIS DRAWING WAS CREATED BY THE  
 LAWRENCE LIVERMORE NATIONAL SECURITY, LLC  
 (LLNL) WHICH OPERATES LAWRENCE  
 LIVERMORE NATIONAL LABORATORY (LLNL)  
 FOR THE U.S. DEPARTMENT OF ENERGY UNDER  
 CONTRACT NO. DE-AC02-07NA27344.  
 ANY REPRODUCTION, DISSEMINATION AND/OR  
 FABRICATION IS PROHIBITED WITHOUT THE  
 PERMISSION OF COGNIZANT LLNS PERSONNEL.

1	LEA09-500013	CONTRACT	LLNL
1	LEA09-500025	HV CONDUCTOR	LLNL
QTY	PART NUMBER	DESCRIPTION	
PARTS LIST			

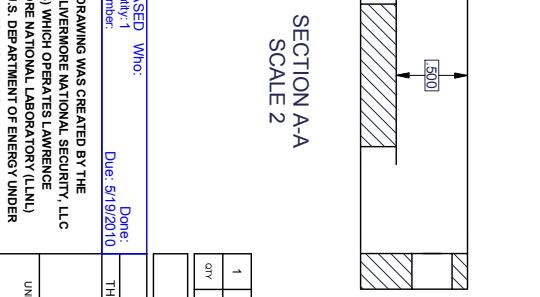
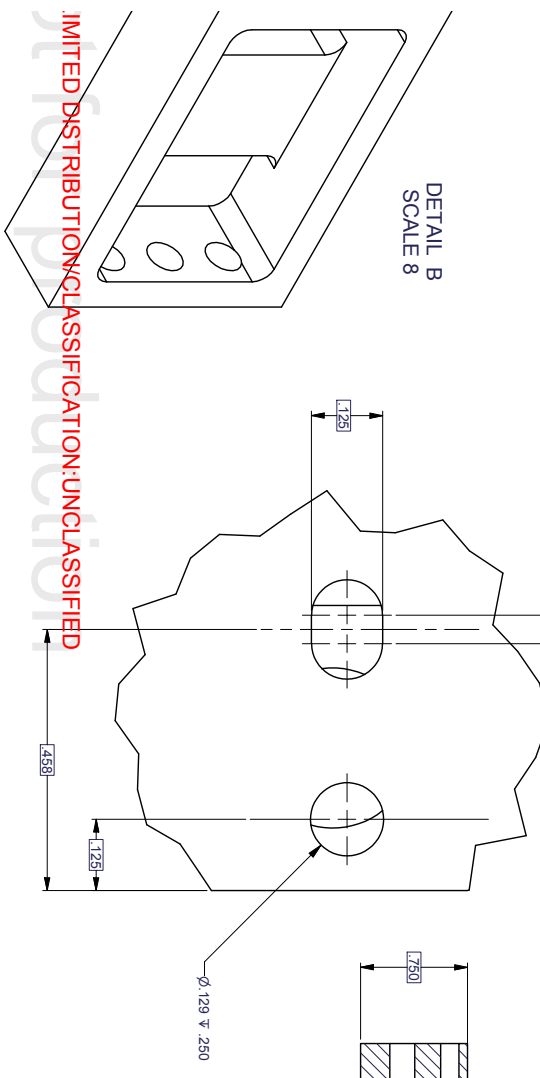
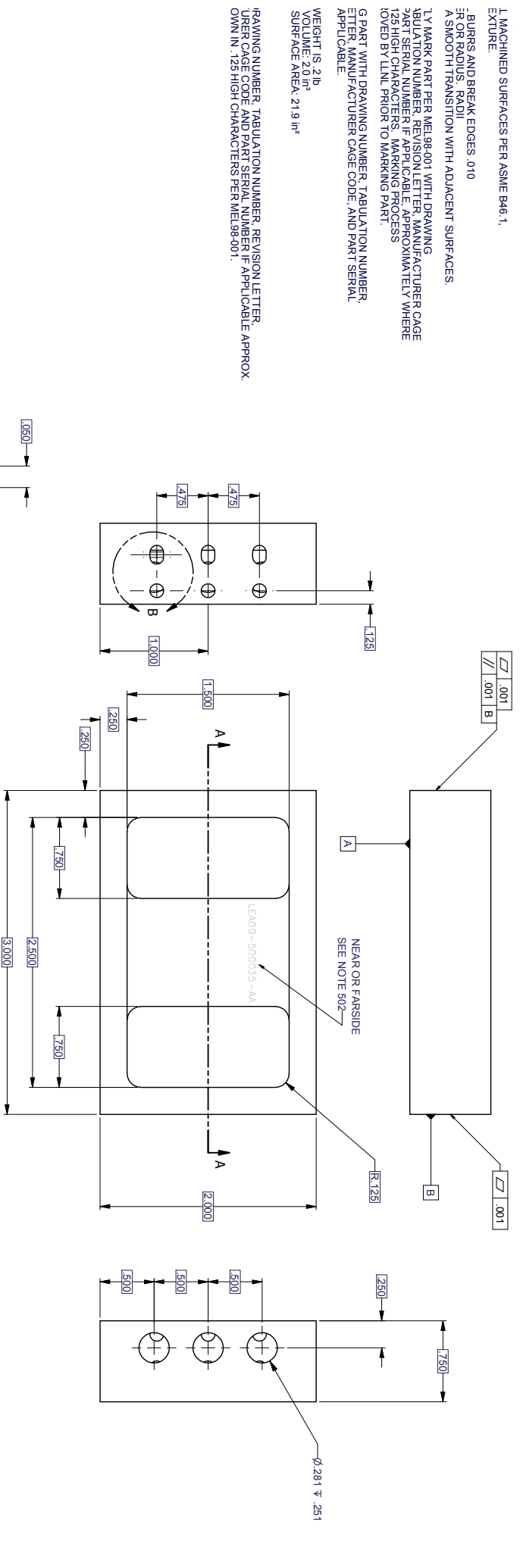
CLASSIFICATION: UNCLASSIFIED

THIRD ANGLE PROJECTION



UNLESS OTHERWISE SPECIFIED DIMENSIONS IN THIS DRAWING TOLERANCES ARE: DO NOT SCALE FROM DIMENSIONS	ORGANIZATION LAWRENCE LIVERMORE NATIONAL LABORATORY	DATE 5/20/10	TITLE ARC INITIATION EXPER
DRAWN BY TANG23	DESIGNED BY TANG23	DATE 5/20/10	TITLE ARC CHAMBER
CHECKED BY TANG23	APPROVED BY TANG23	DATE 5/20/10	TITLE HV LEAD ASSEMBLY
SCALE AS SHOWN	SCALE AS SHOWN	DATE 5/20/10	TITLE HV LEAD ASSEMBLY

UNLIMITED DISTRIBUTION/CLASSIFICATION: UNCLASSIFIED



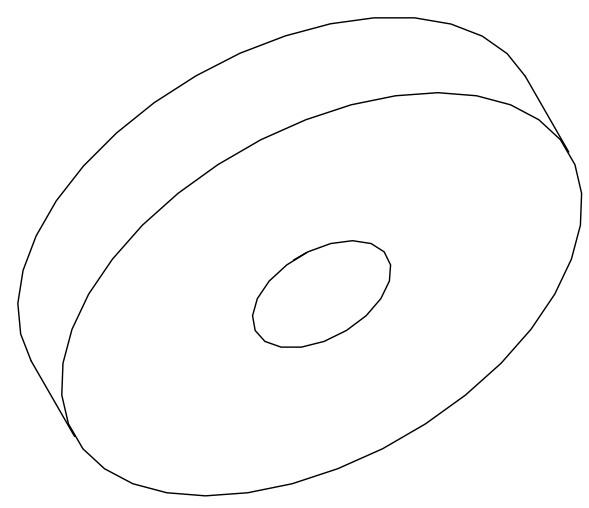
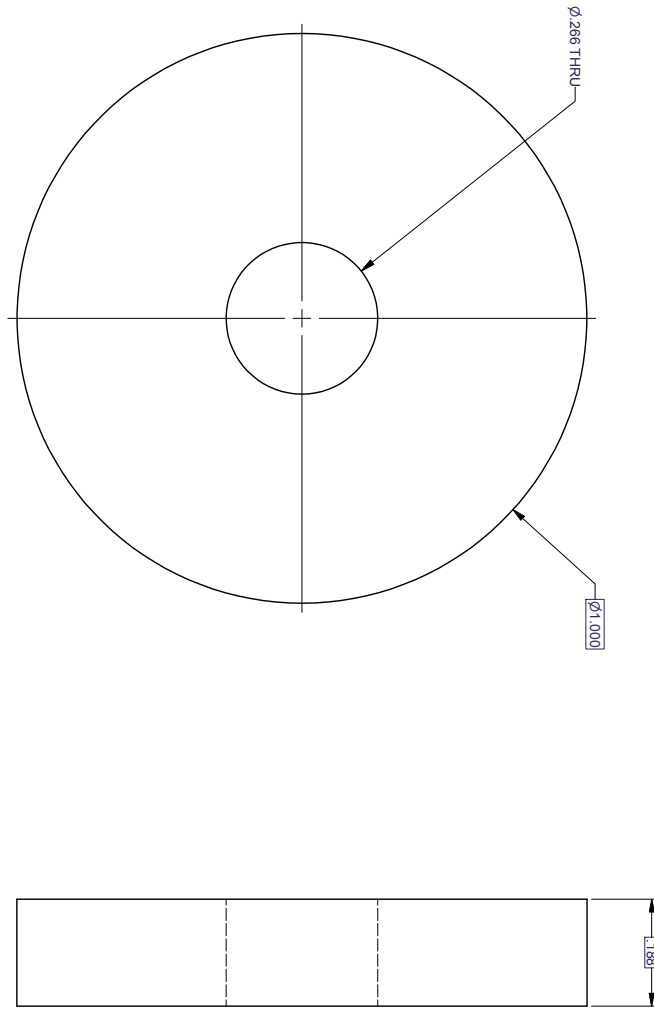
ZONE	LTR	DESCRIPTION	REVISIONS	DRAWN	CHECKED	APP
1	AA	INITIAL RELEASE		HAWKINS4	TANG23	TM

1	PART OR IDENTIFYING NUMBER	ALUMINIUM-6061-T6	
QTY	MATERIAL DESCRIPTION OR IDENTIFICATION		

STATUS: RELEASED Who: _____ Date: 5/19/2010 Fabrication Quantity: 1 Project: Task Number: _____	
THIS DRAWING WAS CREATED BY THE LAWRENCE LIVERMORE NATIONAL SECURITY, LLC (LLNS) WHICH OPERATES LAWRENCE LIVERMORE NATIONAL LABORATORY (LLNL) FOR THE U.S. DEPARTMENT OF ENERGY UNDER CONTRACT NO. DE-AC52-07NA27344. ANY REPRODUCTION, DISSEMINATION AND/OR FABRICATION IS PROHIBITED WITHOUT THE PERMISSION OF COGNIZANT LLNS PERSONNEL.	
CONTRACT NO CLASSIFIED BY TANG23 APPROVALS ORGANIZATION HAWKINS4 DATE 5/10/2010 TITLE ARC INITIATION EXPER ARC CHAMBER MOUNTING BRACKET SIZE CODE CODE 14067 DRAWING NUMBER LEA09-500035-AA SCALE 2	CONTRACT NO CLASSIFIED BY TANG23 APPROVALS ORGANIZATION HAWKINS4 DATE 5/10/2010 TITLE ARC INITIATION EXPER ARC CHAMBER MOUNTING BRACKET SIZE CODE CODE 14067 DRAWING NUMBER LEA09-500035-AA SCALE 2



UNLIMITED DISTRIBUTION/CLASSIFICATION: UNCLASSIFIED

MODEL: LEA09-60038 4" INVENTOR: 2011

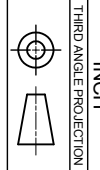
CLASSIFICATION: UNCLASSIFIED

Status: RELEASED Who: Fabrication Quantity: 2 Project Task Number: Due: 5/19/2010

THIS DRAWING WAS CREATED BY THE LAWRENCE LIVERMORE NATIONAL SECURITY, LLC (LLNS) WHICH OPERATES LAWRENCE LIVERMORE NATIONAL LABORATORY (LLNL) FOR THE U.S. DEPARTMENT OF ENERGY UNDER CONTRACT NO. DE-AC02-07NA27344. ANY REPRODUCTION, DISSEMINATION AND/OR FABRICATION IS PROHIBITED WITHOUT THE PERMISSION OF COGNIZANT LLNS PERSONNEL.

2	PART OR IDENTIFICATION NUMBER	ALUMINUM-6061-T6		
QTY		MATERIAL DESCRIPTION/IDENTIFICATION		

CLASSIFICATION: UNCLASSIFIED



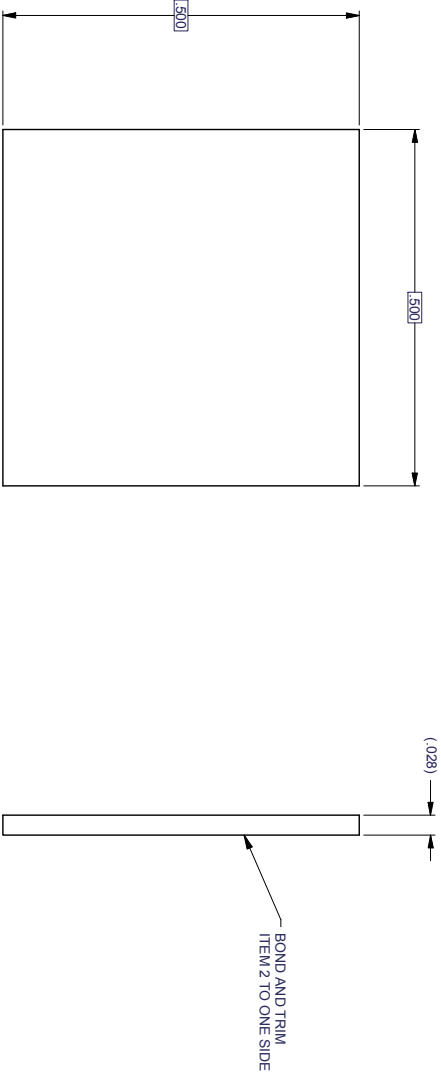
THIRD ANGLE PROJECTION		CONTRACT NO	
INCH		CLASSIFIED BY	
UNLESS OTHERWISE SPECIFIED DIMENSIONS IN THIS DRAWING ARE IN INCHES. TOLERANCES ARE: DECIMALS ± .005 ANGLES ± 1° DO NOT SCALE FROM DRAWING		APPROVALS	
DATE	TITLE	DATE	TITLE
5/10/2010	ARC INITIATION EXPERT	5/10/2010	ARC CHAMBER
5/10/2010	BRACKET SPACER	5/10/2010	BRACKET SPACER
5/10/2010	DRAWING NUMBER	5/10/2010	DRAWING NUMBER
2	SCALE	2	SCALE
2	SCALE	2	SCALE

OTHERWISE SPECIFIED  
 DIMENSIONS ARE IN INCHES.  
 STANDARDS AND SPECIFICATIONS:  
 M-1994, DIMENSIONING AND TOLERANCING  
 18, ABBREVIATIONS AND ACRONYMS  
 1001, SURFACE FINISH SYMBOLS  
 42.4, STANDARD SYMBOLS FOR WELDING  
 L MACHINED SURFACES PER ASME B46.1,  
 EXTURE.  
 BURRS AND BREAK EDGES .010  
 R OR RADIUS, RADI  
 A SMOOTH TRANSITION WITH ADJACENT SURFACES.  
 1 Y MARK PART PER MEL 98-001 WITH DRAWING  
 TABULATION NUMBER, REVISION LETTER, MANUFACTURER CAGE  
 PART SERIAL NUMBER IF APPLICABLE, APPROXIMATELY WHERE  
 125 HIGH CHARACTERS, MARKING PROCESS  
 LOVED BY L1N1 PRIOR TO MARKING PART.  
 G PART WITH DRAWING NUMBER, TABULATION NUMBER,  
 LETTER, MANUFACTURER CAGE CODE, AND PART SERIAL  
 APPLICABLE.  
 WEIGHT IS .016  
 VOLUME IS .016  
 SURFACE AREA, 6 in<sup>2</sup>  
 RE PART PER MEL98-023, ENGINEERING MODEL BASED  
 URING, (EMBM), OF HARDWARE USING COMPUTER GENERATED  
 ELS, DISREGARD MODEL TOLERANCES.  
 IONS ARE BASIC HAVING A PROFILE TOLERANCE OF  
 (SME Y14.3M-1994.  
 HING  
 - PER MEL99-009 G-II.  
 DRAWING NUMBER, TABULATION NUMBER, REVISION LETTER,  
 JER CAGE CODE AND PART SERIAL NUMBER IF APPLICABLE APPROX.  
 200 IN .129 HIGH CHARACTERS PER MEL98-001.

UNLIMITED DISTRIBUTION/CLASSIFICATION: UNCLASSIFIED

CLASSIFICATION:  
UNCLASSIFIED

ZONE	LTR	DESCRIPTION	REVISIONS	CHECKED	APP
/	AA	INITIAL RELEASE	HAWKINS4		TM



UNLIMITED DISTRIBUTION/CLASSIFICATION: UNCLASSIFIED

07:56 PM

MODEL: LEA09-600037.dwg INVENTOR: 2011

CLASSIFICATION:  
UNCLASSIFIED

Status: COMPLETE Who: STEVE HAWKINS  
 Fabrication Quantity: 2 Date: 9/29/2010  
 Project: 684 Number: 32900/89829 Due: 9/29/2010

THIS DRAWING WAS CREATED BY THE  
 LAWRENCE LIVERMORE NATIONAL SECURITY, LLC  
 (LLNS) WHICH OPERATES LAWRENCE  
 LIVERMORE NATIONAL LABORATORY (LLNL)  
 FOR THE U.S. DEPARTMENT OF ENERGY UNDER  
 CONTRACT NO. DE-AC52-07NA27344.  
 ANY REPRODUCTION, DISSEMINATION AND/OR  
 FABRICATION IS PROHIBITED WITHOUT THE  
 PERMISSION OF COGNIZANT LLNS PERSONNEL.

AR		VHB TAPE .006" THICK		
1		STAINLESS STEEL, 304		
QTY	PART OR DRAWING NUMBER	MATERIAL DESCRIPTION/DESCRIPTION		

CLASSIFICATION: UNCLASSIFIED



CONTRACT NO	CLASSIFIED BY	APPROVALS	DATE	TITLE
	TANGZ3	HAWKINS4	9/29/2010	ARC INITIATION EXPER
	TANGZ3	HAWKINS4	9/29/2010	ARC CHAMBER
	TANGZ3	HAWKINS4	9/29/2010	CONNECTOR CLAMP W

UNLESS OTHERWISE SPECIFIED DIMENSIONS IN INCHES TOLERANCES ARE: DO NOT SCALE FROM DRAWING	CHECKED	DATE	DRAWING NUMBER
	TANGZ3	9/29/2010	LEA09-56
NEXT ASST	USED ON	SCALE	
		2:000	

CLASSIFICATION:  
UNCLASSIFIED

ZONE	LT/R	DESCRIPTION	REVISIONS	DRAWN	CHECKED	APP'D
/	AA	INITIAL RELEASE		HAWKINS4	TANG23	TA

UNLIMITED DISTRIBUTION/CLASSIFICATION: UNCLASSIFIED

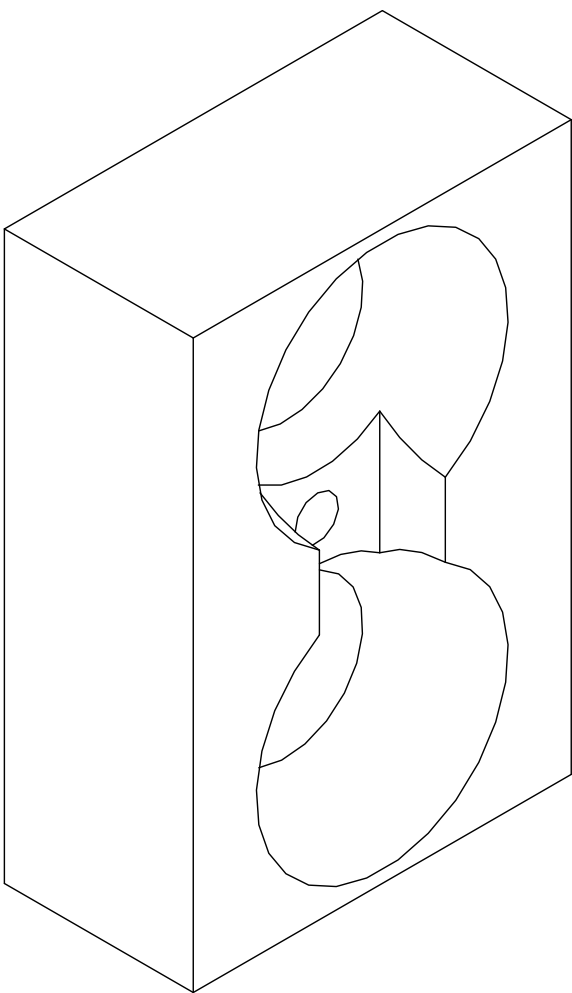
NOTES: UNLESS OTHERWISE SPECIFIED  
101. ALL DIMENSIONS ARE IN INCHES.

- 102. APPLICABLE STANDARDS AND SPECIFICATIONS:  
ASME Y14.5M-1994, DIMENSIONING AND TOLERANCING  
ASME Y14.38, ABBREVIATIONS AND ACRONYMS  
ASME Y14.36M, SURFACE TEXTURE SYMBOLS  
ANSI AWS A2.4, STANDARD SYMBOLS FOR WELDING
- 103. 63 FINISH ALL MACHINED SURFACES PER ASME B46.1, SURFACE TEXTURE.
- 104. REMOVE ALL BURRS AND BREAK EDGES .010 .030 CHAMFER OR RADIUS. RADI MUST MAKE A SMOOTH TRANSITION WITH ADJACENT SURFACES.

- 105. PERMANENTLY MARK PART PER MEL98-001 WITH DRAWING NUMBER, TABULATION NUMBER, REVISION LETTER, MANUFACTURER CAGE CODE AND PART SERIAL NUMBER IF APPLICABLE. APPROXIMATELY WHERE SHOWN IN 3D MODEL FOR CHAIN PRIORITY MARKING PART.
- 106. BAG AND TAG PART WITH DRAWING NUMBER, TABULATION NUMBER, REVISION LETTER, MANUFACTURER CAGE CODE, AND PART SERIAL NUMBER IF APPLICABLE.

- 108. ESTIMATED WEIGHT IS .0111 lb
- ESTIMATED VOLUME: .225 in<sup>3</sup>
- ESTIMATED SURFACE AREA: 3.558 in<sup>2</sup>

IDENTIFICATION  
502. ENGRAVE DRAWING NUMBER, TABULATION NUMBER, REVISION LETTER, MANUFACTURER CAGE CODE AND PART SERIAL NUMBER IF APPLICABLE. APPROX WHERE SHOWN IN .125 HIGH CHARACTERS PER MEL98-001.



PART NUMBER  
FORMERLY LEA09-50016

QTY	PART OR IDENTIFYING NUMBER	MATERIAL DESCRIPTION OR NOMENCLATURE	W/
1	LEA09-500039 -02	MACOR	
2	LEA09-500039 -01	PEEK, UNFILLED	

CLASSIFICATION: UNCLASSIFIED

Status: RELEASED WHO: 01  
Fabrication Quantity: 2 EACH-01, 1 EACH-02  
Project / Task Number: Due: 6/17/2010

THIS DRAWING WAS CREATED BY THE LAWRENCE LIVERMORE NATIONAL SECURITY, LLC (LLNS) WHICH OPERATES LAWRENCE LIVERMORE NATIONAL LABORATORY (LLNL) FOR THE U.S. DEPARTMENT OF ENERGY UNDER CONTRACT NO. DE-AC02-07NA27344. ANY REPRODUCTION, DISSEMINATION AND/OR FABRICATION IS PROHIBITED WITHOUT THE PERMISSION OF COGNIZANT LLNS PERSONNEL.

UNLIMITED DISTRIBUTION/CLASSIFICATION: UNCLASSIFIED

04:43 PM

MODEL: LEA09-500039.dwg INVENTOR: 2011

CLASSIFICATION: UNCLASSIFIED



CONTRACT NO	CLASSIFICATION	DATE	TITLE
	UNCLASSIFIED	04/02/10	ARC INITIATION EXPER
	UNCLASSIFIED	04/02/10	ARC CHAMBER
	UNCLASSIFIED	04/02/10	HEMI INSULATOR CUST

UNLESS OTHERWISE SPECIFIED DIMENSIONS AND TOLERANCES ARE: DECIMALS ± .005 ANGLES ± 1° DO NOT SCALE FROM DRAWING

DATE	BY	CHKD	SCALE
04/02/10	TANG23	D	2
04/02/10	TANG23		2000



LAWRENCE LIVERMORE NATIONAL LABORATORY

ARC INITIATION EXPER

ARC CHAMBER

HEMI INSULATOR CUST

DRAWING NUMBER: LEA09-500039



7

6

5

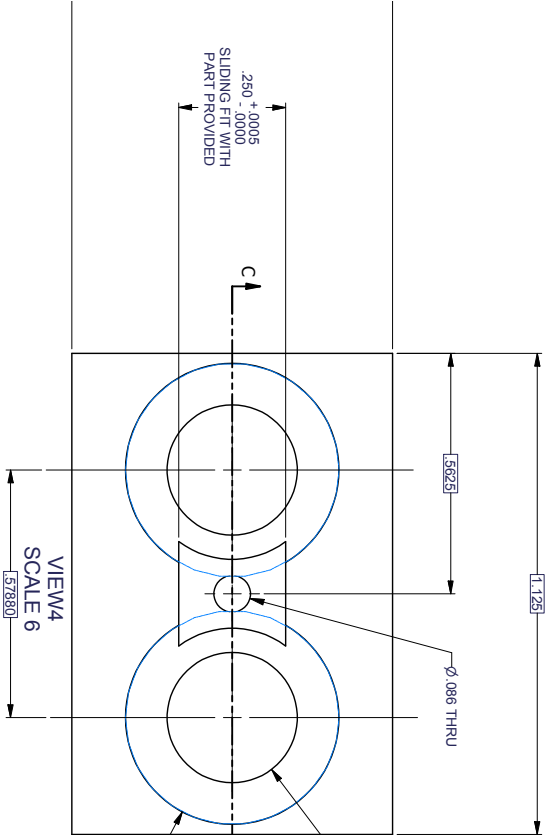
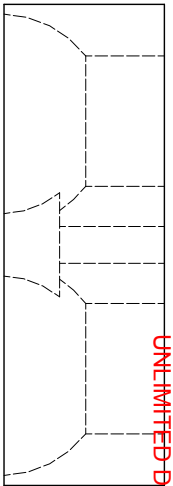
4

3

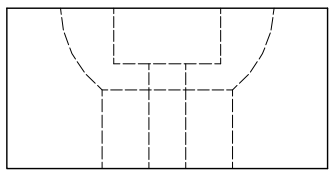
2

CLASSIFICATION:  
UNCLASSIFIED

UNLIMITED DISTRIBUTION/CLASSIFICATION: UNCLASSIFIED



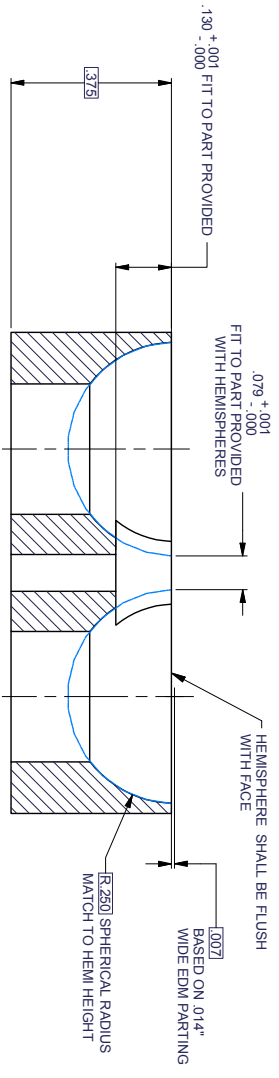
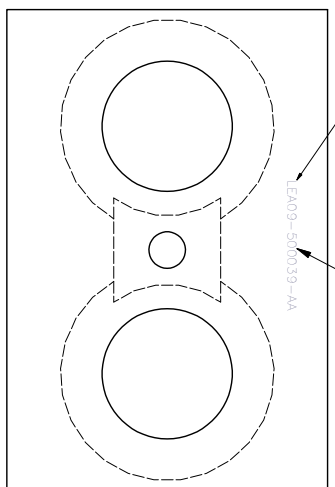
$\phi .4998$   
BASED ON .014"  
WIDE EDM PARTING  
 $\phi .500$  SPHERE



SEE NOTE 502

MARKING OPTION,  
 $\phi .090$  DRILL POINT

LEA09-500039-AA



SECTION C-C  
SCALE 6

UNLIMITED DISTRIBUTION/CLASSIFICATION: UNCLASSIFIED

04:49 PM

MODEL: LEA09-500039-AA

INVENTOR: 2011

CLASSIFICATION:  
UNCLASSIFIED

CLASSIFICATION: UNCLASSIFIED

Beam Research	
WBS	
CONTRACT NO.	14067
SIZE	D
DATE	14067
SCALE	2.000
DRAWING NUMBER	LEA09-50

STANDARDS AND SPECIFICATIONS:  
 M-1894, DIMENSIONING AND TOLERANCING  
 18, ABBREVIATIONS AND ACRONYMS  
 1904, SURFACE FINISHES AND PROFILES  
 A2.4, STANDARD SYMBOLS FOR WELDING  
 L MACHINED SURFACES PER ASME B46.1, FINISH TEXTURE.

BURRS AND BREAK EDGES .010  
 R OR RADIUS, RADI  
 A SMOOTH TRANSITION WITH ADJACENT SURFACES.

1.1. MARK PART PER MEL98-001 WITH DRAWING  
 TABULATION NUMBER, REVISION LETTER, MANUFACTURER CAGE  
 PART SERIAL NUMBER IF APPLICABLE APPROXIMATELY WHERE  
 125 HIGH CHARACTERS, MARKING PROCESS  
 COVERED BY LINTL PRIOR TO MARKING PART.

G PART WITH DRAWING NUMBER, TABULATION NUMBER,  
 LETTER, MANUFACTURER CAGE CODE, AND PART SERIAL  
 APPLICABLE.

WEIGHT IS .009 lb  
 VOLUME IS .0007 in<sup>3</sup>  
 SURFACE AREA .557 in<sup>2</sup>

IRE PART PER MEL98-023, ENGINEERING MODEL BASED  
 URNING, (EMBM), OF HARDWARE USING COMPUTER GENERATED  
 ELS, DISREGARD MODEL TOLERANCES.

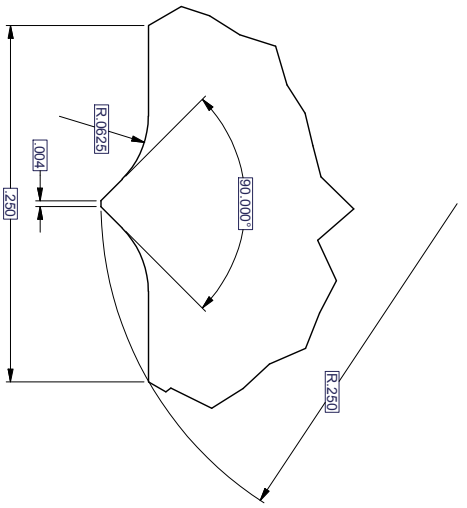
IONS ARE BASIC HAVING A PROFILE TOLERANCE OF  
 (SME Y14.5M-1994).

HING  
 - PER MEL99-009 G-II.

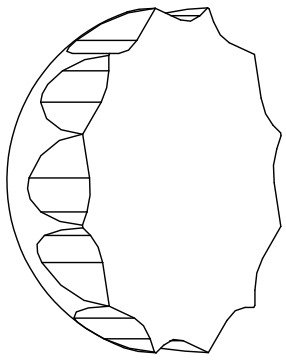
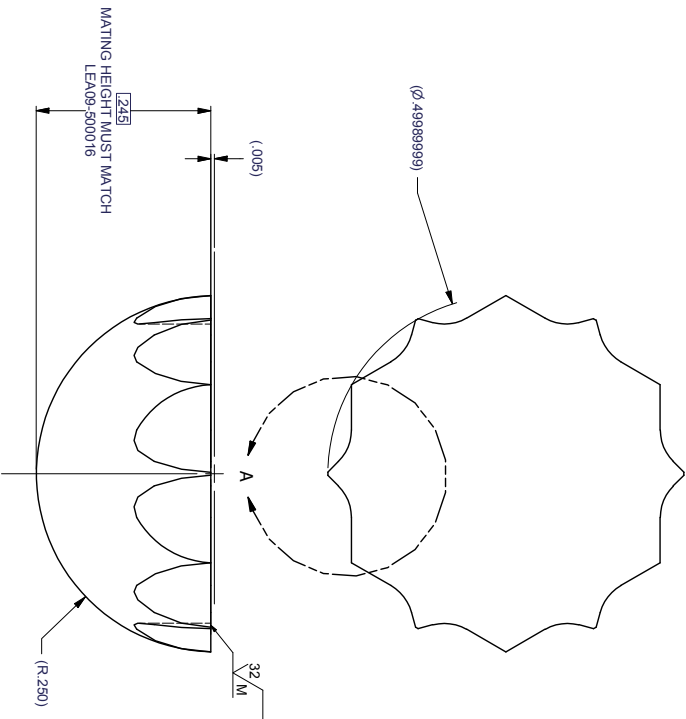
CLASSIFICATION:  
 UNCLASSIFIED

ZONE	LTR	DESCRIPTION	REVISIONS	DRAWN	CHECKED	APP
/	AA	INITIAL RELEASE	HAWKINS4	TANG23	TA	

UNLIMITED DISTRIBUTION/CLASSIFICATION: UNCLASSIFIED



DETAIL A  
 SCALE 20 : 1



Status: QUOTATION Who  
 Fabrication Quantity: 1 PAIR PER MATL  
 Project : task Number : 5290-959023 Due : 10/21/2010

THIS DRAWING WAS CREATED BY THE  
 LAWRENCE LIVERMORE NATIONAL SECURITY, LLC  
 (LLNS) WHICH OPERATES LAWRENCE  
 LIVERMORE NATIONAL LABORATORY (LLNL)  
 FOR THE U.S. DEPARTMENT OF ENERGY UNDER  
 CONTRACT NO. DE-AC02-07NA27344.  
 ANY REPRODUCTION, DISSEMINATION AND/OR  
 FABRICATION IS PROHIBITED WITHOUT THE  
 PERMISSION OF COGNIZANT LLNS PERSONNEL.

PAIR	LEA09-500040 -03	OHFC COPPER
1	LEA09-500040 -02	COPPER TUNGSTEN WISSCLAS
2	LEA09-500041 -01	TUNGSTEN CARBIDE BALL, GRADE 25, TYPE C1 OR C2 6% COBALL, .500 DIAMETER, +/- .0001, 959K87
QTY	PART OR SERIAL NUMBER	MATERIAL, DESCRIPTION OR IDENTIFICATION

CLASSIFICATION: UNCLASSIFIED

INCH  
 THIRD ANGLE PROJECTION

CONTRACT NO  
 CLASSIFIED BY  
 TANG23  
 APPROVALS

DATE  
 10/18/2010  
 TITLE  
 ARC INITIATION EXPER

ORGANIZATION  
 LAWRENCE LIVERMORE NATIONAL SECURITY  
 HAWKINS4  
 DATE  
 10/18/2010  
 TITLE  
 ELECTRODE - HEXAGON

DESIGNS AND DIMENSIONS SPECIFIED  
 UNLESS OTHERWISE SPECIFIED  
 DIMENSIONS IN INCHES  
 TOLERANCES ARE:  
 DECIMALS ± .005 ANGLES ± 1°  
 DO NOT SCALE FROM DRAWING

DATE	BY	DESCRIPTION
10/18/2010	TANG23	DESIGN
10/18/2010	TANG23	CHECK
10/18/2010	TANG23	APPROVE
10/18/2010	TANG23	DRAWING

UNLIMITED DISTRIBUTION/CLASSIFICATION: UNCLASSIFIED

CLASSIFICATION:  
 UNCLASSIFIED

DATE	BY	DESCRIPTION
10/18/2010	TANG23	DESIGN
10/18/2010	TANG23	CHECK
10/18/2010	TANG23	APPROVE
10/18/2010	TANG23	DRAWING

Beam Research  
 LAWRENCE LIVERMORE NATIONAL LABORATORY  
 14067 LEA09-500040-03

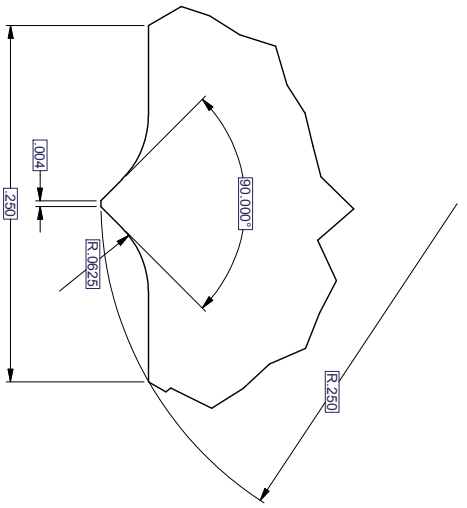
OTHERWISE SPECIFIED	7	6	5	4	3	2
IONS ARE IN INCHES.						
CLASSIFICATION: UNCLASSIFIED						
ZONE /	LTR	DESCRIPTION	REVISIONS	CHECKED	APP	
AA		INITIAL RELEASE	HAWKINS4	TANG23	TM	

UNLIMITED DISTRIBUTION/CLASSIFICATION: UNCLASSIFIED

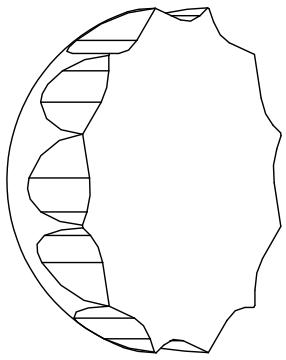
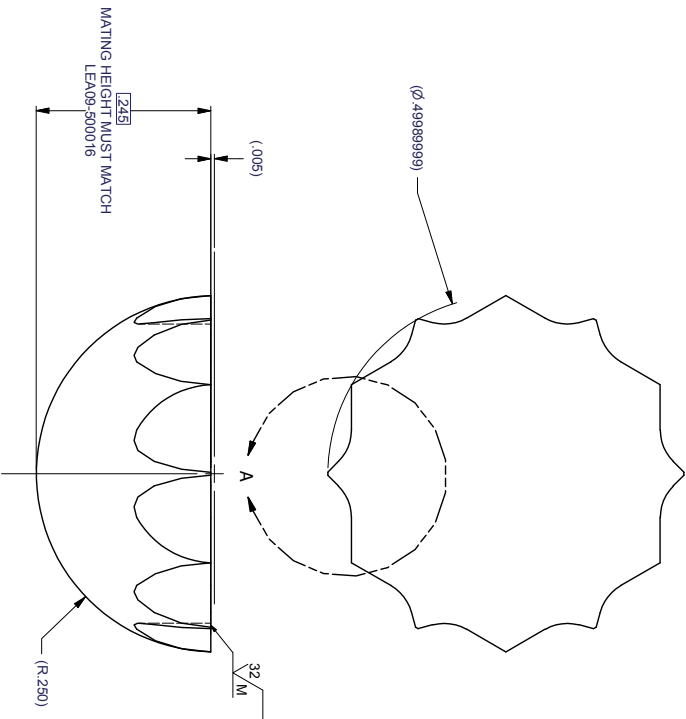
STANDARDS AND SPECIFICATIONS:  
 M-1894, DIMENSIONS AND TOLERANCING  
 18, ABBREVIATIONS AND ACRONYMS  
 604, SURFACE FINISH SYMBOLS  
 42.4, STANDARD SYMBOLS FOR WELDING  
 L MACHINED SURFACES PER ASME B46.1, FINISH  
 BURRS AND BREAK EDGES .010  
 R OR RADIUS, RADI  
 A SMOOTH TRANSITION WITH ADJACENT SURFACES.

1. Y MARK PART PER MEL 98-001 WITH DRAWING  
 TABULATION NUMBER, REVISION LETTER, MANUFACTURER CAGE  
 PART SERIAL NUMBER IF APPLICABLE, APPROXIMATELY WHERE  
 125 HIGH CHARACTERS, MARKING PROCESS  
 COVERED BY LINTL PRIOR TO MARKING PART.  
 G PART WITH DRAWING NUMBER, TABULATION NUMBER,  
 LETTER, MANUFACTURER CAGE CODE, AND PART SERIAL  
 APPLICABLE.  
 WEIGHT IS .009 lb  
 VOLUME IS .001 in<sup>3</sup>  
 SURFACE AREA: .557 in<sup>2</sup>

IRE PART PER MEL98-023, ENGINEERING MODEL BASED  
 URING, (EMBM), OF HARDWARE USING COMPUTER GENERATED  
 ELS, DISREGARD MODEL TOLERANCES.  
 IONS ARE BASIC HAVING A PROFILE TOLERANCE OF  
 (SME Y14.5M-1994).



DETAIL A  
 SCALE 20 : 1

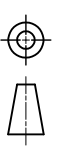


PAIR	LEA09-50004 1 -03	OHFC COPPER
1	LEA09-50004 1 -02	COPPER TUNGSTEN WISSCLAS
2	LEA09-50004 1 -01	TUNGSTEN CARBIDE BALL, GRADE 25, TYPE C1 OR C2 6% COBALT, .500 DIAMETER, +/- .0001
QTY	PART OR SERIAL NUMBER	MATERIAL DESCRIPTION/IDENTIFICATION

CLASSIFICATION: UNCLASSIFIED

Status: QUOTATION Who  
 Fabrication Quantity: 1 PAIR PER MATL  
 Project : task Number: 5290-959023 Due: 10/27/2010

THIS DRAWING WAS CREATED BY THE  
 LAWRENCE LIVERMORE NATIONAL SECURITY, LLC  
 (LLNS) WHICH OPERATES LAWRENCE  
 LIVERMORE NATIONAL LABORATORY (LLNL)  
 FOR THE U.S. DEPARTMENT OF ENERGY UNDER  
 CONTRACT NO. DE-AC52-07NA27344.  
 ANY REPRODUCTION, DISSEMINATION AND/OR  
 FABRICATION IS PROHIBITED WITHOUT THE  
 PERMISSION OF COGNIZANT LLNS PERSONNEL.

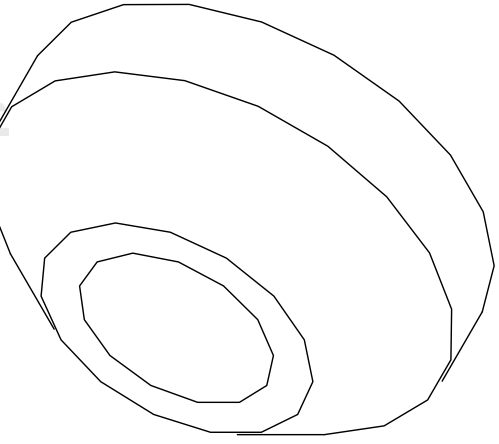
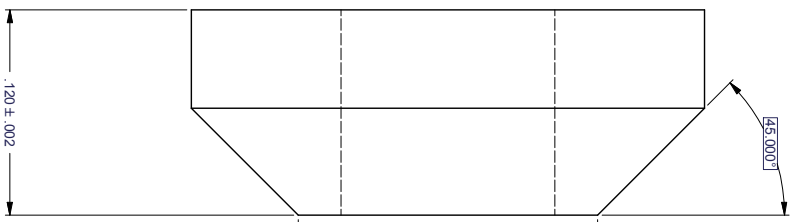
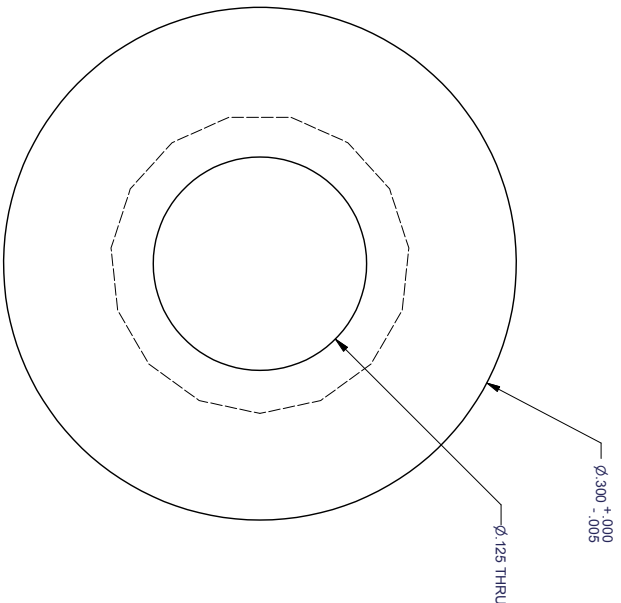


THIRD ANGLE PROJECTION	INCH
CONTRACT NO	WBS
CLASSIFIED BY	LAWRENCE LIVERMORE NATIONAL LABORATORY
APPROVALS	LAWRENCE LIVERMORE NATIONAL SECURITY
DATE	DATE
ORGANIZATION	TITLE
HAWKINS4	ARC INITIATION EXPER
TANG23	ARC CHAMBER
TANG23	ELECTRODE - HEXAGON
TANG23	SIZE
TANG23	CAGE CODE
D	14067
LEA09-50004	LEA09-50004
SCALE	2000

UNLIMITED DISTRIBUTION/CLASSIFICATION: UNCLASSIFIED

CLASSIFICATION:  
UNCLASSIFIED

ZONE	LTR	DESCRIPTION	REVISIONS	DRAWN	CHECKED	APP
/	AA	INITIAL RELEASE		HAWKINS4	TANG23	TM



UNLIMITED DISTRIBUTION/CLASSIFICATION: UNCLASSIFIED

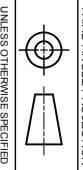
Status: RELEASED Who:   
 Fabrication Quantity: 4  
 Project / Task Number:

Done:   
 Date:   
 THIRD ANGLE PROJECTION

THIS DRAWING WAS CREATED BY THE  
 LAWRENCE LIVERMORE NATIONAL SECURITY, LLC  
 (LLNS) WHICH OPERATES LAWRENCE  
 LIVERMORE NATIONAL LABORATORY (LLNL)  
 FOR THE U.S. DEPARTMENT OF ENERGY UNDER  
 CONTRACT NO. DE-AC52-07NA27344.  
 ANY REPRODUCTION, DISSEMINATION AND/OR  
 FABRICATION IS PROHIBITED WITHOUT THE  
 PERMISSION OF COGNIZANT LLNS PERSONNEL.

QTY	PART OR IDENTIFYING NUMBER	MATERIAL DESCRIPTION OR NOMENCLATURE	W
		BRASS, CDA 360	

CLASSIFICATION: UNCLASSIFIED



UNLESS OTHERWISE SPECIFIED	CONTRACT NO	CLASSIFIED BY	DATE	TITLE
TOLERANCES UNLESS OTHERWISE SPECIFIED ARE: DIMENSIONS IN INCHES: DECIMALS & .005 ANGLES & ° DO NOT SCALE FROM DRAWING		TANG23	09/20/10	ARC INITIATION EXPER
APPROVALS		HAWKINS4	09/20/10	ARC CHAMBER
DESIGNED BY		TANG23	09/20/10	ELECTRICAL CONTACT
CHECKED BY		TANG23	09/20/10	
DATE				
SCALE				